NASA Technical Paper 1040

Study of the Application of an Implicit Model-Following Flight Controller to Lift-Fan VTOL Aircraft

Vernon K. Merrick

NOVEMBER 1977

NASA

NASA Technical Paper 1040

Study of the Application of an Implicit Model-Following Flight Controller to Lift-Fan VTOL Aircraft

Vernon K. Merrick
Ames Research Center
Moffett Field, California

National Aeronautics
and Space Administration

**Scientific and Technical
Information Office**

1977

NOMENCLATURE

$A(s)$	SRFIMF controller compensation transfer function
$A_N(s)$	numerator polynomial of $A(s)$
$A_D(s)$	denominator polynomial of $A(s)$
b	damping term in aircraft rigid-body second-order modes
b_w	wing span
c	stiffness term in aircraft rigid-body second-order modes
$\bar{c}_w$	wing mean aerodynamic chord
C_{pg}	control power gradient
$d(s)$	Laplace transform of external disturbances
$D(s)$	transfer function defining aircraft motion due to external disturbances
$DB_{\delta_{\dot{h}}}$	deadband in vertical motion of MK 1 VC lever or in quadrant motion of MK 2 VC lever
$DB_{\delta_{I_\phi}}$	deadband of lateral stick
$DB_{\delta_{I_\theta}}$	deadband of longitudinal stick
$DB_{\delta_{I_\psi}}$	deadband of rudder pedals
$DB_{\psi H}$	deadband in rudder pedal integrator
$DB\delta_{\dot{v}_x}$	deadband in horizontal motion of MK 1 VC lever or in thumbwheel of MK 2 VC lever
e	reciprocal of time constant of aircraft rigid-body first-order modes
E_{px}, E_{py}, E_{pz}	x, y, and z body axes coordinates of pilot station relative to aircraft center of gravity
f	value of the highly damped root of a simple SRFIMF-controlled system

F_{TFj}, F_{TWj}, F_{TAj}	forces produced by front, wing, and aft fans j = R(right), L(left)
g	acceleration due to gravity
$G(s)$	Laplace transform of airplane rigid-body modes
h	altitude of aircraft center of gravity
h_A	reference approach path altitude at start of horizontal deceleration
h_H	reference hovering altitude
h_R	altitude of reference approach path at distance R from touchdown point
$\dot{h}$	vertical velocity of airplane center of gravity
$\dot{h}_A$	vertical velocity at start of horizontal deceleration
$\dot{h}_C$	vertical velocity indicated by vertical flight director
$\dot{h}_P$	vertical velocity commanded by pilot
$\dot{h}_R$	reference vertical velocity at distance R from point of touchdown
$\ddot{h}$	vertical acceleration of airplane center of gravity
$\ddot{h}_{max}$	reference maximum vertical acceleration
$\ddot{h}_R$	reference vertical acceleration at distance R from touchdown point
h_{D_o}	constant term of polynomial $H_D(s)$
h_{N_o}	constant term of polynomial $H_N(s)$
$H(s)$	transfer function representing the dynamic behavior of control force or moment application
$H_D(s)$	denominator polynomial of $H(s)$
$H_N(s)$	numerator polynomial of $H(s)$
$i(s)$	Laplace transform of flight controller output signal
i_r, i_p, i_y	roll, pitch, and yaw altitude flight controller output signals

i_v, i_l	vertical and lateral flight-path flight controller output signals
IALTPH, *IALTPS*	roll and yaw attitude controller mode selection switch
IALTU	horizontal (longitudinal) flight-path flight controller mode selection switch
IPDAMP, *IQDAMP*, *IRDAMP*	attitude flight controller switches for roll, pitch, and yaw axes
ISASU1, *ISASV1*	flight-path flight controller switches for horizontal/vertical and lateral axes
I_x, I_y, I_z	airplane moments of inertia about x, y, and z body axes
I_{xv}	pilot input to vernier longitudinal force control
I_{xz}	product of inertia of airplane with respect to x and z body axes
I_{yv}	pilot input to vernier lateral force control
$I_{\theta T}$	pitch trim input
$I(s)$	transfer function relating aircraft response $x(s)$ to controller output $i(s)$, $I(s) = H(s)G(s)$
j_o	constant term in polynomial $J(s)$
$J(s)$	polynomial used to define $A(s)$
k, l, m, n	integers
k_{RL}	root locus gain for response-feedback controller
k_x	position feedback gain
$k_{\dot{x}}$	rate feedback gain
K	forward loop gain of SRFIMF controller
K_0	lateral velocity controller coupling gain component
K_1	roll controller forward gain component
K_2	roll controller forward gain component
K_3	roll controller coupling gain
K_4	roll controller rate feedforward gain

K_5	wing spoiler actuator input gain
K_6	lateral velocity controller input gain
K_9	lateral velocity controller coupling gain component
K_{10}	yaw controller forward gain component
K_{20}	yaw controller forward gain component
K_{30}	yaw controller coupling gain
K_{40}	wing louver actuator input gain
K_{50}	rudder actuator input gain
K_{60}	sideslip controller input gain
K_{70}	cascade louver actuator input gain
K_{80}	aft hood actuator input gain
K_{90}	sideslip controller coupling gain
K_{100}	pitch controller forward gain component
K_{200}	pitch controller forward gain component
K_{300}	pitch controller coupling gain
K_{500}	elevator actuator and tailplane actuator input gain
K_B	control mode phase-out gain
K_S	wing spoiler linearizing factor
$K_{\phi H}$	roll stick integrator gain
$K_{r\phi}$	gain of bank angle feedback into yaw controller
$K_{\psi H}$	pedal integrator gain
K_θ	pitch attitude feedback gain
$K_{\dot{\theta}}$	pitch-rate feedback gain
K_ϕ	roll attitude feedback gain
$K_{\dot{\phi}}$	roll-rate feedback gain
K_ψ	yaw attitude feedback gain

$K_{\dot{\psi}}$	yaw-rate feedback gain
K_{β}	sideslip angle feedback gain
$K_{\dot{\beta}}$	sideslip controller compensation gain
K_{w}	vertical velocity feedback gain
$K_{\dot{w}}$	vertical controller compensation gain
K_{2w}	vertical controller input gain
K_{3w}	vertical controller coupling gain
K_{u}	longitudinal velocity feedback gain
$K_{\dot{u}}$	longitudinal controller compensation gain
K_{2u}	longitudinal controller input gain (velocity command mode)
$K_{2\dot{u}}$	longitudinal controller input gain (acceleration command mode)
K_{3u}	longitudinal controller coupling gain
K_{2V_x}	longitudinal controller input gain (vernier velocity command mode)
K_{2V_y}	lateral controller input gain
K_{3V_y}	lateral controller coupling gain
K_{xv}	direct longitudinal force control gain
K_{yv}	direct side-force control gain
K_{v}	lateral velocity feedback gain
$K_{\dot{v}}$	lateral controller compensation gain
K_{x}	position feedback gain
$K_{\dot{x}}$	rate feedback gain
$K_{\ddot{x}}$	acceleration feedback gain or compensation gain
K_{RL}	root locus gain for SRFIMF controller

L_F, M_F, N_F	moments produced by propulsion system about x, y, and z body axes
$LM_{\delta_{I_\phi}}$, $LM_{\delta_{I_\theta}}$, $LM_{\delta_{I_\psi}}$	position limits of roll stick, pitch stick, and yaw pedals
$LM_{\phi c}$, $LM_{\theta c}$, $LM_{\psi c}$	roll, pitch, and yaw controller coupling limits
LM_{vc}	lateral velocity controller compensator limits
$LM_{\phi H}$	roll attitude hold authority limit
$LM_{\delta_{\dot{h}}}$	VC lever vertical controller command limit
LM_{VC_1}, LM_{VC_2}	vertical controller coupling limits
$LM_{\delta_{TH_i}}$	P lever travel limit
$LM_{\delta_{\dot{v}_x}}$	VC lever horizontal controller command limit
LM_{LC_1}, LM_{LC_2}	longitudinal controller coupling limits
LM_{ζ_1}, LM_{ζ_2}	T lever travel limits
$LM_{\delta_{v_x}}$	longitudinal controller vernier velocity command limit
$LM_{I_{xv}}$	direct longitudinal vernier force command limit
$LM_{\delta_{v_y}}$	lateral controller command limit
$LM_{I_{vy}}$	direct lateral vernier force command limit
LM_{LC}	lateral controller coupling limit
n_{xp}, n_{yp}, n_{zp}	load factors at pilot station along x, y, and z body axes
N_{GI}	engine speed command
$O_{\theta T}$	pitch trim actuator output
p_r	SRFIMF compensation poles
p, q, r	airplane rotation rates about x, y, and z body axes

R	horizontal distance between aircraft center of gravity and desired touchdown point
RPM	engine speed, rev/min
$SRFIMF$	state rate feedback implicit model-following
s	Laplace transform variable
t	time
U_E, V_E, W_E	velocities of aircraft relative to earth-fixed axes
v, w	SRFIMF controller internal variables
V_X	airplane longitudinal inertial velocity
V_Y	airplane lateral inertial velocity
V_{XA}	initial value of V_X on approach
V_{XC}	required value of V_X indicated by horizontal flight director
V_{XP}	value of V_X commanded by pilot
$\dot{V}_X$	airplane longitudinal inertial acceleration
$\dot{V}_Y$	airplane lateral inertial acceleration
$\dot{V}_{XC}$	required value of $\dot{V}_X$ indicated by horizontal flight director
$\dot{V}_{XP}$	value of $\dot{V}_X$ commanded by pilot
$\dot{V}_{X_{max}}$	maximum value of $\dot{V}_X$ on reference approach path
W	aircraft weight
$x(s)$	controlled variable
X_F, Y_F, Z_F	total fan thrust forces along x, y, and z body axes
y	localizer error
α_{CA}	thrust deflection angle due to deflection of louvers on forward fan cascades
α_{WI}	thrust deflection angle due to deflection of louvers on wing fan cascades

β	airplane sideslip angle
β_I	inertial sideslip angle; determines lateral position of velocity vector
$\dot{\beta}_I$	time derivative of β_I
γ	flight-path angle
γ_A	initial flight-path angle on approach
γ_{HD}	thrust deflection angle due to deflection of aft fan hoods
δ_E	elevator deflection angle
δ_F	flap deflection angle (constant at 50°)
δ_R	rudder deflection angle
δ_S	spoiler deflection angle
δ_{I_ϕ}, δ_{I_θ}, δ_{I_ψ}	pilot control inputs to roll, pitch, and yaw controllers (stick and pedals)
$\delta_{\dot{h}}$	pilot control input to vertical controller (VC lever)
δ_{v_x}, $\delta_{\dot{v}_x}$	pilot control input to horizontal (longitudinal) controller (VC lever)
δ_{v_y}	pilot control input to horizontal (lateral) controller
δ_{HT}	horizontal tailplane incidence
δ_{TH_i}	pilot control input to engines (P lever)
Δh	altitude deviation from reference approach path
$\Delta\phi_C$	error between lateral flight director bank-angle indication and actual bank angle ($\phi - \phi_C$)
ζ_{CA}	fan thrust deflection angle caused by rotation of forward fan cascades
ζ_{HD}	fan thrust deflection angle caused by aft hood extension
ζ_{TL}	thrust vector angle command input to thrust deflection system actuators

ζ_{WI}	fan thrust deflection angle caused by rotation of wing tip fan cascades
η	digital computer cycle time
θ	airplane pitch angle
$\dot{\theta}$	first time derivative of θ
$\ddot{\theta}$	second time derivative of θ
θ_P	pilot commanded pitch angle
θ_T	pilot commanded pitch trim angle
τ	time constant
τ_1, τ_2, τ_7, τ_8, τ_9	attitude flight controller compensation time constants
τ_u, τ_w, τ_v	flight-path flight controller compensation time constants
ϕ	airplane roll angle
$\dot{\phi}$	first time derivative of ϕ
$\ddot{\phi}$	second time derivative of ϕ
ϕ_C	required bank angle from lateral flight director
ϕ_{CA}	fixed roll inclination angle of forward and wing tip cascades
ψ	airplane yaw angle (heading)
$\dot{\psi}$	first time derivative of ψ
$\ddot{\psi}$	second time derivative of ψ

STUDY OF THE APPLICATION OF AN IMPLICIT MODEL-FOLLOWING FLIGHT CONTROLLER TO LIFT-FAN VTOL AIRCRAFT

Vernon K. Merrick

Ames Research Center

SUMMARY

Past piloted simulations of lift-fan V/STOL transport aircraft employing response feedback flight controllers have demonstrated important limitations of this controller concept. The search for an improved type of flight controller has led to the state rate feedback implicit model-following (SRFIMF) concept presented here. This controller is relatively simple: it provides an input/output relationship approximately that of any selected second-order system; it provides good gust alleviation and cross-axis decoupling; and it is self-trimming.

The SRFIMF flight controller was applied to all axes of a comprehensive mathematical model of a lift-fan V/STOL transport. Power management controls and pilot displays were designed to match the various modes of control provided by the SRFIMF flight controller. A piloted simulation was performed using the Ames six-degree-of-freedom simulator.

The overall fixed-operating-point handling qualities of the aircraft at a series of forward speeds from hover to 120 knots received pilot ratings varying from 1 to 3-1/2, thus indicating generally satisfactory flight controller characteristics.

Both straight and curved decelerating approaches to a vertical landing were tested in IFR zero-zero conditions. The pilot ratings varied from 2-1/2 for a $\gamma = -3°$ straight approach in calm air, to 4 for an initial $\gamma = -9°$ curved approach with 15-knot sidewind, 1.52 m/sec (5 ft/sec) rms turbulence and an engine failure. The improved tracking precision and reduced pilot workload noted in these tests, relative to those noted in previous lift-fan V/STOL simulations, were due both to the use of the SRFIMF controller concept and to the high degree of integration of the flight controller, power management controls, and displays.

INTRODUCTION

From a handling qualities viewpoint, one of the most important and challenging VTOL piloting tasks is that of flying a well-defined, curved, decelerating, IFR approach to a vertical landing. The problems associated with this task have been studied by the NASA in flight tests of the XV-5B (ref. 1) and, more recently, in piloted moving base simulations of a series of proposed

transport-type aircraft (refs. 2-10). In addition, the Navy has sponsored a study of the problem using the X-22A aircraft in a series of flight tests which resulted in the first IFR approach and vertical landing for this class of aircraft (ref. 11).

Because of the large powered-lift flight envelope of VTOL aircraft, the shape of the approach path and the variation of velocity along it need not be as rigidly specified as for CTOL aircraft. The type of approach selected can vary over a wide range to attain such operational objectives as noise and fuel reduction. However, this expanded operational flexibility is accompanied by some major piloting problems. To fly a well-defined VTOL approach, the pilot has to operate, continuously, two primary controls to produce the desired schedule of velocity and rate of descent. Even under ideal circumstances, the pilot workload is considerably greater than for the constant velocity and constant rate of descent approach typical of CTOL aircraft.

Both the NASA simulations and the X-22A flight tests show that significant workload reductions are obtained if the pilot is provided with direct, uncoupled control of the horizontal and vertical motion of the aircraft, rather than the more conventional thrust magnitude and thrust vector angle. The NASA simulations demonstrated that a need to periodically retrim the pitch axis, during an approach, tended to break the pilot's concentration on the principal tracking task and to cause a disproportionately large increase in workload. Furthermore, it was repeatedly demonstrated that sidewinds and turbulence can cause both a large increase in the pilot's workload and a significant degradation of his tracking performance.

These results suggest that, because of the inherently high workload associated with the primary task, important benefits may accrue from decoupling all the pilot control modes and from relieving the pilot of all secondary control tasks. These features, along with the generation of satisfactory stability and response characteristics, can be incorporated into the design of the flight controller. The general controller requirements are summarized as follows:

- Input-output relationship has the type of dynamic characteristics favored by pilots. For most applications, these characteristics approximate a second-order system with appropriate frequency and damping.

- Input-output relationship is insensitive to changes of airframe and propulsion characteristics.

- In the steady state, the commanded variables are independent of the external disturbances (self-trimming).

- Inherently strong gust alleviation.

- Inherently strong cross-axes decoupling.

The first requirement is largely the concern of existing VTOL fixed-operating-point handling qualities criteria (refs. 12 and 13). The remaining requirements go beyond the conventional bounds of VTOL handling qualities criteria. However, their importance to the VTOL approach task has already been demonstrated and there is a need for appropriate quantitative criteria. In the absence of such criteria, a possible approach to the achievement of acceptable VTOL handling qualities is to adopt a flight controller concept that has all the required characteristics to a high degree and, indeed, to a much higher degree than the response feedback controllers used in previous NASA piloted VTOL simulations. This is the approach explored here. The controller concept adopted here gets its high performance by using state rate (acceleration) feedback and is a member of the general class of implicit model-following controllers. These general features have led to the name state rate feedback implicit model follower (SRFIMF) to identify the controller.

This report first describes the controller concept in its simplest form, along with an heuristic argument suggesting a high performance. This introduction to the concept is followed by a more detailed, single-axis analysis of its application to the control of both position and velocity of a vehicle. The results of this analysis are compared with those obtained using a response feedback controller. It is then shown how the SRFIMF controller has been applied to all axes of one of the lift-fan VTOL transport models previously used in NASA piloted simulations. In addition, a pilot's master power management console, flight-director laws, and electronic display formats, designed to match the flight controller, are described. The entire system has been tested on a piloted six-degree-of-freedom simulator to obtain preliminary performance data. This simulation is described and the principal results are discussed.

PERFECT SRFIMF FLIGHT CONTROLLER

Consider the flight controller configuration shown in figure 1. The variable to be controlled is x, and both x and its time derivative $\dot{x}$ are assumed to be measured and used in feedback loops to modify the command signal x_c. The system element with the transfer function $K_x/(S + K_{\dot{x}})$ is used to provide the desired closed-loop dynamic performance. The analysis of this system is particularly simple. Thus, at junction 1,

$$v = w - s\dot{x} \tag{1}$$

and at junction 3,

$$w = v - \frac{K_x(x - x_c)}{s + K_{\dot{x}}} \tag{2}$$

Equations (1) and (2) when added give

$$-sx - \frac{K_x(x - x_c)}{s + K_{\dot{x}}} = 0 \tag{3}$$

or

$$(s^2 + K_{\dot{x}}s + K_x)x = K_x x_c$$

Equation (3) describes the closed-loop dynamic behavior of the entire system, including the airframe. If K_x and $K_{\dot{x}}$ are constant, the system is of second order and is independent of the airframe characteristics. The frequency and damping can be set to any desired values by choosing the appropriate values for K_x and $K_{\dot{x}}$. Since equation (3) is independent of external disturbances, the controller provides both self-trimming and perfect gust alleviation. Finally, each controlled variable of a multivariable controller of this type is governed by an equation similar to equation (3). Such a multivariable system is therefore uncoupled. The type of controller shown in figure 1 apparently satisfies, perfectly, all the requirements set forth in the Introduction.

The results of the analysis clearly run counter to basic engineering intuition and suggest that the perfect behavior of the controller must result from an unstated, unrealistic assumption. It is readily seen that the offending assumption is that the signal paths between the system elements have no transmission lags. The assumption is realistic when applied to any closed path containing a system element whose dynamic response is slow compared to the signal transmission time between the system elements. However, in any closed path containing no system elements (such as loop 1234 in fig. 1), the assumption is unrealistic since the response of this type of loop to an input is instantaneous. The instantaneous response of loop 1234 gives the controller its perfect performance, but also makes it physically unrealizable.

The significance of the controller shown in figure 1 is that it represents the limiting case of a class of realizable controllers whose performance resembles that of the unrealizable controller. The response of these controllers approximates that of any selected second-order system and this, plus the incorporation of state rate ($\dot{x}$) feedback, provides the rationale for the name "state rate feedback implicit model follower (SRFIMF)."

REALIZABLE SRFIMF FLIGHT CONTROLLERS

To make the controller configuration shown in figure 1 realizable, in the sense that analysis using the standard assumptions of control-system theory does not predict a performance that is physically impossible, it is clear from the previous discussion that loop 1234 must be modified. However, any modification that produces realizability also brings with it more analytical complexity and reduced generality. Thus, it becomes desirable, from both

conceptual and analytical viewpoints, to identify two types of SRFIMF controllers according to whether the controlled variable is either an aircraft position or velocity. The configurations of these two types of controllers are shown in figures 2 and 3. In figures 2 and 3, the modification adopted to produce realizability involves the addition of an element with a transfer function $A(s)$ in path 41. With this modification of loop 1234, additional control over the dynamic behavior of the system is obtained by introducing a controller coupling gain K (figs. 2 and 3).

The remainder of this section describes a rational procedure for selecting an appropriate $A(s)$. It is assumed, from the outset, that $A(s)$ can be expressed as a rational algebraic function; thus

$$A(s) = \frac{A_N(s)}{A_D(s)} \tag{4}$$

where $A_N(s)$ and $A_D(s)$ are polynomials in s of degree m and n, respectively.

If the systems shown in either figure 2 or 3 are to be realizable, then $A(s)$ must be such that $m < n$. The validity of this statement can be seen by considering the case where $A(s)$ is such that $m = n$. It is then possible to write $A(s)$ as a constant plus another rational algebraic function. The presence of the constant term makes a component of the response of loop 1234, due to an input, instantaneous. It follows that the system is unrealizable.

Position Controller

Consider now the position controller configuration shown in figure 2. At junction 1,

$$v(s) = A(s)w(s) - \ddot{x}(s) \tag{5}$$

and at junction 3,

$$w(s) = v(s) - K_{\dot{x}}\dot{x}(s) + K_x[x_c(s) - x(s)] \tag{6}$$

By adding equations (5) and (6), $v(s)$ is eliminated to produce

$$[1 - A(s)]w(s) = -(s^2 + K_{\dot{x}}s + K_x)x(s) + K_x x_c(s) \tag{7}$$

where it has been assumed that the initial conditions are zero.

Since, from figure 2,

$$i(s) = Kw(s)$$

equation (7) becomes

$$\left[\frac{1 - A(s)}{K}\right] i(s) = -(s^2 + K_{\dot{x}} s + K_x) x(s) + K_x x_c(s) \tag{8}$$

Equation (8) is the controller equation. This equation does not contain any terms that explicitly relate to either the airframe or the disturbances acting on it. The quantities K, K_x, $K_{\dot{x}}$, and the transfer function $A(s)$ are all available to the designer.

Before further progress in the analysis is possible, it is necessary to make some assumptions about the form of the equations that describe the airframe. This task is easier if approached with the following line of reasoning. If the realizable controller is to be successful, then it must meet the performance requirements given in the Introduction. Since the unrealizable limit of this class of controllers satisfies the requirements perfectly, it provides a large measure of confidence that the realizable controller will also satisfy the requirements. Since the performance of the unrealizable controller is independent of the airframe, it is highly probable that the realizable controller performance will not be strongly influenced by the form of the airframe equations. It follows that at least the major features of the realizable controller performance should be revealed even if the aircraft equations are assumed to be of the simplest reasonable form; furthermore, these features should be retained even if the true airframe equations depart markedly from the assumed form. The assumptions leading to a particularly simple form for the airframe equations are

- The equations are linear.
- The airframe transfer function can be approximated by the product of two transfer functions, one of which represents the high-frequency control actuation dynamics and the other the low-frequency rigid-body dynamics.
- The low-frequency rigid-body dynamics can be approximated by a single mode corresponding to each of the controlled variables. All modal coupling is therefore assumed to be rendered negligible by the controller.
- The coupling between the basic airframe controls (force and moment producers) is sufficiently small to be rendered negligible by the controller.

The direct implication of these assumptions is that the total aircraft system can be represented by a set of uncoupled, single-input, single-output controllers. It is essential, of course, that the controller design approached in this simplified way be checked by a more comprehensive analysis or by simulation.

The airframe equation of motion for a single variable $x(s)$ can now be expressed as

$$x(s) = I(s) i(s) + D(s) d(s) \tag{9}$$

with

$$I(s) = H(s)G(s) \tag{10}$$

where

$I(s)$ airframe transfer function between controller input $i(s)$ and controlled variable $x(s)$

$H(s) = \dfrac{H_N(s)}{H_D(s)}$ control actuation transfer function normalized so that $H_N(s) = H_D(s) = 1$ when $s = 0$

$G(S)$ rigid-body transfer function

$D(s)$ transfer function between disturbance $d(s)$ and controlled variable $x(s)$

For the position controller, the principal rigid-body mode transfer function is of the form

$$G(S) = \frac{C_{pg}}{s^2 + bs + c} \tag{11}$$

where C_{pg} is the control power gradient.

Combining equations (8), (9), (10), and (11) gives the following equation governing the controlled variable $x(s)$:

$$\left[1 - \frac{A_N(s)}{A_D(s)}\right] \frac{H_D(s)}{H_N(s)} \frac{s^2 + bs + c}{KC_{pg}} [x(s) - D(s)d(s)] = -(s^2 + K_{\dot{x}}s + K_x)x(s) + K_x x_c(s) \tag{12}$$

Since $A_N(s)$ and $A_D(s)$ are subject only to restrictions on their relative degree, they may be chosen to satisfy:

$$A_D(s) = H_D(s) \tag{13}$$

$$\left[1 - \frac{A_N(s)}{A_D(s)}\right] \frac{H_D(s)}{H_N(s)} = sJ(s) \tag{14}$$

where the polynomial $J(s)$ is open to selection. The restrictions on the selection of $J(s)$, necessary to ensure the correct relative degree of $A_N(s)$ and $A_D(s)$, is established later.

Equation (14) can be used to simplify equation (12):

$$\frac{j_o s}{kC_{pg}} \prod_{r=1}^{l} (s+p_r)(s^2+bs+c)[x(s) - D(s)d(s)] = -(s^2+K_x^{\bullet}s+K_x)x(s) + K_x x_c(s) \tag{15}$$

where $J(s)$ is assumed to be of the form $j_o \prod_{r=1}^{l}(s+p_r)$ where p_r, $r = 1,2,\ldots,l$ and j_o are all real and, when $l = 0$, $\prod_{r=1}^{l}(s + p_r) = 1$ by definition.

If $d(s)$ and $x_c(s)$ are both step functions at $t = 0$, then multiplying each side of equation (15) by s and applying the final value theorem shows that

$$\lim_{t\to\infty} x(t) = x_c(0^+) \tag{16}$$

Equation (16) shows that, in the steady state, the controlled variable $x(s)$ is equal to the commanded value $x_c(0^+)$ even in the presence of a steady disturbance $d(0^+)$. Therefore, the system is self-trimming (type 1 servo), a fact that provides the rationale for selecting equation (14) to define $A(s)$.

Combining equations (13) and (14) gives the following expression for $A_N(s)$:

$$A_N(s) = H_D(s) - sJ(s)H_N(s) \tag{17}$$

Let the degrees of $A_N(s)$, $J(s)$, $H_D(s)$, and $H_N(s)$ be m, l, n, and k, respectively. The degree of $sJ(s)H_N(s)$ is $l + k + 1$; $J(s)$ may be chosen so that

$$l + k + 1 = n \tag{18}$$

and

$$j_o h_{N_o} = h_{D_o} \tag{19}$$

where h_{D_o} and h_{N_o} are the coefficients of the highest power of s in $H_D(s)$ and $H_N(s)$, respectively. Conditions (18) and (19) simply ensure that the coefficient of s^n on the right-hand side of equation (17) is identically zero. Thus m, the degree of $A_N(s)$, is equal to or less than $n - 1$, thereby satisfying the relative degree of $A_N(s)$ and $A_D(s)$ required for the system to be realizable ($m < n$).

It follows from equations (18) and (19) that a suitable rational polynomial $J(s)$ is obtained if its degree, l, is equal to $n-k-1$ and its leading coefficient j_o is equal to h_{D_o}/h_{N_o}. The value of p_r, $r = 1,2,\ldots,l$ may be selected arbitrarily. The transfer function $A(s)$ can be determined, as a rational polynomial, from the expression:

$$A(s) = 1 - \frac{sH_N(s)}{H_D(s)} j_o \prod_{r=1}^{l}(s + p_r) \tag{20}$$

Velocity Controller

Consider now the velocity controller configuration shown in figure 3. The steps taken to obtain equation (8) yield the following analogous equation for the velocity controller:

$$\left[\frac{1 - A(s)}{K}\right] i(s) = \frac{-(s^2 + K_{\ddot{x}}s + K_{\dot{x}})\dot{x}(s) + K_{\dot{x}}\dot{x}_c(s)}{s + K_{\ddot{x}}} \tag{21}$$

The airframe equation of motion for the single variable $\dot{x}(s)$ has the form:

$$\dot{x}(s) = I(s)i(s) + D(s)d(s) \tag{22}$$

with

$$I(s) = H(s)G(s) \tag{23}$$

For the velocity controller, the principal rigid-body mode transfer function is of the form:

$$G(s) = \frac{C_{pg}}{s + e} \tag{24}$$

The equation governing $\dot{x}(s)$, analogous to equation (12) for the position controller, is

$$\left[1 - \frac{A_N(s)}{A_D(s)}\right] \frac{H_D(s)}{H_N(s)} \frac{s + l}{KC_{pg}} [\dot{x}(s) - D(s)d(s)]$$

$$= \frac{-(s^2 + K_{\ddot{x}}s + K_{\dot{x}})\dot{x}(s) + K_{\dot{x}}\dot{x}_c(s)}{s + K_{\ddot{x}}} \tag{25}$$

If equation (25) is multiplied by $s + K_{\ddot{x}}$ and quantities b and c are defined by

$$b \triangleq K_{\ddot{x}} + e \tag{26}$$

$$c \triangleq K_{\ddot{x}}e \tag{27}$$

then equation (25) has a form identical with equation (12). It follows that the procedure for selecting $A(s)$ for the velocity controller is identical to that for the position controller. Furthermore, the dynamic behavior of the velocity-controlled system is governed by equation (15) with $x(s)$ and $x_c(s)$ replaced by $\dot{x}(s)$ and $\dot{x}_c(s)$.

A Key SRFIMF Controller Example

Consider a control actuation transfer function of the form:

$$H(s) = \frac{H_N(s)}{H_D(s)} = \frac{1}{\tau s + 1} \tag{28}$$

This simple lag function provides a reasonably accurate description of the dynamic characteristics of many control actuation devices. An example using this lag function reveals the essential behavior of the SRFIMF controller in the simplest way.

From equation (28),

$$h_{N_o} = 1$$

$$h_{D_o} = \tau$$

$$n = 1$$

$$k = 0$$

Therefore, from equations (18) and (19),

$$\left.\begin{aligned} l &= 0 \\ j_o &= \tau \end{aligned}\right\} \tag{29}$$

and, from equation (20), noting that $\prod_{r=1}^{0}(s + p_r) \triangleq 1$,

$$A(s) = 1 - \frac{s\tau}{\tau s + 1} = \frac{1}{\tau s + 1} \tag{30}$$

Substituting the values for l and j_o from equations (29) into equation (15) gives the following characteristic stability polynomial in root locus form:

$$1 + \frac{K_{RL}(s^2 + K_{\dot{x}}s + K_x)}{s(s^2 + bs + c)} = 0 \tag{31}$$

where the root locus gain, K_{RL}, is given by

$$K_{RL} = \frac{KC_{pg}}{\tau} \tag{32}$$

Three distinct types of root loci correspond to equation (31) (shown in fig. 4). The zeros shown in figure 4 represent the selected (model) stability desired for the system, namely, second order with a damping factor of 0.75. The different types of root loci occur because the denominator polynomial $(s^2 + bs + c)$, corresponding to the stability of the rigid-body mode, may have either conjugate complex or real roots. If the roots are conjugate complex, the root loci is of the type shown in figure 4(a); if the roots are real, the root loci may be of the type shown in either figure 4(b) or 4(c). The root locus for the position-controlled system may be any of the types shown in figure 4, whereas the root locus for the velocity-controlled system can be only of the type shown in figure 4(c). The restriction on the form of the root locus for the velocity-controlled system occurs because, in this case, $s^2 + bs + c = (s + K_{\ddot{x}})(s + e)$ and, since $K_{\ddot{x}}$ is always selected to be positive, one of the poles must always be located on the negative real axis (fig. 4(c)).

The important point to note about figure 4 is that, as gain K_{RL} is increased, two of the roots tend toward the desired values (model) and the third root moves out along the negative real axis. Thus, when K_{RL} is sufficiently large,

$$s(s^2 + bs + c) + K_{RL}(s^2 + K_{\dot{x}}s + K_x) \approx (s^2 + K_{\dot{x}}s + K_x)(s + f) \tag{33}$$

Also, it follows from equation (33) that

$$f \to K_{RL} \quad \text{as} \quad K_{RL} \to \infty \tag{34}$$

Using equation (33) in conjunction with equation (15) and assuming $d(s) = 0$ gives the following expression for the response of the position-controlled vehicle due to an input $x_c(s)$:

$$x(s) \approx \frac{K_{RL}K_x x_c(s)}{(s + f)(s^2 + K_{\dot{x}}s + K_x)} \tag{35}$$

where it is assumed that K_{RL} is sufficiently large for equation (33) to be valid. The response of the velocity-controlled vehicle due to an input is identical in form to equation (35). Equation (35) shows that the response of the realizable SRFIMF controller is that of an ideal SRFIMF controller whose input is prefiltered with the simple lag function $K_{RL}/(s + f)$. Clearly, if f is large, the effect of this lag on the response of the controller will be small. In applications to aircraft control, it is desirable to make f higher than the effective frequency cutoff for pilot inputs. It can be seen, from the limit relationship (34), that when K_{RL} becomes infinite the lag function $K_{RL}/(s + f)$ can be replaced by unity, and the response to inputs becomes identical to that of the ideal controller. However, as before, the system is then unrealizable.

To obtain some idea of the response of the system to external disturbances, the frequency response of acceleration due to external forces or moments is required. If $d(s)$ is a force or moment on the vehicle, expressed as an acceleration, then

$$D(s) = \frac{G(s)}{C_{pg}} \tag{36}$$

Consider first the position-controlled vehicle (fig. 2). Substituting equation (29) into (15), using equations (11) and (36) for $D(s)$, and assuming $x_c(s) = 0$ yields

$$[s(s^2 + bs + c) + K_{RL}(s^2 + K_{\dot{x}}s + K_x)]x(s) = sd(s) \tag{37}$$

or

$$\frac{\ddot{x}(s)}{d(s)} = \frac{s^3}{s(s^2 + bs + c) + K_{RL}(s^2 + K_{\dot{x}}s + K_x)} \tag{38}$$

Substituting equation (33) into (38) and arranging the result in Bode form gives

$$\frac{x(i\omega)}{d(i\omega)} \approx \frac{(i\omega)^3}{K_x f\left(1 + \frac{K_{\dot{x}}}{K_x} i\omega - \frac{\omega^2}{K_x}\right)\left(1 + \frac{i\omega}{f}\right)} \tag{39}$$

In subsequent applications of the SRFIMF controller to VTOL aircraft, the position controller is used largely for attitude control. Published data on attitude control handling qualities criteria (ref. 14) indicate that preferred values of $K_{\dot{x}}$ and K_x are 3 and 4, respectively. These values are equivalent to an undamped frequency of 2 rad/sec and a damping factor of 0.75. The asymptotic Bode plot of equation (39), using these values of $K_{\dot{x}}$ and K_x, is shown in figure 5 for various values of f. Figure 5 shows that the controller attenuates the response of the vehicle to external disturbances for all disturbance frequencies, although the attenuation becomes negligibly small for frequencies greater than f. Below a frequency of $f/2$, the amplitude ratio is always less than 0.5; below a frequency of about 1 rad/sec, the amplitude ratio is insignificant for all practical purposes. The important point to note here is the powerful effect of f (position of the pole on the real axis in fig. 4) in determining the response of the system to external disturbances.

If the analysis that yielded equation (39) is repeated for the velocity controller, the corresponding result is

$$\frac{\ddot{x}(i\omega)}{d(i\omega)} \approx \frac{K_{\ddot{x}}(i\omega)^2\left(1 + \frac{i\omega}{K_{\ddot{x}}}\right)}{K_{\dot{x}} f\left(1 + \frac{K_{\ddot{x}}}{K_{\dot{x}}} i\omega - \frac{\omega^2}{K_{\dot{x}}}\right)\left(1 + \frac{i\omega}{f}\right)} \tag{40}$$

In subsequent applications, the velocity controller is used largely for flight-path control. Unfortunately, there is very little data available from which to obtain flight-path-control handling-qualities criteria for VTOL

aircraft. However, an undamped natural frequency of 1.25 rad/sec and a damping factor of 0.75 appear to be reasonable, as verified by simulation results described later. The values of $K_{\ddot{x}}$ and $K_{\dot{x}}$ corresponding to this frequency and damping are 1.76 and 1.57, respectively. The asymptotic Bode plot of equation (40), for these values of $K_{\ddot{x}}$ and $K_{\dot{x}}$, is shown in figure 6. Figures 5 and 6 are identical for frequencies above 2 rad/sec. Below 2 rad/sec, the velocity controller does not provide as much attenuation as the position controller, but is nevertheless still effective.

Note that if K_{RL} increases, so does f and, as shown in figures 5 and 6, the vehicle response to external disturbances decreases. In the limit when K_{RL} is infinite, f is also infinite and, as for the perfect SRFIMF controller, the vehicle does not respond to external disturbances. However, when this point is reached, the controller again becomes unrealizable.

Comparison of SRFIMF and Response Feedback Controllers

The type of response feedback attitude (position) controller used in the previous lift-fan V/STOL simulations (refs. 2, 4, and 7) is shown in figure 7. The corresponding controller equation is

$$i(s) = -k_{\dot{x}}\left(s + \frac{k_x}{k_{\dot{x}}}\right)x(s) + k_x x_c(s) \tag{41}$$

Combining equations (9), (10), (11), (28), (36), and (41) gives the following equation that describes the dynamics of the controlled vehicle:

$$\left[(\tau s + 1)(s^2 + bs + c) + C_{pg}k_{\dot{x}}\left(s + \frac{k_x}{k_{\dot{x}}}\right)\right]x(s) = C_{pg}k_x x_c(s) + (\tau s + 1)d(s) \tag{42}$$

If $d(s)$ and $x_c(s)$ are both step functions at $t = 0$, then multiplying each side of equation (42) by s and applying the final value theorem shows that

$$\lim_{t\to\infty} x(t) = \frac{C_{pg}k_x x_c(0^+) + d(0^+)}{c + C_{pg}k_x} \tag{43}$$

Equation (43) shows that this type of response feedback controller is not self-trimming (eq. (43) may be compared with eq. (16) for the SRFIMF controller). In other words, the system is a type 0 servo.

The characteristic stability polynomial corresponding to equation (42), expressed in root locus form, is

$$1 + \frac{k_{RL}\left(s + \frac{k_x}{k_{\dot{x}}}\right)}{\left(s + \frac{1}{\tau}\right)(s^2 + bs + c)} = 0 \tag{44}$$

where the root locus gain, k_{RL}, is given by

$$k_{RL} = \frac{k_{\dot{x}} C_{pg}}{\tau} \tag{45}$$

Equations (44) and (45) are comparable with equations (31) and (32) for the SRFIMF controller.

Typical root loci for the response feedback controlled vehicle are shown in figure 8. These loci are comparable with those shown in figures 4(a) and 4(b) for the SRFIMF-controlled vehicle. Unlike the SRFIMF controller root loci, those for the response feedback controller have a pole that depends explicitly on the time constant, τ, of the control actuator. To find the values of k_x and $k_{\dot{x}}$ that give a reasonably good approximation to the desired second-order stability characteristic (defined by the selected values of $K_{\dot{x}}$ and K_x), it is assumed that the form of the stability polynomial is

$$(s^2 + K_{\dot{x}} s + K_x)(s + f) = 0 \tag{46}$$

Equating coefficients of equations (44) and (46) yields the following equations for the real root f, the root locus gain, k_{RL}, and the feedback gain ratio, $k_x/k_{\dot{x}}$, corresponding to given values of K_x and $K_{\dot{x}}$:

$$f = \frac{1}{\tau} + b - K_{\dot{x}} \tag{47}$$

$$k_{RL} = K_{\dot{x}} f + K_x - \frac{b}{\tau} - c \tag{48}$$

$$\frac{k_x}{k_{\dot{x}}} = \frac{K_{\dot{x}} f - c/\tau}{k_{RL}} \tag{49}$$

Thus, with figure 8(a) as an example, as the root locus gain, k_{RL}, is increased from zero, one branch of the locus starts at the poles given by $s^2 + bs + c = 0$ and passes through the roots of $s^2 + K_{\dot{x}} s + K_x = 0$ when $k_{RL} = 30.75$. This value of k_{RL} is given by equation (48), using values of K_x and $K_{\dot{x}}$ of 4 and 3, respectively. The other branch of the locus starts at the pole given by $s + (1/\tau)$, and moves toward the zero given by $s + (k_x/k_{\dot{x}})$, where, from equation (49), $k_x/k_{\dot{x}} = 0.37$. At $k_{RL} = 30.75$, the value of the real root, f, is 6 (eq. (47)).

It can be seen by comparison of figures 4 and 8 that the root loci for the SRFIMF- and response-feedback-controlled vehicles differ considerably. With the SRFIMF-controlled vehicle, provided the real root f is greater than $K_{\dot{x}}$, the dominant roots establishing the vehicle stability are given, approximately, by $s^2 + K_{\dot{x}} s + K_x = 0$. Therefore, if the gain is set, initially, so that f is large compared with $K_{\dot{x}}$, then the SRFIMF-controlled vehicle stability is relatively insensitive to variations in the fundamental airframe parameters τ, C_{pg}, b, and c, since such variations primarily influence the value of f.

Examples of the root loci of the response-feedback-controlled vehicle shown in figure 8 demonstrate that variations in C_{pg}, b, and c can cause significant changes in all the roots and can therefore significantly change the stability characteristics of the vehicle. In addition, figure 9 shows that the value of f at the design point can be quite small, particularly if the control actuation time constant τ is large. Thus, for example, when $\tau = 0.25$ (fig. 9(c)), $f = 1$, which is considerably less than the value of 4 selected for $K_{\dot{x}}$. Moreover, equation (47) shows that if $(1/\tau) + b < K_{\dot{x}}$, then $f < 0$, the vehicle is unstable and the particular type of response-feedback controller considered here is unworkable.

It follows from equations (42) and (46) that, at the design point, the response $x(s)$ of the response-feedback-controlled vehicle to an input $x_c(s)$ is

$$x(s) = \frac{k_{RL}(k_x/k_{\dot{x}})x_c(s)}{(s+f)(s^2 + K_{\dot{x}}s + K_x)} \tag{50}$$

where it is assumed that $d(s) = 0$. Equation (50) is similar in form to equation (35) for the SRFIMF controller. The main difference between the performance of the two types of controller, in this instance, is in the magnitude of f at the design point. For example, figure 9(c) shows a value of 1 for the response-feedback-controlled vehicle, whereas the value of f for an SRFIMF-controlled vehicle is theoretically unlimited. However, in practice, other considerations will limit the value of f to about 10 for the SRFIMF-controlled vehicle. Therefore, the effective prefilter time constant for the response feedback controller can be as much as an order of magnitude higher than for the SRFIMF controller and this can cause the response to differ significantly from the desired second-order system response characteristic.

At the design point, equations (42) and (46) show that the frequency response of vehicle accelerations due to external forces or moments of the response-feedback-controlled vehicle is given by

$$\frac{\ddot{x}(i\omega)}{d(i\omega)} = \frac{1}{\tau K_x f}\left[1 + (K_{\dot{x}}/K_x)i\omega - \omega^2/K_x\right]\frac{(1 + \tau i\omega)}{(1 + i\omega/f)} \tag{51}$$

Figure 10 shows the amplitude response, given by equation (51), for the three cases shown in figure 9. Figure 10 also shows comparable results for the SRFIMF-controlled vehicle obtained using equation (39). It can be seen that the SRFIMF controller attenuates the effects of external disturbances much more than does the response feedback controller. Indeed, over a range of frequencies, the response-feedback controller amplifies the effect of the external disturbances. The principal reason for the better performance of the SRFIMF controller is because of its much smaller Bode gain. The ratio of the Bode gains of the SRFIMF and response-feedback controllers is $\tau f_{RF}/f_{SRFIMF}$, where f_{RF} and f_{SRFIMF} are the values of f for the two controllers. Typically, this Bode gain ratio lies between 0.01 and 0.1, which is equivalent to a dB difference between -20 and -40.

LIMITATIONS AND PROBLEMS OF THE SRFIMF FLIGHT CONTROLLER

It is important to examine, at least qualitatively, the effect of control actuation dynamics of higher order than the simple lag used in the previous example. Higher-order control actuation dynamics are common in certain types of VTOL aircraft, especially those that rely on engine and fan speed changes to produce the control forces and moments.

The general characteristic equation for an SRFIMF-controlled vehicle follows from equation (15); thus

$$1 + \frac{K_{RL}(s^2 + K_{\dot{x}}s + K_x)}{s\prod_{r=1}^{l}(s + p_r)(s^2 + bs + c)} = 0 \tag{52}$$

where

$$K_{RL} = \frac{KC_{pg}}{j_O} \tag{53}$$

Since the parameters p_r, $r = 1,2,\ldots,l$ are arbitrary, they can be given large, real, positive values, thus producing a series of poles distributed along real-negative axes of the s plane. Although, within the framework of the present theory, the values of p_r, $r = 1,2,\ldots,l$ can be made indefinitely large, in practice the corresponding transfer function $A(s)$ becomes progressively more difficult to produce. The difficulty of producing the desired $A(s)$ becomes particularly acute if the flight controller computer is digital since, generally, the larger the values of p_r the smaller the cycle time must be to provide an adequate representation of $A(s)$. This same problem is evident in the digital simulation of an SRFIMF-controlled vehicle. A rough, but useful, criterion here is that, if η is the cycle time of the computer, then to maintain an adequate representation of the continuous SRFIMF controller, $|(p_r)_{max}\ \eta| < 0.5$. Thus, for example, if the cycle time is 25 msec, then $|(p_r)_{max}|$ should be less than 20.

If the SRFIMF controller is mechanized using analog techniques, then it is likely that the values of p_r, $r = 1,2,\ldots,l$ can be set to higher values. However, again some physical limit to the magnitude of $(p_r)_{max}$ will exist, possibly because of the excitation of some high-frequency structural mode of the vehicle.

For second-order control actuation, where $l = 1$, typical root loci for $b = c = 0$ are shown in figure 11. It is evident that there can be two types of root locus depending on the value of p_1. Note that, as the gain is increased, one oscillatory mode approaches the desired mode given by $s^2 + K_{\dot{x}}s + K_x = 0$, while another oscillatory mode of progressively increasing frequency also eventually occurs. If the damping factor of this second oscillatory mode becomes small, its effect will become evident in the step response

of the overall system. Thus, unlike the previous example with its assumed first-order control actuation dynamics, it is not possible to obtain an increasingly better performance with increasing gain. To improve the performance of the systems shown in figure 11 beyond that corresponding to a certain limiting value of the gain, the value of p_1 must first be increased. But, as noted earlier, there is a limit to the maximum value of p_1 depending on other considerations. It is clear therefore that, as with other linear controllers, the SRFIMF controller has well-defined performance limitations. Furthermore, as the order of the control actuation dynamics increases, the problems previously noted become progressively more serious and the maximum performance progressively degraded.

The SRFIMF controller described thus far can cause some piloting problems in the event of saturation of the control forces or moments. Consider, for example, the case in which a value of $x_c(s)$ (fig. 2) is commanded which causes the control to saturate. The value of the acceleration, $\ddot{x}(s)$, will then fall to a relatively small value, but an error will exist, generally between $x_c(s)$ and $x(s)$. Since the controller is self-trimming, the loop 1234 in figure 2 will behave like an integrator. Any error of constant sign between $x_c(s)$ and $x(s)$ will cause the signal $w(s)$ to increase without bound. If, after a period of time during which the control is saturated, the input command $x_c(s)$ is reversed, it will take some time before the integrating function of loop 1234 reduces $w(s)$ to a value such that the control becomes unsaturated. This kind of behavior will appear to a pilot as an undesirable lag in the response of the vehicle to his control input.

A solution to this problem is to place a signal limiter in loop 1234, as shown in figure 12. The limits are set to the values of $\dot{i}(s)/K$ that cause steady-state control saturation.

Finally, a possible difficulty with the implementation of SRFIMF controllers may be caused by noise in the acceleration sensor output used in one of the feedback loops. This question must be examined in detail both theoretically and in practice.

SIMULATION MODEL OF LIFT-FAN VTOL TRANSPORT

General Description of Aircraft

The simulated aircraft (fig. 13) is a conceptual modification of a DC-9-10. The wings are reduced in span, a lift fan is added to each wing tip, two lift fans are submerged in the forward fuselage, and the original turbofan engines, located on the aft fuselage, are replaced by two lift/cruise fans. The fans are interconnected with ducting to permit gas energy transfer between pairs of fans (fig. 13) both for control and to prevent large unbalanced forces if an engine fails. In the powered-lift flight regime, change of forward speed, at a constant pitch angle, is achieved by forward and aft deflection of the thrust vectors of all six fans. Lateral translation, at a constant bank angle, is achieved by lateral deflection of the thrust vectors of

all six fans. Pitch and roll control at low speeds is achieved by differential fan thrust modulation using hot gas "energy transfer and control" (ETaC) (ref. 15). Yaw control at low speeds is achieved by differential lateral deflection of the thrust vector of the forward and aft fans. The low-speed control system is coupled in parallel with the conventional flight-control surfaces of the aircraft. The latter are the same as for the unmodified DC-9-10, except that the ailerons are assumed to be removed and roll control is obtained exclusively through wing spoilers.

Originally, this V/STOL transport was assumed to be equipped with a response-feedback controller and was simulated on the Ames six-degree-of-freedom simulator (S.01) and on the Ames Flight Simulator for Advanced Aircraft (FSAA). The results of these simulations are given in references 5, 6, and 8. For the simulation described here, the response-feedback controller is replaced by an SRFIMF flight controller. This controller concept is applied to all axes of the aircraft. The basic philosophy adopted in the design of the flight controller is that the pitch attitude and the horizontal and vertical translation modes should be uncoupled. This decision reflects the opinion of pilots who participated in a previous lift-fan V/STOL transport simulation (ref. 8). With the adoption of this design philosophy, it becomes convenient to divide the controller into two parts: an attitude flight controller (fig. 14) and a flight-path flight controller (fig. 15). It is assumed that the controller operates in parallel with a "straight-through" system that connects the pilot controls directly to the force- and moment-producing devices on the aircraft. It is further assumed that the controller is a duplex system and has full control authority. If the flight controller in a given axis fails, it is assumed that its output is automatically disconnected from the straight-through system. The pilot then continues to control the axis that contains the failed controller with the straight-through system. It follows that single-channel flight controller failures are passive.

Figures 14 and 15 provide a complete flow diagram of the simulation model of the aircraft. A complete description of the mathematical models used to simulate the various components shown in figures 14 and 15 is given in appendices A to D. Appendix A gives the numerical values of the flight controller parameters shown in figures 14 and 15 and gives the mathematical models used to simulate the various actuators in the control system. The engine and fan simulation models, including the failure logic, are described in appendix B, while the total forces and moments on the aircraft due to the propulsion system are calculated from equations given in appendix C. Appendix D contains the equations, coefficients, and stability derivatives required to compute the aerodynamic forces and moments acting on the aircraft. Since the investigation is restricted to powered-lift flight (0-120 knot), the aerodynamic data in appendix D are given for a constant wing flap angle of 50°. The kinematic equations, equation of motion, atmospheric turbulence model, and landing gear equations are the standard ones used for flight simulation at Ames Research Center (ref. 16).

The principal weight, inertia, and dimensional characteristics of the aircraft are given in table 1.

Pilot Controls

The pilot controls consist of an articulated stick (smaller moment arm for roll than for pitch), conventional rudder pedals, and a three-lever master power management console. The control stick and rudder pedal displacements and forces are given in tables 2 and 3.

The two types of master power management controls tested are shown in figures 16 to 20. Normally, with the flight-path flight controller in operation, the pilot controls the aircraft's longitudinal velocity (or longitudinal acceleration) and vertical velocity with the velocity command (VC) lever. The power (P) lever and the transition (T) lever are driven by servomotors so that, in normal operation, their positions always correspond closely to the power and thrust vector angle commanded by the flight-path flight controller. The servomotors drive the P and T levers through electric clutches at rates up to 50°/sec.

If the flight-path controller fails, the servomotors are automatically stopped the VC lever electrically disconnected from the flight-path flight controller. The pilot then pushes the VC lever forward through a spring-loaded stop (and switch) at the end of its active travel farthest awas from the pilot (fig. 16). This action moves the VC lever out of the way of the pilot and causes the electric clutches, in both the P and T lever servodrives, to disengage. The pilot can then resume flight-path control by operating the P and T levers manually.

A thumb control on the right side of the P lever (figs. 16 and 17) activates the clutch on the T lever and drives the T lever at a rate proportional to thumb pressure. The maximum T lever angular rate, when operated by the P lever thumb control, is 20°/sec. This thumb control effectively enables both engine power and thrust-vector angle to be controlled from a single lever. The other thumb control located on top of the P lever (figs. 16 and 17) is a two-axis proportional force transducer used by the pilot to command vernier thrust forces (through thrust deflection) in the horizontal plane. Both thumb controls on the P lever are available to the pilot only when the flight-path flight controller is not operating.

There are two types of VC lever. The MK1 VC lever is shown in figures 16, 17, and 18, and the MK2 VC lever in figures 19 and 20. The MK1 VC lever is a two-axis linear motion device. A detent is located at the midpoint of the vertical travel and corresponds to zero vertical velocity. A detent is also located on the horizontal travel, but this has two alternate, selectable, positions corresponding to the zeros of the two selectable horizontal (longitudinal) controller modes: namely, horizontal velocity command and horizontal acceleration command. To provide the pilot with tactile indication of the vertical position of the MK1 lever, three protrusions are provided on the handle (figs. 16 and 18). As the lever is moved vertically, the location of one of the protrusions relative to the other two changes, and this change is sensed through the palm of the pilot's hand. When all the protrusions are in line, the lever is in the vertical detent.

The MK2 VC lever (figs. 19 and 20) is of the quadrant type and resembles the P lever. However, unlike the P lever, the thumb-operated control on the

top left of the handle is a small, nonself-centering wheel potentiometer (figs. 19 and 20). The potentiometer has a travel of ±70°, a detent at zero, and a small protrusion on the rim at the center of its travel. The protrusion provides the pilot with a tactile indication of the wheel rotation relative to zero (detent). The lever has a detent at its midtravel point. Lever displacement is used to command the vertical velocity and the thumb wheel is used to command either of the alternate horizontal (longitudinal) control modes. The angular travel of the MK2 VC lever is the same as that of the P lever and has the same type of spring-loaded stop and inactive region as for the MK1 VC lever.

On top of both types of VC levers is a thumb-operated, two-axis proportional force transducer similar to that on the P lever. This thumb control permits the pilot to command vernier translational velocities in the horizontal plane and is used to precisely position the aircraft over the required touchdown point. The location of the power management console relative to the control stick and pilot seat is shown in figure 17.

Flight Controller

The flight controller is designed to provide the pilot with the control modes shown in table 4. Most of these control modes were tested in previous lift-fan V/STOL transport simulations and were found to be satisfactory for most tasks. The alternate control modes shown in table 4 for roll in the 0-20-knot speed range, yaw in the 30-120-knot speed range, and longitudinal axis in the 0-120-knot speed range are included because they hold promise of providing more desirable handling qualities for some tasks. Also, a vernier horizontal velocity command mode (in both horizontal axes), using thrust deflection, is included in the SRFIMF controller design in the hope that it will provide the pilot with a control mode more suitable for precise station keeping in hover.

The pilot commands to the attitude flight controller are through a conventional stick and pedals. The stick inputs into the pitch, roll, and yaw channels are denoted by δ_{I_θ}, δ_{I_ϕ}, and δ_{I_ψ} (fig. 14). The output from the pitch controller, i_p, passes to the elevator and tailplane actuators and to the energy transfer and control (ETaC) valve and thrust spoiler actuators of the forward and aft fuselage-mounted fans. Whereas in the previous simulations (refs. 5, 6, and 8) the tailplane was operated separately from the elevator and was used for trim only, in the present arrangement the elevator and tailplane are operated together, with the signal to the tailplane passing first through a low-pass filter and deadband (see fig. 54 in appendix A). Thus, the tailplane does not respond to the high-frequency components in the pitch controller signal and acts in a "pitch trim follow-up" mode to ensure that full elevator power is always available. Pitch trim in the present arrangement is achieved by biasing the input signal to the pitch controller at a constant rate equivalent to 4° of pitch per second.

The output of the roll controller, i_r, passes to the wing spoiler actuators and to the ETaC valve and thrust spoiler actuators of the wing-tip fans. The wing spoilers are assumed to be operated through a cam system

designed to "linearize" the spoiler rolling moment/deflection characteristic (see fig. 51, appendix A).

The output of the yaw controller, i_y, passes to the rudder actuator and to actuators that move the fan nozzle cascades to produce differential sideways thrust components from the forward and aft fuselage fans.

Note that the quantities used in the feedback loops of the attitude controller are the Euler angle rates and accelerations rather than the corresponding quantities measured relative to the aircraft's body-fixed axes. Although body-fixed angular rates and accelerations are probably easier to obtain, their use can result in significant controller errors. For example, it is well known that, with zero rate of change of pitch angle ($\dot{\theta} = 0$),

$$q = r \tan \phi \tag{54}$$

where

q pitch rate in body axes

r yaw rate in body axes

ϕ bank angle

and, in a steady-state banked turn,

$$r = \frac{g \tan \phi}{V_a} \tag{55}$$

where

g gravitational acceleration

V_a true airspeed

Combining equation (54) and (55) yields

$$q = \frac{g \tan^2 \phi}{V_a} \tag{56}$$

Therefore, in a 30° banked turn at 30-knots TAS, the pitch rate (from eq. (56)) is 12.13°/sec even though $\dot{\theta} = 0$. If q rather than $\dot{\theta}$ were used in the pitch-controller feedback loop, a steady-state error of magnitude $(K_{\dot{\theta}}/K_{\theta}) \times 12.13 = 9.1°$ would result. This pitch error is clearly unacceptably large.

The aircraft transient responses due to input pulses in roll, pitch, and yaw at hover, 60 knots, and 120 knots are shown in figure 21. It can be seen that, allowing for the changes of roll control mode with speed (table 4), the aircraft responses are similar to those of the desired second-order system.

The response in yaw at 120 knots differs from that at hover and 60 knots because of saturation of the yaw control. However, this latter example serves to demonstrate that the controller is well behaved, even when control saturation occurs.

A comparison of the response of the aircraft to a roll input pulse for the two types of yaw control mode (table 4) at 30 knots is shown in figure 22. The only difference between these two responses is that, for the yaw rate system with bank-angle feedback, the sideslip angle tends to build up slowly with time, reaching about 5° after 35 sec.

The pilot commands to the flight-path flight controller are through the master power management control console described under "Pilot Controls." The inputs from the master power management control console to the flight-path controller are shown in figure 15.

The output of the vertical-axis flight controller (fig. 15) is passed through a "throttle gearing" (see fig. 55, appendix A) before being used to command the engine *RPM* (N_{GI}). The purpose of this throttle gearing is to compensate for the severe nonlinearities in the variation of thrust with engine speed. The output of the horizontal (longitudinal) axis flight controller is used to command the thrust vector angle, ζ_{TL} (defined to be zero when the thrust is vertical). The choice of engine *RPM* and thrust vector angle as the control quantities for the vertical and horizontal flight controller results in a particularly simple controller implementation, but the inherent control coupling at the higher thrust vector angles ($\zeta_{TL} > 50°$) severely tests the decoupling effectiveness of the SRFIMF concept.

The output of the horizontal (lateral) axis flight controller, i_l (fig. 15), passes to the thrust deflection cascades of all six fans (fig. 14).

The inertial velocities, V_X and V_Y, and their time derivatives, $\dot{V}_X$ and $\dot{V}_Y$, used as feedback quantities in the flight controller, are measured relative to a set of axes that are rotated, relative to the earth-fixed vertical axis, through the aircraft's heading. Thus

$$V_X = U_E \cos \psi + V_E \sin \psi$$

$$V_Y = V_E \cos \psi - U_E \sin \psi$$

$$\dot{V}_X = (\dot{U}_E + V_E\dot{\psi})\cos \psi + (\dot{V}_E - U_E\dot{\psi})\sin \psi$$

$$\dot{V}_Y = (\dot{V}_E - U_E\dot{\psi})\cos \psi - (\dot{U}_E + V_E\dot{\psi})\sin \psi$$

where

U_E, V_E inertial velocities along the earth-fixed x and y axes

ψ heading

Examples of the transient response of the aircraft to command pulses in vertical velocity, horizontal velocity, and horizontal acceleration, at hover, 60 knots, and 120 knots, are shown in figures 23, 24, and 25. Significant deviations from the desired second-order system response and significant cross-axes decoupling occur only when control action is limited by maximum engine *RPM* and thrust vector angle limits.

Figure 26 compares the aircraft response in hover to a lateral velocity command pulse when each alternate lateral velocity controller is used (table 4). So far as lateral velocity response is concerned, figure 26 shows that there is little to choose between the two types of controller. Figure 26 also shows the response due to a roll command pulse with the lateral velocity controller (using thrust deflection) engaged. This latter example demonstrates the power of the SRFIMF concept in decoupling the attitude and translational motion in hover.

Finally, the response of the aircraft to a wing-tip engine failure at hover, 60 knots, and 120 knots is shown in figure 27. It is clear that the SRFIMF has a fast response to disturbances. Thus the maximum roll-angle deviation recorded was about 1° and altitude and velocity deviations were below the recorder threshold.

Table 4 shows that a significant amount of control mode blending is required as the speed changes. This blending takes place over a speed range of 20-30 knots. For this simulation, a simple linear blending technique is used whereby the output of one control mode is multiplied by a factor K_B, the output of the other control mode is multiplied by a factor $1 - K_B$, and the results are added together (see figs. 14 and 15). The blending factor is zero below 20 knots, unity above 30 knots, and linear in the 20-30-knot interval (see fig. 50 in appendix A).

Cockpit Instrumentation and Displays

The cockpit instrument panel is shown in figures 28 and 29. In the center of the panel is a display CRT whose format is described later. On the far left of the panel (fig. 28) is the engine status instrumentation consisting of six engine *RPM* gauges arranged in a pattern similar to the engine location in a plan view of the aircraft, along with engine and fan status lights mounted near each *RPM* gauge. If an engine or fan fails, the appropriate light flashes.

To the immediate left of the display CRT is a standard airspeed indicator; mounted above this are touchdown indicator lights for each of the three wheels (fig. 28). Below the airspeed indicator is the attitude controller status panel. This panel contains roll, pitch, and yaw controller status lights that are off, on, or flashing according to whether the controller is operating, off or has failed. Below the status lights are roll and yaw mode selection switches; above the status lights are control travel status strip gauges that give normalized values (0-10) of the controller output quantities i_p, i_r, and i_y (fig. 14). On the left of the attitude flight controller status panel is a flight-path flight controller status panel that contains status lights and

control mode selection switches. The horizontal (longitudinal) and vertical axes of the flight controller are treated as a single unit so far as operating status is concerned. The right side of the instrument panel (fig. 29) contains a barometric altimeter, angle-of-attack and sideslip indicators, and a standard horizontal situation indicator.

The main aim of the electronically generated display is to provide sufficient situation and flight director information to permit a pilot to fly precise curved decelerating approaches and vertical landings in category 3C weather conditions. The display format (figs. 30 and 31) is intended for eventual use as a head-up display. Unfortunately, the simulator available for the tests cannot accommodate the equipment required for head-up display projection. However, little is lost in using the display format in conjunction with the head-down arrangement (fig. 29) since the prime concern in this simulation is with a task flown in category 3C conditions, for which head-up display offers no special advantages.

Figure 30 shows the display format used in conjunction with the horizontal (longitudinal) velocity controller option. The definition of the format symbols for the variables and the particular values depicted in figure 30 are given in table 5.

The display format used in conjunction with the horizontal acceleration controller option is given in figure 31. The major difference between figures 30 and 31 is that the display format for horizontal velocity and horizontal acceleration is reversed. The details of the differences between figures 30 and 31 are given in table 6.

The large symbol ⊠ in figures 30 and 31 represents the landing pad; distances y and R are proportional to the lateral and longitudinal displacement of the landing pad relative to the aircraft. The landing pad appears on the display only when it is within 152 m (500 ft) horizontal range of the airplane. The symbol ⊗ relative to the horizon and pitch ladder gives the direction of the inertial velocity vector. The quantities γ_I and β_I are the angles the velocity vector makes with the horizon and with a plane defined by the earth-fixed vertical and the x-body-fixed axis of the aircraft. Thus,

$$\gamma_I = \tan^{-1}\left(\frac{-W_E}{\sqrt{U_E^2 + V_E^2}}\right) \tag{57}$$

$$\beta_I = \tan^{-1}\frac{V_E}{U_E} - \psi \tag{58}$$

When the vertical position of the velocity vector symbol ⊗ exceeds 15°, it is removed from the display.

If the pitch axis flight controller is not operating (either failed or switched off), the pitch trim (θ_T) symbol is removed from the display. If the

flight-path flight controller is not operating (either failed or switched off), the symbols representing V_{XP}, $\dot{V}_{XP}$, and $\dot{h}_P$ are removed from the display.

Flight Director

It is assumed that the variables describing the desired approach path and the required variation of aircraft's horizontal and vertical speed along the approach path are known functions of the distance from the touchdown point. Furthermore, it is assumed that both the desired and actual values of these variables are available for use as inputs to a three-axis (lateral, horizontal, vertical) flight director. The flight director provides guidance information that is presented on the pilot's electronic display (figs. 30 and 31).

The lateral flight director provides bank-angle commands ($\Delta\phi_C$) to aid the pilot in tracking the localizer beam. For large localizer errors (large y), the flight director produces roll commands needed to maintain a heading of ±45° relative to the localizer. Figure 32 is a block diagram of the lateral flight director. The output $\Delta\phi_C$ is the error between the commanded and actual bank angles. This parameter controls the lateral position of the lateral flight director bar shown on the electronic display. The value of $\Delta\phi_C$ is limited to ±20° of bank angle. The internal loop (fig. 32) containing the lag function, $1/(14.9s + 1)$, is provided to give the flight director a self-trimming property similar to that provided in the SRFIMF controller. Thus, the flight director will give bank-angle commands such that, in the steady state, the localizer error y becomes zero independent of any steady-state disturbances acting on the aircraft (e.g., sidewind). The gain values shown in figure 32 are such that, with $\Delta\phi_C = 0$, the effective time constant of the entire system of flight director and aircraft is about 20 sec.

The horizontal (longitudinal) flight director is designed to operate in conjunction with the flight-path flight controller (fig. 15). Figure 33 is a block diagram of the flight director. The output of the flight director is either a horizontal velocity command, V_{XC}, or a horizontal acceleration command, $\dot{V}_{XC}$, depending on which flight-path flight controller mode is selected. The commanded quantities V_{XC} and $\dot{V}_{XC}$ are shown on the appropriate scale of the electronic display. The pilot's horizontal velocity or horizontal acceleration input command to the flight-path flight controller (V_{XP} or $\dot{V}_{XP}$) is also shown on the display. To achieve the required horizontal velocity, the pilot moves his controls (VC lever) to superimpose the flight director and his own command symbols on the display. The gain values shown in figure 33 are such that, with $\dot{V}_{XP} = \dot{V}_{XC}$ (horizontal acceleration mode), the effective time constant of the entire system of flight director and aircraft is about 4 sec.

The vertical flight director is also designed to operate in conjunction with the flight-path flight controller. Figure 34 is a block diagram of the director. The output is a commanded vertical velocity, $\dot{h}_C$. This quantity is shown on the VVI scale of the display, along with the pilots input to the flight director, $\dot{h}_P$. As with the horizontal flight director, the pilot moves his control (VC lever) to superimpose the display symbols representing $\dot{h}_C$ and

$\dot{h}_P$. The gain values are such that, with $\dot{h}_P = \dot{h}_C$, the effective time constant of the flight director and aircraft is about 4 sec.

TEST PLAN

Scope of Piloted Simulation

The broad aims of the simulation were to evaluate the fixed-operating-point handling qualities of the aircraft equipped with the SRFIMF flight controller and to obtain an operational evaluation of the complete system of flight controller, pilot controls, and displays in IFR decelerating approaches along specified flight paths.

To meet the aims of the simulation, a three-part test plan was devised. In part 1, the pilot was required to evaluate the fixed-operating-point handling qualities by performing the series of tasks shown in table 7. The tasks in part 2 (table 8) were designed to permit an evaluation of the aircraft during the critical period, just before "let-down," when final position changes in the horizontal plane are required to bring the aircraft to a hover vertically above the landing pad. In part 3, the pilot was required to perform a series of curved and straight IFR (zero, zero) approaches from 120 knots to a vertical touchdown. The tasks in parts 1 and 2 were performed with various combinations of pilot control modes, with the best set being selected for the part 3 tests. All parts of the simulation were performed with and without winds and turbulence.

The type of curved approach path used in the simulation is shown in figure 35. The first segment, *XA*, is flown at a constant ground speed and a constant flight-path angle γ_A. From point A, the longitudinal (horizontal) deceleration is increased at a constant rate to point B, held constant to point C, and then reduced at a constant rate to zero at the hover point H. The magnitude of the constant deceleration during segment *BC* is such that, at point H, the ground speed is zero. The rate of descent is maintained constant to point E. From point E to point H, the rate of descent deceleration schedule is of the same general type as the ground-speed deceleration schedule from point A to H (appendix E). The magnitude of the constant rate of descent deceleration during segment *FC* is such that, at *H*, the rate of descent is zero. The deceleration transition segments *AB*, *EF*, and *CH* are provided to avoid discontinuous deceleration commands. The time duration of all deceleration transition segments is 4 sec.

The straight approach (fig. 35) may be regarded as a special case of the curved approach in which points A and E coincide and points B and F coincide and the rate of descent is proportional to the ground speed.

The equations defining the approach paths, including the required accelerations and velocities, are given in appendix E. The selected input values used to calculate the particular approach paths used in the simulation are given in table 9. The important approach path parameters, expressed as

functions of both the distance and time to initial hover, for both the curved and straight approaches, are shown in figures 36 and 37.

The prime reason for attempting to fly curved approaches rather than the conceptually simpler straight approaches is the promise of some noise reduction, primarily because of increased altitude. The magnitude of this increased altitude may be seen by comparing corresponding approaches shown in figures 36 and 37. A useful fact in this connection is that, for ground ranges in excess of that at the start of the longitudinal deceleration (R_A in fig. 35), the altitude of the curved approach is approximately $h_A/2$ (229 m (750 ft) in the examples) higher than for the corresponding (same γ_A) straight approach. However, to fly the type of curved approach path under discussion, the pilot must hold his initial rate of descent to much lower altitudes than for the straight approach. This fact is clearly evident in figure 38, which shows rate of descent as a function of altitude for both curved and straight approaches. For example, with $\gamma_A = -6°$ at 60 m (197 ft) altitude, the rate of descent of an aircraft flying the curved approach is 6.45 m/sec (1270 ft/min), almost twice the value of 3.25 m/sec (640 ft/min) for an aircraft flying the straight approach. It follows that the acceptability of curved approaches depends strongly on the pilot's opinion of the additional psychological stress implied by high rates of descent near the ground and of his workload in reducing this high rate of descent both quickly and accurately.

Simulator

The tests were conducted using the Ames six-degree-of-freedom simulator (S.01) shown in figure 39. The motion limits of the simulator cab are given in table 10, along with the frequency at 30° phase lag for each degree of freedom of the basic simulator (no motion washout filters, etc.). The frequency response of the basic simulator is given in greater detail in reference 17.

The simulator cab has a single seat and was equipped as shown in figures 17, 18, 28, and 29. Details of the pilot controls, instruments, and displays have already been given under "Simulation Model of Lift-Fan VTOL Transport." The loading devices on the pilot's stick and rudder pedals were adjusted to provide the characteristics given in tables 2 and 3.

The simulator tests were all conducted with the cab closed (pilot cannot see outside the cab). In the first two parts of the tests, the pilot was provided with a black and white television picture of a model of a landing approach scene, while in part 3, the picture provided a representation of fog (IFR zero, zero). The model used represented part land and part sea with the VTOL landing pad marked by a circle on the deck of a fixed model aircraft carrier. The picture of the model was generated by a computer-driven TV camera whose motion (suitably scaled in the translational degrees of freedom) followed that of the aircraft. The translational motion scale factor was set to 1/600. With this scale, the landing pad diameter was equivalent to 54.25 m (178 ft).

The limits of the visual simulation system are given in table 11, along with the frequency at 30° of phase lag for each degree of freedom. The frequency response is given in greater detail in reference 17.

Pilot Experience

Because of the preliminary nature of these simulation tests, only one NASA test pilot participated. However, this pilot has extensive flight experience in all categories of aircraft, including helicopters and vectored thrust V/STOL aircraft. Furthermore, he participated in all previous lift-fan V/STOL aircraft simulations conducted at Ames (refs. 3, 5, 6, 8, and 10). Table 12 summarizes his flight experience.

The pilot gave ratings for the various tests based on the Cooper-Harper handling qualities rating scale given in figure 40.

SIMULATION RESULTS

Fixed-Operating-Point Handling Qualities (Part 1)

The dynamic effects of commanded pitch, roll, and yaw attitude changes in hover and of commanded pitch attitude changes at several speeds were evaluated in tasks 1, 2, and 3 (table 7). The pilot rating for all three tasks was 1-1/2, independent of winds and turbulence. The speed of response and damping of the attitude changes were judged to be very good. These results verify the frequency and damping criteria (frequency = 2 rad/sec, damping factor = 0.75) given in reference 14 for hovering flight, and indicate that these criteria are valid for pitch attitude changes throughout the powered-lift flight envelope. The insignificant effects of wind and turbulence on the precision with which the pilot could perform the tasks suggest that the self-trimming and disturbance-alleviating properties of the SRFIMF flight controller are of considerable value.

During the task-1 tests, the pilot made some pitch attitude changes using the trim switch. The rate of change of commanded pitch trim (4°/sec) was judged to be satisfactory, and the pilot appreciated the display of his commanded trim attitude (fig. 30) — a feature possible only with a self-trimming flight controller. This pitch trim display enabled the pilot to quickly command precise changes of pitch attitude. The value of this feature was most apparent in the type of high workload situation characteristic of the VTOL approaches (discussed later).

The dynamic effects of commanded horizontal speed changes, commanded altitude changes, and engine failures were evaluated in tasks 6, 7, and 8. The pilot rating for all three tasks was, again, 1 to 1-1/2, independent of winds and turbulence. These results show that the frequency of 1.25 rad/sec and damping factor of 0.75, selected for the translational motion, were satisfactory, at least for these simple tasks. The insignificant effects of

winds, turbulence, and engine failures again demonstrated the effectiveness of the SRFIMF flight controller.

The pilot ratings for tasks 6, 7, and 8 were not influenced by the type of horizontal longitudinal controller mode selected (acceleration or velocity). The pilot expressed a preference for the horizontal acceleration controller mode because it offered him an inherently smoother ride. If, while in the horizontal velocity controller mode, the pilot made a sudden, large, horizontal velocity command change, then large and rather uncomfortable longitudinal accelerations resulted. This behavior led the pilot to describe the velocity controller mode as "jerky." The horizontal acceleration controller mode removed this problem by giving the pilot complete control of his longitudinal acceleration and therefore his ride comfort. On the other hand, once the potency of the horizontal velocity controller mode was recognized by the pilot, and he learned to move the VC lever smoothly and slowly, it was almost as easy and comfortable for him to use the velocity controller mode to achieve the changes in horizontal velocity required for task 6.

In performing tasks 6 and 7, the pilot generally preferred the MK2 VC lever (fig. 19). The reasons for this preference are given in the section "Additional Pilot Comments."

Lateral-directional dynamics at speeds above 30 knots were evaluated in tasks 4 and 5. These tests showed that the rate-command-attitude-hold controller mode, chosen for the roll axis, provided good response and damping characteristics (stick sensitivity = 262°/sec/m of stick (6.67°/sec/in. of stick), frequency = 2 rad/sec, damping factor = 0.75) and, by itself, was rated at 1 to 1-1/2, independent of winds and turbulence. Neither of the yaw controller modes provided were entirely satisfactory, and yaw controller mode deficiencies were largely responsible for problems the pilot experienced while performing tasks 4 and 5. The pilot ratings given for the turn coordination task are given in figure 41. In calm air, the sideslip command mode consistently provided better turn coordination handling qualities than the rate-command bank-angle feedback mode. The main reason for this result was that, with "pedal-fixed" turns, the sideslip command system maintained zero sideslip angle — thereby providing virtually perfect coordination characteristics — whereas the yaw command system permitted a small amount of sideslip to develop slowly (fig. 22). This gradual increase of sideslip is because the bank-angle feedback technique of turn coordination is "open-loop" so far as sideslip is concerned, and any small errors in the commanded rate of turn due to the bank-angle feedback loop eventually becomes evident as a slowly increasing sideslip angle. However, even at the 30-knot worst case condition, the sideslip angle did not exceed 5° and could be removed easily by applying yaw control. The increase in pilot ratings at 30 knots (fig. 41) was also due to a tendency of the pilot to overshoot the desired heading. Since the overshoot tendency occurred when using either yaw controller mode, it appears likely that the increased rate of turn, as forward speed was reduced (at constant bank angle), made it more difficult for the pilot to judge when to begin the roll out onto the new heading. Thus, for example, in a 10° banked turn, the rate of turn doubles from 3.21°/sec at 60 knots to 6.42°/sec at 30 knots. In retrospect, the task may not have been well conceived. It might have been better to have

specified a bank angle for each speed so that the rate of turn was a constant, thereby defining a task of more uniform difficulty.

The introduction of winds alone (no turbulence) did not significantly influence the turn coordination task when the sideslip command mode was used since the sideslip controller still maintained zero sideslip. In contrast, when the yaw-rate controller mode was used, the pilot noted that the task became more difficult because of the need to apply progressively increasing amounts of yaw control to maintain a small sideslip angle. This result points to the main disadvantage of bank-angle feedback as a technique for coordinating turns. The system, as implemented for this simulation, maintains a yaw rate equal to $(g \tan \phi)/V_X$ (fig. 14). Thus, if the bank angle ϕ and the inertial horizontal speed V_X are maintained constant, the yaw rate is also constant (provided the pilot does not introduce a yaw control input). While this constant yaw rate will maintain zero sideslip in the absence of winds, with winds the yaw rate necessary to maintain zero sideslip is no longer constant. The result is that, with winds, sideslip angle varies cyclically, reaching a maximum numerical value twice in a complete 360° turn. Moreover, when the inertial speed V_X is small ($\approx$30 knots), the sideslip deviations from zero can be unacceptably large. The problem is evident in figure 42, which shows the variation of sideslip angle and yaw rate, using each type of yaw controller mode, for the aircraft in a constant 10° banked turn, at 30-knot inertial velocity in a 15-knot wind. It is clear from figure 42 that, with the sideslip command mode, the sideslip angle remains zero and yaw rate varies cyclically, whereas with the yaw-rate command mode, the yaw rate remains constant and the sideslip angle varies cyclically through angles as large as 30°. Note that large sideslip angles at low speed can introduce dangerously high rolling moments and have resulted in at least two accidents with VTOL aircraft. Interestingly, this problem was apparently not revealed in previous lift-fan V/STOL aircraft simulations, even though a similar form of bank-angle feedback turn coordination scheme was used. The reason for this may be that the turn was not continued long enough for large sideslip angles to develop.

The introduction of turbulence, in addition to winds, in task 4 did not significantly influence the turn coordination performance when the yaw-rate controller mode was used, because the yaw-rate controller mode uses inertial quantities in its feedback loops and therefore tends to counter the effects of turbulence so far as aircraft response is concerned. However, the introduction of turbulence when using the sideslip controller mode caused the pilot to experience severe buffeting. The buffeting was chiefly because of the large yaw accelerations produced as the controller acted to maintain zero sideslip angle. As shown in figure 42, 1.52-m/sec (5-ft/sec) RMS turbulence produced 0.1 g RMS side forces at the pilot station. The ride experienced by the pilot was decidedly unpleasant and was responsible for the increase in pilot rating (fig. 41).

It follows from the previous results that, so far as the yaw controller mode is concerned, there is a dilemma. If inertial quantities are used exclusively in the controller loops, then large pilot yaw control inputs may be required to maintain low sideslip angles, and if air-mass-referenced quantities are used exclusively, then turbulence induces buffeting. It is

conceivable that a yaw controller mode can be devised, using both inertial and air-mass-referenced quantities, which will be an adequate compromise. For example, a possible solution may be to use a yaw-rate command with a bank-angle feedback mode whose feedback gain is proportional to the reciprocal of the airspeed rather than the inertial speed. Such a system would not require large pilot yaw control inputs to counter the effects of steady winds in turning flight. If, in addition, the airspeed signal were passed through a suitable filter before being used as a component in the bank-angle feedback gain, it may be possible to reduce the buffet due to turbulence to an acceptable level.

The results for task 5 (constant 10° sideslips with constant heading) were all within a pilot rating of 1/2 of those of task 4 for the corresponding conditions. The problems experienced could be traced to those outlined above for the yaw controller mode.

In addition to rating each task in the part 1 tests, the pilot also gave composite ratings for the overall handling qualities of the aircraft at the various forward speeds. These composite pilot ratings are given in figure 43 and, as might be expected, they closely follow those given for the turn coordination and steady sideslip tasks, indicating that the handling qualities problems of the aircraft are largely associated with the yaw controller mode. Note that this problem is not a deficiency in the basic SRFIMF controller concept, but rather reflects on the choice of yaw controller mode.

It is appropriate at this point to briefly compare the fixed-operating-point, handling-qualities results obtained in the present test with those obtained in a previous lift-fan V/STOL simulation. Figure 44 gives the composite pilot ratings for the current tests, for the same aircraft equipped with a response-feedback controller (ref. 5) and the same aircraft without an active flight controller. These pilot ratings are for the aircraft handling qualities in calm air. It is evident that an aircraft without a flight controller is virtually unflyable at low speeds. Adding a response-feedback controller greatly improves the handling qualities. The SRFIMF controller provides even greater improvement. Some care should be used in interpreting these results. Further improvements are possible in the application of both the response feedback and SRFIMF controllers to this aircraft. Moreover, the current test results represent the opinion of a single pilot, whereas those for the response-feedback-controlled aircraft represent the opinion of several pilots. However, some continuity of opinion exists in that the pilot who provided the results for the current tests also participated in the previous tests.

Additional Fixed-Operating-Point, Handling Qualities in Hover (Part 2)

The problems involved in making final position changes, in the horizontal plane, to bring the aircraft to a hover vertically above the landing pad were investigated in the second part of the simulation tests (table 8). The main aim was to evaluate the effectiveness of various types of pilot controls and flight controller modes that could be used for this task (table 4). The pilot used the electronic display to judge the position of the aircraft relative to

the landing pad (fig. 30). Therefore, the task was performed essentially in IFR conditions.

In essence, two dynamically distinct types of translational control were examined, which may be termed "direct force command" and "velocity command." In the former, the pilot was given direct control of the orientation of the gross thrust vector; in the latter, he was given control of translational velocity through the action of the flight-path flight controller. Both types of control were implemented, first through aircraft attitude operated from the stick, and then through gross thrust deflection operated from one or other of the thumb controls located on top of the P and VC levers (figs. 16 and 19). An evaluation of the influence of the type of VC lever arrangement on the ease with which the thumb controller could be used is given in the section "Additional Pilot Comments."

Pilot ratings for each of the four control techniques used are given in figure 45. It is unnecessary to distinguish between longitudinal and lateral position changes (tasks 1 and 2 in table 8) since both received the same pilot ratings. It is evident from figure 45 that precise horizontal positioning of the aircraft, using direct force control implemented through aircraft attitude, was relatively difficult (PR 5-6). This difficulty was caused by the virtual absence of natural translational damping and by the relatively long time lag between a pilot input to the stick and the establishment of a significant change in translational velocity. In an attempt to cope with these deficiencies, the pilot usually tended to apply too much control and often overshot the landing pad. This type of problem has been observed in past VTOL simulations. The use of direct force command implemented through gross thrust deflection reduced the lag substantially, but improved the pilot rating by only one point (fig. 45). This result strongly suggests that the major problem involved in the use of direct force command was a lack of translational damping.

Tests performed using translational velocity command, implemented either through aircraft attitude or thrust deflection, dramatically improved the performance over that using direct force command (PR 1 to 1-1/2). This result tends to reinforce the earlier results suggesting that translational damping was the critical factor in determining the ease with which the task could be performed. Note in figure 45 that the pilot ratings using the deflected thrust implementation of velocity command were slightly higher than for the aircraft attitude implementation. This result was not because that task was more difficult with deflected thrust, but because the ride was less comfortable. Deflecting the thrust changes the nongravitational forces acting on the aircraft and the pilot feels the reaction to these force changes. This situation also occurs when thrust deflection is used to implement direct force command. However, the associated ride quality problem was less evident in this case because the pilot did not command thrust deflections as large or as fast as the flight-path flight controller did in response to pilot velocity commands.

The good results obtained using the aircraft attitude implementation of translational velocity command verify the results reported in reference 18

for a simulated VFR hovering task. The pilot's chief objection to this control technique was the atypical variation of aircraft attitude with stick input. For example, following a step lateral input at the stick, the roll angle increases to a maximum value and then decreases to a relatively small value as the translational velocity approaches the value equivalent to the stick input (fig. 26).

Figure 45 also shows that, when the translational velocity command was used, winds and turbulence had no effect on the pilot's opinion of the task. This result was obtained because the flight-path flight controller attenuated the turbulence and automatically trimmed the effects of steady winds. Since the flight-path flight controller must be switched off for the pilot to use direct force command for translation, winds and turbulence made the task more difficult and resulted in a pilot rating increase of one unit.

IFR Landing Approaches and Touchdown (Part 3)

The results of the part-1 tests showed that the use of sideslip command to control the yaw axis led to poor ride qualities in turbulence, especially at low speeds (≈30 knots). It was decided, therefore, to use yaw-rate command with bank-angle feedback for all approach and landing tests.

The results of the part-2 tests showed that final positioning of the aircraft over the landing pad was best accomplished using some form of translational velocity command. The thrust deflection implementation (operated through the thumb control on the VC lever) was used for all approach and landing tests, even though it appeared from the part-2 tests that the attitude implementation may be slightly better. The attitude implementation was not selected because the flight controller had been designed to provide this mode only for the roll axis (table 4). In retrospect, it would have been desirable to have extended this controller mode to include the pitch axis so that this system could have been evaluated in approach and landing tests.

The tests were performed using both the straight and curved approaches, with initial flight-path angles of -3°, -6°, and -9° (see "Scope of Piloted Simulation"). During the familiarization period, before the start of systematic testing, the pilot flew several approaches to compare the two alternate types of horizontal longitudinal flight-controller mode (table 4). The major problem when the velocity command mode was used was that the pilot tended to change velocity in a series of steps, rather than smoothly. This tendency occurred because the pilot moved his velocity command thumb wheel (fig. 19) only when his attention was on the horizontal flight director display. Since the horizontal flight director command symbol was moving continuously, in accordance with the required deceleration schedule, the pilot moved his thumb wheel in a series of "catch-up" steps, at the frequency of his scan pattern. This technique introduced lags, which caused a deterioration of tracking accuracy. Furthermore, the pilot often did not have time to move the thumb wheel slowly in his attempt to catch up with the flight director and, as a result, the ride problem noted in part 1 occasionally became evident. In contrast, when the acceleration command mode was used, the pilot found that he

only had to move the thumb wheel once to match his commanded deceleration with that indicated by the flight director. No further significant inputs to the thumb wheel were required until the aircraft was close to the landing pad. The result was a smooth ride, with high precision, achieved with relatively low workload. The pilot therefore concluded that the acceleration command was preferable for the types of approach to be studied and it was decided to use this mode exclusively in the formal testing program.

All approaches were started with the aircraft offset, laterally, 152 m (500 ft) from the localizer and trimmed, nose down, to zero angle of attack. The nose-down attitude was required because the maximum aft thrust vector angle was insufficient to enable the aircraft to fly, with a deck-level attitude, at 120 knots, on the steeper glide slopes (-6° and -9°).

The pilots' preferred technique for performing a curved approach and landing is shown in figure 46. Before the start of the test, the pilot set his VC lever and thumb wheel positions so that his commanded rate of descent and horizontal acceleration matched those indicated by the corresponding flight directors. The aircraft initial conditions, and the positions of the VC lever and thumb wheel at the start of the flight, are shown at point 1 in figure 46.

The pilots first action was to remove the 152 m (500 ft) localizer error by banking the aircraft to null the lateral flight director indicator. This process was essentially completed during the constant-speed segment *XA*. A typical view of the display and power management controls during segment *XA* is shown at point 2 (fig. 46). At *A*, the horizontal flight director starts to indicate a required deceleration. This required deceleration increases at a constant rate to *B* and then remains nominally constant to *C*. The pilot used his thumb wheel to match his acceleration command indicator with the horizontal flight director indicator (fig. 31). A typical view of the display and power management controls shortly after the maximum deceleration was established is shown at point 3 (fig. 46). On segment *BC*, when the horizontal speed was about 100 knots, the pilot used his pitch trim switch to rotate the aircraft to a deck-level attitude (point 4 in fig. 46).

Figure 46 shows that, although the aircraft was heading along the localizer (ψ = 90°) at the start of the flight, the sidewind gradually yawed the aircraft toward the relative wind vector. This effect was slow and the change of heading never exceeded about 20°. The pilot did not find it necessary to reestablish the initial heading. At a distance of 152 m (500 ft) from the touchdown point (point 5 in fig. 46), the landing pad appeared on the display. Since the aircraft was yawed to the left, the landing pad first appeared at the top right-hand corner of the display, even though the localizer error was zero (*LAT* = 0).

From E onward, the vertical flight director indicates a progressively reduced rate-of-descent requirement which the pilot followed using his VC lever (points 6 and 7 in fig. 46). Shortly thereafter, at *C*, the horizontal flight director indicates a progressively reduced horizontal deceleration requirement, which the pilot followed using his thumb wheel. From E onward,

the pilot paid particular attention to the altitude and his commanded horizontal velocity (shown below *VEL* on the display). When the altitude was about 30.5 m (100 ft), the pilot broke off the descent by commanding zero rate of descent. He then continued to follow the horizontal flight director until his commanded velocity was approximately zero, at which point he quickly moved his thumb wheel to command zero acceleration (point 8 in fig. 46). At this point, the aircraft was hovering 15-23 m (50-75 ft) above ground, within a radius of 30.5 m (100 ft) of the touchdown point. The pilot then used the two-axis, thumb-operated vernier velocity command control to translate the aircraft to a position vertically above the landing pad. Finally, he used his VC lever to command a rate of descent of about 1 m/sec (200 ft/min) and the aircraft settled onto the landing pad (point 9 in fig. 46).

The greatest pilot activity took place at the end of the horizontal deceleration, where both the VC lever and thumb wheel must be used simultaneously and several variables noted carefully. The most crucial part of the landing was the removal of the horizontal deceleration when the pilot's commanded velocity was close to zero (within ±5 knots). Failure to perform this operation accurately resulted in a pronounced tendency of the aircraft to drift relative to the touchdown point and made the task of final positioning over the touchdown point, with the vernier velocity control, more difficult.

Pilot ratings for the various types of approach are shown in figure 47. For straight approaches, these ratings were less than 3-1/2, independent of the initial approach angle. Side winds and turbulence increased the workload slightly, as reflected in the small increase in pilot rating (fig. 47). The curved approaches received slightly higher pilot ratings because the pilot was less comfortable with the higher rates of descent near the ground (fig. 38). In addition, the curved approaches required more concentration from the pilot to bring the aircraft, to a hover, in a satisfactory position relative to the landing pad. The flight controller yaw mode deficiencies (noted in part 1 tests) did not interfere with the approach and landing task largely because the pilot did not feel the need to apply large lateral stick and rudder pedal inputs at low speeds (≈30 knots).

Time histories of most of the important variables during typical 6° curved and straight approaches are shown in figures 48 and 49, respectively. Also shown are the points at which the important pilot actions (described earlier) take place.

Note that, when flying straight approaches, the required gradual decrease in rate of descent is performed by the pilot in a series of discrete steps (fig. 49). This type of behavior is similar to that described earlier in connection with the use of the horizontal velocity mode, and was one of the reasons this mode was rejected in favor of the horizontal acceleration mode. Although the required reduction in rate of descent could probably be made smoother and require fewer pilot inputs if a vertical acceleration mode were used, questions of safety alone would probably preclude its use. In any case, the pilot did not comment on the workload required to follow the vertical flight director. In contrast, note that, when flying the curved approach (fig. 48), the required rate-of-descent reduction takes place quickly and the

pilot can apparently afford to devote most of his attention to it for the short period of time needed.

A series of tests were carried out in which flight-path flight controller failures were simulated at altitudes varying from 30-150 m (100-500 ft). After the failures, the pilot was to follow the procedure outlined earlier under "Pilot Controls" to assume flight-path control using the P and T levers and abort the landing. In all the tests, the pilot was able to check the rate of descent with less than 15.2 m (50 ft) loss in altitude, and at no point did the rate of descent exceed that at the failure point. The procedure, as an emergency measure, was regarded by the pilot as being both simple and effective and was given a pilot rating of 4-1/2. These failure tests were not extensive and more work is required to fully define the safe rate of descent/altitude envelope.

In recognition of the concern over the relatively high rates of fuel consumption of lift-fan VTOL aircraft in the powered-lift flight mode, the pilot was requested to complete all VTOL landings in the minimum time. However, the pilot was reluctant to maintain a rate of descent all the way to touchdown, favoring, instead, a technique of flaring first to a hover. Unfortunately, this technique requires a considerable time in hover, typically 20-40 sec (as shown in figs. 48 and 49). Table 13 shows the deviation from the ideal minimum landing time, from 4570 m (15,000 ft) range to touchdown, for a series of 27 VTOL landings. These landings included curved and straight approaches, performed with and without winds, turbulence and engine failure. Also shown in table 13 are the corresponding rates of descent at touchdown and the touchdown distance dispersion. Table 13 provides some idea of the kind of landing performance to be expected. However, in evaluating these data, note that the pilot's total testing time was 8 hr, only 3 of which were devoted to approaches and landings.

Additional Pilot Comments

During the tests, the pilot was able to evaluate the effectiveness of the power management lever arrangement (MK1 and MK2, see figs. 16 and 19) and the electronic display.

The pilot found the MK1 controller to be objectionable for two reasons. First, he found that moving the handle vertically for height control was awkward and the zero descent-rate detent hard to locate (the tactile detent indicator (fig. 16) was of little value). Second, he found that there was a tendency for him to move the handle vertically while operating the thumb controller. This pilot-induced coupling increased the workload sufficiently to be annoying. The MK2 controller exhibited neither of these objectionable characteristics. Furthermore, the pilot found that there was a more natural feel with the MK2 lever in that it was mechanized in the same way as a conventional power lever. This latter point was particularly important since, in the event of a flight-path flight controller failure, the pilot is required to revert to a conventional power lever.

The pilot stated that the information presented on the electronic display permitted IFR zero-zero approaches and landings with consistent accuracy. However, he also stated that the digital information was sometimes hard to read and the task would have been easier to perform if the display could have been projected in a "head-up" form. As far as the display format was concerned, the pilot suggested the following changes to improve its effectiveness:

(a) Add a vertical line, starting at the bottom and center of the display, so that the distance from the top of the line to the airplane symbol is a measure of altitude. This line should be scaled so that it appears only when the altitude is less than 60 m (200 ft). This addition would alert the pilot to his low altitude and could make it easier for him to judge the final vertical descent.

(b) Make the touchdown square rotate with a change of aircraft heading. This would give a pictorial view of aircraft heading relative to the localizer and would generally add to the realism of the horizontal situation representation.

(c) Transpose the acceleration and vertical velocity scales. This change would make the relative location of the scales agree with the relative location of the corresponding VC controls (thumb wheel to the right of the VC lever and acceleration scale to the right of the vertical velocity scale).

CONCLUSIONS

A state rate feedback implicit model-following (SRFIMF) flight controller has been advanced as a possible approach to improving the handling qualities of lift-fan VTOL aircraft. It has been shown that, conceptually, the SRFIMF flight controller is relatively simple: it provides an input-output relationship approximately that of any selected second-order system; it provides good gust alleviation and cross-axes decoupling; and it is self-trimming.

The SRFIMF flight controller has been applied to all axes of a comprehensive mathematical model of a lift-fan V/STOL transport. Power management controls and pilot displays have been designed to match the various modes of control provided by the SRFIMF flight controller. A piloted simulation was performed using the Ames six-degree-of-freedom simulator. The principal conclusions derived from this simulation are:

(a) The aircraft with the SRFIMF flight controller had satisfactory ($PR \leq 3\text{-}1/2$) fixed-operating-point handling qualities throughout the powered-lift flight envelope. These handling qualities were generally better than had been achieved in previous simulations of the aircraft (equipped with a response-feedback flight controller).

(b) Neither of the yaw controller modes tested (yaw-rate command with bank-angle feedback and sideslip command) was entirely satisfactory. With the yaw-rate command mode, steady winds caused large sideslip angles to

develop in steady turns. On the other hand, with the sideslip command mode, turbulence induced large yaw accelerations, felt by the pilot as large sideways accelerations. Both problems were most acute at low speeds (≈30 knots).

(c) With the exceptions noted in (b), the self-trimming feature of the SRFIMF flight controller compensated automatically for steady winds, and the disturbance alleviating property attenuated the effects of turbulence. The overall result was that winds and turbulence did not materially affect the fixed-operating-point handling qualities.

(d) Disturbances due to engine failures were quickly and completely compensated by the flight controller and required no action from the pilot.

(e) VTOL approaches and landings, in IFR zero-zero conditions, using either straight or curved approach paths, were flown with acceptable pilot workload. The pilot preferred the straight approach paths because they resulted in the smallest rates of descent near the ground. Wind and turbulence increased the workload only slightly. Pilot ratings varied from 2-1/2 for straight approaches in calm air to 4 for an initial $\gamma = -9°$ curved approach, with 15-knot side wind, 1.52-m/sec (5-ft/sec) RMS turbulence, and an engine failure.

(f) The pilot preferred the longitudinal acceleration flight controller mode over the longitudinal velocity mode. The longitudinal acceleration mode provided the pilot with a smoother ride and a smaller workload. The major problem with the acceleration mode was switching to a velocity mode for hover.

(g) The pilot preferred the MK2 power management control since it avoided the awkward arm action and control coupling associated with the MK1 control and, in addition, closely resembled a conventional power lever in both mechanization and function.

(h) The major difficulty encountered while performing VTOL approaches and landings was switching from longitudinal acceleration command to longitudinal velocity command. The technique adopted by the pilot was satisfactory, but further improvement is required.

(i) The system designed to handle the problem of flight-path flight controller failure and the corresponding piloting procedures were satisfactory.

(j) VTOL approaches and landings, when performed by the pilot, took an average of 30 sec longer than the ideal minimum. This additional time was required because the pilot, rather than following the vertical flight director to touchdown, preferred to break off to a hover at 15.2 to 30.5 m (50 to 100 ft) and then to descend at about 1.02 m/sec (200 ft/min) to touchdown.

(k) Touchdown dispersion averaged 3.94 m (12.94 ft) for the series of landings performed. However, the pilot could probably reduce the dispersion substantially with practice.

Ames Research Center
National Aeronautics and Space Administration
Moffett Field, Calif., 94035, June 14, 1977

TABLE 1.- AIRCRAFT DIMENSIONS, WEIGHT, AND INERTIA

Dimensions		
Parameter	Symbol	Value
Wing area	S_w	71.00 m^2 (764.2 ft^2)
Wing mean aerodynamic chord	$\bar{c}_w$	3.968 m (13.02 ft)
Wing span	b_w	18.65 m (61.17 ft)
Horizontal tailplane area	S_t	25.60 m^2 (275.54 ft^2)
x coordinate of pilot station	E_{px}	11.05 m (36.25 ft)
y coordinate of pilot station	E_{py}	-.482 m (-1.58 ft)
z coordinate of pilot station	E_{pz}	-.152 m (-0.50 ft)
Weight and inertia		
Weight	W	267,000 N (60,000 lb)
Inertia about x body axis	I_x	325,800 kg m^2 (240,300 slug ft^2)
Inertia about y body axis	I_y	872,300 kg m^2 (643,400 slug ft^2)
Inertia about z body axis	I_z	1,071,900 kg m^2 (790,600 slug ft^2)
Product of inertia with respect to x and z body axes	I_{xz}	70,500 kg m^2 (52,000 slug ft^2)

TABLE 2.- CONTROL STICK TRAVEL LIMITS

Control	Maximum travel	Deadband
Lateral	±0.1156 m (±4.55 in.)	±0.0013 m (±0.05 in.)
Longitudinal	±.1156 m (±4.55 in.)	±.0013 m (±.05 in.)
Directional	±.0838 m (±3.30 in.)	±.0013 m (±.05 in.)

TABLE 3.- CONTROL STICK FORCES

Control	Breakout force	Maximum force	Force gradient
Lateral	5.56 N (1.25 lb)	27.58 N (6.2 lb)	193 N/m (1.1 lb/in.)
Longitudinal	5.56 N (1.25 lb)	49.82 N (11.2 lb)	387 N/m (2.2 lb/in.)
Directional	22.24 N (5.0 lb)	166.81 N (37.5 lb)	1752 N/m (10.0 lb/in.)

TABLE 4.- PILOT CONTROL MODES

	Attitude flight controller (stick and rudder pedals)			Flight-path flight controller (VC lever system)		
Speed range	Roll axis	Pitch axis	Yaw axis	Longitudinal x axis	Lateral y axis	Vertical z axis
0-20 knots	Bank-angle command[a] or side velocity[b] command	Pitch attitude[a] command	Yaw-rate[a] command with heading hold	Velocity[a] command or acceleration command with velocity hold	Side velocity[b] command	Vertical velocity[a] command
20-30 knots	Blend		Blend		Phase out	
30 knots-conversion speed (≈120 knots)	Roll-rate[a] command with bank-angle hold		Yaw rate-command[a] with bank-angle feedback for turn coord. or sideslip angle command		---	

[a]Nominal set of pilot control modes.

[b]These controller modes are mutually exclusive.

TABLE 5.- DEFINITION OF FORMAT SYMBOLS USED IN FIGURE 30

	Variable (description of its representation in fig. 30)	Symbol in fig. 30	Display values and units
Airplane state	Bank to right (horizon and pitch ladder rotated to left)	ϕ	8°
	Pitch attitude (fixed airplane symbol ⊣⊙⊢ on horizon)	θ	0°
	Heading (moving horizontal scale above pitch ladder; note: 8 means 80°)	ψ	87°
	Sideslip to left (lateral accel. ball below heading scale displaced to left)	n_{yp}	≈0.1 g
	Flight-path angle (inertial velocity vector symbol ⊗ relative to horizon)	γ_I	-7°
	Angle of attack (airplane symbol ⊣⊙⊢ relative to velocity vector symbol ⊗)	α	7°
	Inertial horizontal velocity (< on vel scale)	V_X	42 knots
	Inertial horizontal acceleration (bottom left digital readout)	Accel	0.46 m/sec^2 (1.5 ft/sec^2)
	Vertical velocity (> on VVI scale - note: 1 means (1000 ft/min))	$\dot{h}$	2.95 m/sec (-580 ft/min)
	Ground range (bottom midleft digital readout)	Long	3413 m (11,200 ft)
	Localizer error (bottom midright digital readout)	Lat	-45.7 m (-150 ft)
	Radar altitude (bottom right digital readout)	Alt	640.1 m (2100 ft)
	Flight-path altitude error (horizontal bar relative to airplane symbol ⊣⊙⊢)	Δh	-22.8 m (≈ -75 ft)
	Resultant thrust vector angle (top left digital readout)	Vect	15°
	Engine speed (top right digital readout)	RPM	99.8% of max. continuous

TABLE 5.- Concluded

	Variable (description of its representation in fig. 30)	Symbol in fig. 30	Display values and units
	Pitch trim (▷ ◁ on pitch ladder)	θ_T	6°
Pilot commands	Commanded inertial horizontal velocity (▷ on vel scale)	V_{XP}	59 knots
	Commanded vertical velocity (◁ on VVI scale)	$\dot{h}_P$	0.81 m/sec (160 ft/min)
	Localizer director (vert. bar relative to airplane symbol ⊣○+)	$\Delta\phi_C$	≈15°
Flight director	Inertial horizontal velocity director (▬ on vel scale)	V_{XC}	88 knots
	Vertical velocity director (▬ on VVI scale)	$\dot{h}_C$	-6.1 m/sec (-1200 ft/min)

TABLE 6.- DEFINITION OF FORMAT SYMBOLS USED IN FIGURE 31

	Variable (description of its representation in fig. 31)	Symbol in fig. 31	Display values and units
Airplane state	Inertial horizontal velocity (bottom right upper digital readout)	*VEL*	102 knots
	Inertial horizontal acceleration (< on accel scale)	$\dot{V}_X$	-0.27 m/sec^2 (-0.9 ft/sec^2)
Pilot commands	Commanded inertial horizontal acceleration (▷ on accel scale)	$\dot{V}_{XP}$	0.305 m/sec^2 (1 ft/sec^2)
	Commanded inertial horizontal velocity (bottom right lower digital readout)	*VEL*	121 knots
Flight director	Inertial horizontal acceleration director (═ on accel scale)	$\dot{V}_{XC}$	1.25 m/sec^2 (4.1 ft/sec^2)

Note: Definitions of all other format symbols used in figure 31 are given in table 5.

TABLE 7.- SIMULATION TEST PLAN, PART 1

No.	Fixed-operating-point handling qualities evaluation tasks at 0, 30, 60, 90, 120 knots and 152 m (500 ft) altitude	Primary pilot controls	Pilot control modes
1	Change pitch attitude by ±5° and hold steady	Long. stick	Nominal (table 4)
2	Change roll attitude by ±5° and hold steady (hover only)	Lat. stick	Nominal
3	Change heading by ±40° and hold steady (hover only)	Pedals	Nominal
4	Coordinated turns using ±10° of bank and roll out to a heading change of ±40° (hover excluded)	Lat. stick & pedals	Nominal and alternate yaw
5	Change sideslip by ±10° maintaining heading (hover excluded)	Lat. stick & pedals	Nominal and alternate yaw
6	Change horizontal velocity by ±20 knots and hold steady	VC lever	Nominal and alternate long.
7	Change altitude by ±30.5 m (±100 ft) and hold steady	VC lever	Nominal
8	Recover initial attitude, altitude, and speed following an engine failure	Stick pedals VC lever	Nominal

TABLE 8.- SIMULATION TEST PLAN, PART 2

No.	Additional fixed-operating-point handling qualities evaluation tasks at hover	Primary pilot controls	Pilot control modes
1	From an initial hover, change the longitudinal position by 30.5 m (100 ft) and reestablish hover, maintaining a constant 30.5 m (100 ft) altitude	Long. stick	Nominal
		VC lever	Nominal and alternate long.
		Vernier velocity control	Nominal
		Vernier force control	Nominal attitude flight-path off
2	From an initial hover, change the lateral position by 30.5 m (100 ft) and reestablish hover, maintaining a constant 30.5 m (100 ft) altitude	Lat. stick	Nominal and alternate roll
		Vernier velocity control	Nominal plus lateral velocity
		Vernier force control	Nominal attitude flight-path off

TABLE 9.- VTOL LANDING APPROACH PATHS: VALUES OF INPUT QUANTITIES (SEE APPENDIX E)

Input variable	Curved approach	Straight approach	
V_{XA}, knot	120	120	
h_A	457.2 m (1500 ft)	---	
h_H	6.10 m (20 ft)	6.10 m (20 ft)	
$\ddot{h}_{max}$	0.61 m/sec^2 (2 ft/sec^2)	---	
t_c, sec	4	4	
γ_A, deg	-3, -6, -9	-3, -6, -9	-7.5
$\dot{V}_{X_{max}}$	---	-0.91 m/sec^2 (-3 ft/sec^2)	-0.49 m/sec^2 (-1.61 ft/sec^2)

TABLE 10.- SUMMARY OF SIX-DEGREE-OF-FREEDOM (S.01) SIMULATOR CHARACTERISTICS

Axis	Displacement limits, ±	Velocity limits, ±	Acceleration limits, ±	Frequency at 30° phase lag
Roll	35°	1.3 rad/sec	10 rad/sec^2	0.63 Hz
Pitch	35°	1.7 rad/sec	4.5 rad/sec^2	.60 Hz
Yaw	35°	3.0 rad/sec	3.0 rad/sec^2	.80 Hz
Longitudinal	2.7 m (9 ft)	2.7 m/sec (9.0 ft/sec)	2.3 m/sec^2 (7.5 ft/sec^2)	.70 Hz
Lateral	2.7 m (9 ft)	2.4 m/sec (8.0 ft/sec)	2.8 m/sec^2 (9.2 ft/sec^2)	.45 Hz
Vertical	2.7 m (9 ft)	2.3 m/sec (7.5 ft/sec)	2.7 m/sec^2 (8.8 ft/sec^2)	1.59 Hz

TABLE 11.- SUMMARY OF VISUAL FLIGHT ATTACHMENT (VFA-2) CHARACTERISTICS

Axis	Displacement limits	Velocity limits, ±	Acceleration limits, ±	Frequency at 30° phase lag
Roll	100°	2 rad/sec	4.2 rad/sec^2	1.70 Hz
Pitch	+20°, -30°	3 rad/sec	16 rad/sec^2	8.50 Hz
Yaw	Unlimited	0.333 rad/sec	2 rad/sec^2	.80 Hz
Longitudinal[a]	6.44 km (4 mi)	185 knots	15 g	.40 Hz
Lateral[a]	±0.81 km (0.5 mi)	180 knots	8.5 g	.56 Hz
Vertical[a]	228.6 m (750 ft)	16.76 m/sec (3300 ft/min)	5.5 g	.75 Hz

[a]At scale 1:600.

TABLE 12.- PILOT EXPERIENCE (FLIGHT HOURS)

Aircraft type	Hours
Fixed-wing V/STOL	282
Helicopter	774
Other aircraft	5436
Total	6492

TABLE 13.- SUMMARY OF SELECTED TOUCHDOWN DATA FOR VTOL LANDINGS

Type of approach and conditions	Time from 4572 m (15,000 ft) downrange, sec	Excess time over ideal, sec	Touchdown rate of descent, m/sec (ft/sec)	Touchdown dispersion error, m (ft)
-3° curved	190	46	0.515 (1.69)	8.52 (27.95)
-3° curved	194	50	.399 (1.31)	5.47 (17.94)
-3° curved W+T+EF	192	48	.671 (2.20)	4.19 (13.75)
-3° curved W+T+EF	168	24	.911 (2.99)	3.90 (12.80)
-6° curved	133	22	.786 (2.58)	2.31 (7.58)
-6° curved	153	42	.783 (2.57)	5.60 (18.36)
-6° curved W+T+EF	147	36	1.055 (3.46)	7.73 (25.72)
-6° curved W+T+EF	126	15	1.911 (6.27)	.74 (2.42)
-6° curved W+T+EF	147	36	.683 (2.24)	3.16 (10.36)
-6° curved W+T+EF	117	6	1.094 (3.59)	4.78 (15.69)
-9° curved	122	22	1.155 (3.79)	3.00 (9.84)
-9° curved	131	31	.847 (2.78)	2.88 (9.46)
-9° curved	127	27	.985 (3.23)	7.87 (25.83)
-9° curved W+T+EF	143	43	1.149 (3.77)	10.20 (33.45)
-9° curved W+T+EF	133	33	.933 (3.06)	.72 (2.36)
-9° curved W+T+EF	119	19	.643 (2.11)	.87 (2.85)
-3° straight	126	20	.515 (1.69)	1.54 (5.04)
-3° straight W+T+EF	118	12	.957 (3.14)	.71 (2.32)
-6° straight	151	45	.710 (2.33)	4.24 (13.92)
-6° straight	133	27	.981 (3.22)	3.12 (10.22)
-6° straight	124	18	1.417 (4.65)	2.12 (6.95)
-6° straight W+T+EF	161	55	.680 (2.23)	2.83 (9.29)
-6° straight W+T+EF	142	36	.765 (2.51)	2.07 (6.78)
-6° straight W+T+EF	118	12	1.161 (3.81)	9.90 (32.47)
-9° straight	144	38	.408 (1.34)	2.66 (8.74)
-9° straight	120	14	.951 (3.12)	3.05 (10.01)
-9° straight W+T+EF	131	25	.860 (2.82)	2.19 (7.18)
Mean		30	.887 (2.91)	3.94 (12.94)
Standard deviation		13	.314 (1.03)	2.71 (8.88)

Note: W = 15-knot sidewind
T = 1.52-m/sec (5-ft/sec) turbulence
EF = Engine failure

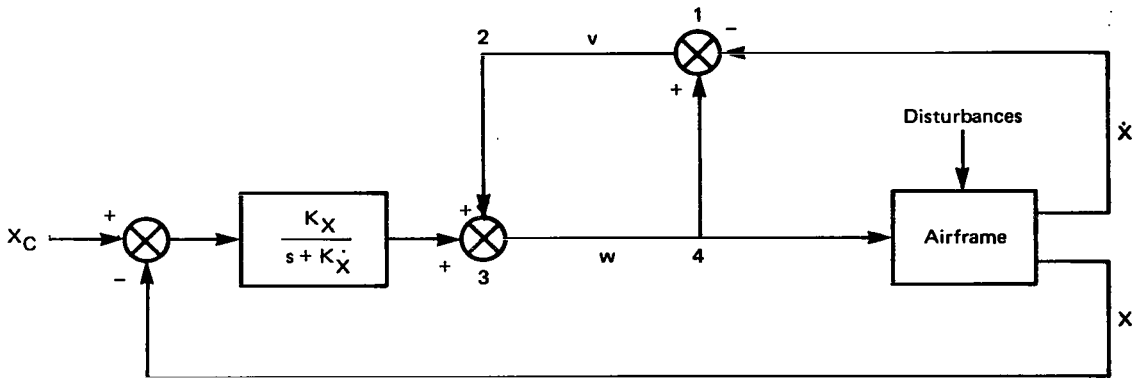

Figure 1.- Ideal state rate feedback implicit model following (SRFIMF) controller.

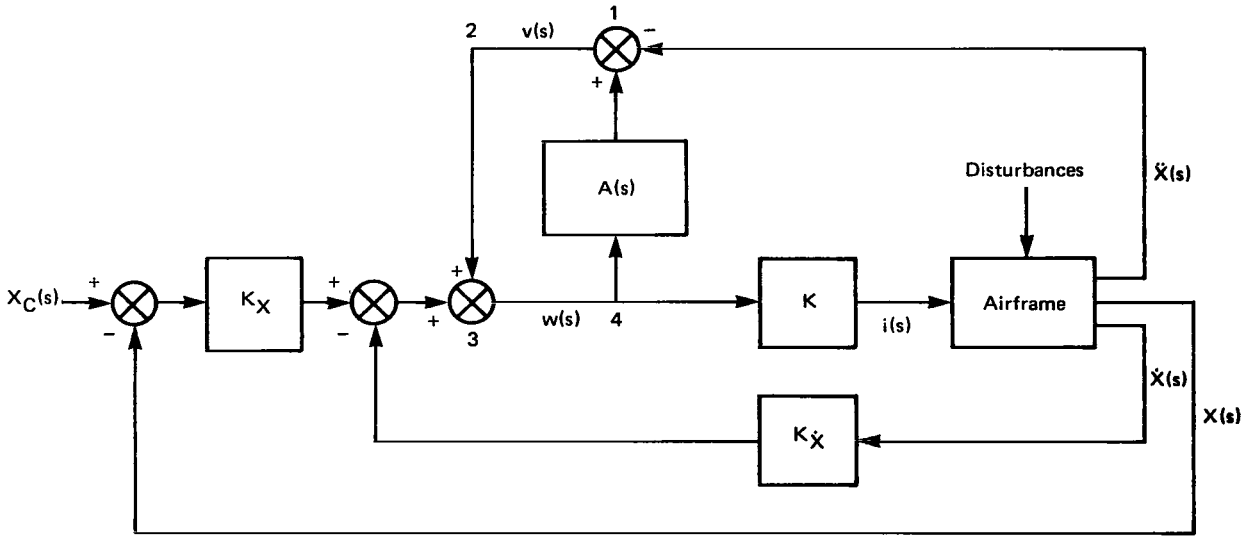

Figure 2.- Physically realizable SRFIMF position controller.

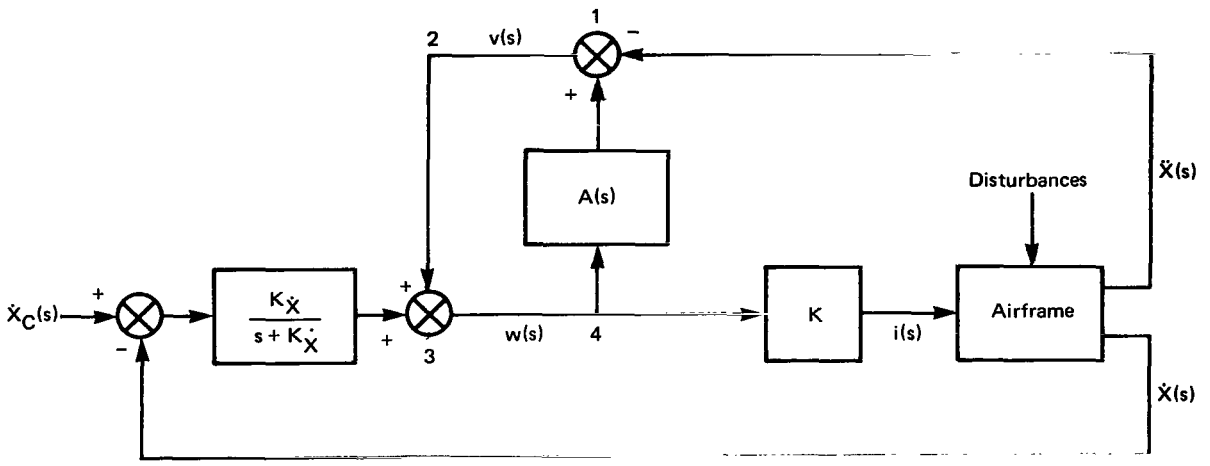

Figure 3.- Physically realizable SRFIMF velocity controller.

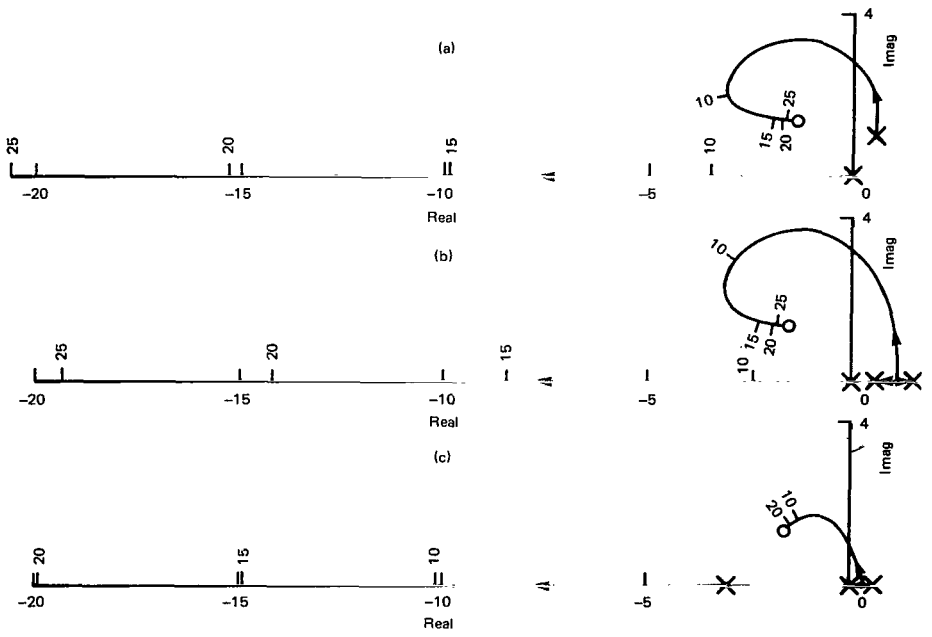

Figure 4.- Typical root loci for characteristic equation

$$1 + \frac{K_{RL}(s^2 + K_{\dot{x}}s + K_x)}{s(s^2 + bs + c)} = 0$$

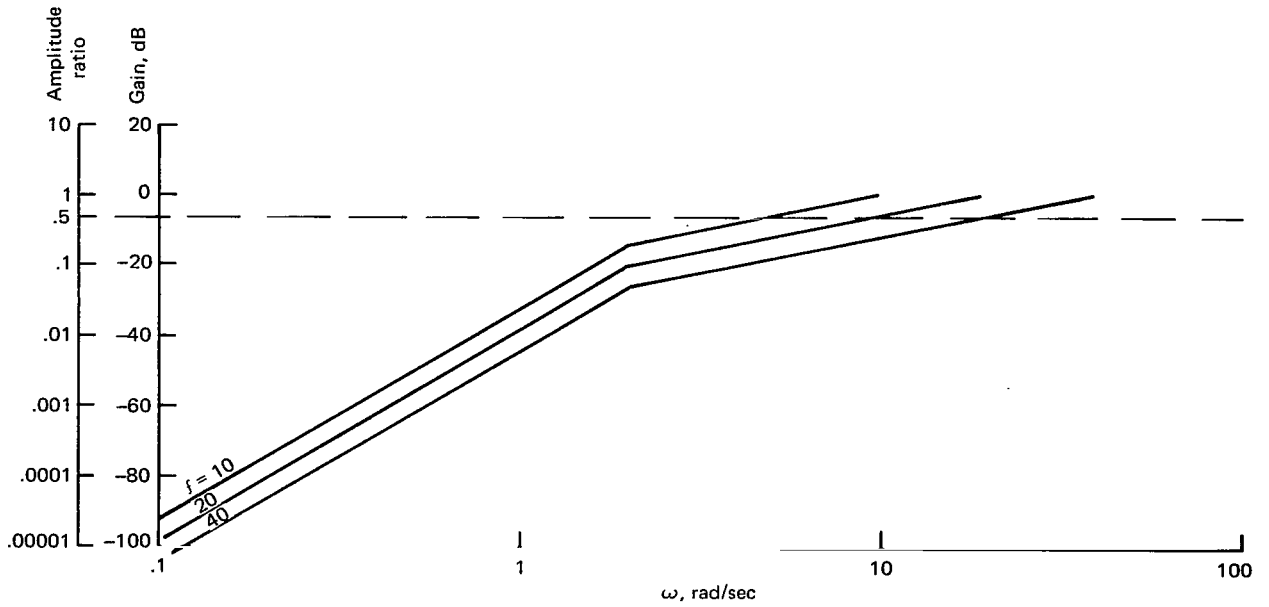

Figure 5.- Frequency response of acceleration due to external disturbances for vehicle with SRFIMF position controller.

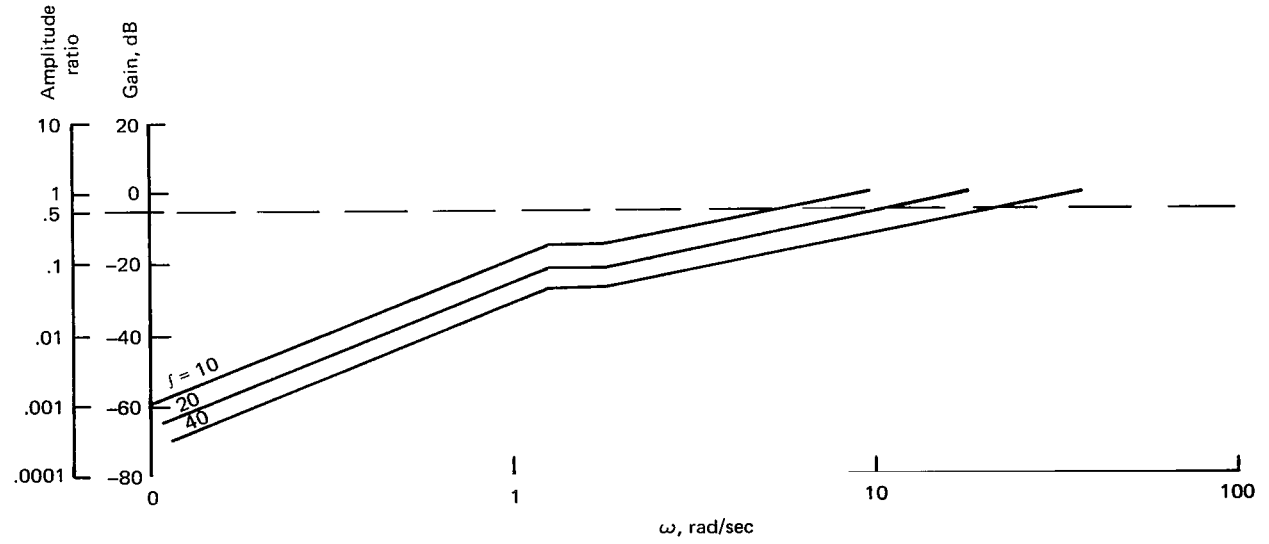

Figure 6.- Frequency response of acceleration due to external disturbances for vehicle with SRFIMF velocity controller.

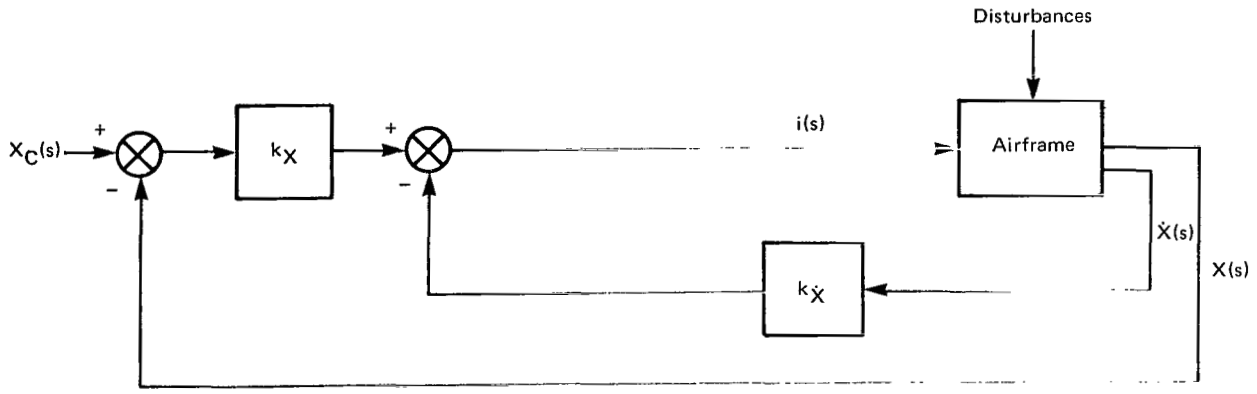

Figure 7.- Response feedback position controller.

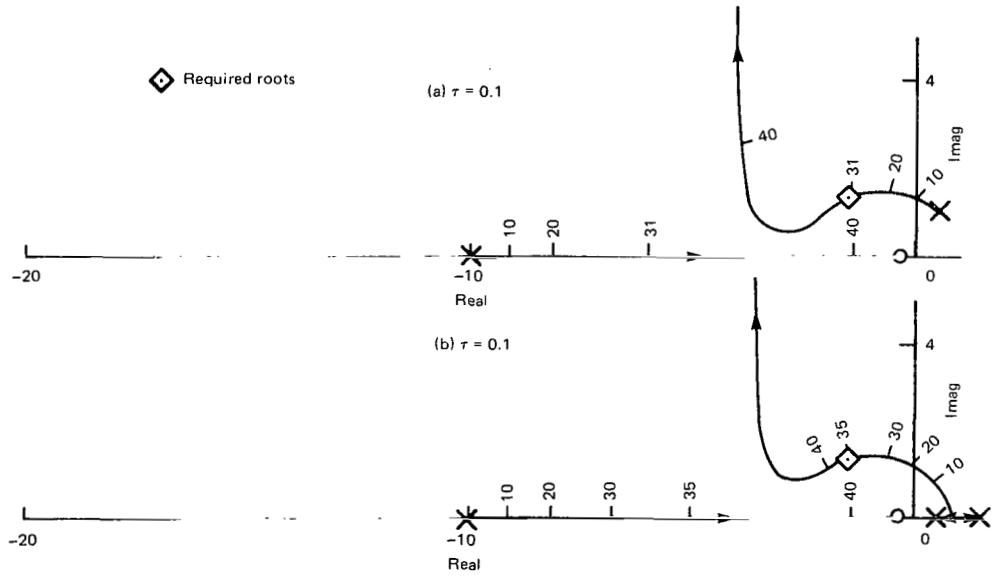

Figure 8.- Typical root loci for characteristic equation

$$1 + \frac{k_{RL}\left(s + \frac{k_x}{k_{\dot{x}}}\right)}{\left(s + \frac{1}{\tau}\right)(s^2 + bs + c)} = 0$$

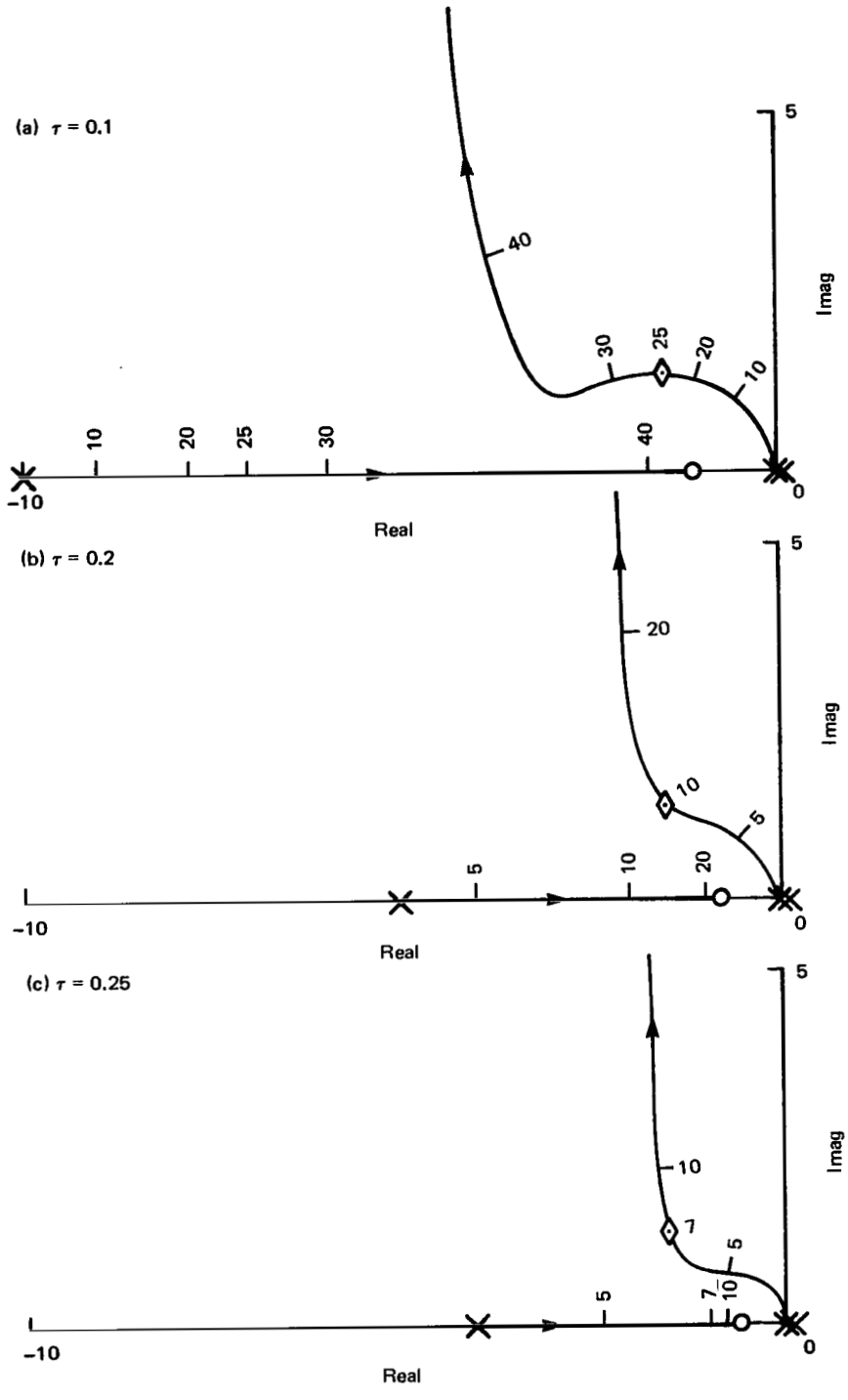

Figure 9.- Typical root loci for characteristic equation

$$1 + \frac{k_{RL}\left(s + \frac{k_x}{k_{\dot{x}}}\right)}{\left(s + \frac{1}{\tau}\right)s^2} = 0$$

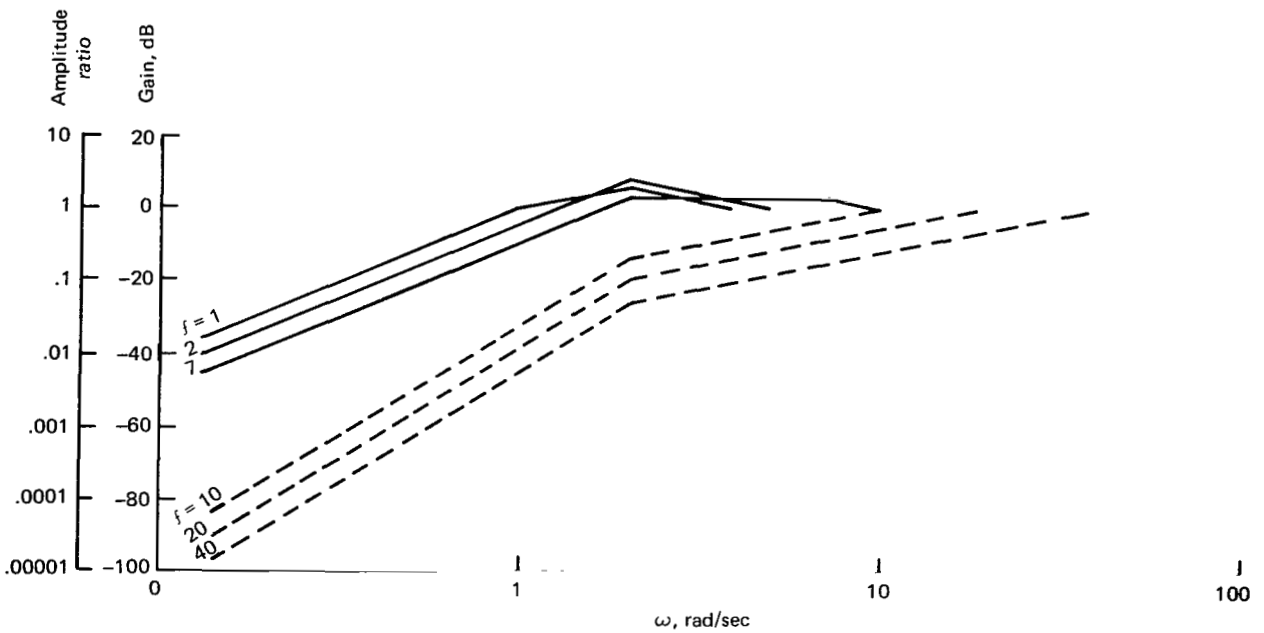

Figure 10.- Comparison of frequency response of vehicle with response feedback controller and SRFIMF position controller.

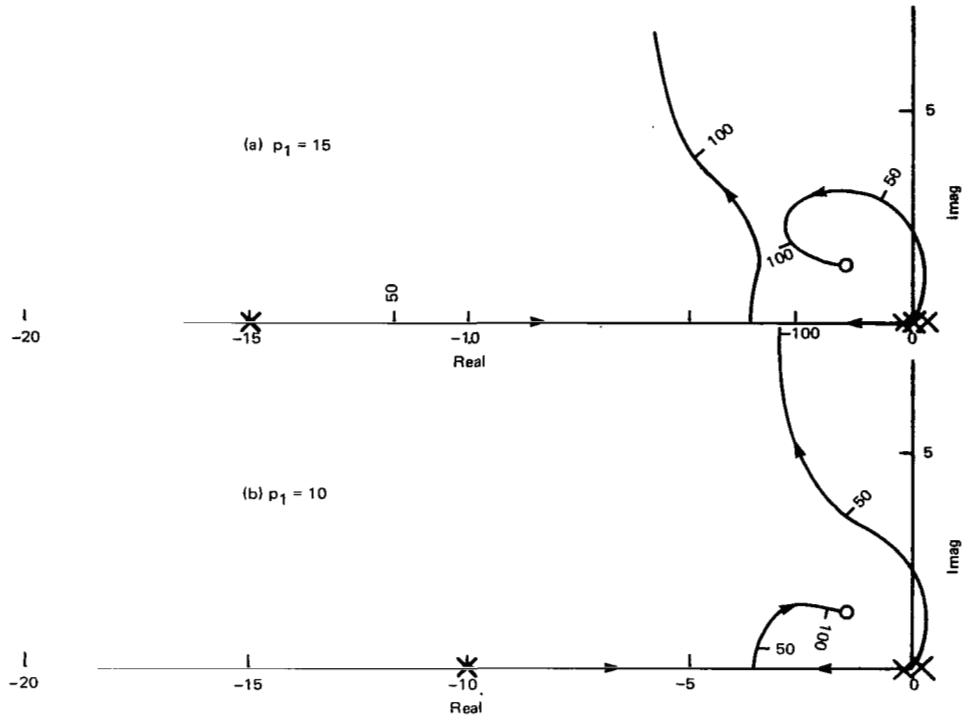

Figure 11.- Typical root loci for characteristic equation

$$1 + \frac{K_{RL}(s^2 + K_x s + K_x)}{s^3(s + p_1)} = 0$$

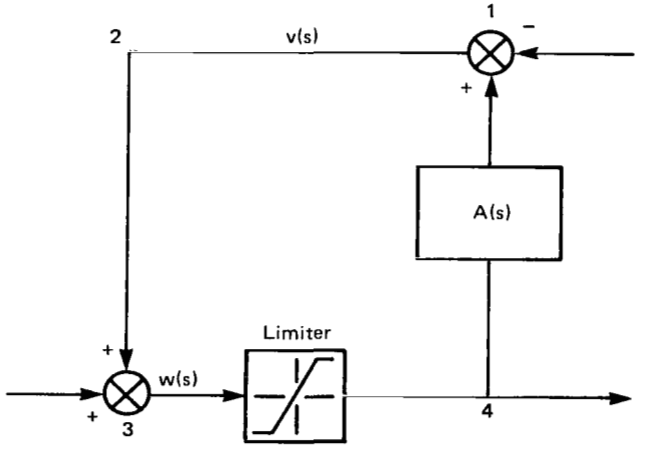

Figure 12.- Location of controller output limiter.

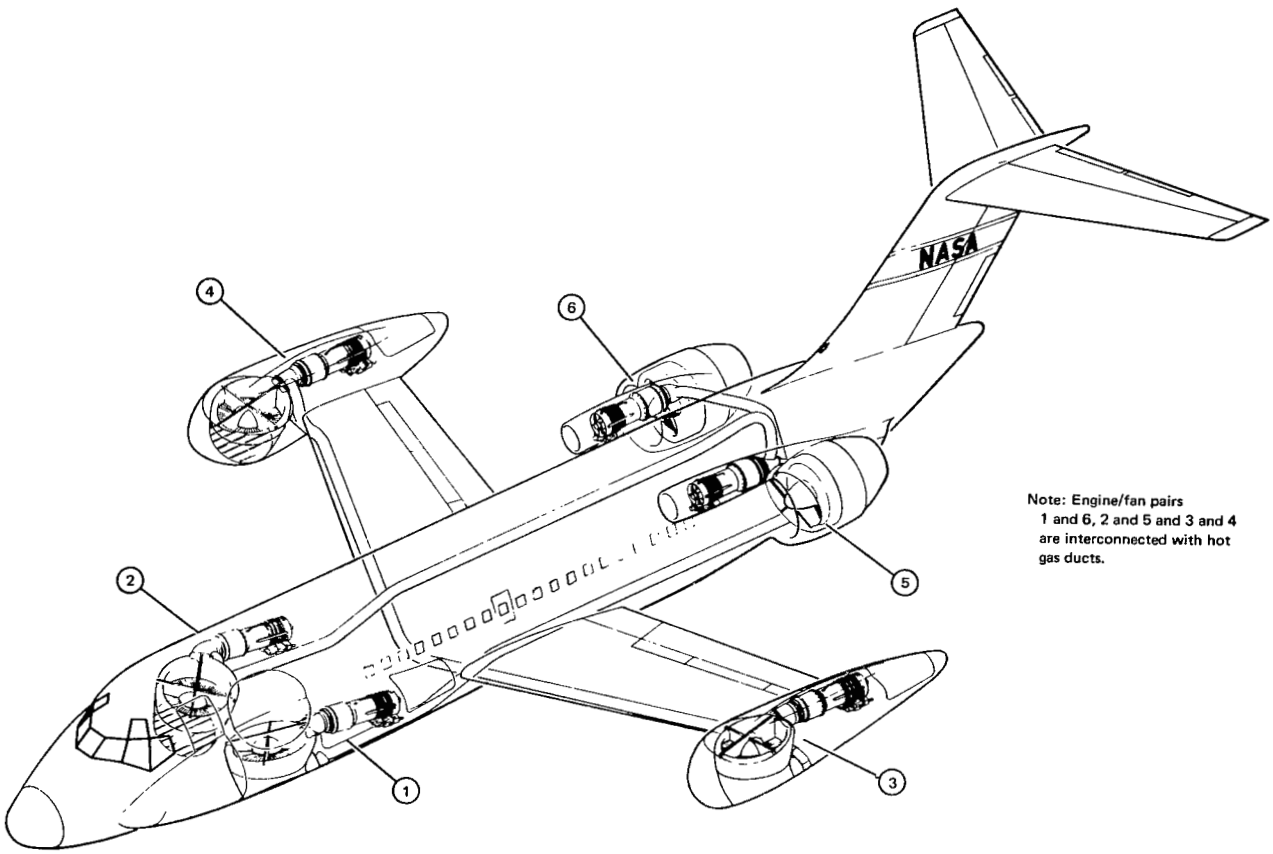

Figure 13.- Simulated lift-fan V/STOL transport.

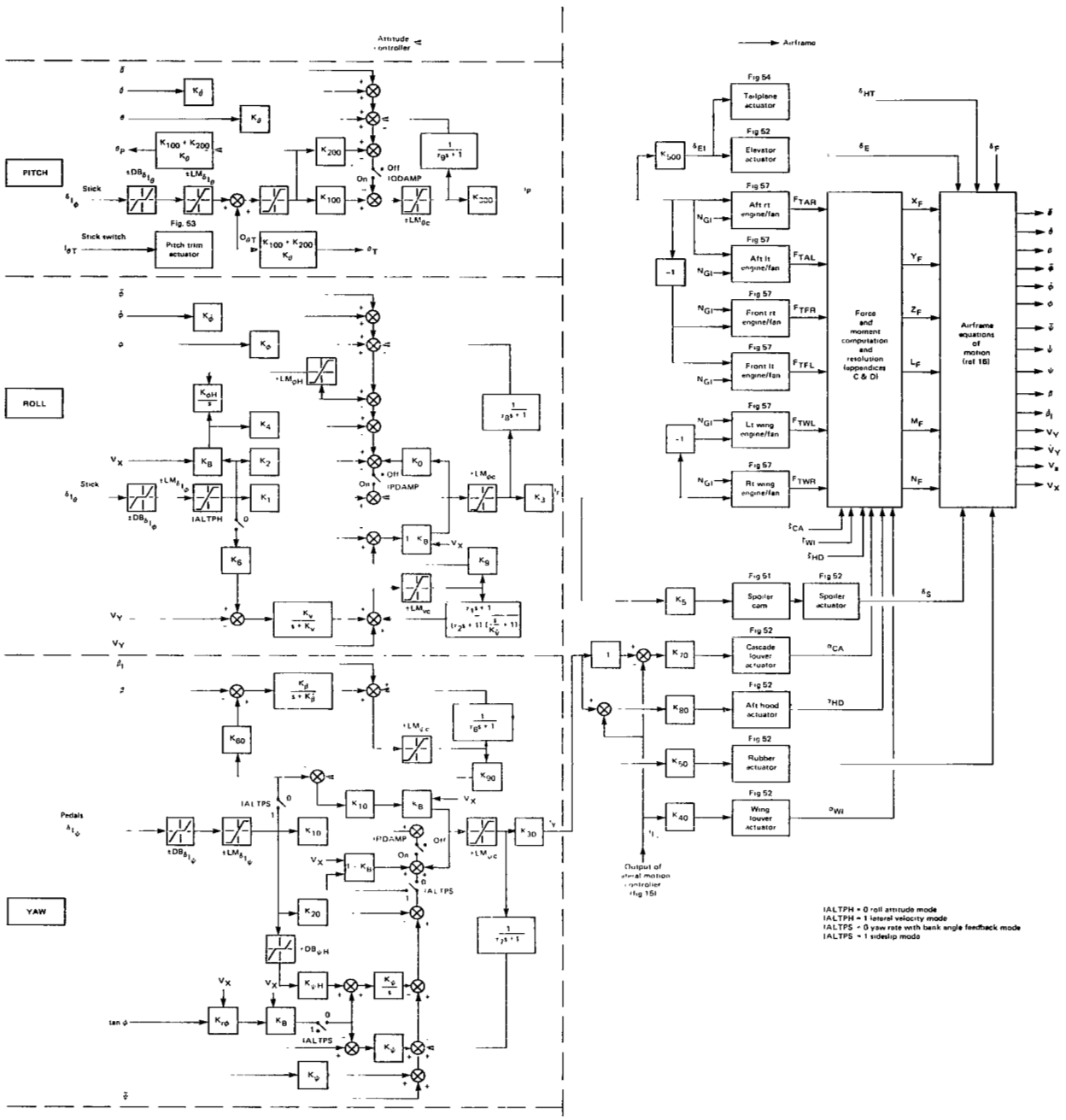

Figure 14.- SRFIMF attitude flight controller.

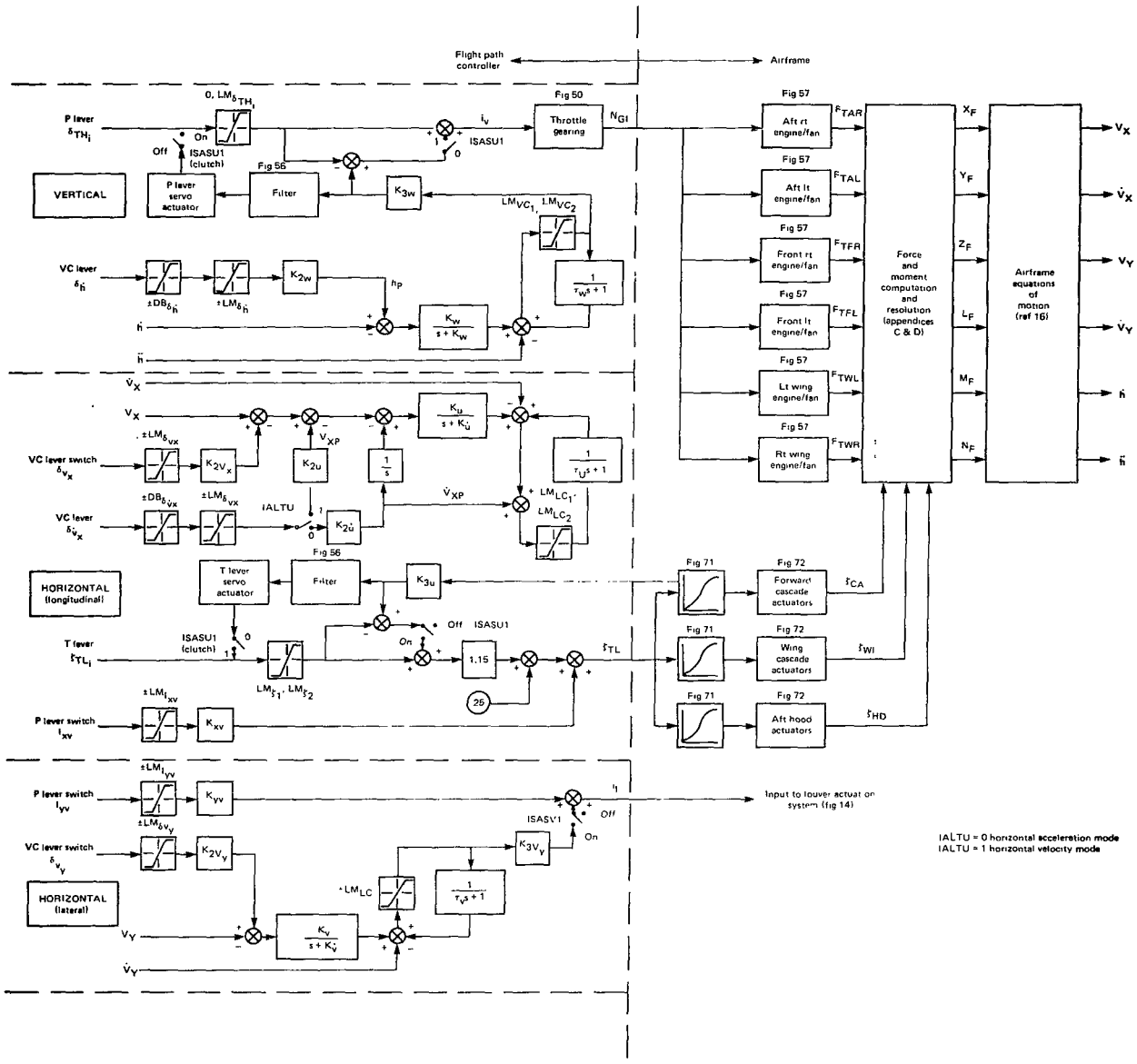

Figure 15.- SRFIMF flight-path controller.

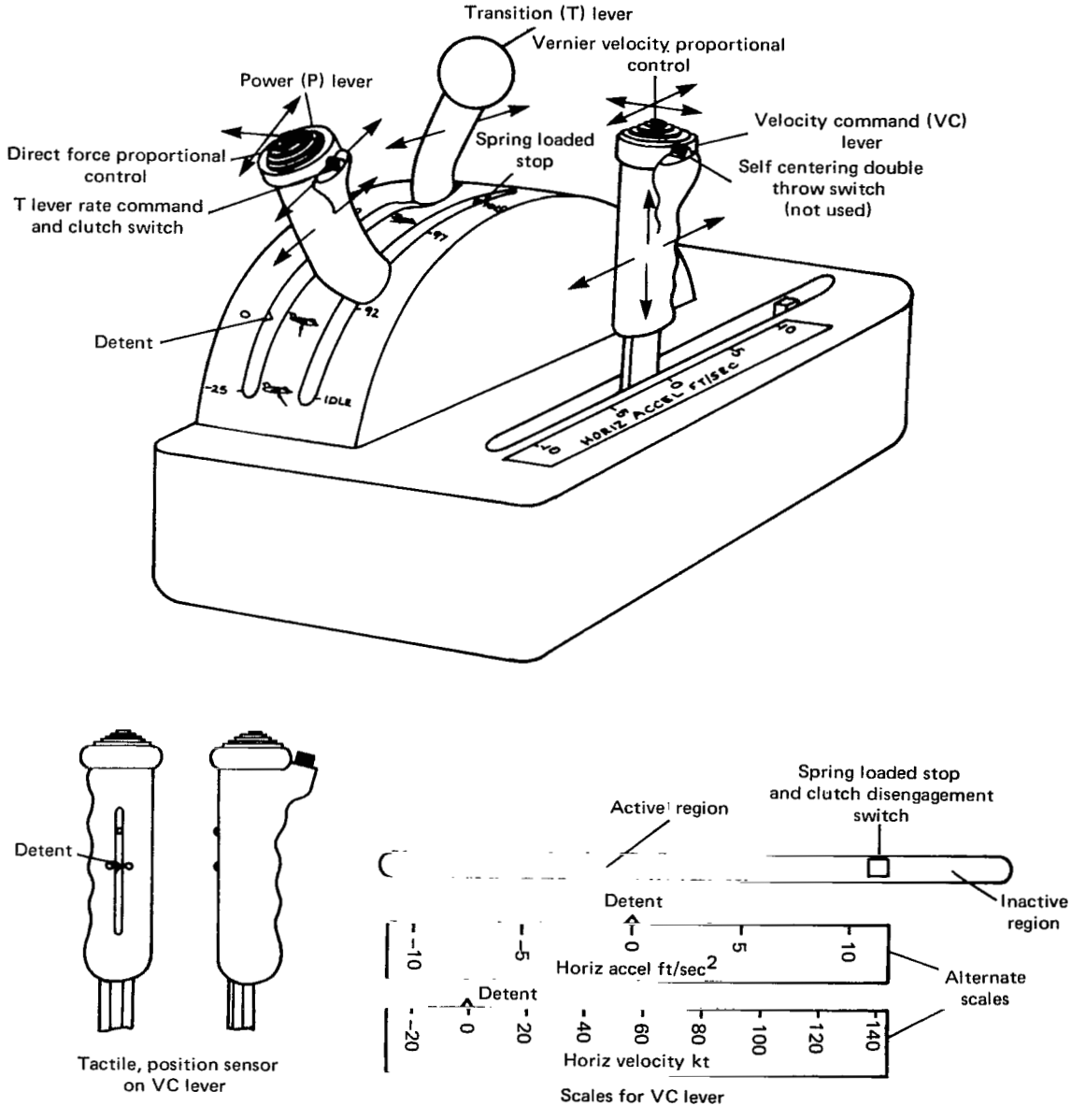

Figure 16.- Lift-fan transport master power management controls (MK1).

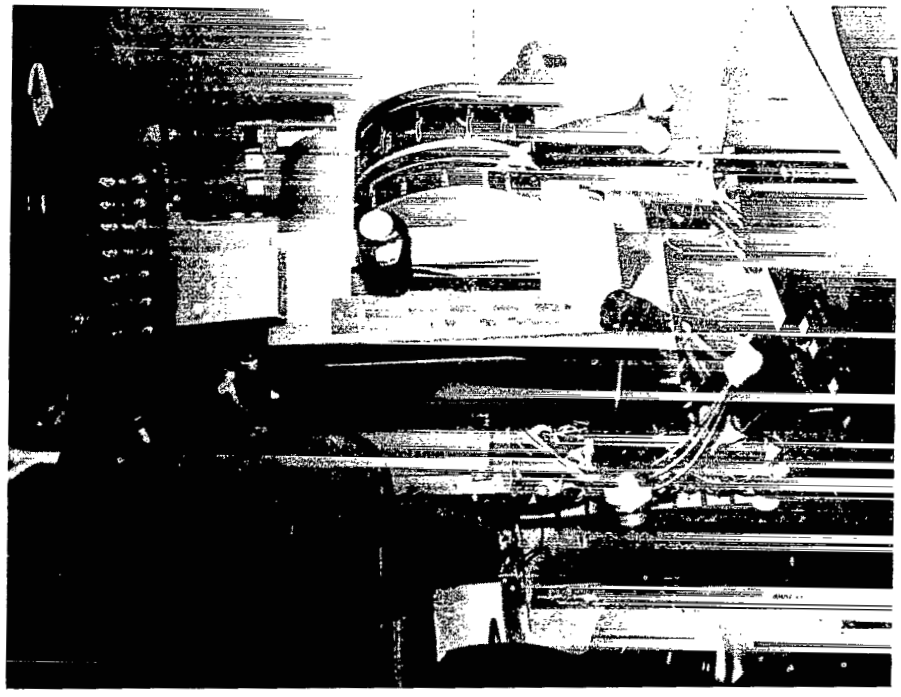

Figure 17.- Lift-fan transport master power management controls (MK1).

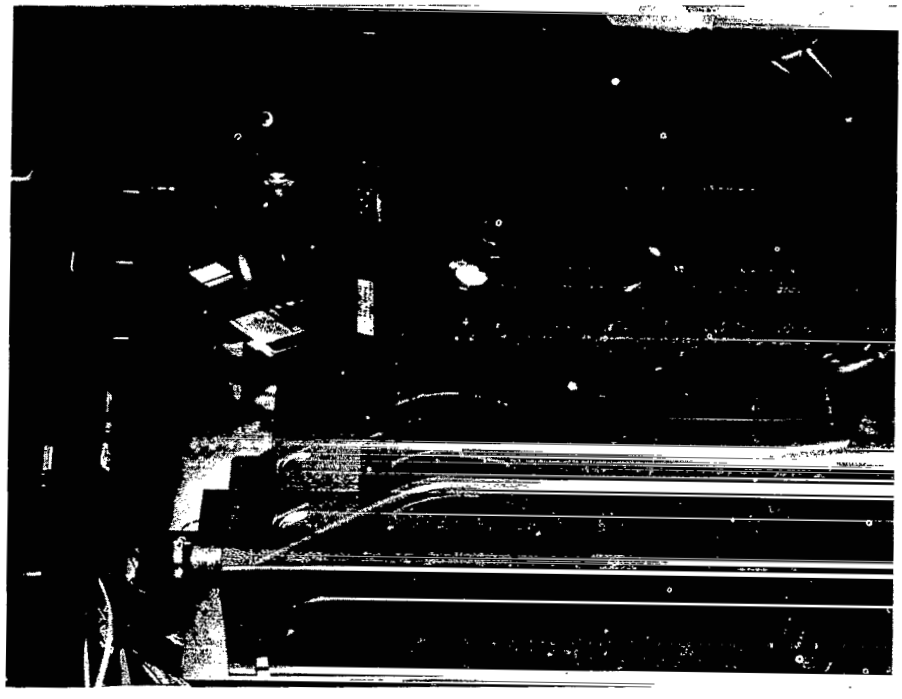

Figure 18.- Lift-fan transport master power management controls (MK1)

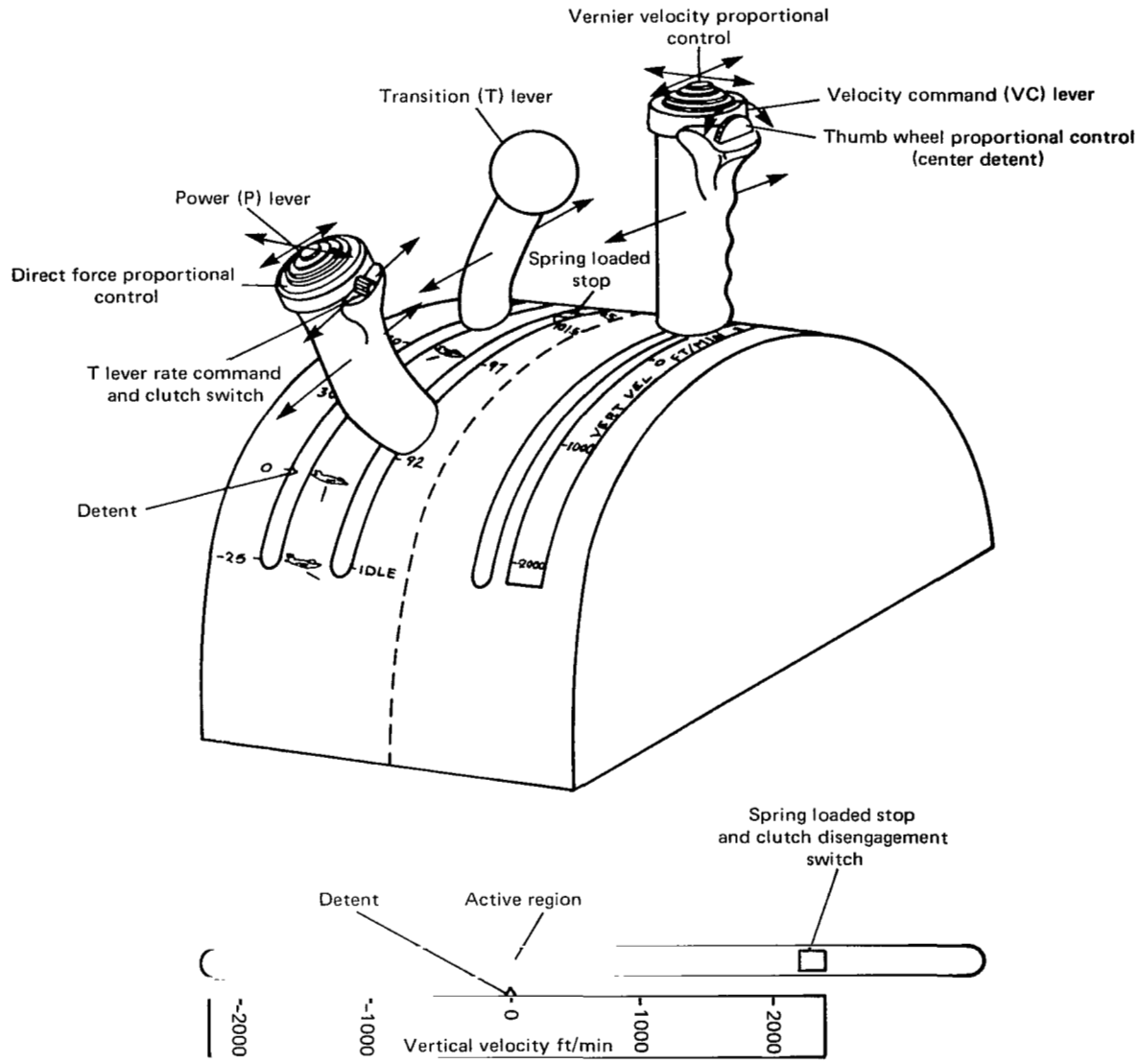

Figure 19.- Lift-fan transport master power management controls (MK2).

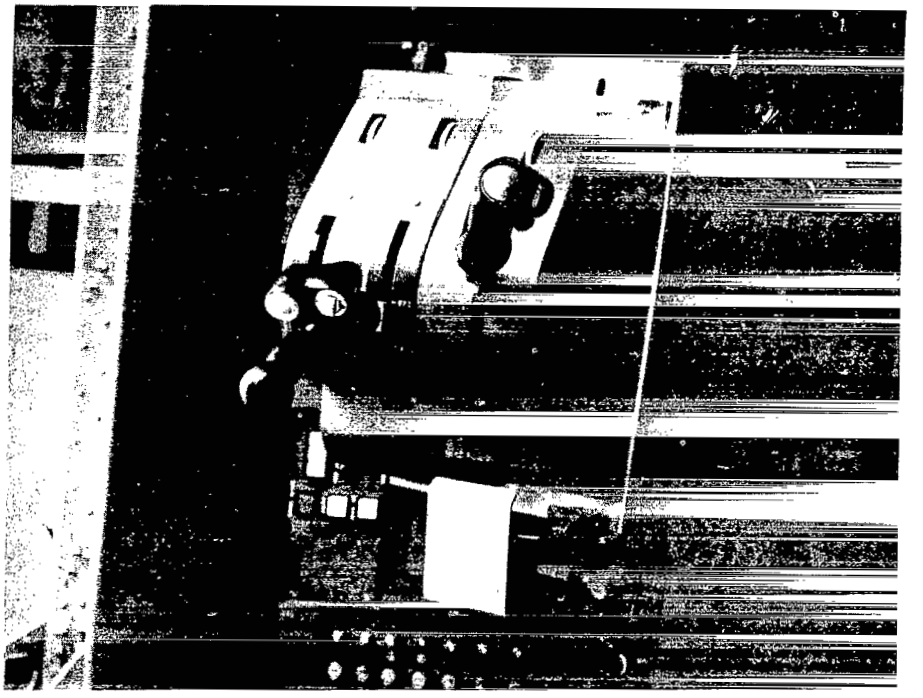

Figure 20.- Lift-fan transport master power management controls (MK2).

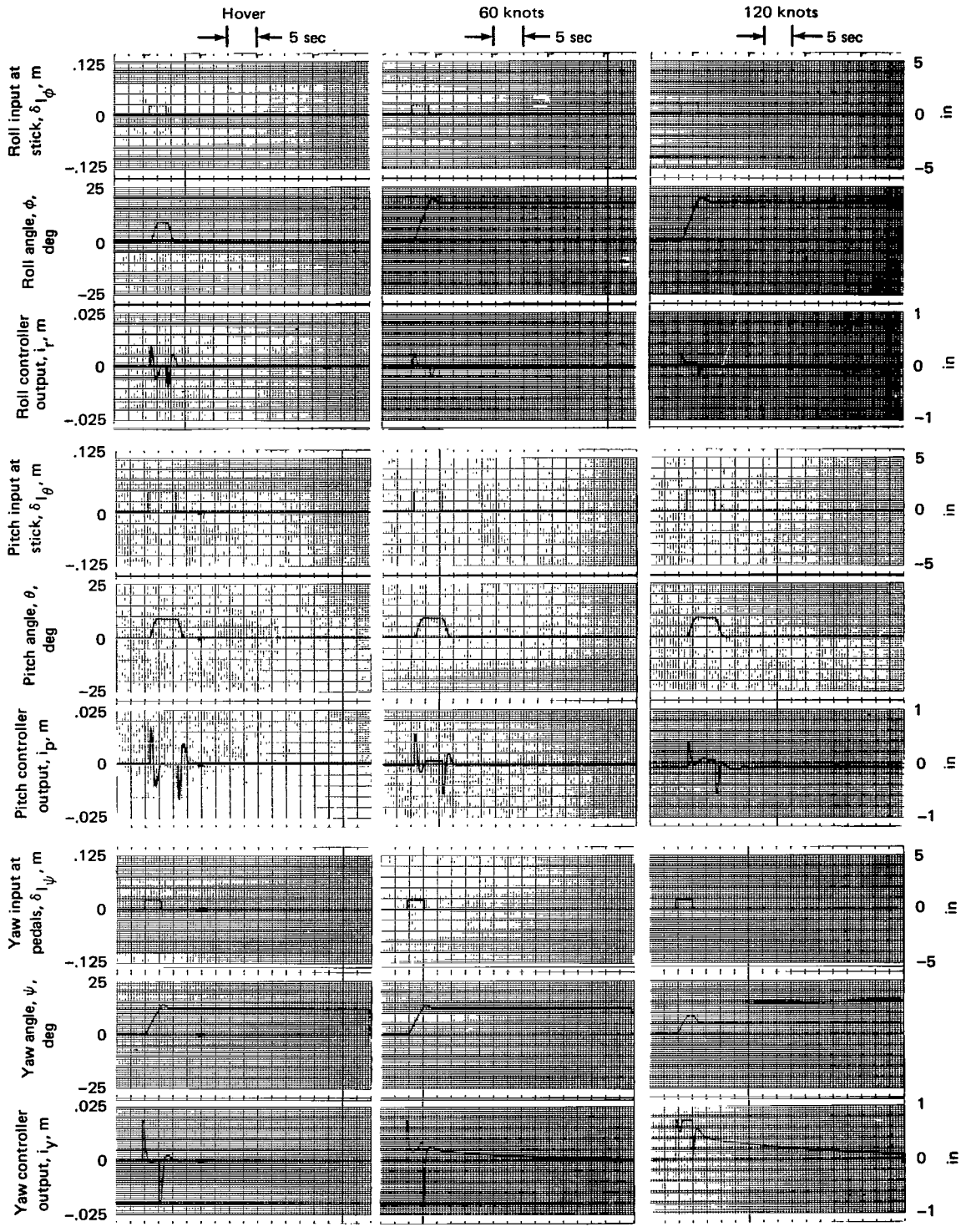

Figure 21.- Attitude response due to single pulse inputs in roll, pitch, and yaw at hover, 60 knots and 120 knots.

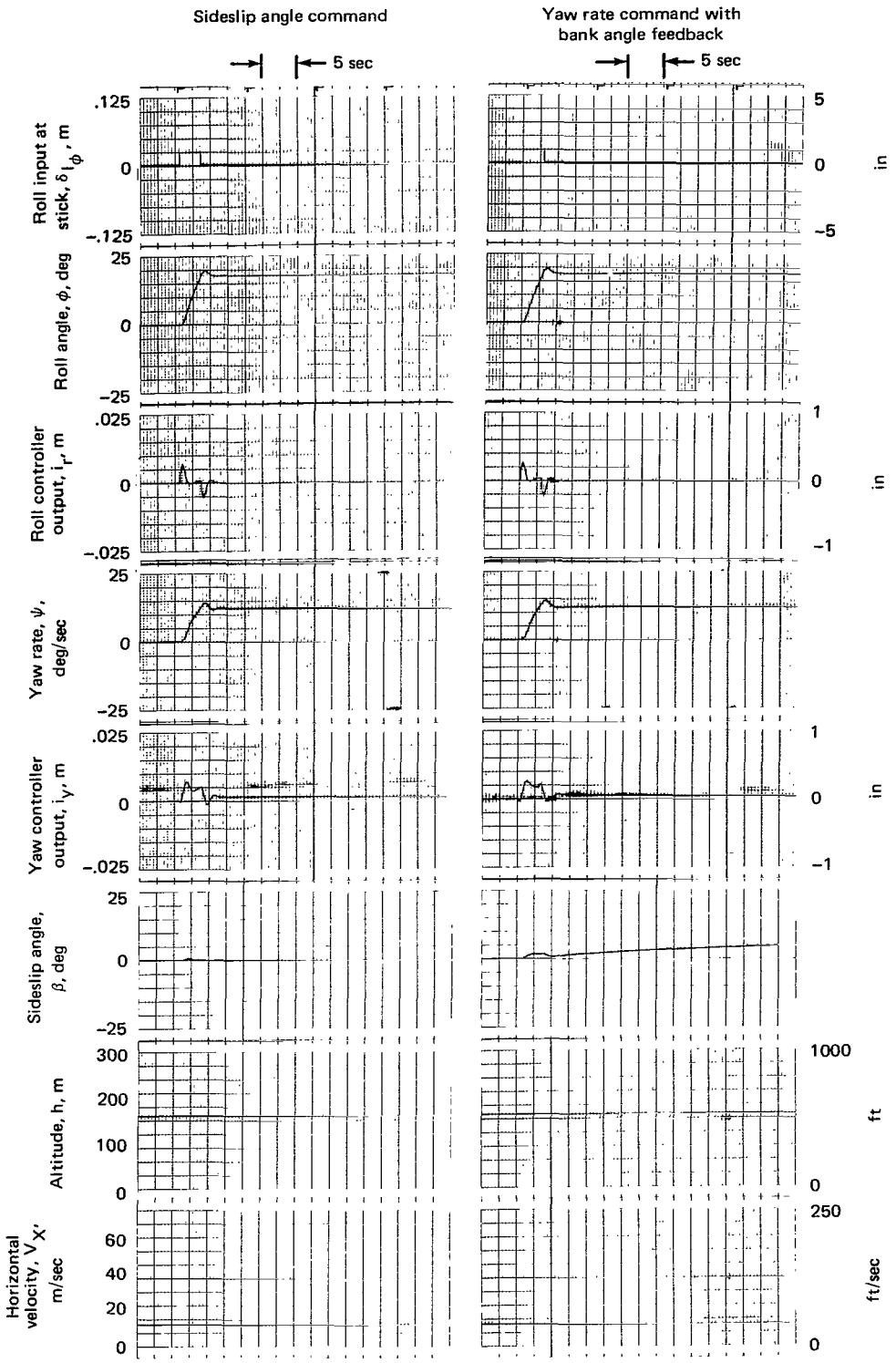

Figure 22.- Response to roll input pulse at 30 knots for two types of yaw controller modes.

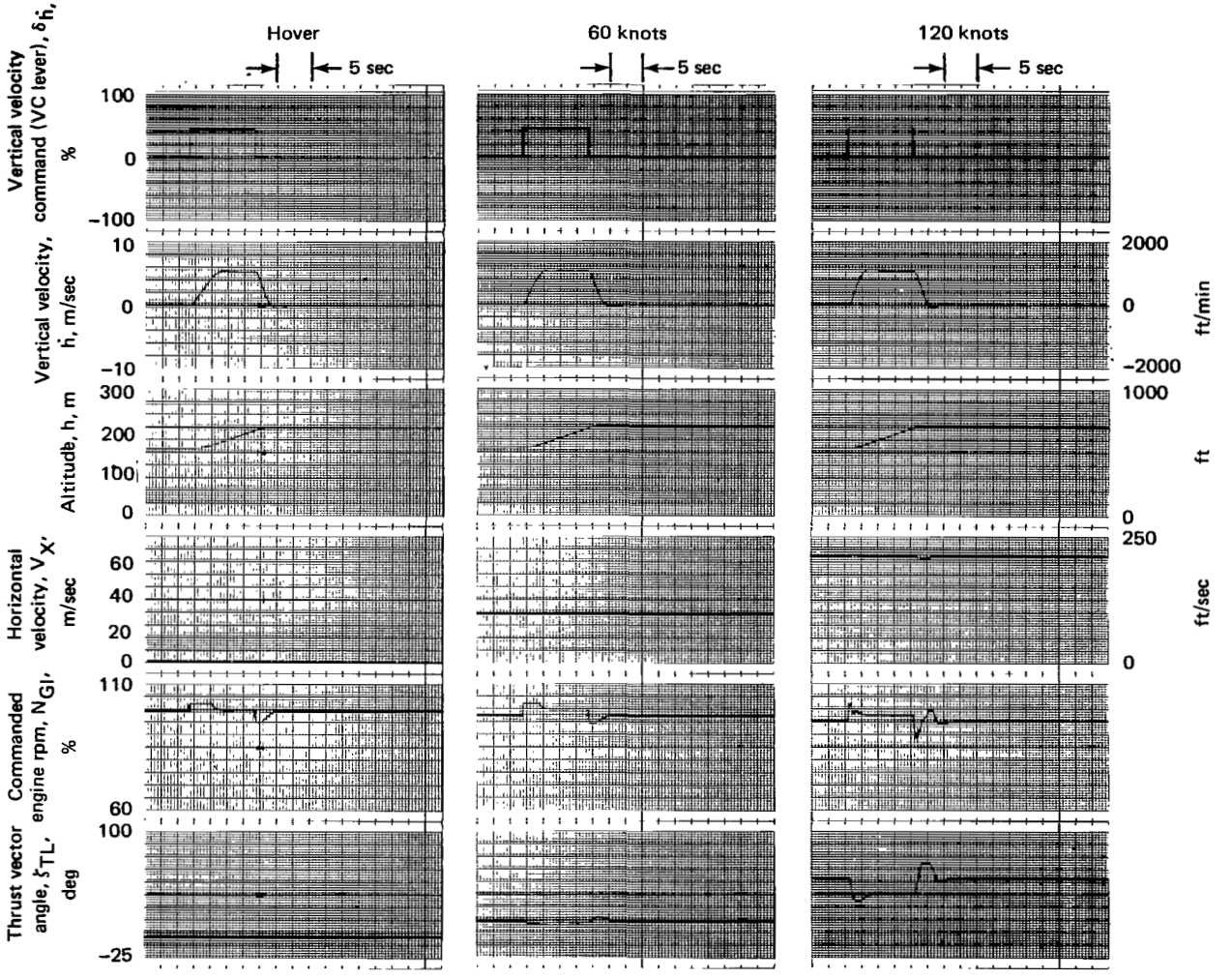

Figure 23.- Response to a vertical velocity command pulse at hover, 60 knots and 120 knots.

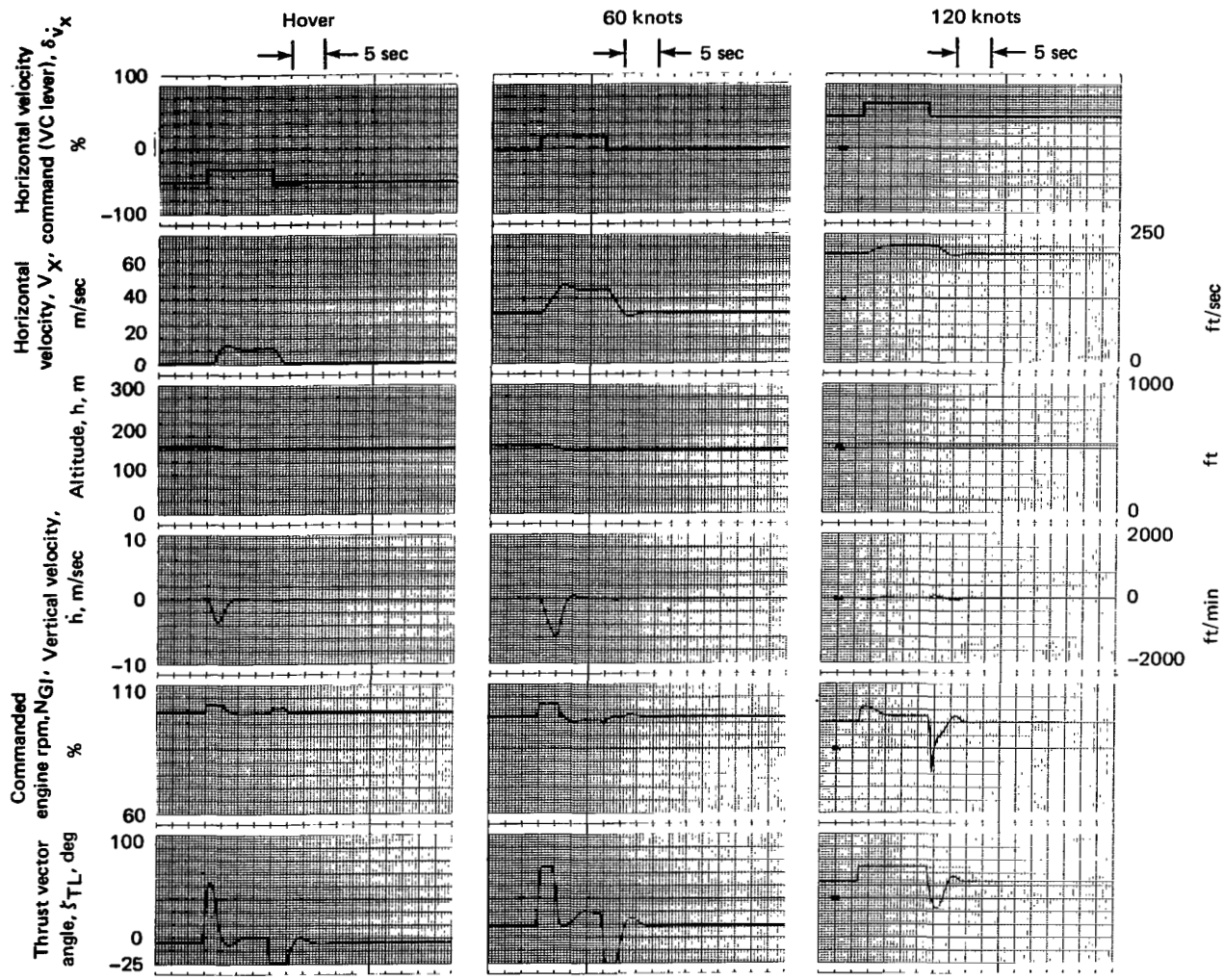

Figure 24.- Response to a horizontal velocity command pulse at hover, 60 knots and 120 knots.

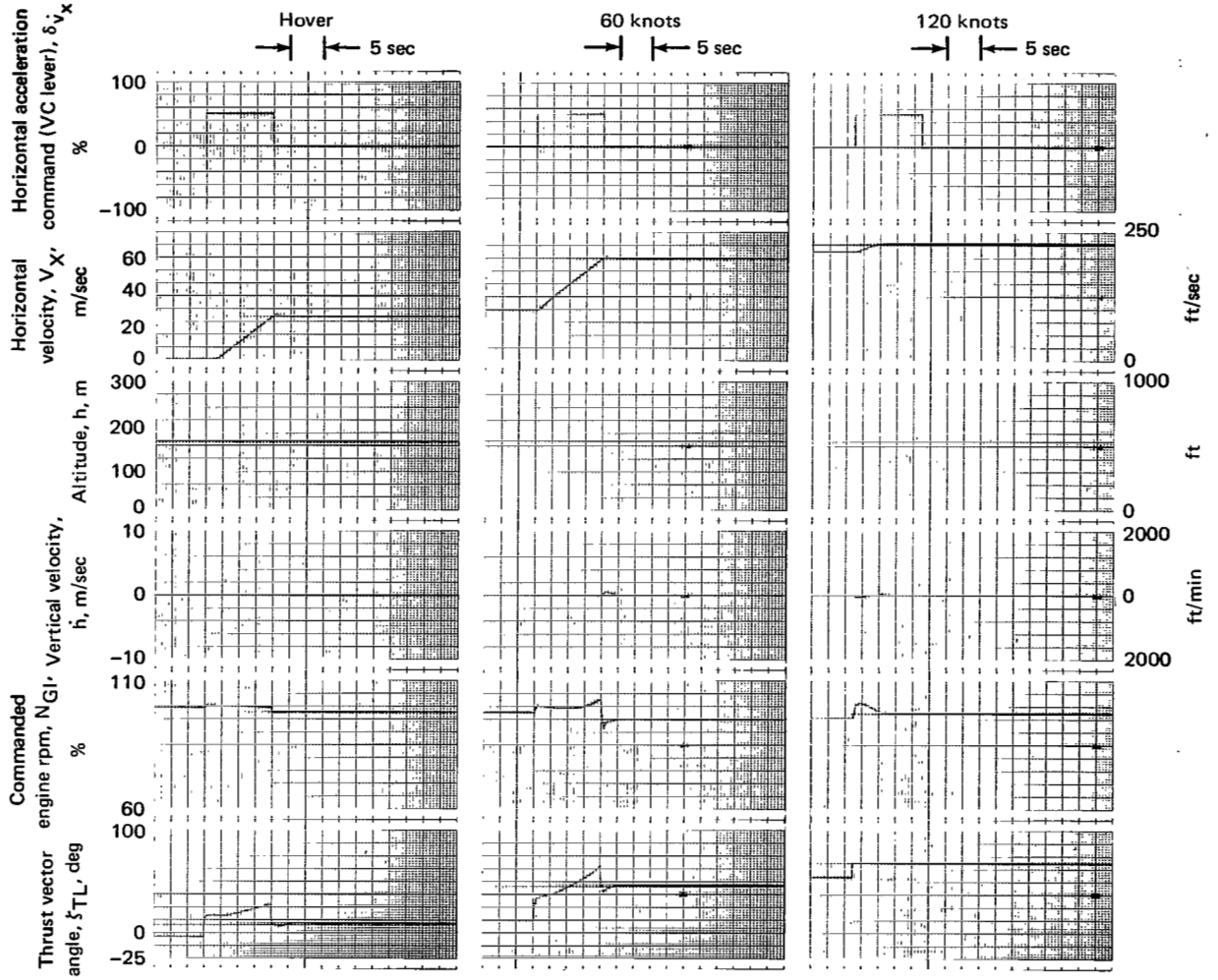

Figure 25.- Response to horizontal acceleration command pulse at hover, 60 knots and 120 knots.

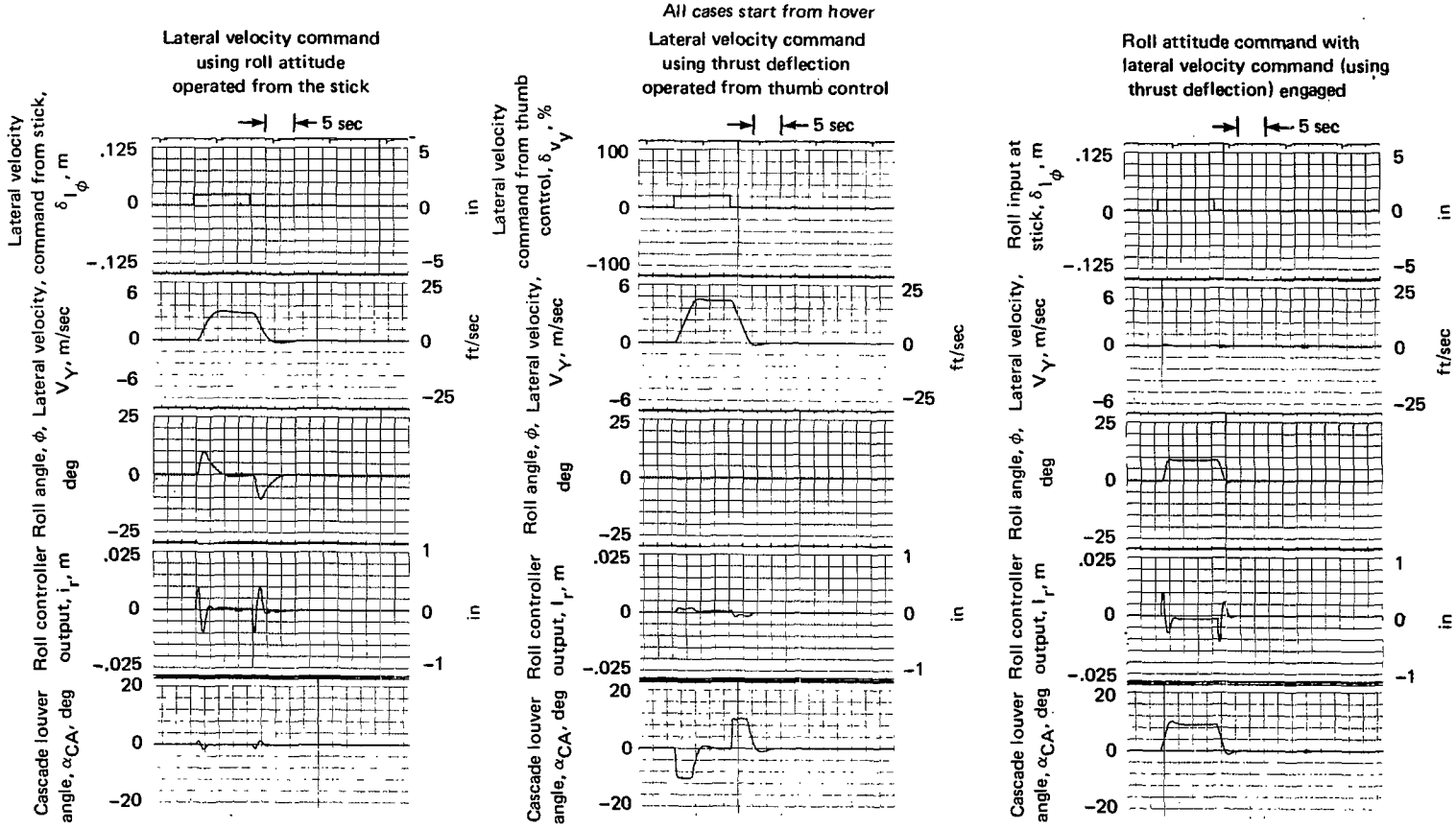

Figure 26.- Comparison of two methods of lateral velocity command (see table 4); roll response with lateral velocity controller engaged.

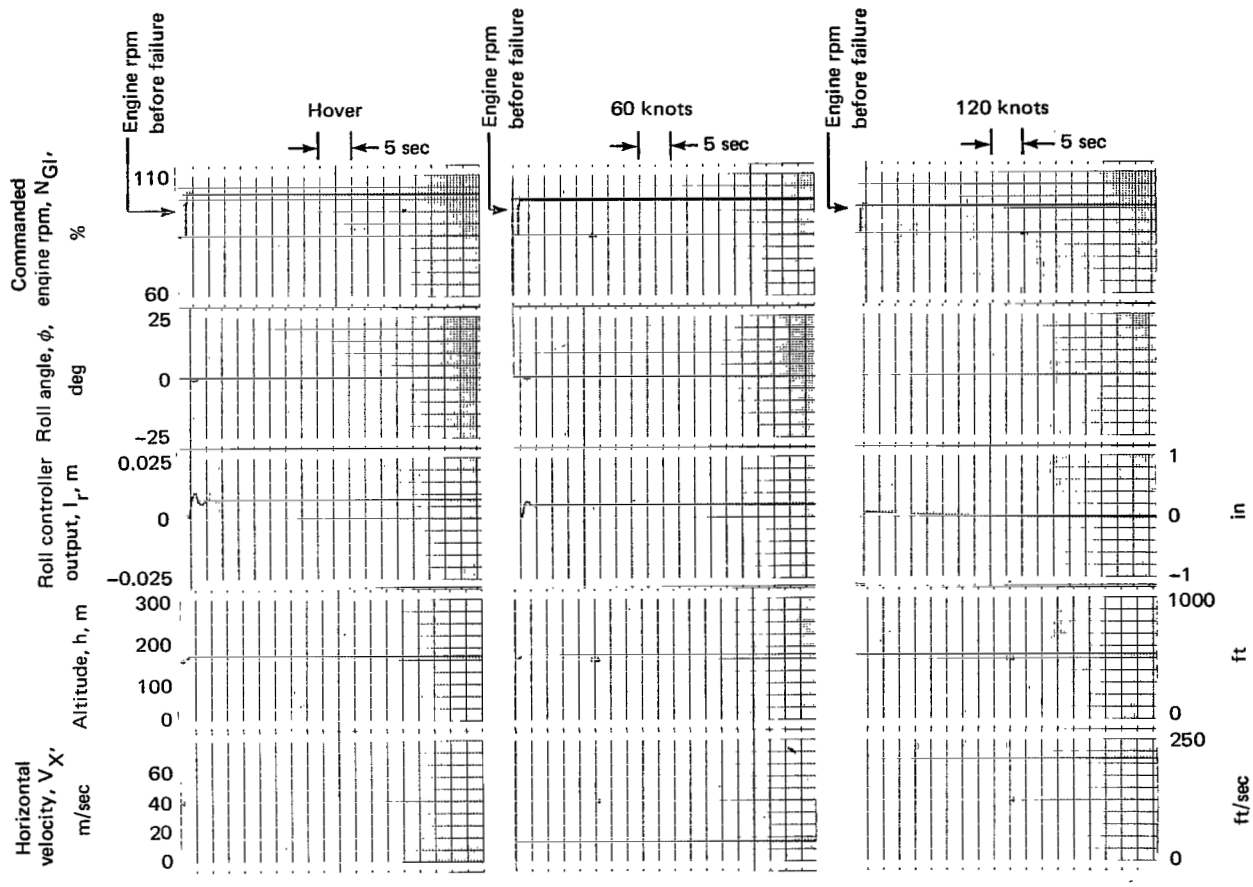

Figure 27.- Roll response following a wing-tip engine failure at hover, 60 knots and 120 knots.

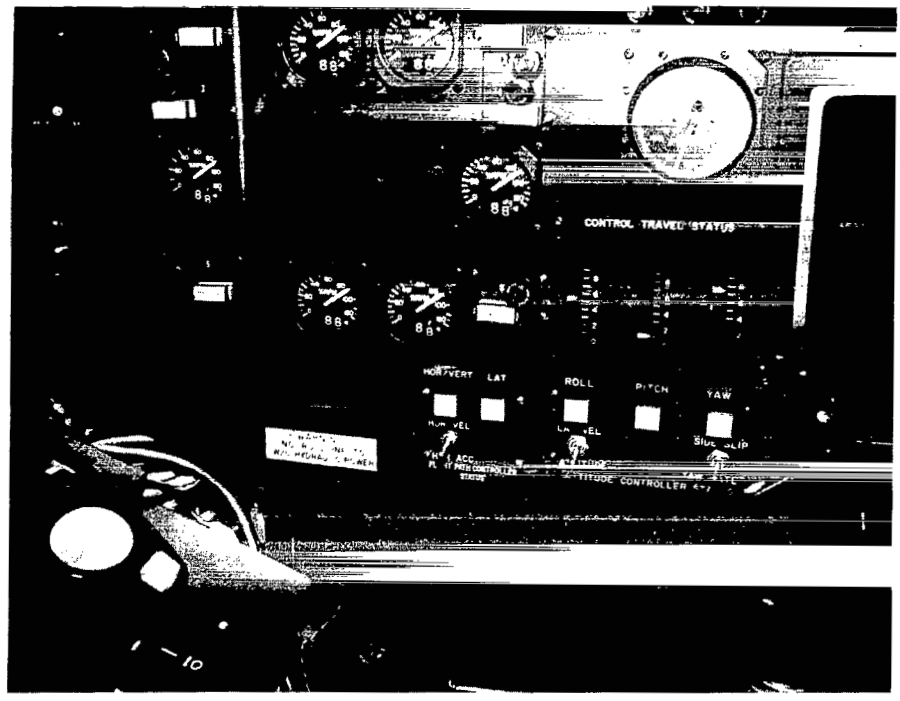

Figure 28.- Cockpit instrument panel (left side).

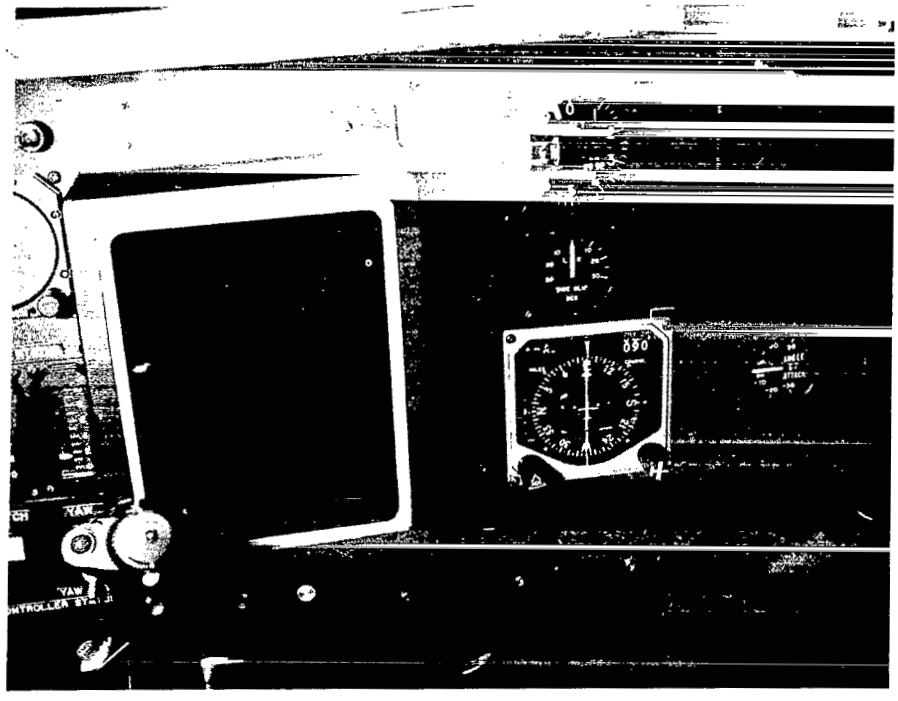

Figure 29.- Cockpit instrument panel (right side).

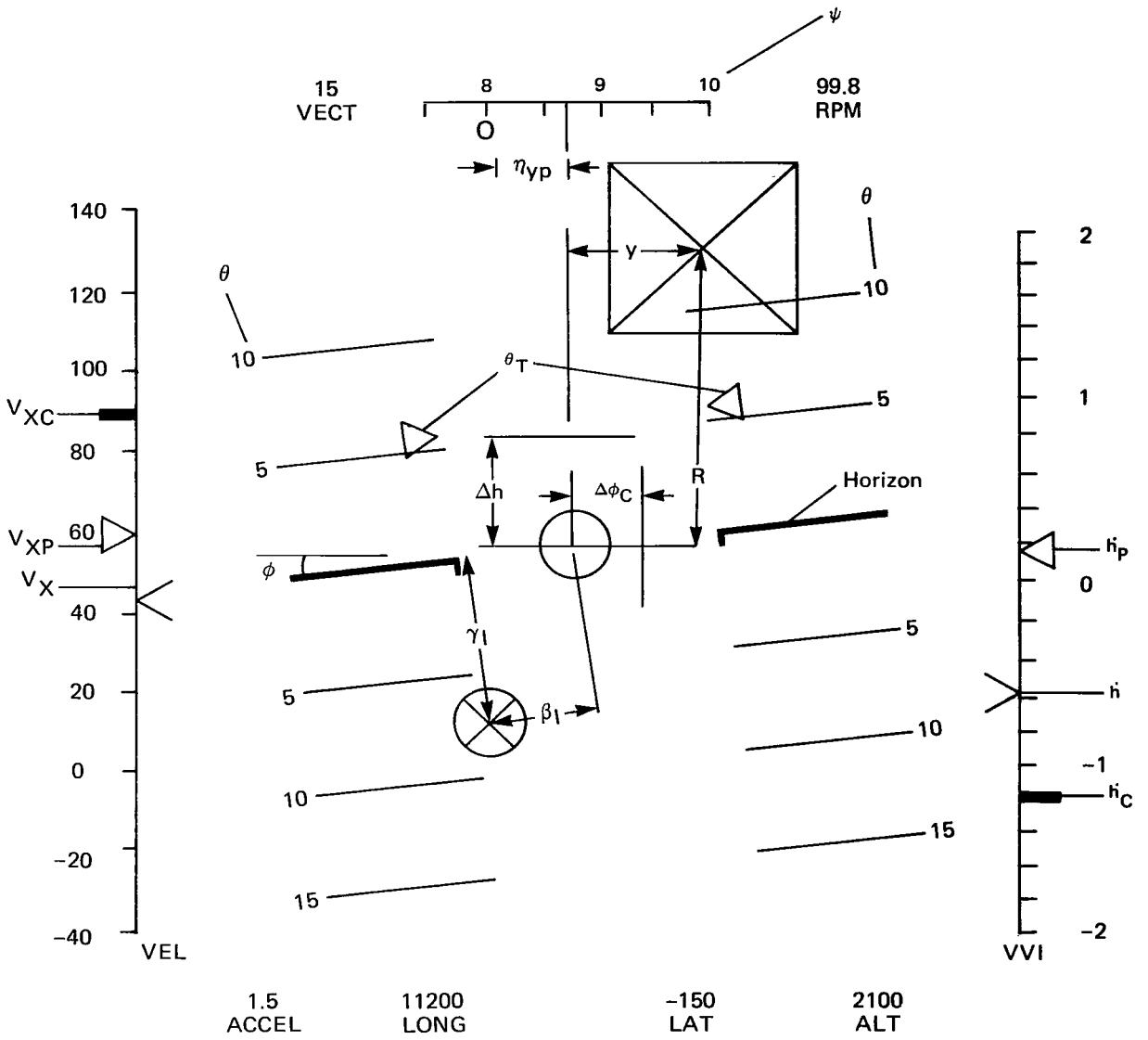

Figure 30.- Electronic display format for longitudinal velocity and vertical velocity command system.

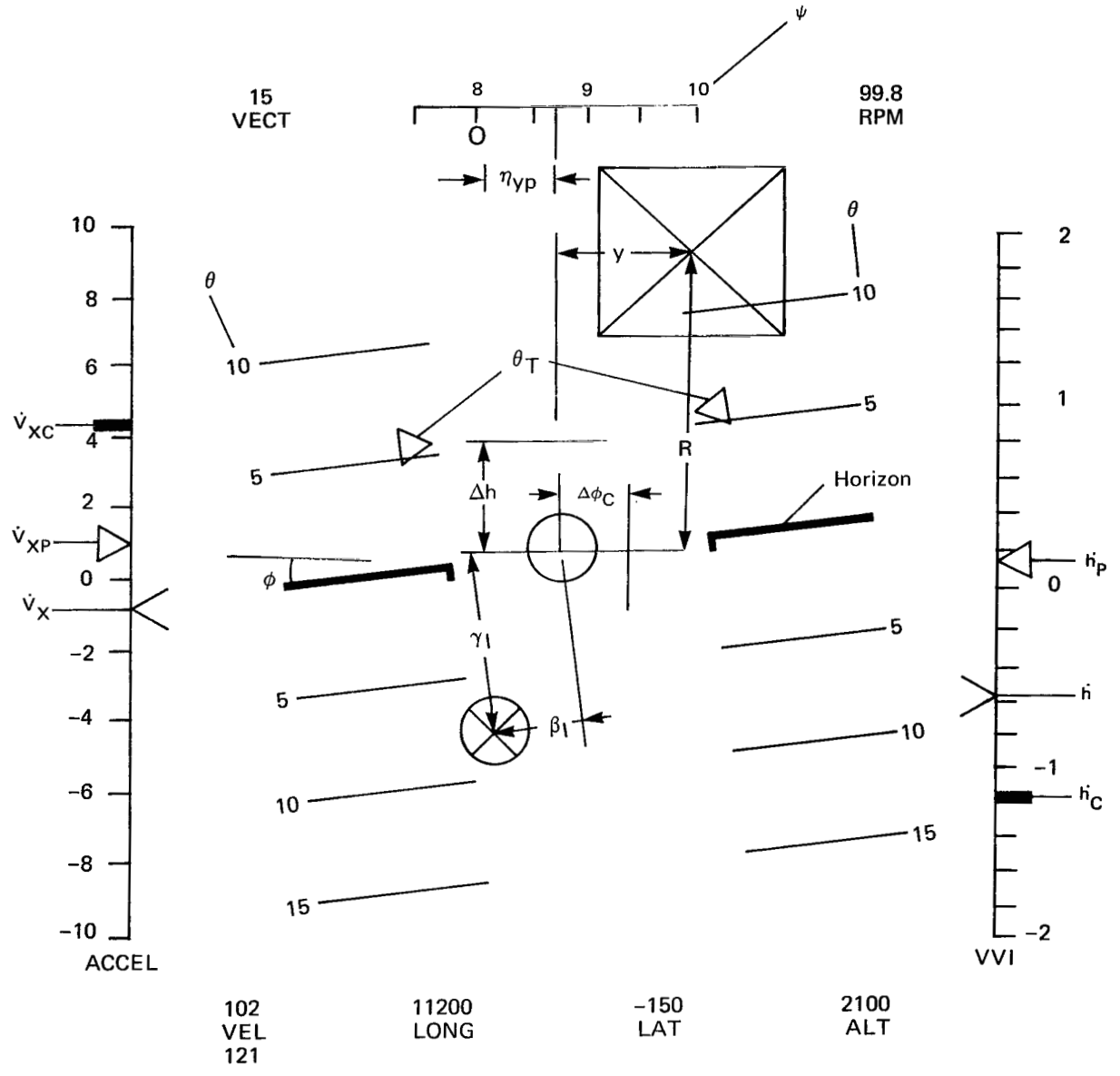

Figure 31.- Electronic display format for longitudinal acceleration and vertical velocity command system.

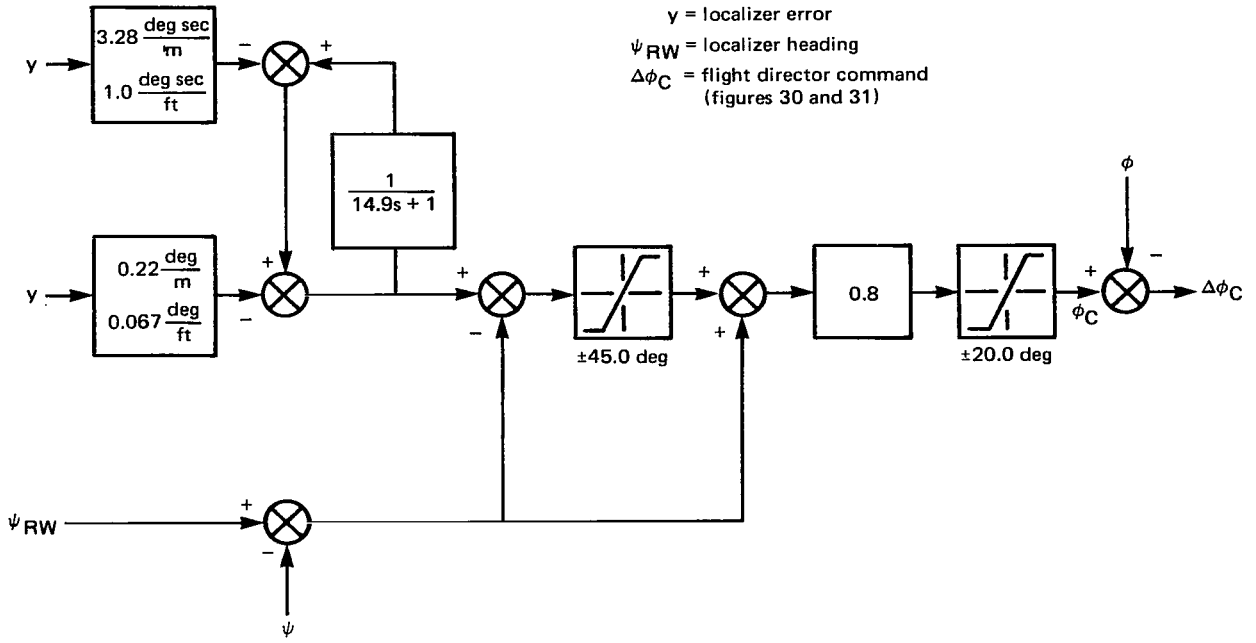

Figure 32.- Lateral flight director.

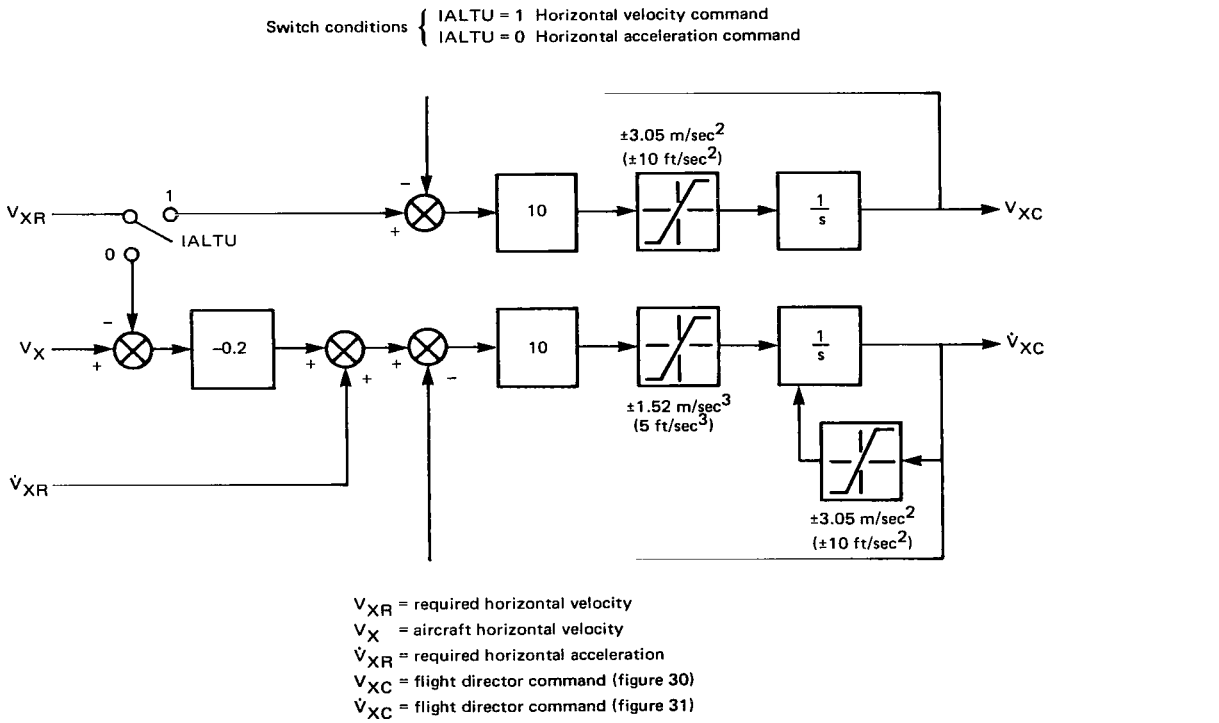

Figure 33.- Horizontal flight director.

h_R = required altitude
h = aircraft altitude
$\dot{h}_R$ = required vertical velocity
$\ddot{h}_R$ = required vertical acceleration
$\dot{h}_C$ = flight director command (figures 30 and 31)

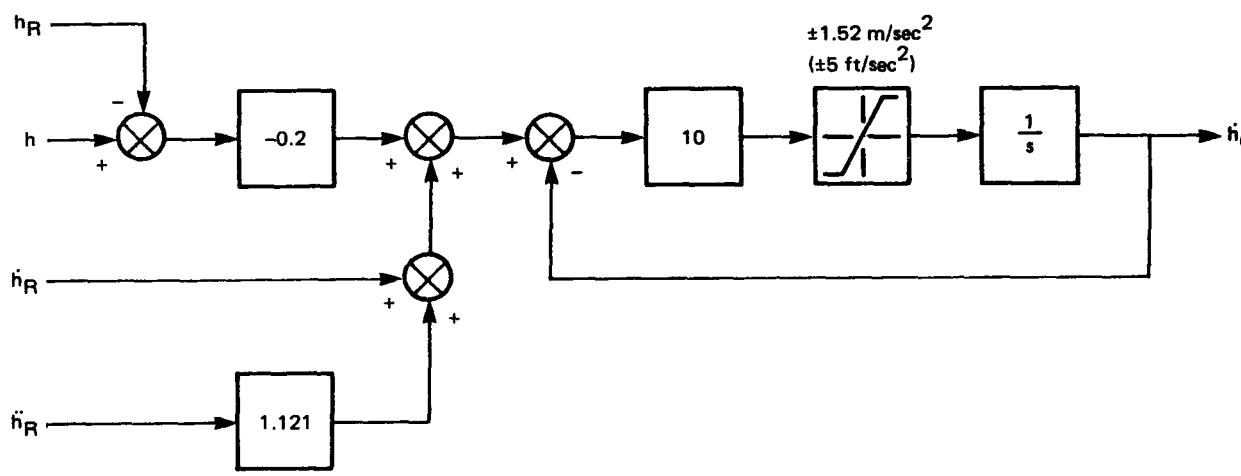

Figure 34.- Vertical flight director.

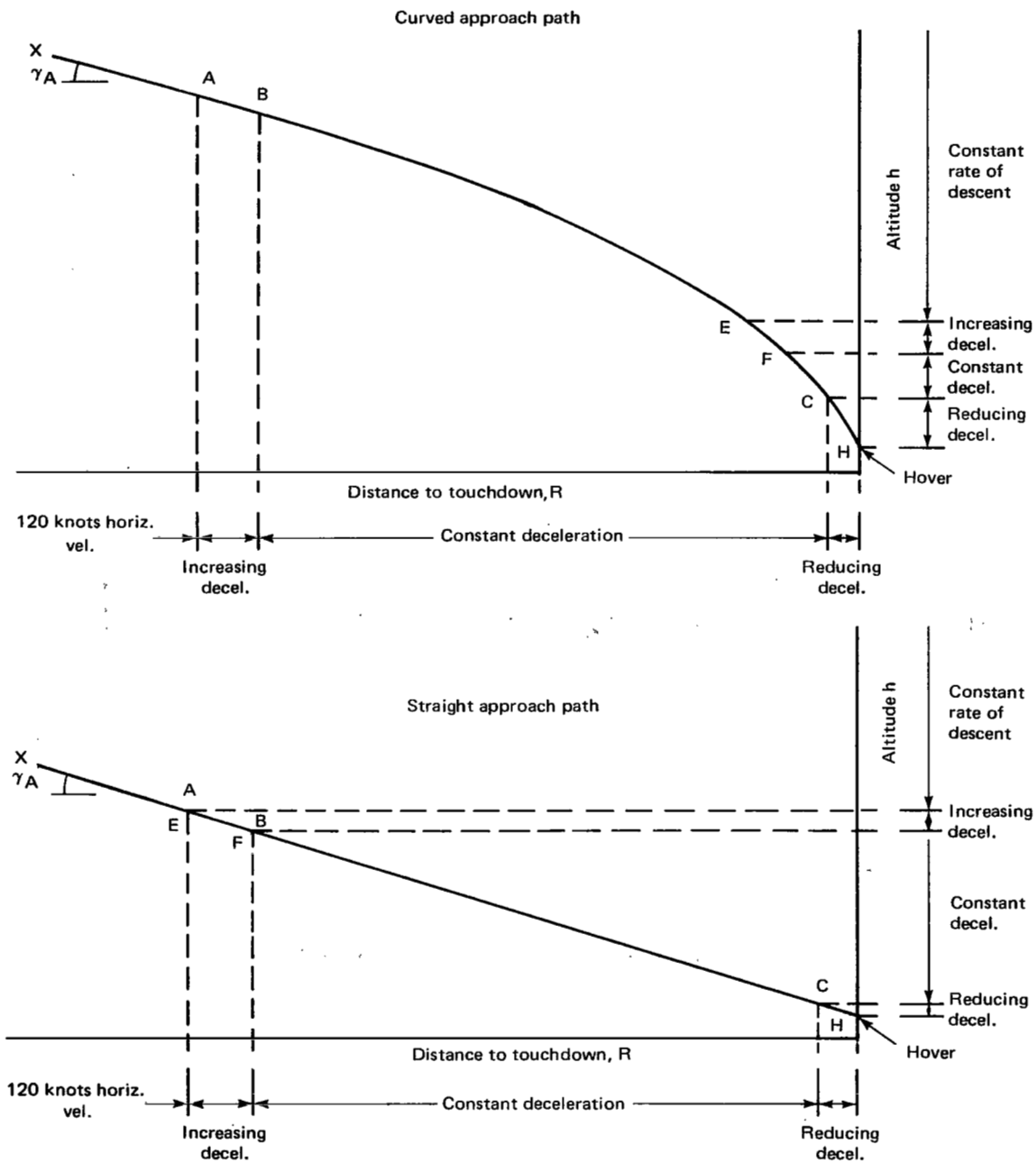

Figure 35.- Types of VTOL approach path.

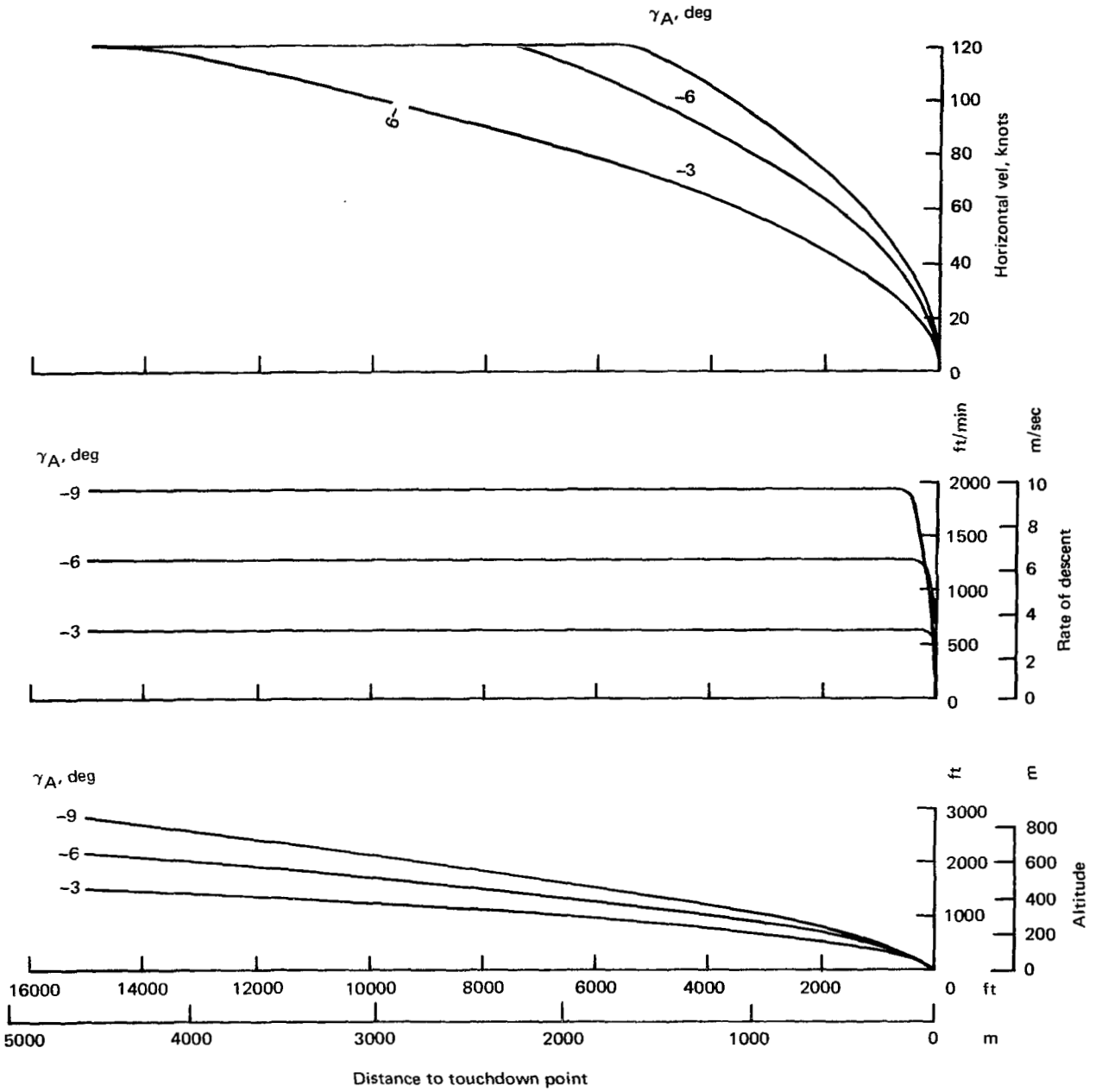

(a) Parameters as functions of distance to touchdown point.

Figure 36.- Curved VTOL landing approaches.

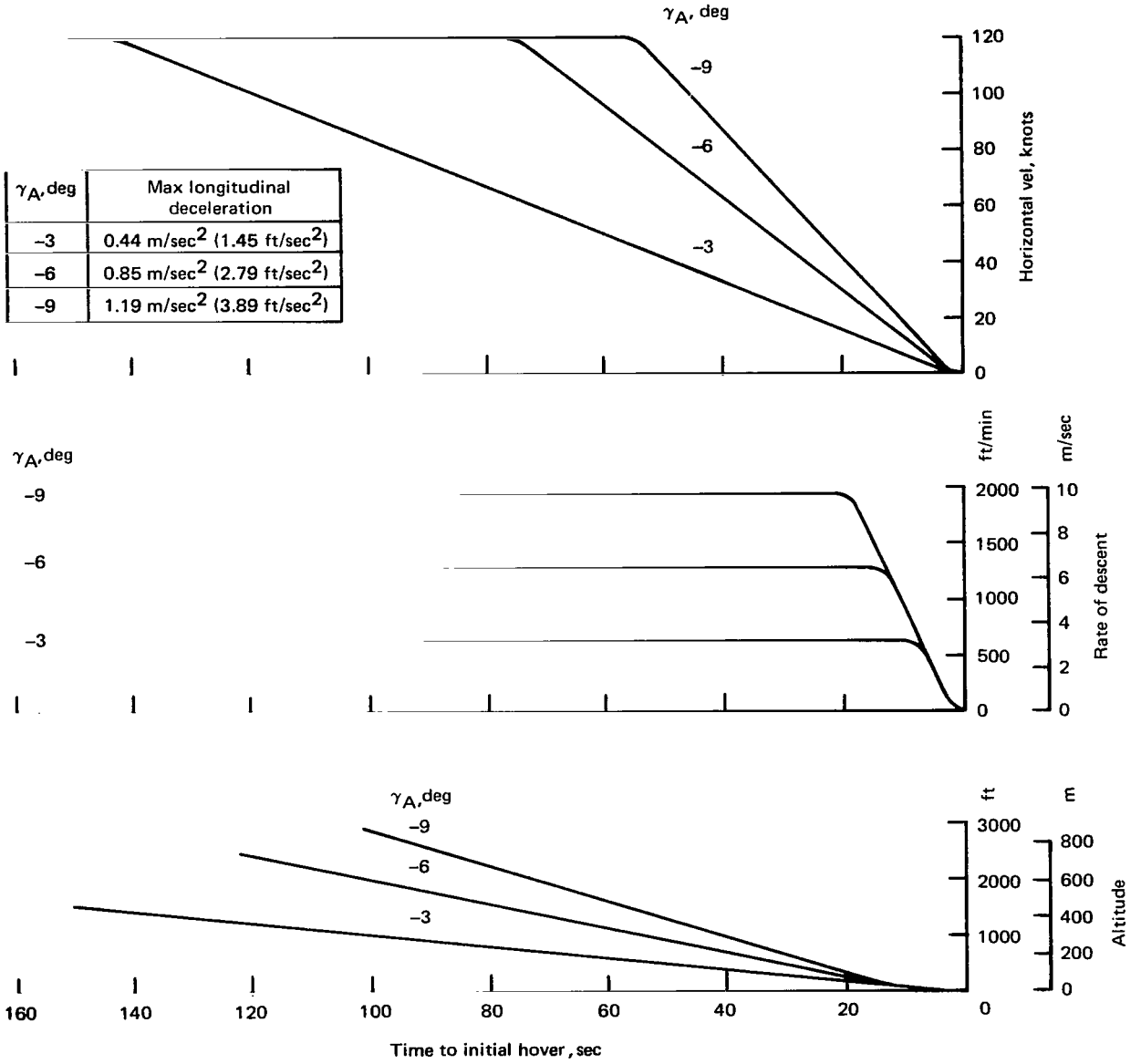

(b) Parameters as functions of time to initial hover.

Figure 36.- Concluded.

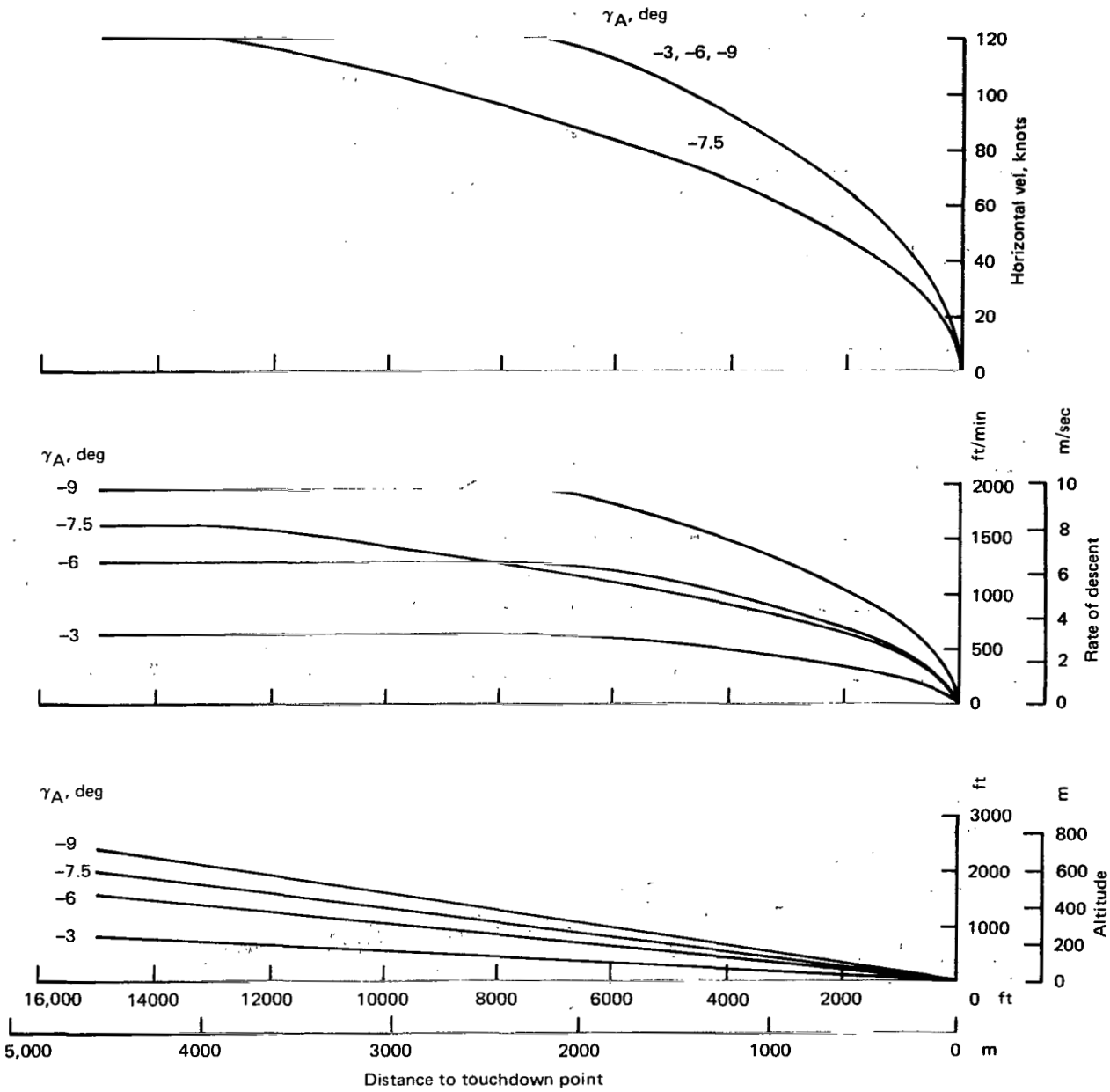

(a) Parameters as functions of distance to touchdown point.

Figure 37.- Straight VTOL landing approaches.

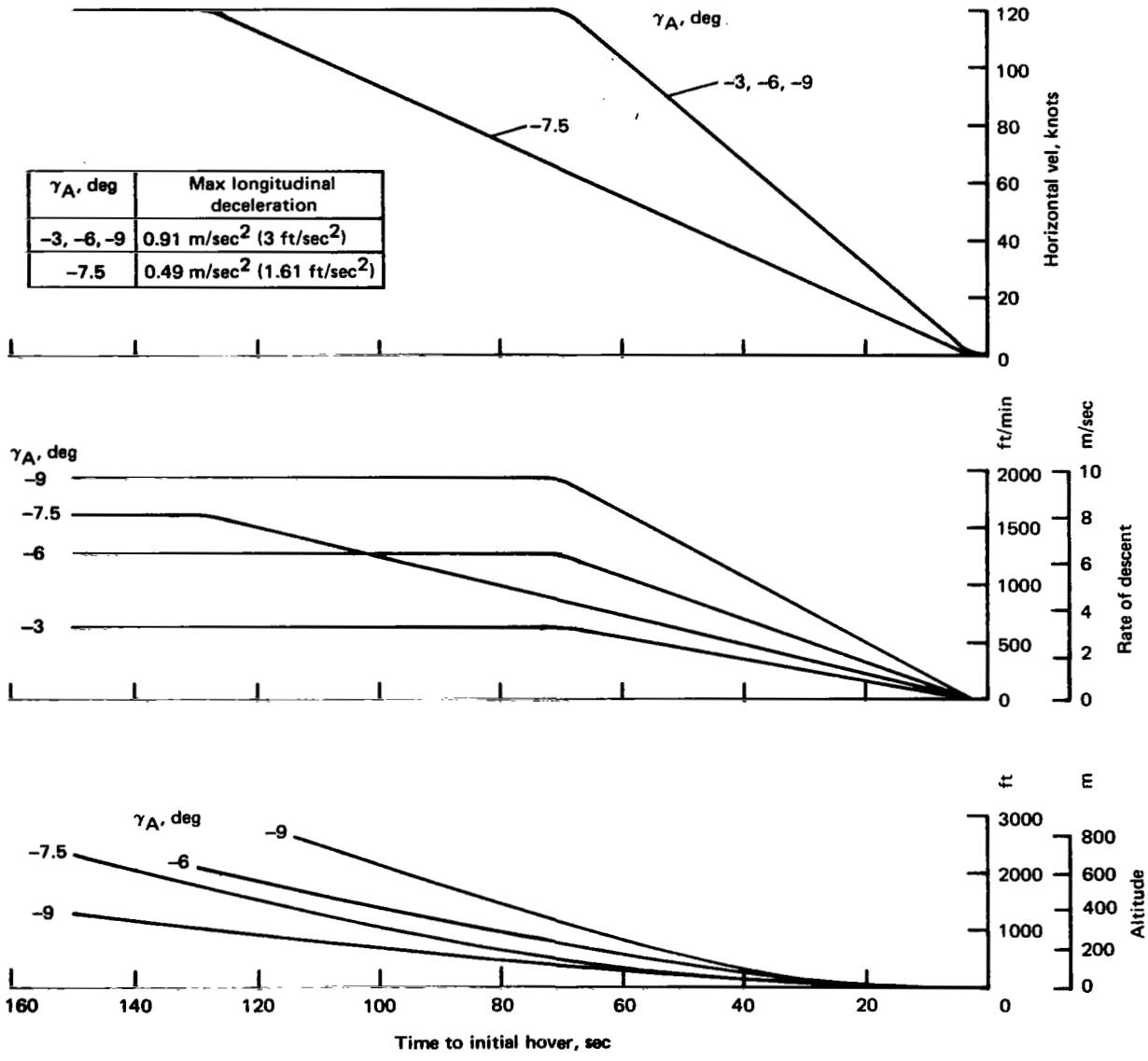

(b) Parameters as functions of time to initial hover.

Figure 37.- Concluded.

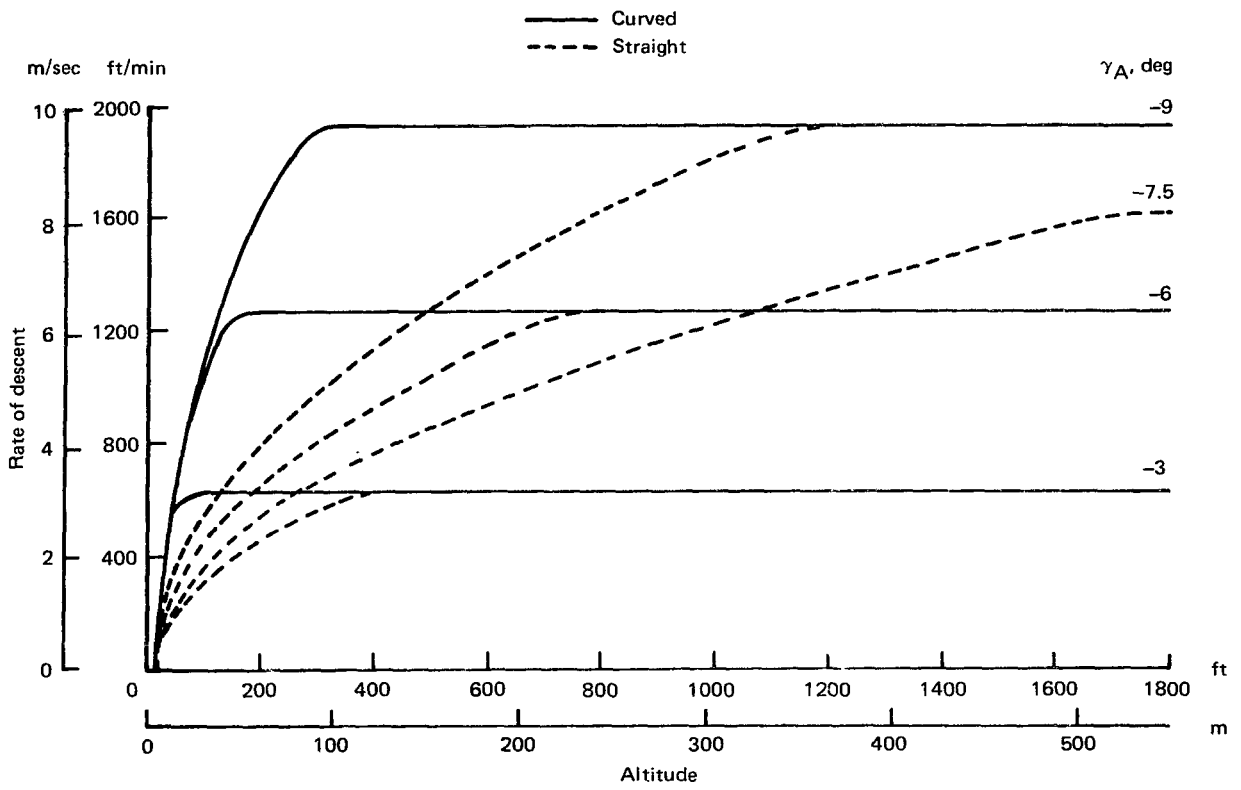

Figure 38.- Variation of rate of descent with altitude for VTOL landing approaches.

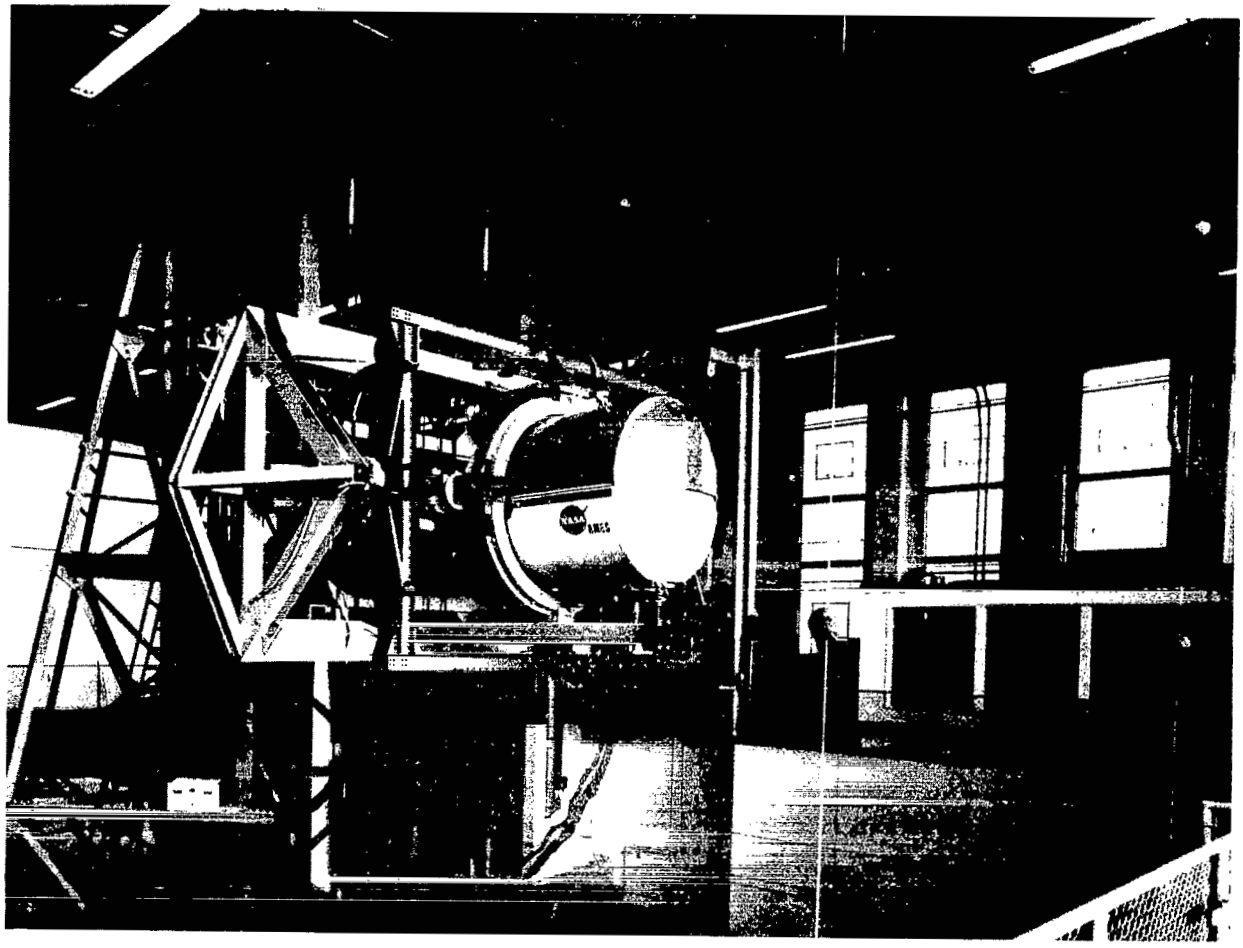

Figure 39.- Ames six-degree-of-freedom moving base simulator.

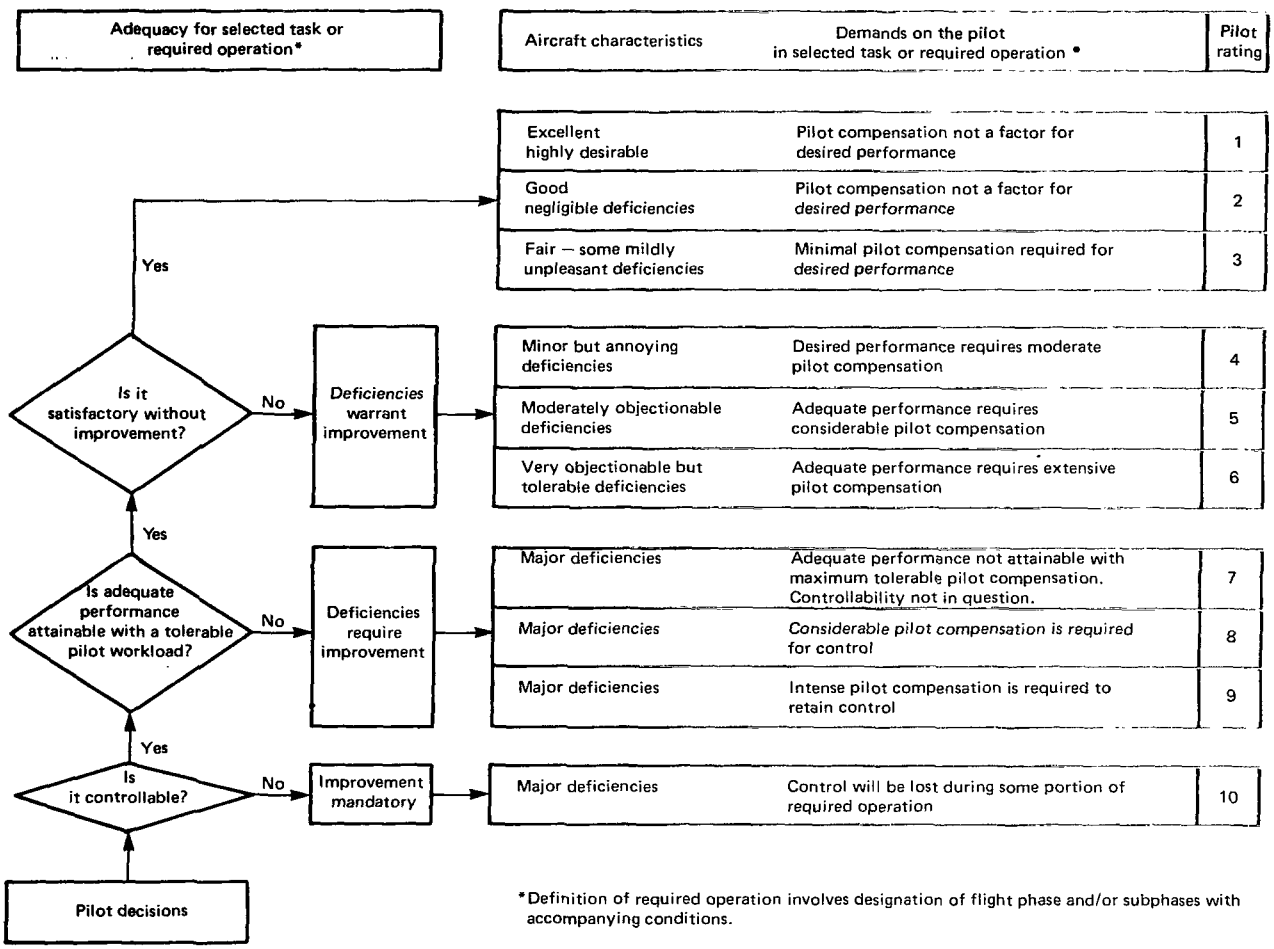

Figure 40.- Handling qualities rating scale.

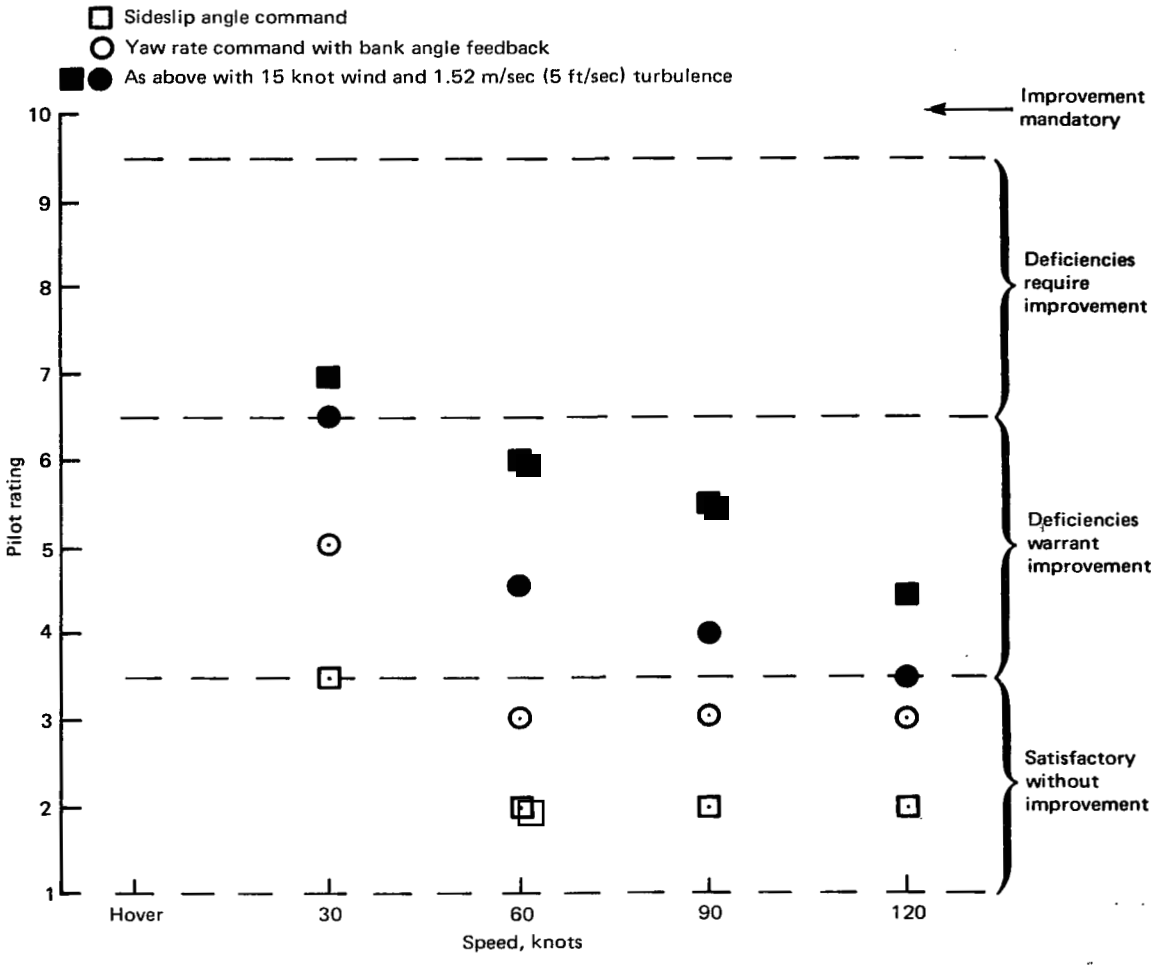

Figure 41.- Fixed-operating-point handling qualities (±10° banked turns to change heading by ±40°).

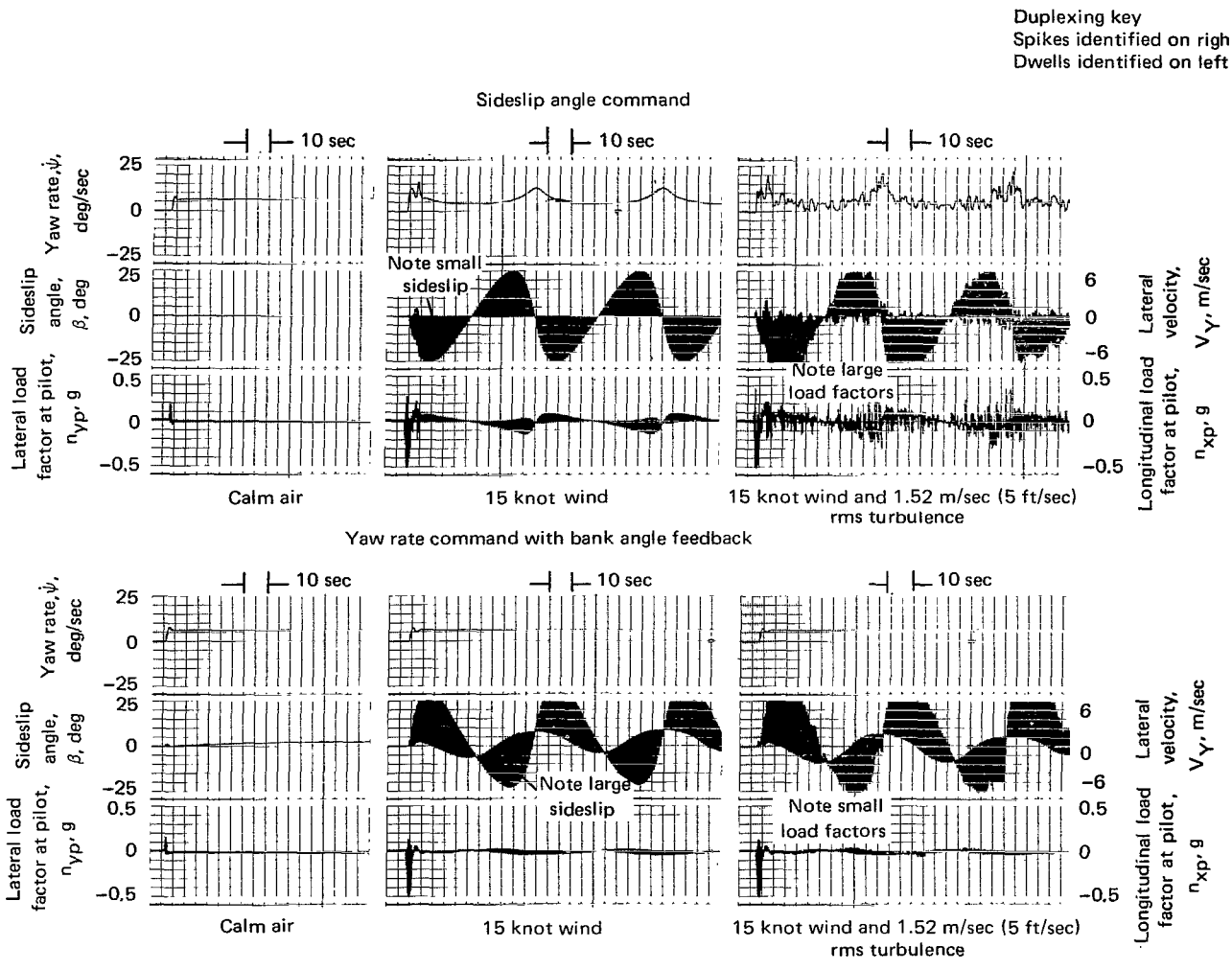

Figure 42.- Comparison of two types of yaw controller modes in steady 10° banked turns.

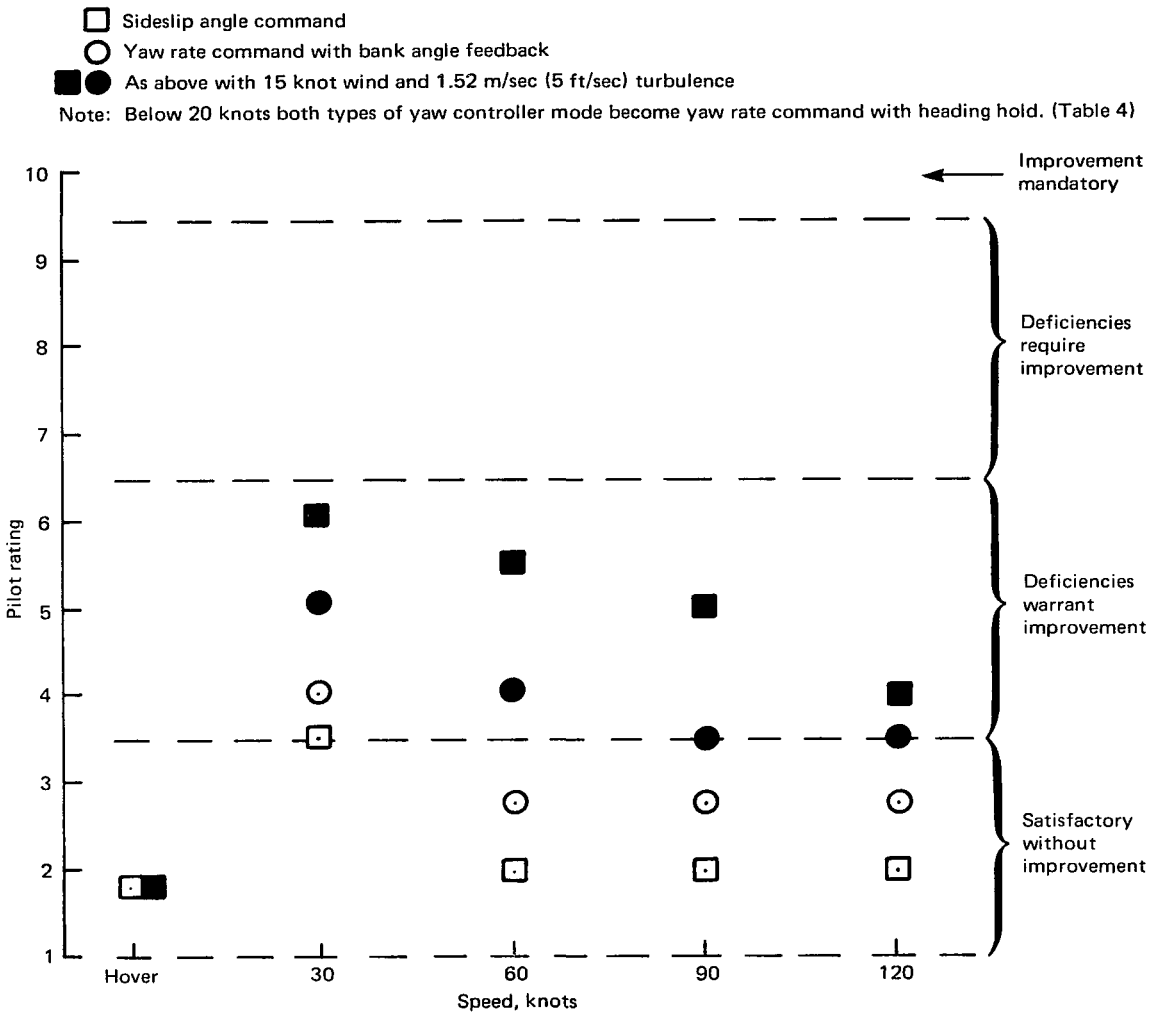

Figure 43.- Fixed-operating-point handling qualities overall.

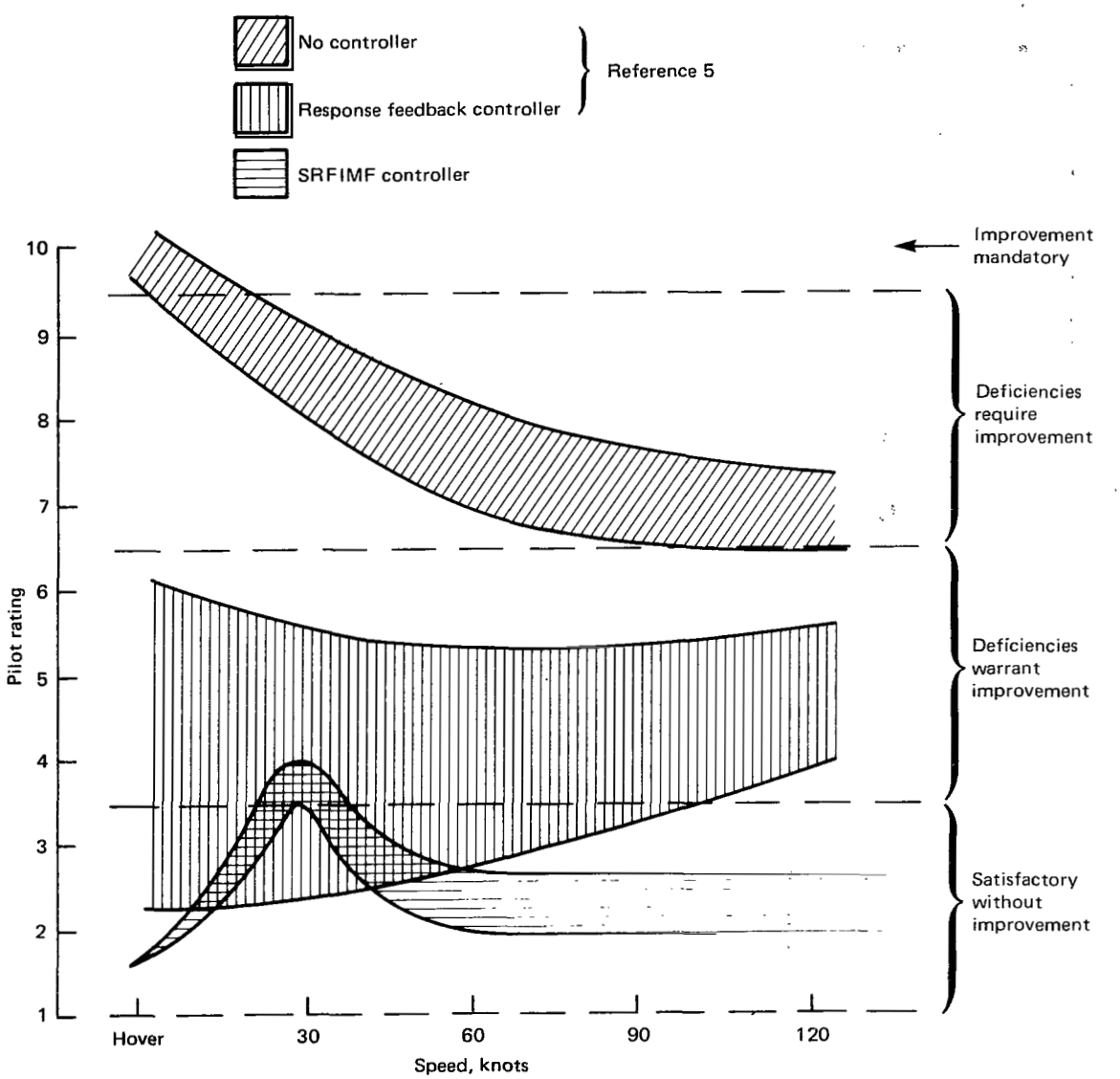

Figure 44.- Fixed-operating-point handling qualities.

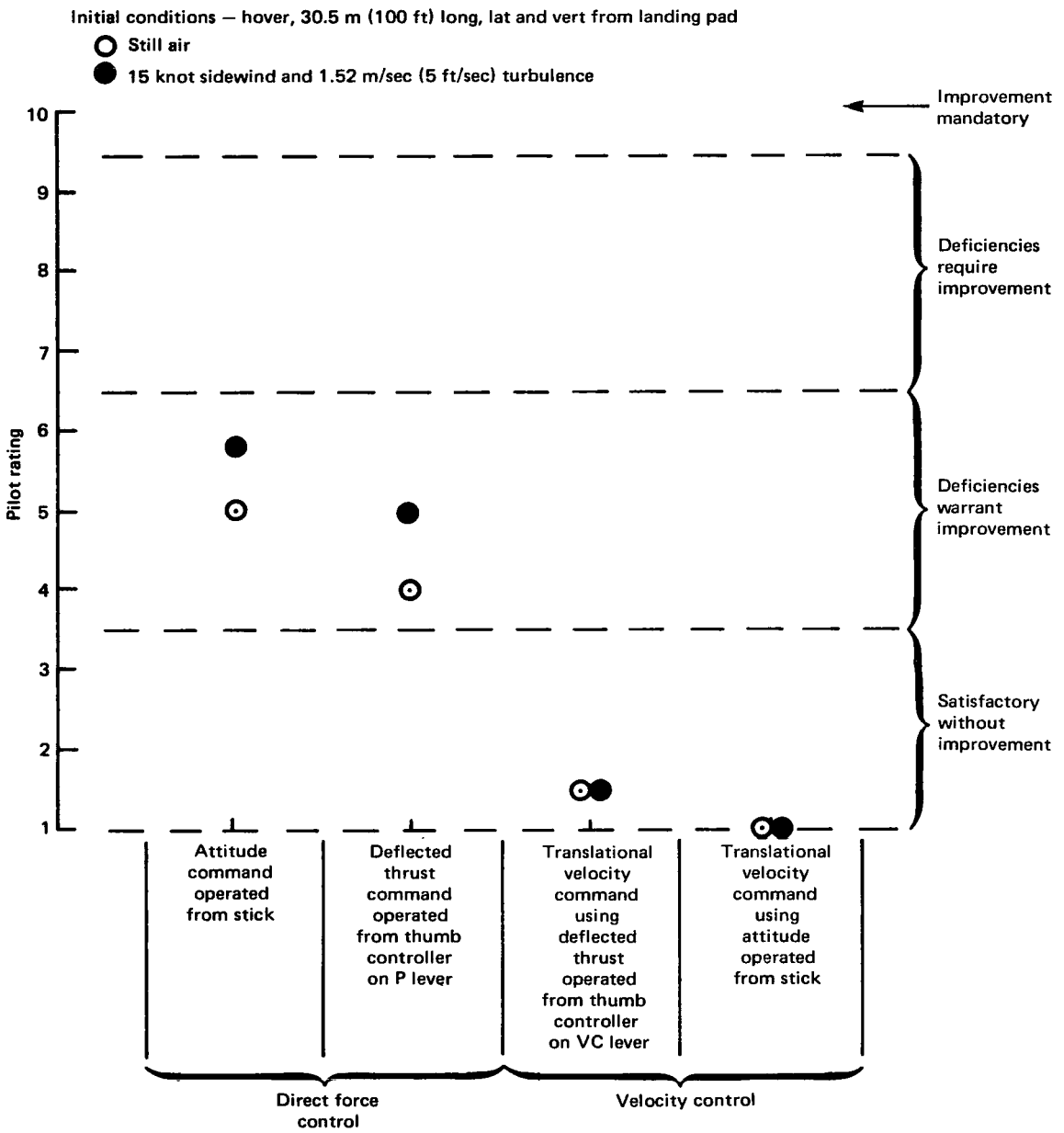

Figure 45.- Precision hover task - translate aircraft horizontally to landing pad as indicated on electronic display.

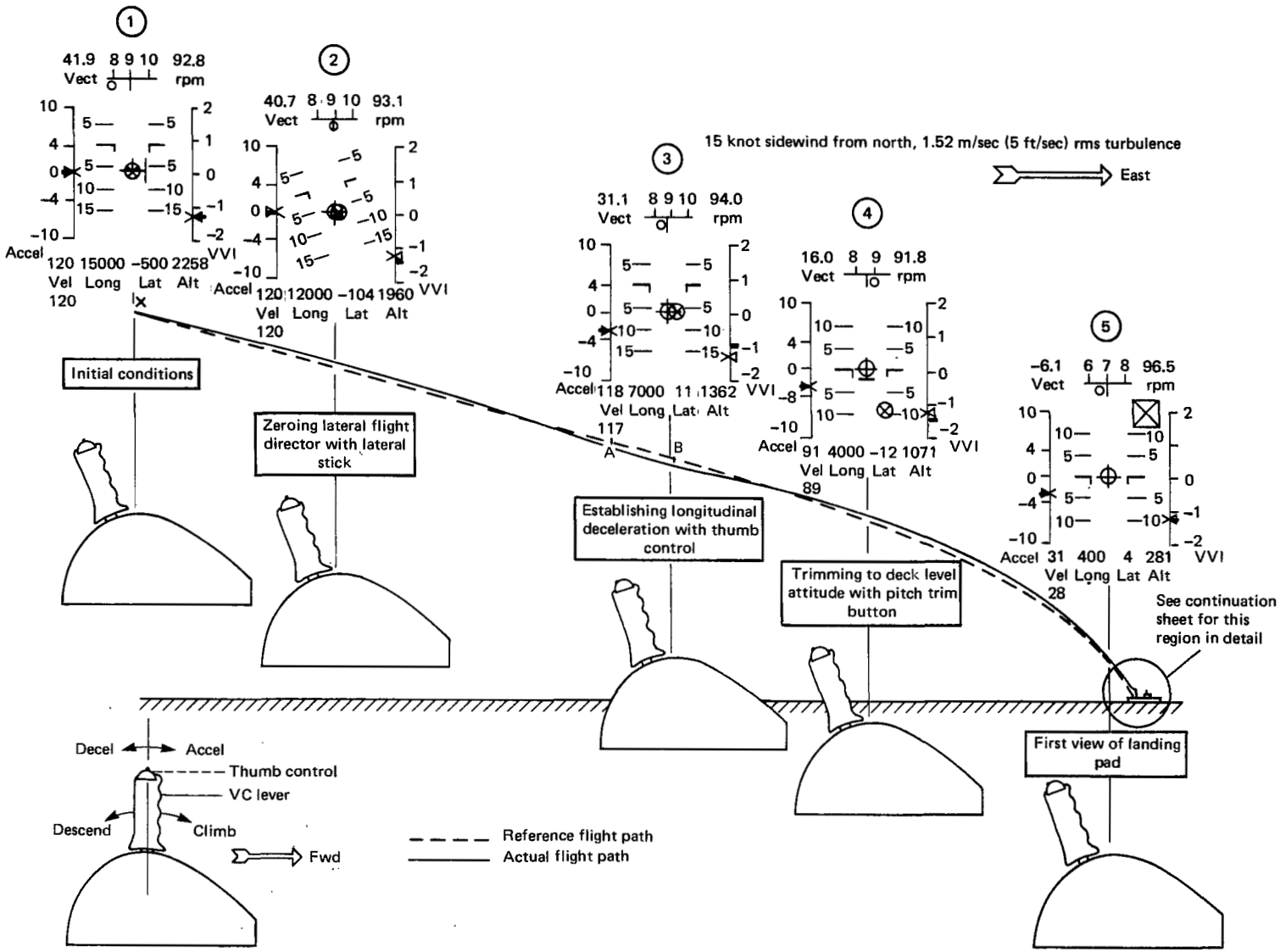

(a) Overall view of approach and landing.

Figure 46.- Display and flight-path controls (MK2) during typical -6° curved approach and landing.

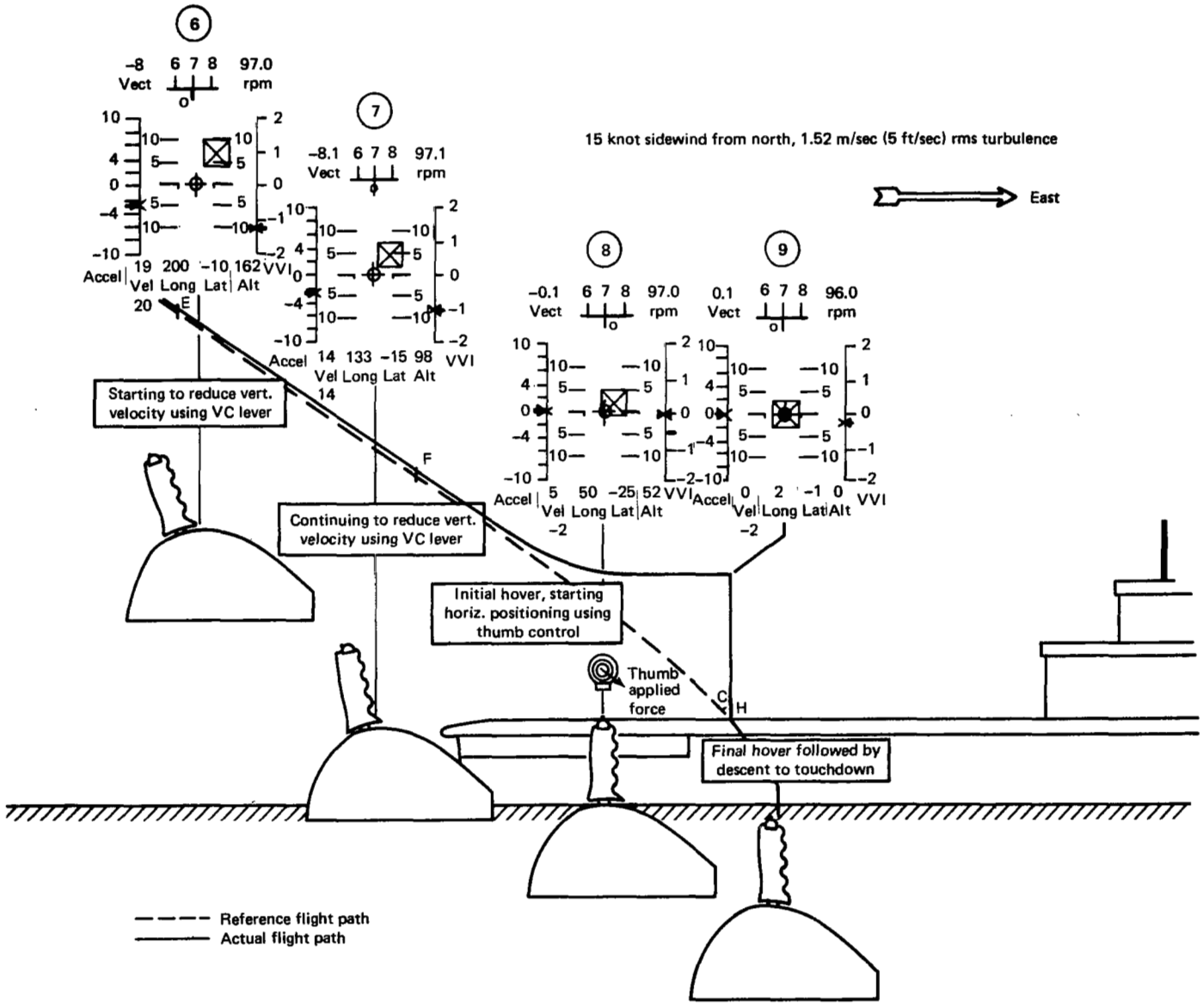

(b) Final approach and landing on the ships.

Figure 46.- Concluded.

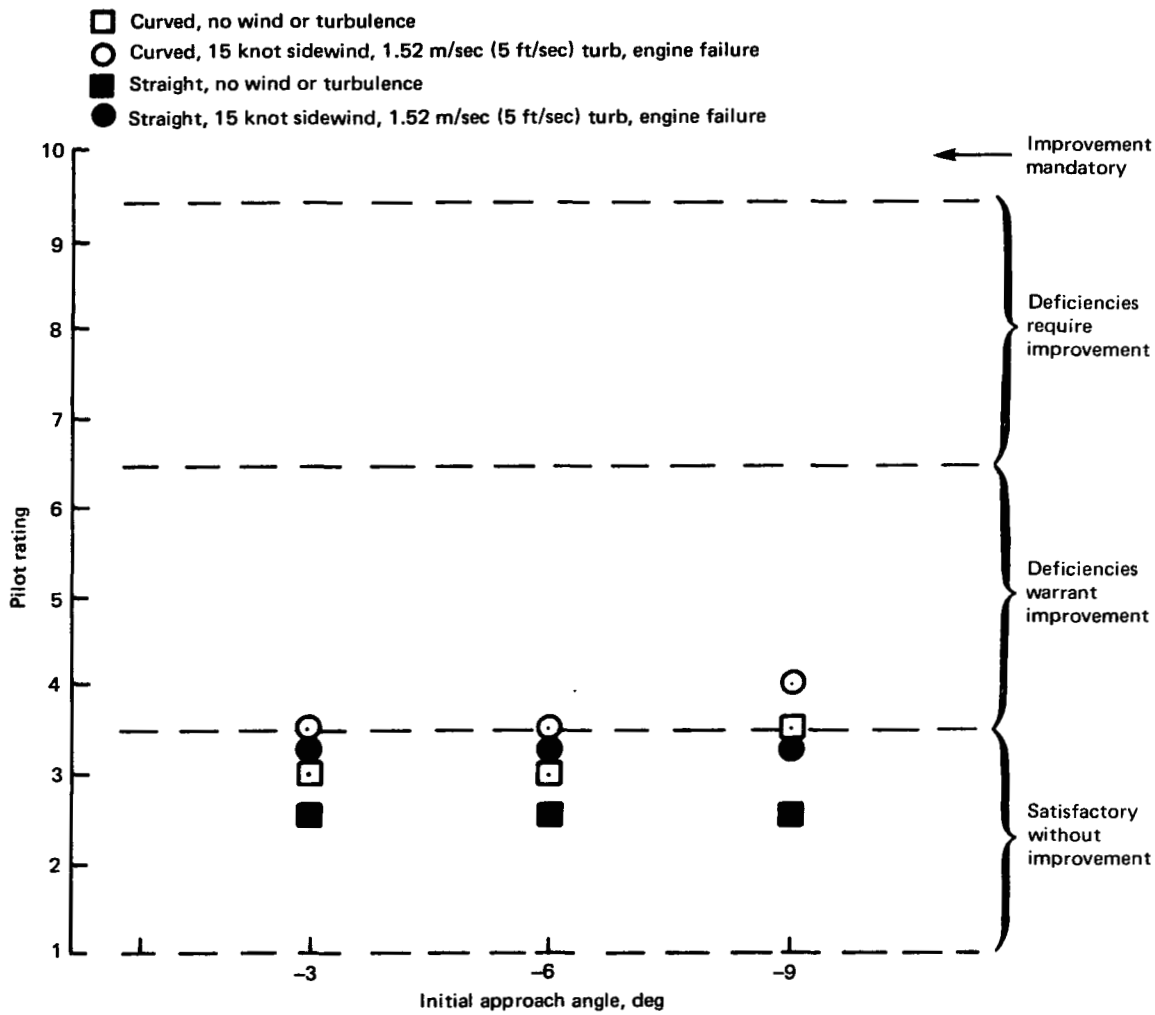

Figure 47.- Approach and vertical landing (IFR zero-zero, MK2 controls).

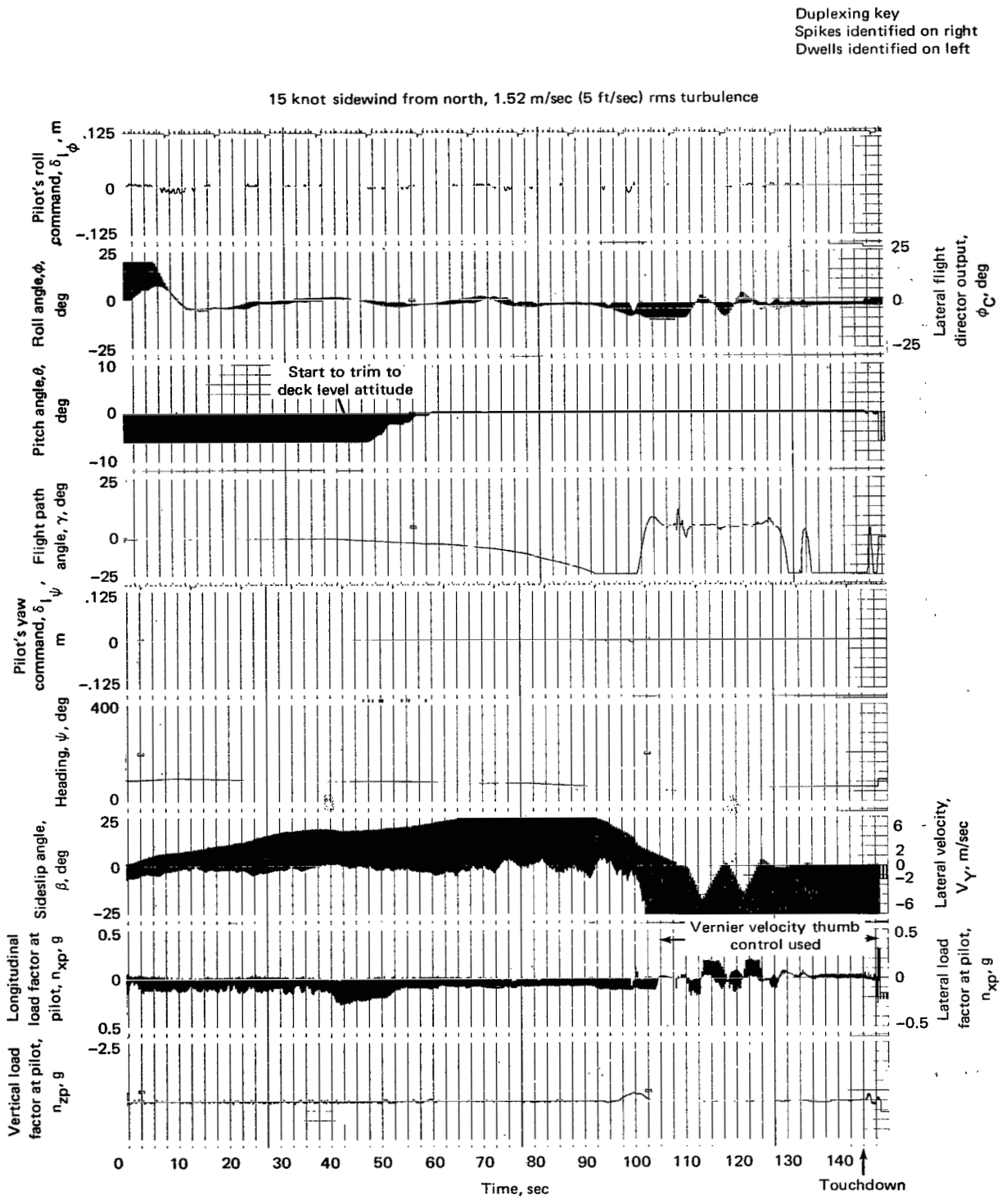

Figure 48.- Typical -6° curved approach and vertical landing.

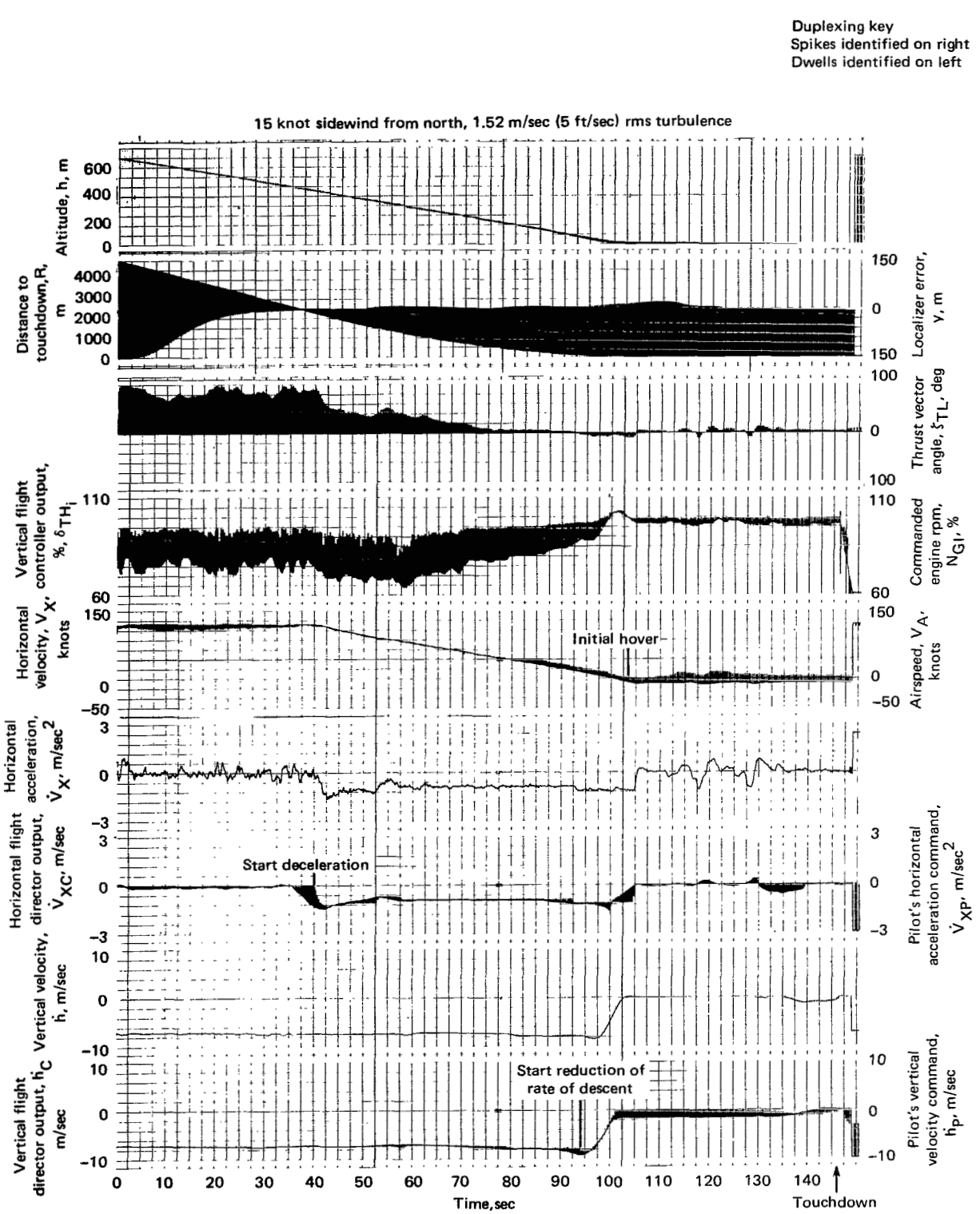

Figure 48.- Concluded.

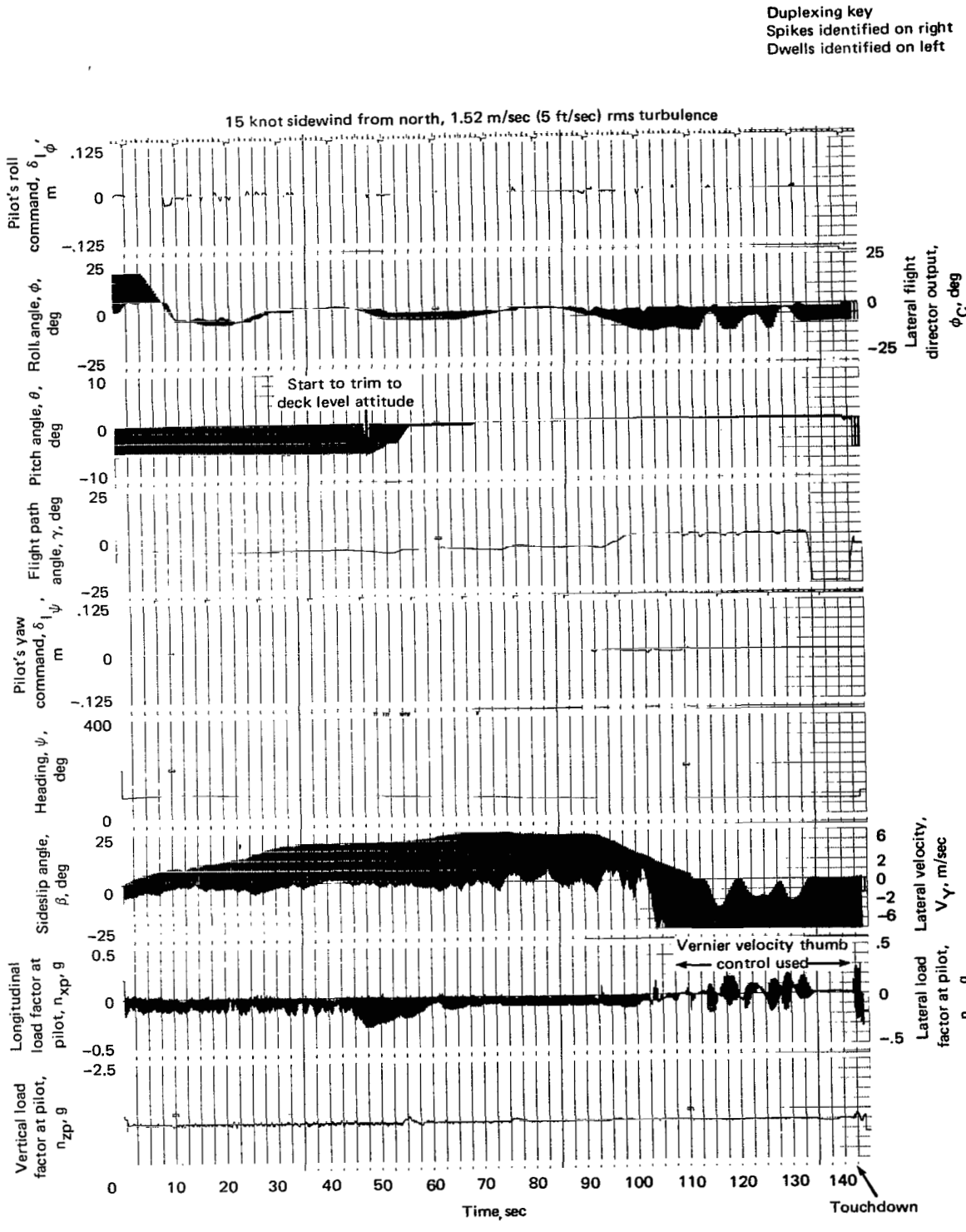

Figure 49.- Typical -6° straight approach and vertical landing.

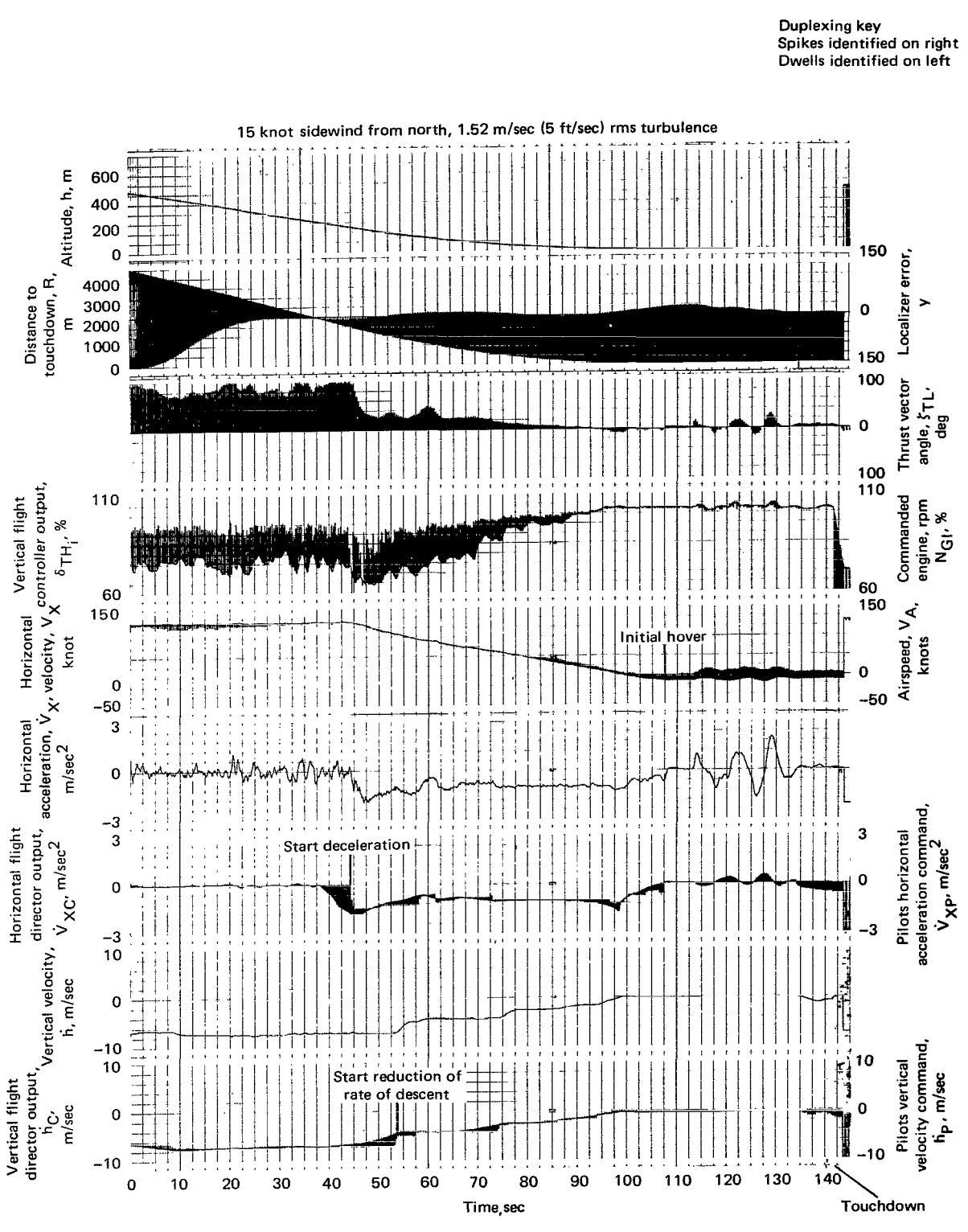

Figure 49.- Concluded.

APPENDIX A — FLIGHT CONTROLLER AND CONTROL-SYSTEM ACTUATORS

NOMENCLATURE FOR APPENDIX A

DB_{HT}	deadband in horizontal tailplane actuator
HT	horizontal tailplane rotation rate
i_{HT}	horizontal tailplane incidence measured from airplane waterline, positive for leading-edge up
LM_{AE}	position limit in elevator actuator output
LM_{AR}	position limit in rudder actuator output
LM_{AS}	position limit in spoiler actuator output
LM_{CH}	position limit in cascade louvers and hood rotation actuator output
LM_{HT}	position limit in horizontal tailplane actuator output
LM_{TR}	pitch trim limit
LM_{F}	rate limit in P and T lever servo actuator prefilters
TR	pitch trim rate gain
ζ	P and T lever servo actuator prefilter damping factor
τ_{AC1}	time constant of elevator and rudder actuators
τ_{AC2}	time constant of spoiler, cascade louver, wing louver, and hood rotation actuators
τ_{HT}	horizontal tailplane input signal prefilter time constant
ω_{O}	P and T lever servo actuator prefilter undamped frequency

The numerical values of the parameters used in the attitude flight controller shown in figure 14 are given in tables 14, 15, and 16.

TABLE 14.- PITCH ATTITUDE CONTROLLER PARAMETERS

Parameter	Symbol	Value
Pitch attitude feedback gain	K_{θ}	4.0 1/sec^2
Pitch rate feedback gain	$K_{\dot{\theta}}$	3.0 1/sec
Basic feedforward gain	K_{100}	11.717 rad/sec^2 m (0.2976 rad/sec^2 in.)
Controller feedforward gain	K_{200}	0.50 rad/sec^2 m (0.0127 rad/sec^2 in.)
Controller coupling gain	K_{300}	0.0178 sec^2 m/rad (0.7 sec^2 in./rad)
Controller time constant	τ_9	0.03 sec
Elevator actuator input gain	K_{500}	839.9 deg/m (21.333 deg/in.)
Longitudinal stick deadband	$DB_{\delta_{I_\theta}}$	0.0013 m (0.05 in.)
Longitudinal stick limits	$LM_{\delta_{I_\theta}}$	0.1156 m (4.55 in.)
Controller coupling limiter	$LM_{\theta c}$	1.3393 rad/sec^2

TABLE 15.- ROLL ATTITUDE CONTROLLER PARAMETERS

Parameter	Symbol	Value
Roll attitude feedback gain	K_{ϕ}	4.0 1/sec^2
Roll-rate feedback gain	$K_{\dot{\phi}}$	3.0 1/sec
Basic feedforward gain	K_1	16.402 rad/sec^2 m (0.4166 rad/sec^2 in.)
Controller attitude feed-forward gain	K_2	11.083 rad/sec^2 m (0.2815 rad/sec^2 in.)
Controller rate feedforward gain	K_4	-13.772 rad/sec^2 m (-0.3498 rad/sec^2 in.)
Controller coupling gain	K_3	0.0127 sec^2 m/rad (0.5 sec^2 in./rad)
Roll attitude hold stick integrator gain	$K_{\phi H}$	18.323 rad/sec^3 m (0.4654 rad/sec^3 in.)
Controller time constant	τ_8	0.05 sec
Roll attitude authority limit	$LM_{\phi H}$	3.141 rad/sec^2
Controller coupling limit	$LM_{\phi c}$	1.875 rad/sec^2
Spoiler actuator input gain	K_5	2519.7 deg/m (64.0 deg/in.)
Lateral velocity cont (LVC) input gain	K_6	160 1/sec (13.333 ft/sec in.)
Lateral velocity feedback gain	K_v	1.57 1/sec^2
Lateral acceleration compensation gain	$K_{\dot{v}}$	1.76 1/sec
LVC compensator time constant	τ_1	-1.6667 sec
LVC compensator time constant	τ_2	1.0 sec
LVC coupling gain	K_0	27.51 rad/sec^2 m (0.6988 rad/sec^2 in.)
LVC coupling gain	K_9	0.0111 sec^2 (0.1335 sec^2 in./ft)
LVC compensator limit	LM_{vc}	10.278 m/sec^2 (33.719 ft/sec^2)
Lateral stick deadband	$DB_{\delta_{I_\theta}}$	0.0013 m (0.05 in.)
Lateral stick limit	$LM_{\delta_{I_\phi}}$	0.1156 m (4.55 in.)

TABLE 16.- YAW ATTITUDE CONTROLLER PARAMETERS

Parameter	Symbol	Value
Yaw attitude feedback gain	K_{ψ}	4.0 $1/sec^2$
Yaw-rate feedback gain	$K_{\dot{\psi}}$	3.0 1/sec
Basic feedforward gain	K_{10}	4.543 rad/sec^2 m (0.1154 rad/sec^2 in.)
Controller rate feedforward gain	K_{20}	20.83 rad/sec^2 m (0.529 rad/sec^2 in.)
Controller coupling gain	K_{30}	0.0508 sec^2 m/rad (2.0 sec^2 in./rad)
Heading hold stick integrator gain	$K_{\psi H}$	8.457 rad/sec m (0.2148 rad/sec in.)
Turn coordination assist gain	$K_{r\phi}$	$32.2/V_X$ 1/sec
Controller time constant	τ_7	0.05 sec
Rudder actuator input gain	K_{50}	-1574.8 deg/m (-40.0 deg/in.)
Cascade louver actuator input gain	K_{70}	839.9 deg/m (21.333 deg/in.)
Hood rotation actuator gain	K_{80}	839.9 deg/m (21.333 deg/in.)
Sideslip angle feedback gain	K_{β}	4.0 $1/sec^2$
Sideslip controller (SC) comp. gain	$K_{\dot{\beta}}$	3.0 1/sec
SC input gain	K_{60}	-6.343 rad/m (-0.1611 rad/in.)
SC coupling gain	K_{90}	1.466 sec m/rad (57.71 sec in./rad)
SC coupling limiter	$LM_{\psi c}$	0.375 rad/sec
Rudder pedal integrator deadband	$DB_{\psi H}$	0.0038 m (0.15 in.)
Rudder pedal deadband	$DB_{\delta_{I_{\psi}}}$	0.0127 m (0.05 in.)
Rudder pedal limits	$LM_{\delta_{I_{\psi}}}$	0.0838 m (3.30 in.)
Wing louver actuator gain	K_{40}	-839.9 deg/m (-21.333 deg/in.)
SC time constant	τ_6	0.333 sec

The phase-out gain, K_B, used in both roll and yaw channels, is a function of the horizontal inertial speed, V_X (see fig. 50).

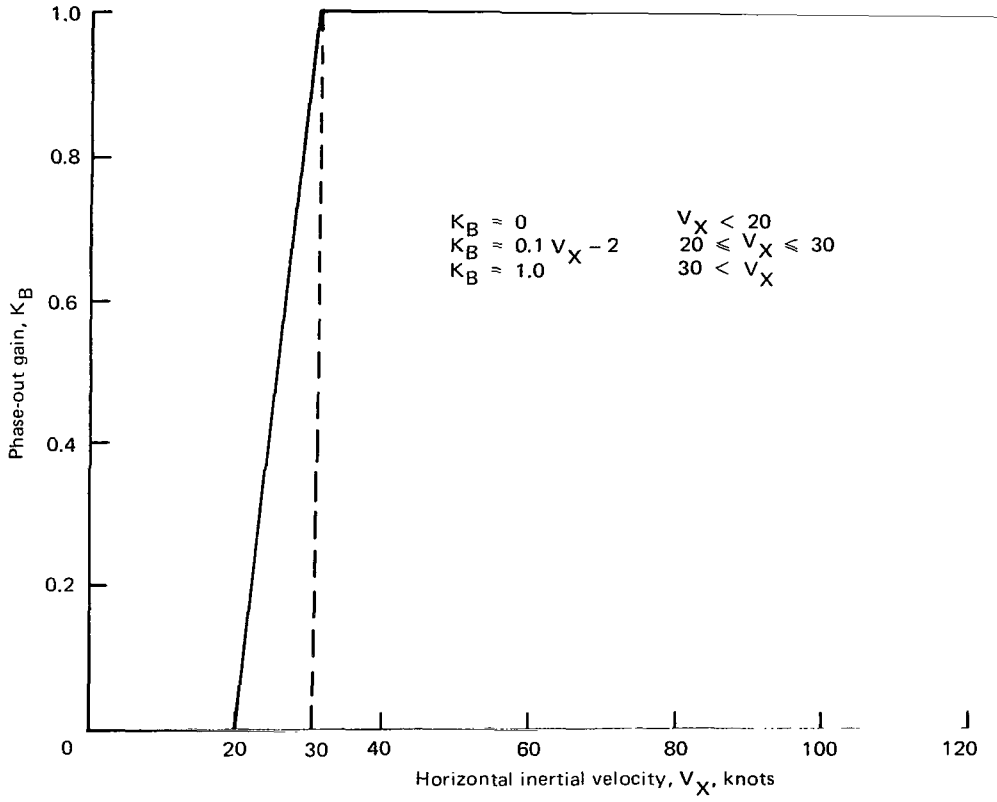

Figure 50.- Variation of phase-out gain with horizontal inertial velocity.

The input-output characteristics of the spoiler cam, shown in the roll system (fig. 14), are given in figure 51. This spoiler cam is used to make the rolling moment, at a given airspeed, approximately proportional to the cam input.

The actuators for the elevators, spoilers, cascade louvers, aft hoods, and rudder are represented by the block diagram shown in figure 52. The time constants and position limits of the various actuators are defined in table 17 and the corresponding values are given in table 18.

The pilot's pitch trim switch biases the input from the stick at a constant rate (see fig. 53). Values of the parameters shown in figure 53 are given in table 18.

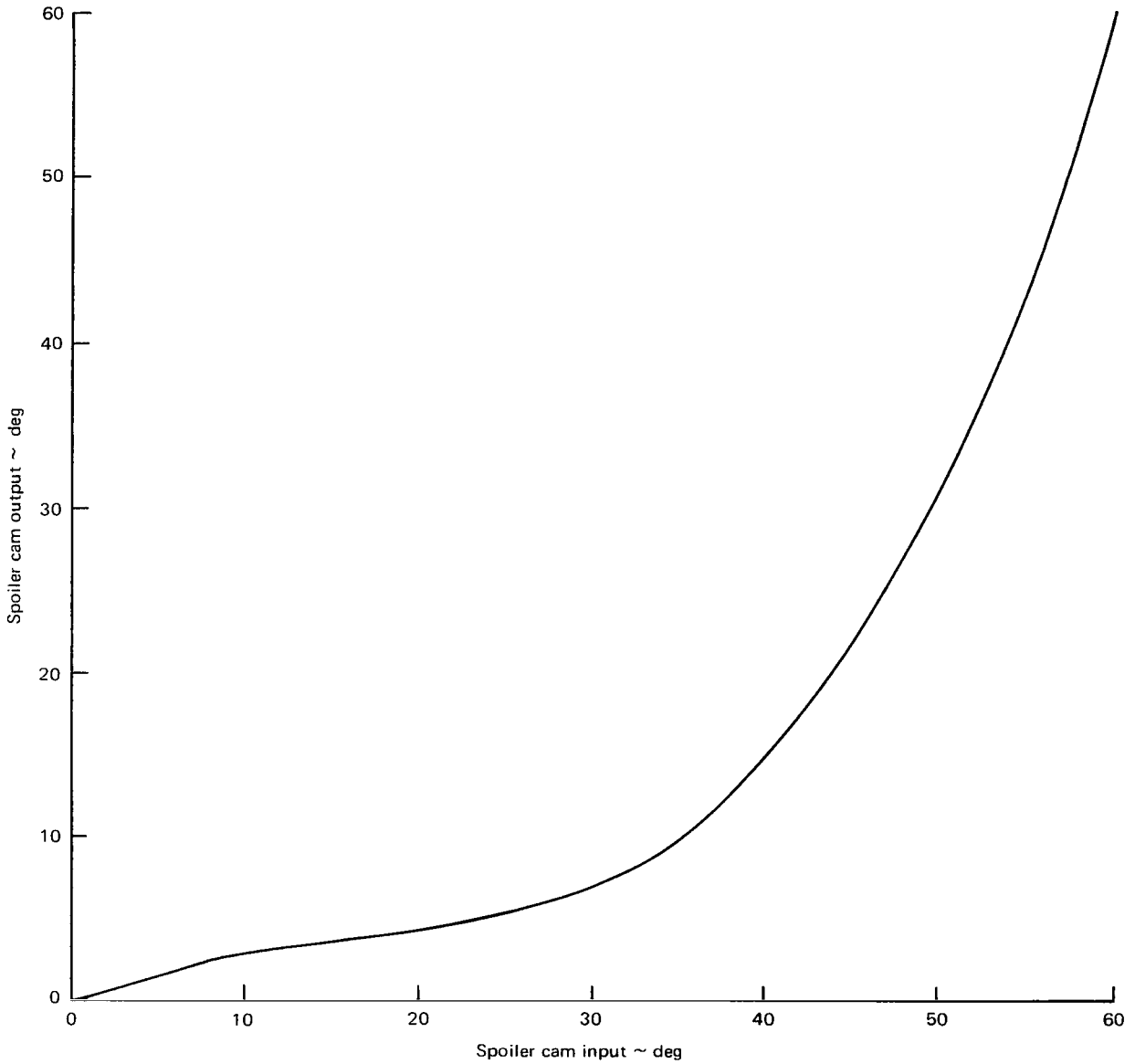

Figure 51.- Simulated spoiler cam.

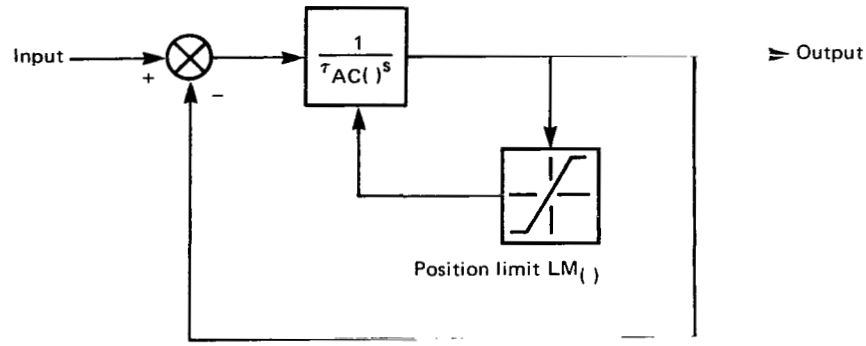

Figure 52.- Actuator model.

TABLE 17.- ACTUATOR NOTATION

Actuator	Time constant $\tau_{AC(\ )}$	Position limit $LM_{(\ )}$
Elevator	τ_{AC1}	$\pm LM_{AE}$
Rudder	τ_{AC1}	$\pm LM_{AR}$
Spoiler	τ_{AC2}	$\pm LM_{AS}$
Cascade louver	τ_{AC2}	$\pm LM_{CH}$
Hood rotation	τ_{AC2}	$\pm LM_{CH}$
Wing louver	τ_{AC2}	$\pm LM_{CH}$

TABLE 18.- ACTUATOR PARAMETERS

Parameter	Symbol	Value
Elevator actuator position limit	LM_{AE}	20.0 deg
Rudder actuator position limit	LM_{AR}	30.0 deg
Spoiler actuator position limit	LM_{AS}	60.0 deg
Cascade louvers and hood rotation limit	LM_{CH}	16.0 deg
Elevator and rudder actuator time constant	τ_{AC1}	0.05 sec
Spoiler, cascade louver, and hood rotation actuator time constant	τ_{AC2}	0.1 sec
Tailplane position limit	LM_{HT}	10.0 deg
Tailplane rate	HT	1 deg/sec
Pitch trim limit	LM_{TR}	0.114 m (4.5 in.)
Pitch trim rate	TR	0.0229 m/sec (0.9 in./sec)
Tailplane deadband	DB_{HT}	2 deg
Tailplane prefilter time constant	τ_{HT}	2.0 sec

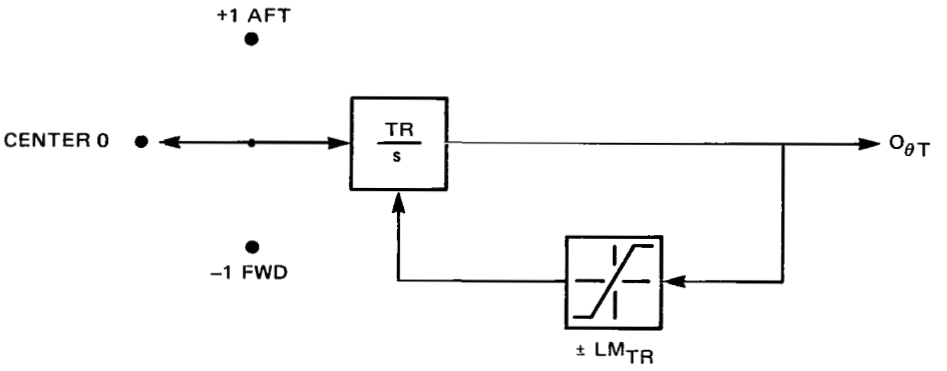

Figure 53.- Pitch trim actuator model.

The tailplane is arranged to move automatically, at a constant rate, in a direction such that the elevator angle to trim a given maneuver is reduced to zero in the steady state. The tailplane actuator is shown in figure 54. The values of the parameters shown in figure 54 are given in table 18.

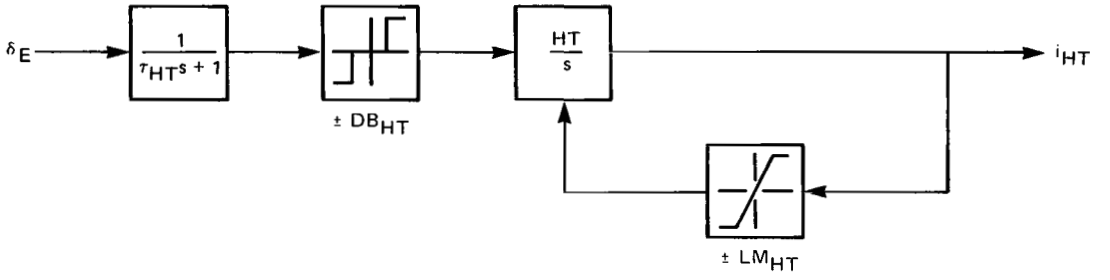

Figure 54.- Tailplane actuator model.

The numerical values of the parameters used in the flight-path flight controller (fig. 15) are given in tables 19, 20, and 21.

The "throttle gearing" (referred to in fig. 15) is a device used to obtain a roughly constant change in thrust per unit change in power lever displacement. Throttle gearing is shown in figure 55 as a schedule of commanded engine speed as a function of the vertical flight controller output i_v. The prefilters (referred to in fig. 15) are used to provide control over the motion of the P and T levers, when driven by the flight controller output. Figure 56 is a block diagram showing the rate limited second-order prefilter used in the simulation. The values of the prefilter parameters are given in table 22.

TABLE 19.- VERTICAL-AXIS CONTROLLER PARAMETERS

Parameter	Symbol	Value
Vertical velocity feedback gain	$K_{\dot{w}}$	1.57 1/sec^2
Controller compensation gain	$K_{\dot{w}}$	1.76 1/sec
Controller input gain	K_{2w}	0.152 m/sec % (0.5 ft/sec %)
Controller coupling gain	K_{3w}	-32.81 sec^2 %/m (-10.0 sec^2 %/ft)
Controller time constant	τ_w	0.3 sec
Controller upper coupling limit	LM_{VC_1}	0 m/sec^2 (0 ft/sec^2)
Controller lower coupling limit	LM_{VC_2}	-2.606 m/sec^2 (-8.55 ft/sec^2)
Pilot's control deadband	$DB_{\delta_{\dot{h}}}$	5%
Pilot's control limit ($\delta_{\dot{h}}$)	$LM_{\delta_{\dot{h}}}$	100%
Pilot's control limit (δ_{TH_i})	$LM_{\delta_{TH_i}}$	100%

Note: % refers to % of appropriate design maximum control input (fig. 15).

TABLE 20.- HORIZONTAL (LONGITUDINAL) AXIS CONTROLLER PARAMETERS

Parameters	Symbol	Value
Horizontal velocity feedback gain	K_u	1.57 1/sec^2
Controller compensation gain	$K_{\dot{u}}$	1.76 1/sec
Controller input gain (velocity command mode)	K_{2u}	0.686 m/sec % (2.25 ft/sec %)
Controller input gain (acceleration command mode)	$K_{2\dot{u}}$	0.0152 m/sec^2 % (0.05 ft/sec^2 %)
Vernier velocity command input gain	K_{2V_x}	0.0914 m/sec % (0.3 ft/sec %)
Controller coupling gain	K_{3u}	3.281 sec^2 %/m (1.0 sec^2 %/ft)
Controller time constant	τ_u	0.15 sec
Controller lower coupling limit	LM_{LC_1}	0 m/sec^2 (0 ft/sec^2)
Controller upper coupling limit	LM_{LC_2}	28.854 m/sec^2 (78.261 ft/sec^2)
Vernier force command gain	K_{xv}	0.1 deg/%
Pilot's control deadband (δ_{v_x})	$DB_{\delta_{v_x}}$	5%
Pilot's control limit ($\delta_{\dot{v}_x}$)	$LM_{\delta_{\dot{v}_x}}$	100%
Pilot's control limit (δ_{v_x})	$LM_{\delta_{v_x}}$	100%
Pilot's control lower limit (ζ_{TL_i})	LM_{ζ_1}	0%
Pilot's control upper limit (ζ_{TL_i})	LM_{ζ_2}	100%
Pilot's control limit (I_{xv})	$LM_{I_{xv}}$	100%

Note: % refers to % of appropriate design maximum control input (fig. 15).

TABLE 21.- HORIZONTAL (LATERAL) AXIS CONTROLLER PARAMETERS

Parameter	Symbol	Value
Lateral velocity feedback gain	K_v	1.57 $1/sec^2$
Controller compensation gain	$K_v^{\bullet}$	1.76 1/sec
Controller input gain	K_{2V_y}	0.0914 m/sec % (0.3 ft/sec %)
Controller coupling gain	K_{3V_y}	0.00781 sec^2 (0.09375 in. sec^2/ft)
Controller time constant	τ_v	0.1 sec
Controller coupling limit	LM_{LC}	0.174 m/sec^2 (5.0 ft/sec^2)
Direct force command gain	K_{YV}	1.191×10^{-4} m/% (4.688×10^{-3} in./%)
Pilot's control limit (δ_{v_y})	$LM_{\delta_{v_y}}$	100%
Pilot's control limit (I_{YV})	$LM_{I_{YV}}$	100%

Note: % refers to % of appropriate design maximum control input (fig. 15).

TABLE 22.- P AND T LEVER SERVO ACTUATOR PREFILTER PARAMETERS

Parameter	Symbol	Value
Undamped natural frequency	ω_o	3 rad/sec
Damping factor	ζ	0.7
Rate limit	LM_F	30% of max input/sec

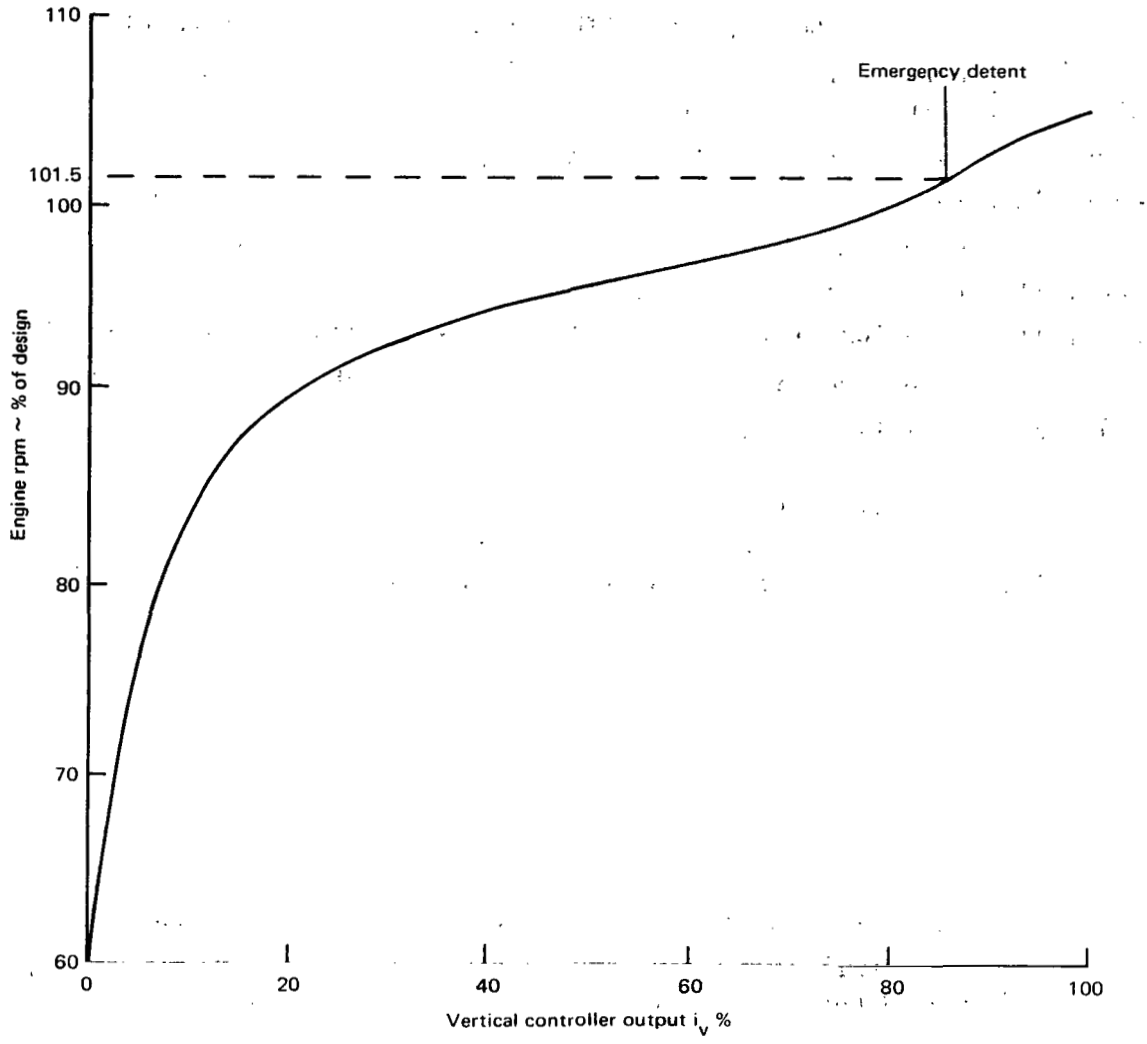

Figure 55.- Simulated throttle gearing.

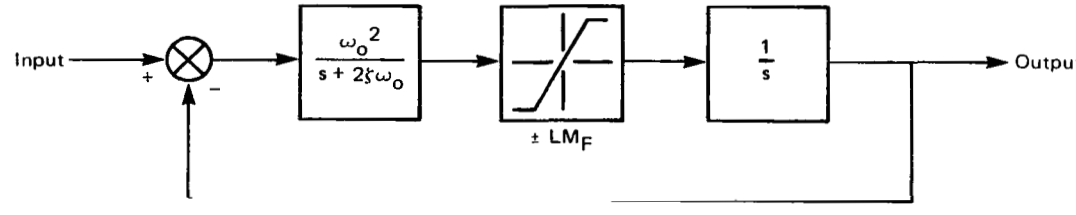

Figure 56.- Servo actuator prefilter.

APPENDIX B — ENGINE AND FAN MODEL

NOMENCLATURE FOR APPENDIX B

F_{N_k} $(k = 1, 2 \ldots, 6)$	fan thrust due to fan rotor
F_{NT_k} $(k = 1, 2 \ldots, 6)$	total fan thrust before spoiling
F_{T_k} $(k = 1, 2 \ldots, 6)$	total fan thrust after spoiling
F_{TT_k} $(k = 1, 2 \ldots, 6)$	tip turbine thrust
F_{TFR}, F_{TWR}, F_{TAR}	total thrust of the forward-right, wing-right, and aft-right fans
F_{TFL}, F_{TWL}, F_{TAL}	total thrust of the forward-left, wing-left, and aft-left fans
F_{TTSS}	steady-state value of tip turbine thrust
HP_k $(k = 1, 2 \ldots, 6)$	tip turbine gas horsepower
HP_{SS}	steady-state tip turbine gas horsepower
I_p	fan rotor polar moment of inertia
k	engine number (fig. 13)
K_{ESP1}	thrust spoiler actuator input gain
K_{EVA1}	ETaC valve actuator input gain
K_{EVA3}	forward branch gain in thrust spoiler and ETaC valve actuators
K_S	fan thrust spoiler coefficient
K_{HP_k} $(k = 1, 2 \ldots, 6)$	horsepower coefficient compensation for engine failures
K_{TT_k} $(k = 1, 2 \ldots, 6)$	tip turbine thrust coefficient compensation for engine failures
K_{SLOPE}	slope of thrust spoiler curve
LM_{EVP}	ETaC valve actuator position limit
LM_{EVR}	ETaC valve actuator rate limit
N_{GI}	engine RPM command

N_{G_k} $(k = 1, 2 \ldots, 6)$	engine RPM
N_{F_k} $(k = 1, 2 \ldots, 6)$	fan rotor RPM
T_{F_k} $(k = 1, 2 \ldots, 6)$	fan torque
T_{TT_k} $(k = 1, 2 \ldots, 6)$	tip turbine torque
ΔA	ETaC valve area change
ΔC_i $(i = \phi, \theta)$	ETaC value input
ΔS	fan thrust spoiler actuator output
η_{fwd}, η_{wing}, η_{aft}	nozzle efficiencies (to account for variation in thrust recovery)
η_{lift}	efficiency (to account for thrust variations due to backward-facing engines)
η_{LC}	efficiency (to account for effect of airspeed on lift/cruise fans)
τ_{ENG}	engine time constant
τ_{DCT}	duct gas-flow time constant

The simulated VTOL aircraft has six identical engine/fan lift units, one of which is shown schematically in figure 57. The input quantities to each engine/fan unit are the commanded engine RPM, N_{GI}, and the attitude control commands. The attitude control commands to the engines on the aft-right, aft-left, forward-right, forward-left, left wing, and right wing are ΔC_θ, ΔC_θ, $-\Delta C_\theta$, $-\Delta C_\theta$, $-\Delta C_\phi$, and ΔC_ϕ, respectively.

The ETaC valve actuator model is shown in figure 58 and the fan thrust spoiler model, in figure 59. The operation of the thrust spoiler is illustrated in figure 57. The output of the thrust spoiler actuator is multiplied by the thrust spoiler factor, K_S, to produce the total fan thrust. The thrust spoiler factor, K_S, as a function of ΔS, is shown in figure 60, and the gains and limits (figs. 58 and 59) are given in table 23 and figure 61.

Provision is made for the simulated failure of the left-wing engine (number 3) and the right-aft engine (number 6). Engine failure is simulated by a change in the tip turbine horsepower coefficient, K_{HP_k}, and the tip turbine thrust coefficient, K_{TT_k}, for both the failed engine and the engine connected to it. The logic used for changing K_{HP_k} and K_{TT_k}, following an engine failure, is shown in figure 62. The coefficients K_{HP_k} and K_{TT_k} for engines 1, 2, 4, and 5 are always unity.

Engine and duct lags are simulated using linear transfer functions (fig. 63). The values of the time constants shown in figure 63 are given in table 23.

The curves marked HP_{SS} and $F_{TT_{SS}}$ (fig. 57) represent the variation of steady-state tip turbine horsepower and thrust, with ETaC valve area change, for various engine speeds. The HP_{SS} and $F_{TT_{SS}}$ curves are given in detail in figures 64 and 65.

The equations for fan thrust and fan torque as functions of fan speed are listed in table 24.

The fan thrust is added to the tip turbine thrust and the resulting quantity is multiplied by the thrust spoiling factor to obtain the fan thrust output for each of the six fans. The thrust outputs of the forward, wing, and aft fans are multiplied by the nozzle efficiencies η_{fwd}, η_{wing} and η_{aft}, respectively, to represent the effects of the various thrust deflection systems. The thrust of each lift fan is multiplied by an additional efficiency η_{lift} to account for the reduction in thrust, with increasing forward speed, because of aft-facing engine air inlets. The lift-cruise fan thrust is multiplied by a factor η_{LC} to account for the increase in thrust due to the ram air effect on the forward-facing engine inlets. The thrust efficiency relationships are summarized in table 25.

The final thrust output from each of the engine/fan units is used, in the force and moment model in appendix C, to compute the overall engine and fan forces and moments acting on the aircraft.

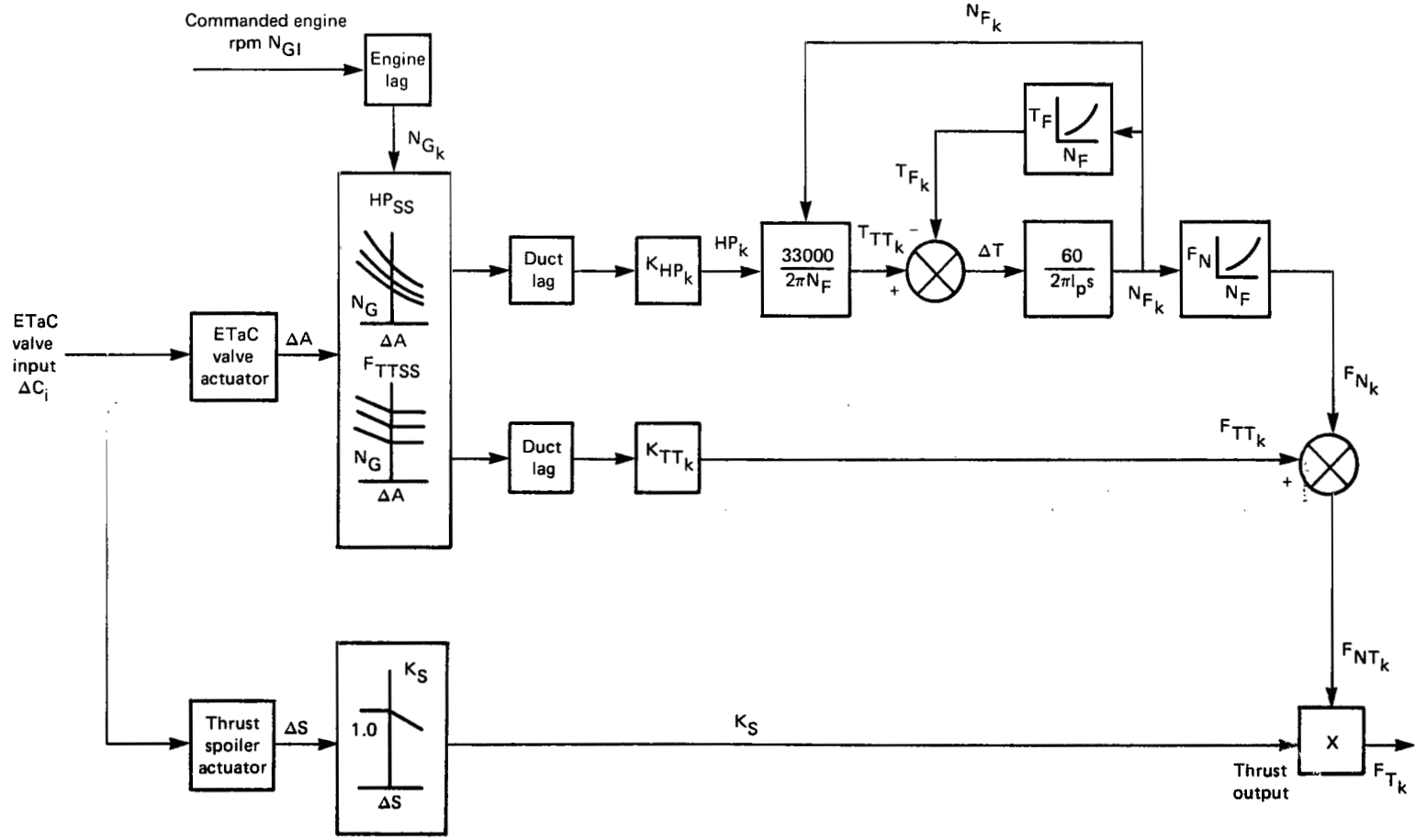

Figure 57.- Typical engine/fan flow diagram.

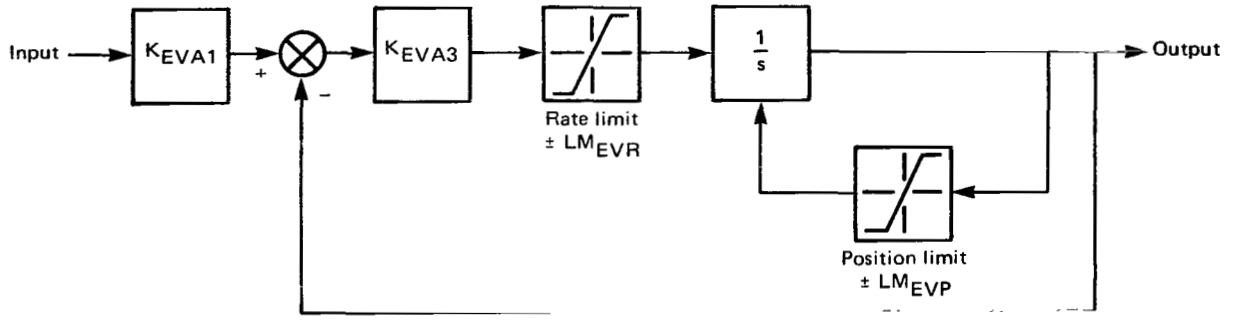

Figure 58.- ETaC valve actuator model.

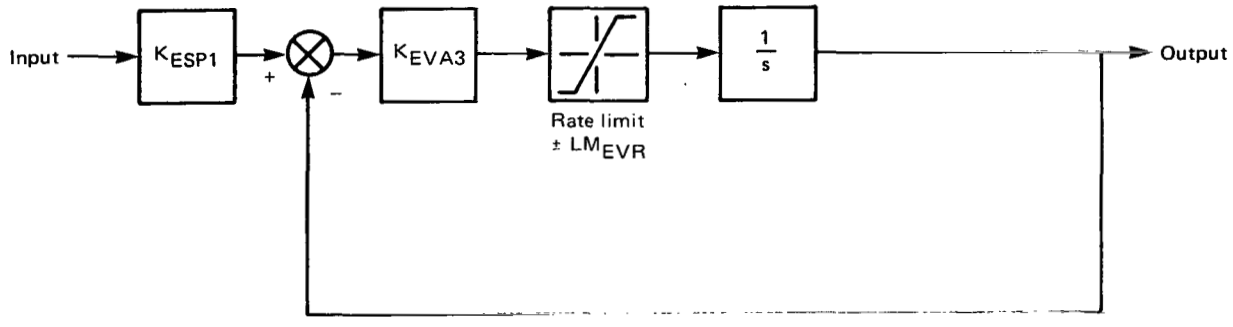

Figure 59.- Thrust spoiler actuator model.

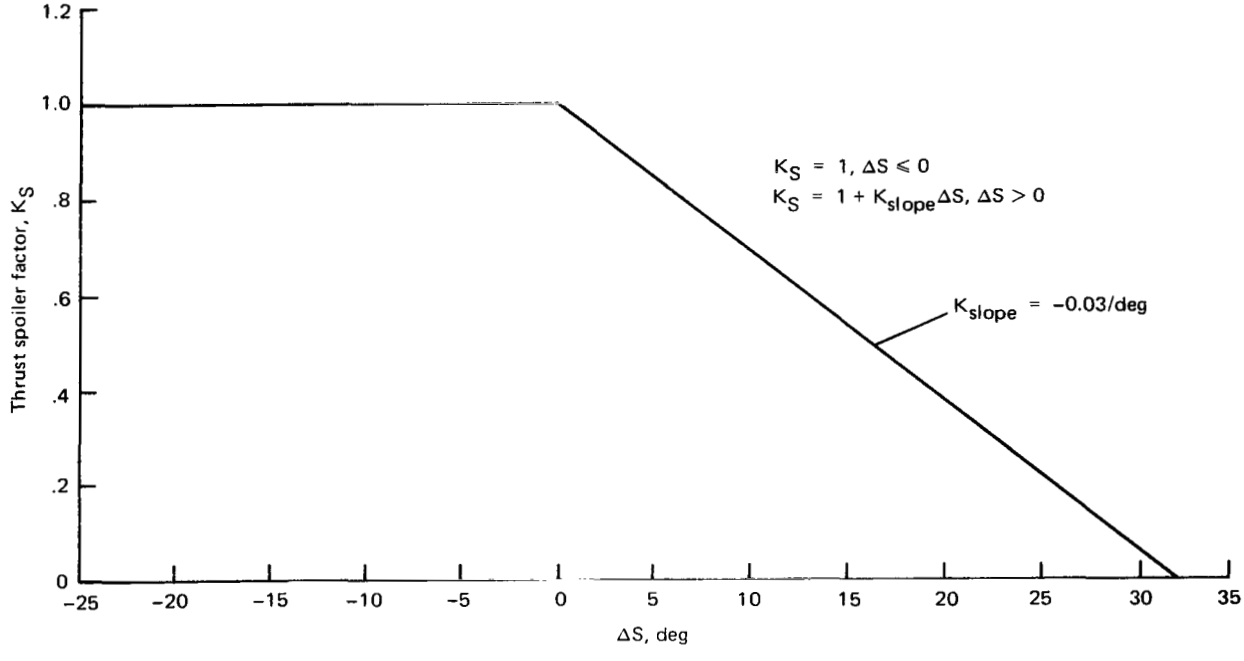

Figure 60.- Fan thrust spoiler curve.

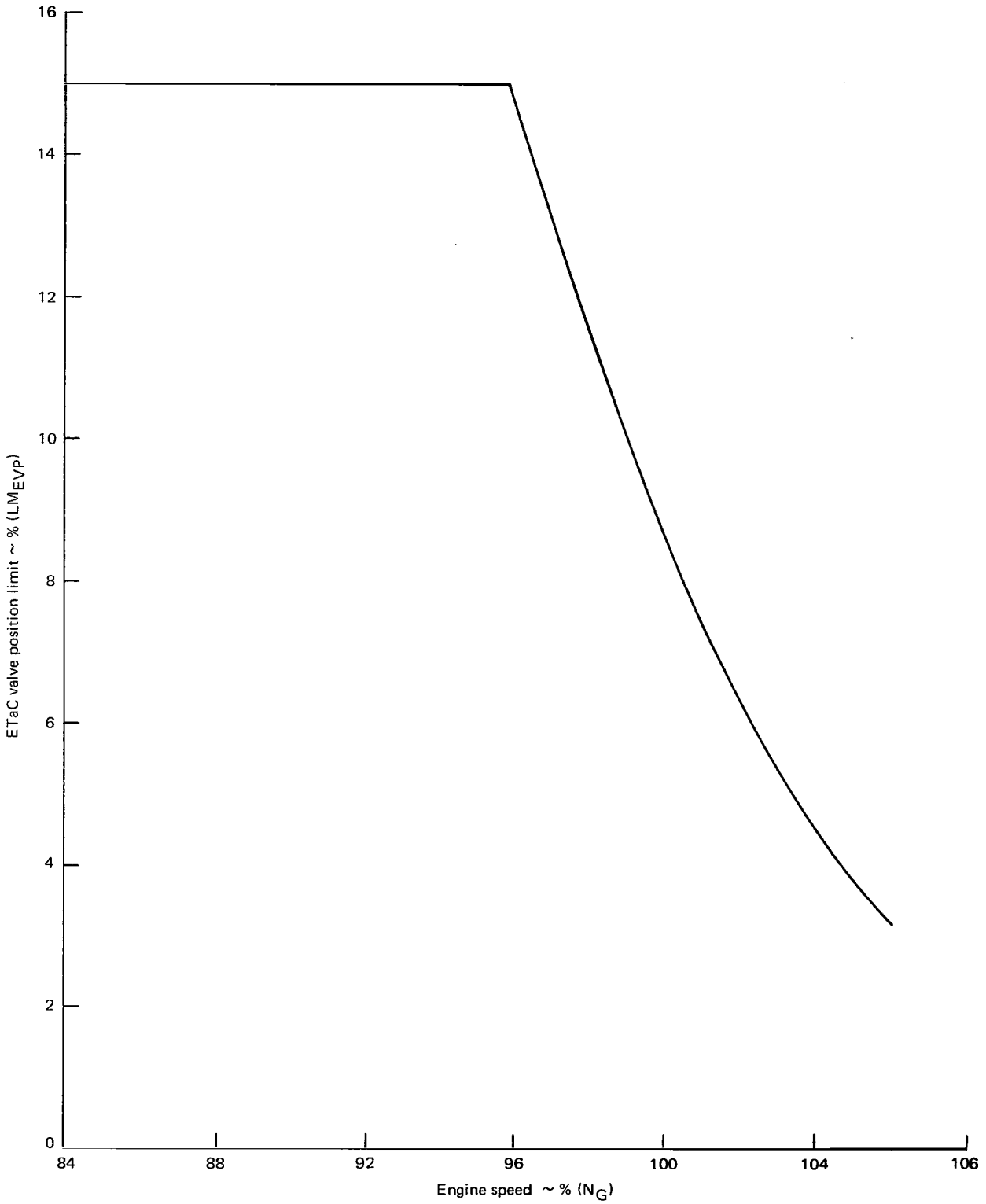

Figure 61.- ETaC valve position limit.

TABLE 23.- ENGINE AND FAN PARAMETERS

Parameter	Symbol	Value
Engine time constant	τ_{ENG}	0.0763 sec
Duct flow time constant	τ_{DUCT}	0.045 sec
Fan polar moment of inertia	I_p	26.44 kg m^2 (19.5 slug ft^2)
ETaC valve actuator input gain	K_{EVA1}	629.9 %/m (16.0 %/in.)
ETaC valve actuator forward gain	K_{EVA3}	629.9 %/m (16.0 %/in.)
Thrust spoiler actuator input gain	K_{ESP1}	629.9 %/m (16.0 %/in.)
ETaC valve actuator position limit	LM_{EVP}	(See figure 65)
ETaC valve actuator rate limit	LM_{EVR}	112.5 %/sec
Slope of thrust spoiler curve	K_{SLOPE}	-0.03 1/deg

Note: % refers to % of maximum flow area in vicinity of ETaC valve.

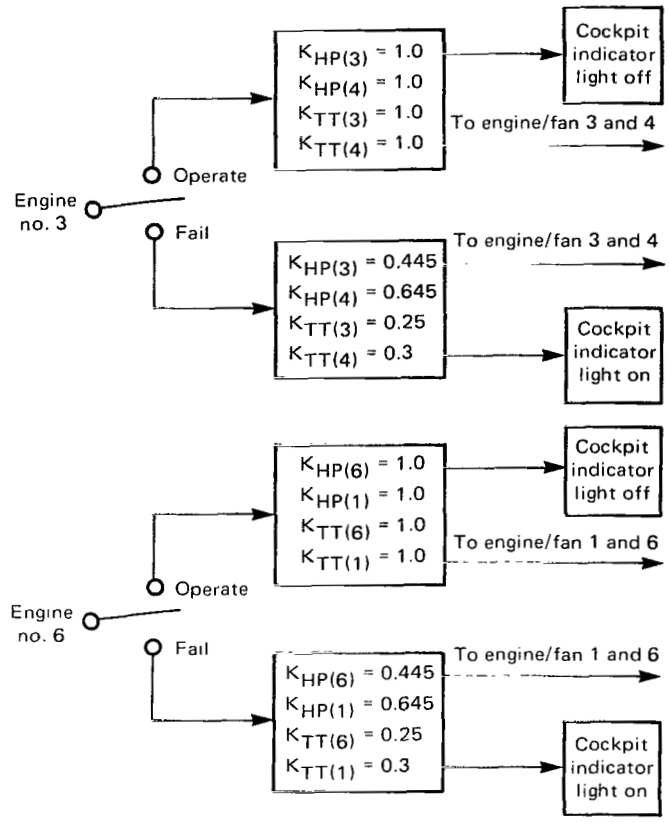

Note: Engine failures are simulated only for engines no. 3 (left wing tip) and no. 6 (right aft fuselage)

Figure 62.- Engine failure logic.

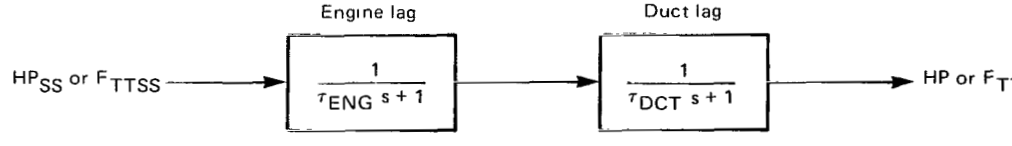

Figure 63.- Engine and duct lags.

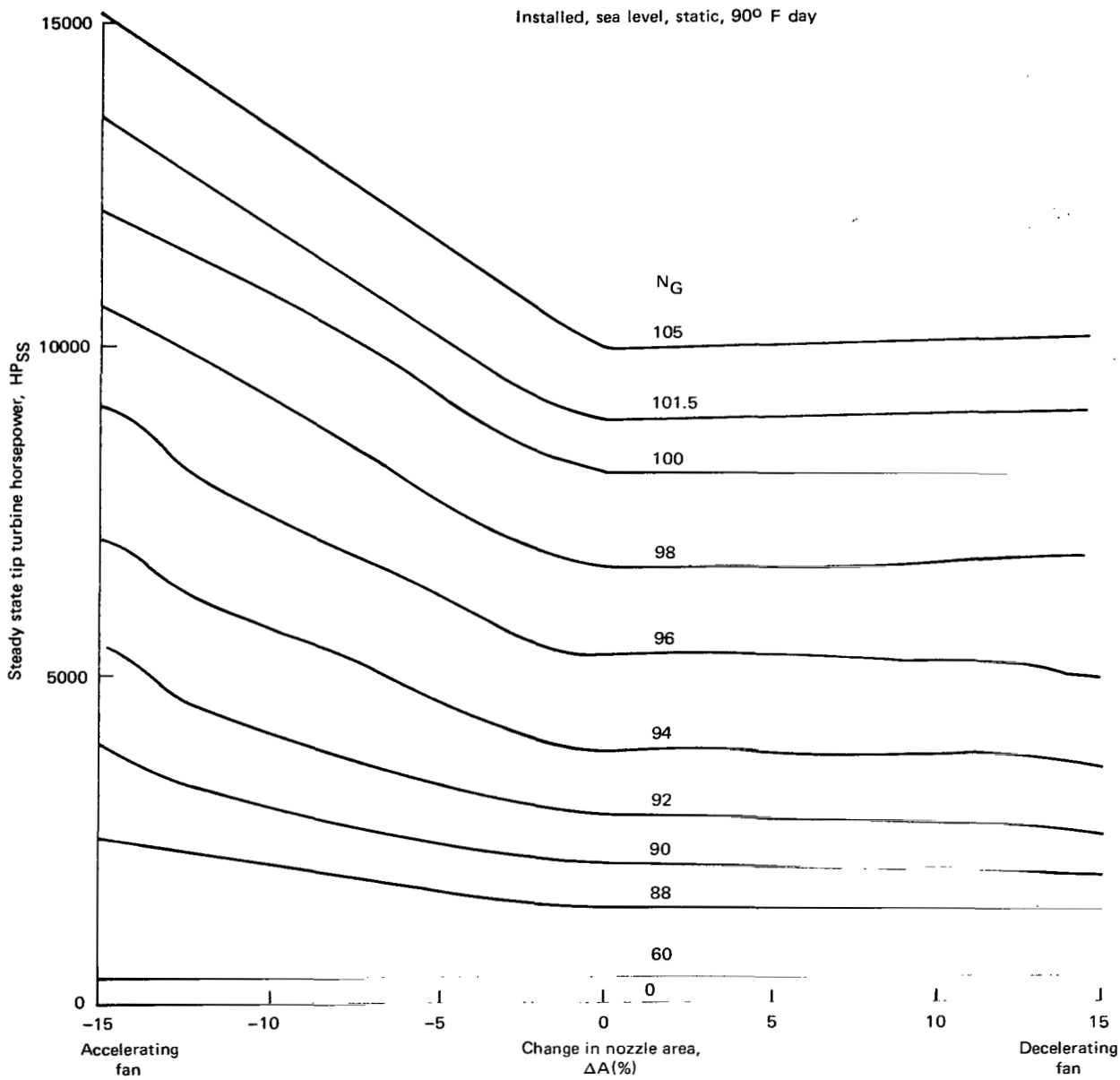

Figure 64.- Steady-state tip turbine horsepower.

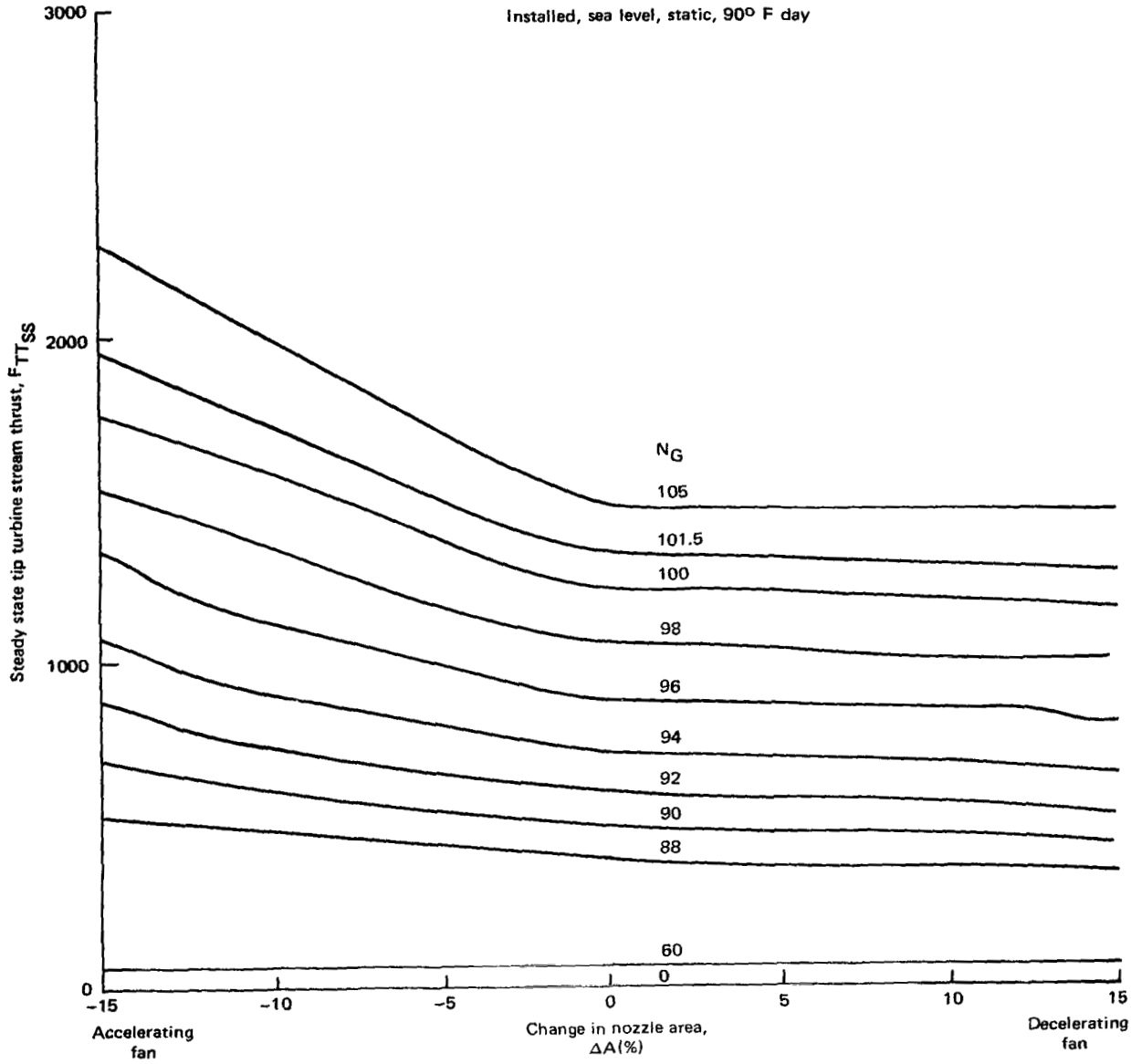

Figure 65.- Steady-state tip turbine stream thrust.

TABLE 24.- FAN THRUST AND TORQUE EQUATIONS

$$F_{N_k} = 2445.68 \left(\frac{N_{F_k}}{1000}\right)^{2.1541} \text{ N} \quad \left\{549.81 \left(\frac{N_{F_k}}{1000}\right)^{2.1541} \text{ lb}\right\}$$

$$T_{F_k} = 850.0 \left(\frac{N_{F_k}}{1000}\right)^{2.1298} \text{ Nm} \quad \left\{627.16 \left(\frac{N_{F_k}}{1000}\right)^{2.1298} \text{ lb ft}\right\}$$

Note: N_{F_k} is the RPM of the kth fan.

TABLE 25.- GROSS THRUST EFFICIENCY FACTORS

$$F_{TFL} = \eta_{fwd}\, \eta_{lift}\, F_T(1)$$

$$F_{TFR} = \eta_{fwd}\, \eta_{lift}\, F_T(2)$$

$$F_{TWL} = \eta_{wing}\, \eta_{lift}\, F_T(3)$$

$$F_{TWR} = \eta_{wing}\, \eta_{lift}\, F_T(4)$$

$$F_{TAL} = \eta_{aft}\, \eta_{LC}\, F_T(5)$$

$$F_{TAR} = \eta_{aft}\, \eta_{LC}\, F_T(6)$$

$$\eta_{fwd} = 0.98079$$

$$\eta_{wing} = 1.0$$

$$\eta_{aft} = 0.92314 \quad \zeta_{HD} \leq 70°$$

$$= 0.65413 + 0.003843\, \zeta_{HD} \quad 70° < \zeta_{HD} < 90°$$

$$= 1.0 \quad \zeta_{HD} \geq 90°$$

$$\eta_{lift} = 1.0 - 738.2\times10^{-6} U_B - 2.69\times10^{-6} U_B^2 \quad (U_B \text{ in m/sec})$$

$$= 1.0 - 225\times10^{-6} U_B - 0.25\times10^{-6} U_B^2 \quad (U_B \text{ in ft/sec})$$

$$\eta_{LC} = 1.0 + 15.91\times10^{-4} U_B + 6.73\times10^{-6} U_B^2 \quad (U_B \text{ in m/sec})$$

$$= 1.0 + 4.85\times10^{-4} U_B + 0.625\times10^{-6} U_B^2 \quad (U_B \text{ in ft/sec})$$

APPENDIX C — PROPULSION SYSTEM FORCE AND MOMENT COMPUTATION AND RESOLUTION

NOMENCLATURE FOR APPENDIX C

E_{iFj}, E_{iWj}, E_{iAj} $i = X, Y, Z$ $j = R$(right), L(left)	body axes coordinates of forward, wing, and aft fan thrust application points
F_{iFj}, F_{iWj}, F_{iAj} $i = X, Y, Z$ $j = R$(right), L(left)	body axes thrust components of forward, wing, and aft fans
K_{VACT}	thrust vectoring actuator forward gain
k	engine number (fig. 13)
L_F, M_F, N_F	moments produced by fan thrust about x, y, and z body axes
L_{RAM}, M_{RAM}, N_{RAM}	moments produced by ram drag forces about x, y, and z body axes
LM_{CA}	forward cascade actuator rate limit
LM_{WI}	wing cascade actuator rate limit
LM_{HDRAT}	hood actuator rate limit
$\overline{LP}$, $\overline{LR}$, $\overline{LV}$	ram drag rolling moment due to roll rate, yaw rate, and y body axis speed
$\dot{M}_{Fj}$, $\dot{M}_{Wj}$, $\dot{M}_{Aj}$ $j = R$(right), L(left)	air mass flow through front, wing, and aft fans
$\overline{MQ}$, $\overline{MU}$, $\overline{MW}$	ram drag pitching moment due to pitch rate, speed along x body axis, and speed along z body axis
$\overline{NP}$, $\overline{NV}$, $\overline{NR}$	ram drag yawing moment due to roll rate, speed along y body axis, and yaw rate
$\dot{W}_{F_k}$ ($k = 1, 2, \ldots, 6$)	air mass flow through fan k
X_F, Y_F, Z_F	total fan thrust forces acting along x, y, and z body axes
X_{FE}, X_{WE}, X_{AE}	body axes x coordinates of forward, wing, and aft engine inlets
X_{FF}, X_{WF}, X_{AF}	body axes x coordinates of forward, wing, and aft fan inlets

X_{RAM}, Y_{RAM}, Z_{RAM}	ram drag forces along x, y, and z body axes
$\overline{XQ}$, $\overline{XU}$	ram drag forces along x body axis due to pitch rate and speed along x body axis
Y_{FE}, Y_{WE}, Y_{AE}	body axes y coordinate of forward, wing, and aft engine inlets
Y_{FF}, Y_{WF}, Y_{AF}	body axes y coordinate of forward, wing, and aft fan inlets
$\overline{YP}$, $\overline{YR}$, $\overline{YV}$	ram drag forces along y body axis due to roll rate, yaw rate, and speed along y body axis
Z_{FE}, Z_{WE}, Z_{AE}	body axes z coordinate of forward, wing, and aft engine inlets
Z_{FF}, Z_{WF}, Z_{AF}	body axes z coordinate of forward, wing, and aft fan inlets
$\overline{ZQ}$, $\overline{ZW}$	ram drag forces along z body axis due to pitch rate and speed along z body axis
Λ	ratio of engine air mass flow to fan air mass flow
ϕ_{CA}	fixed roll inclination angle of the forward- and wing-mounted cascades

The thrust of the forward fans is deflected by a rotating cascade system shown in figures 66 and 67. The louver angle, α_{CA}, is the lateral thrust deflection angle used to obtain both yaw control and direct side-force control. The cascade rotation angle, ζ_{CA}, is used to deflect the thrust forward and aft for transition.

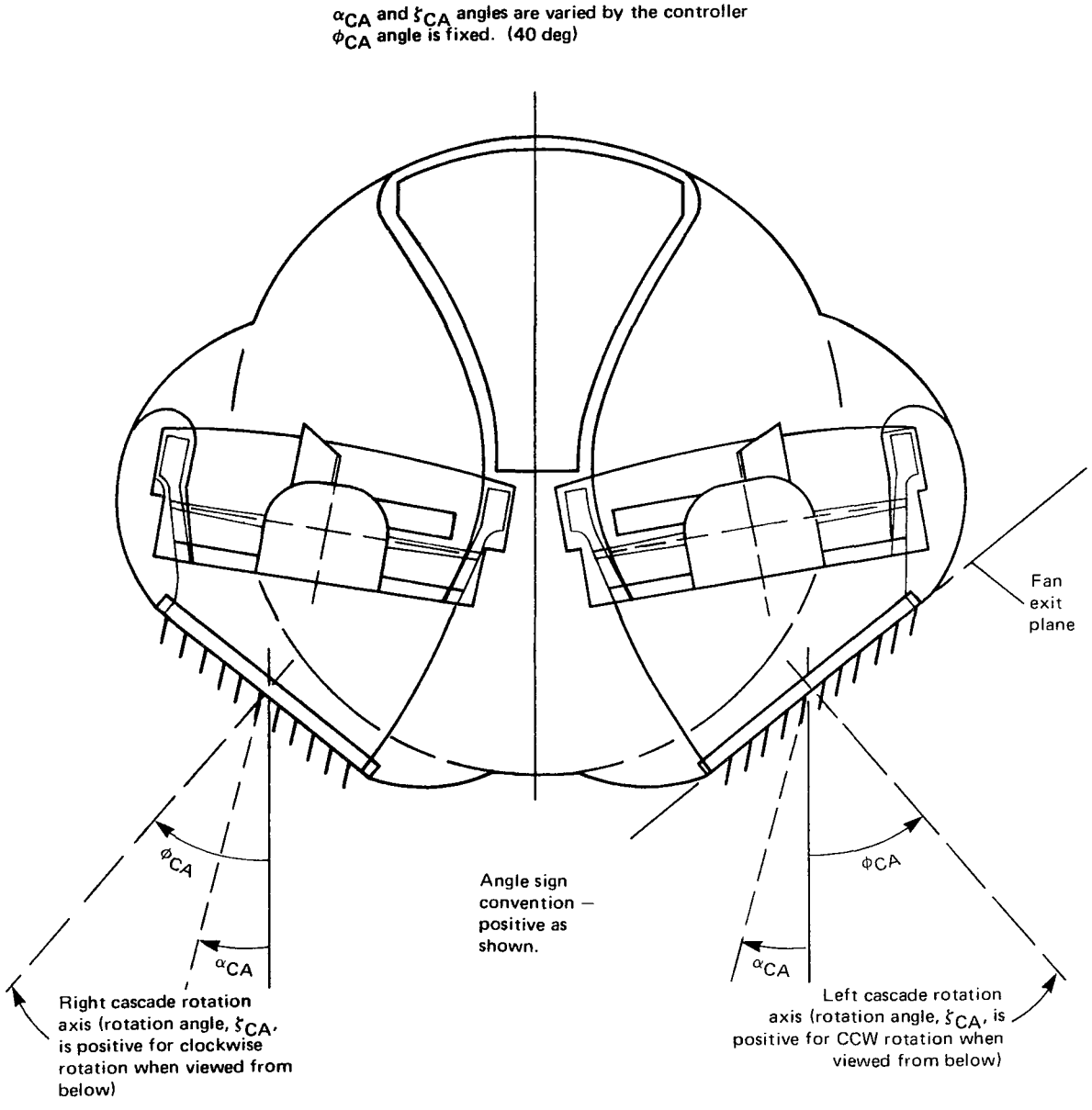

Figure 66.- View of the forward fans (looking aft).

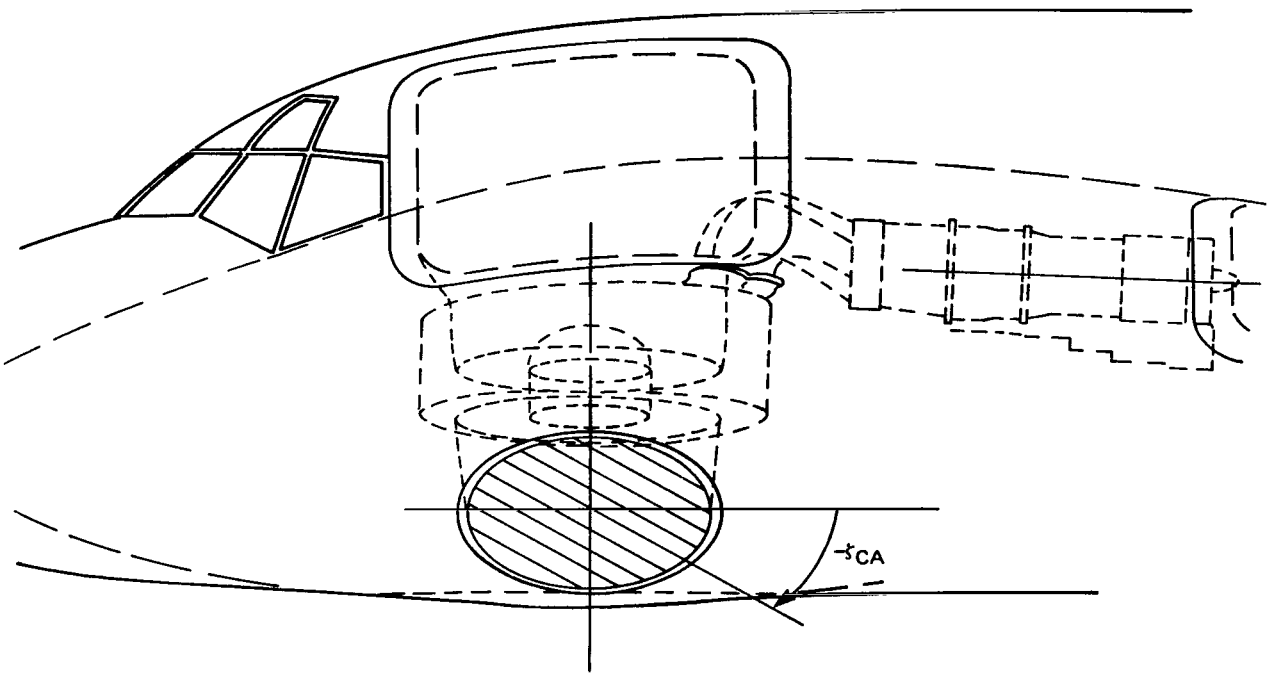

Figure 67.- Side view of the forward left engine and fan.

The thrust of the aft fans is deflected by a rotating hood assembly shown in figures 68 and 69. The hood rotation angle, γ_{HD}, is the lateral thrust deflection angle used for both yaw control and direct side-force control. The hood extension angle, ζ_{HD}, is used to deflect the thrust forward and aft for transition.

The thrust of the wing fans is deflected by a rotating cascade system identical to that used for the forward fans (see fig. 70). The louver angle, α_{WI}, is the lateral thrust deflection angle used for direct side-force control. The cascade rotation angle, ζ_{WI}, is used to deflect the thrust forward and aft for transition.

The output from the horizontal (longitudinal) controller, ζ_{TL}, is used to drive the forward cascades, wing cascades, and aft hood through angles ζ_{CA}, ζ_{WI}, and ζ_{HD}, respectively. To ensure that the pitching moment remains small as the total thrust vector is deflected from full-forward to full-aft, the thrust deflection systems must be driven through suitable nonlinear gearing (fig. 15). A suitable set of gearing functions is shown in figure 71.

The model of the cascade and hood actuators is shown in figure 72. The numerical values of the actuator parameters (fig. 72) are given in table 26.

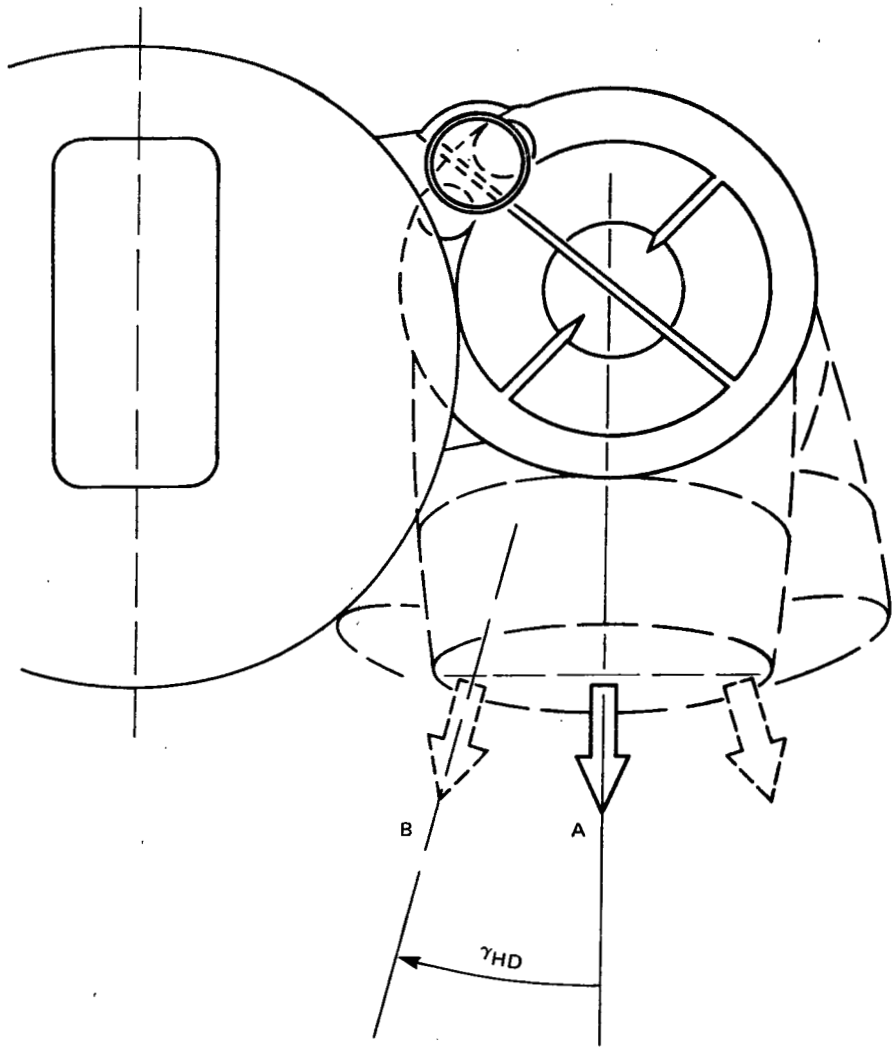

Hood centerline plane is shown in vertical (A) and deflected (B) position.
Position B corresponds to positive γ_{HD} angle.

For the right aft fan, positive γ_{HD} is obtained with the same direction of hood rotation.

Figure 68.- Aft left engine and fan (looking aft).

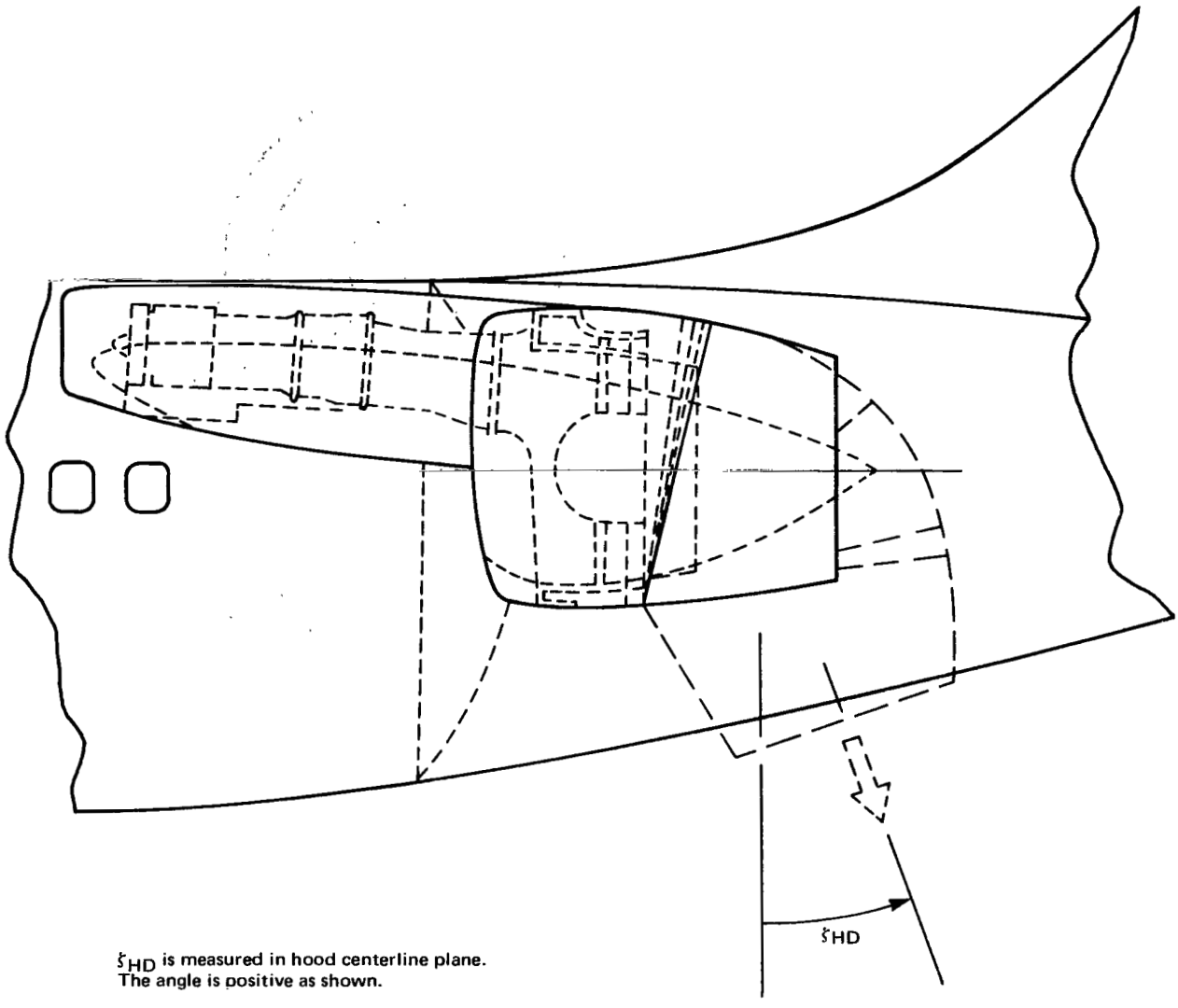

Figure 69.- Aft left engine and fan.

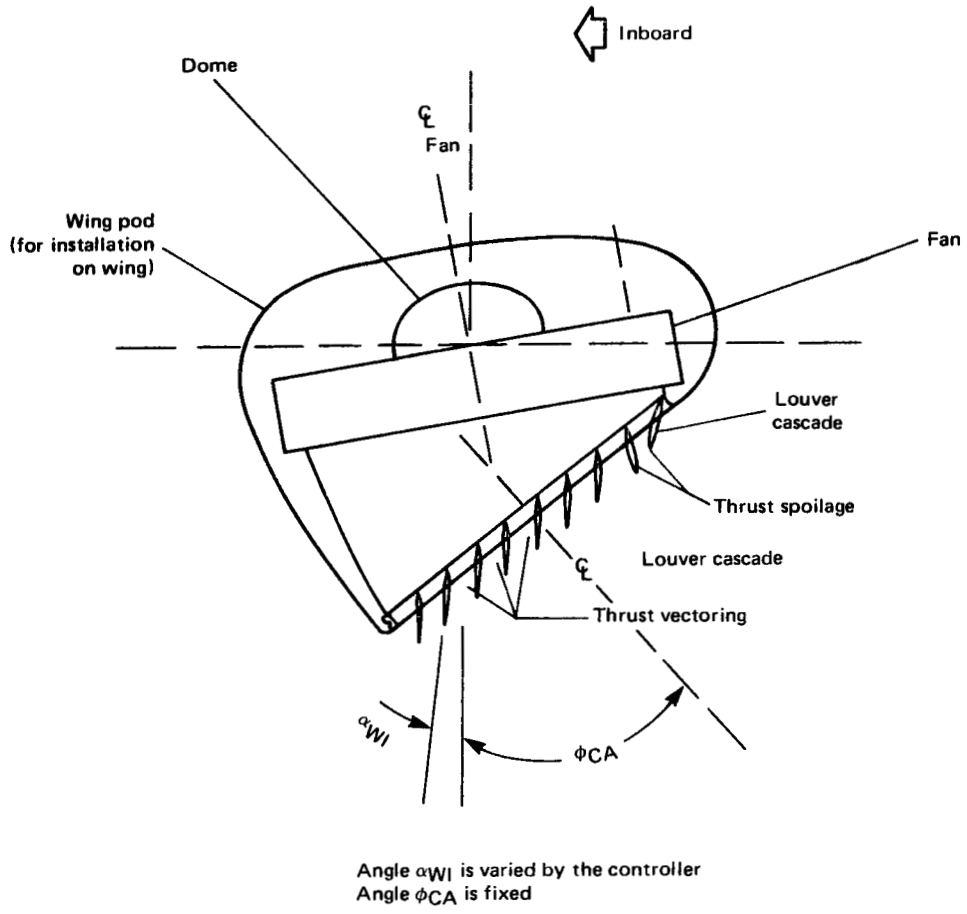

Figure 70.- Thrust vectoring control wing fans (looking aft).

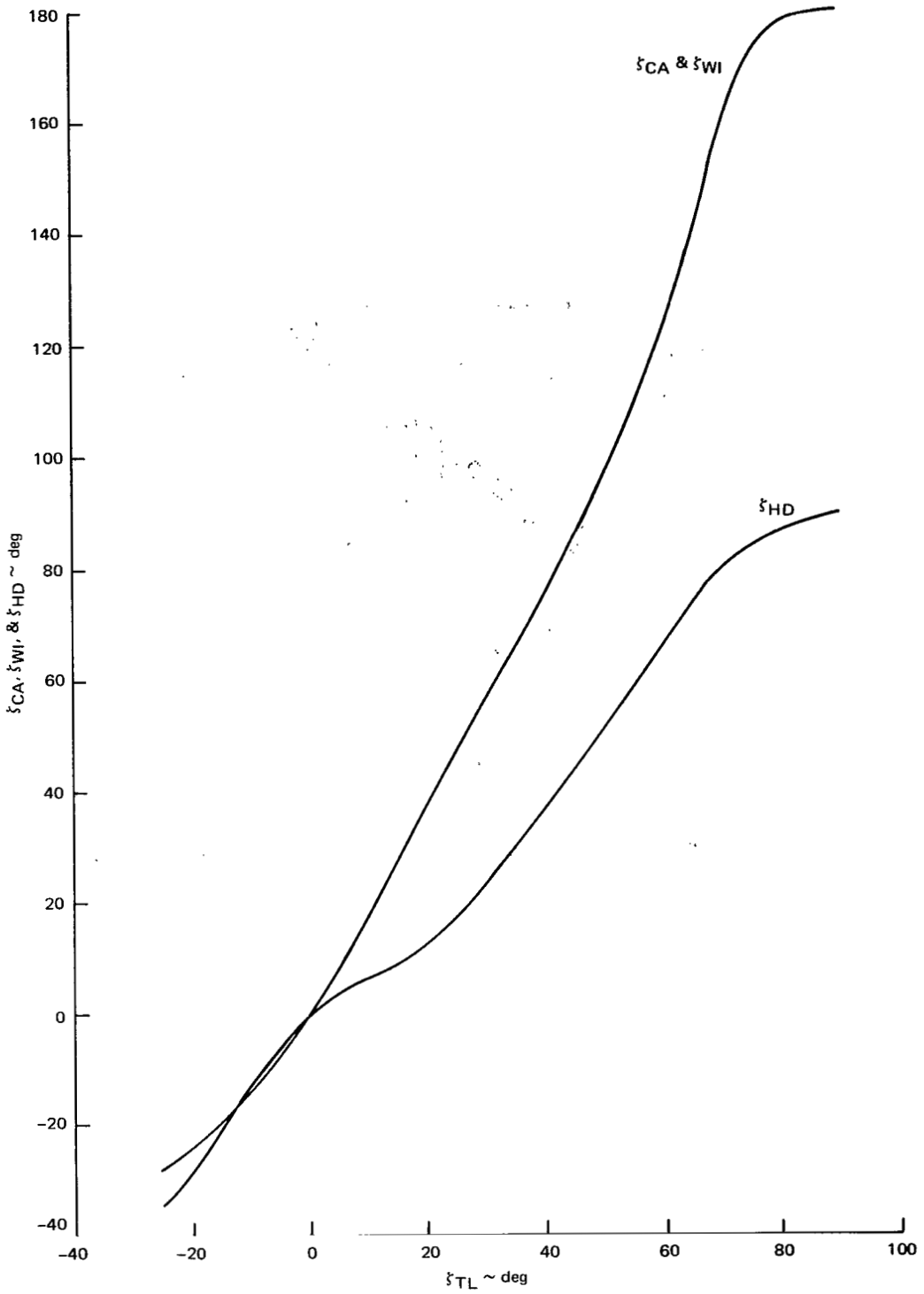

Figure 71.- Simulated thrust vectoring schedule.

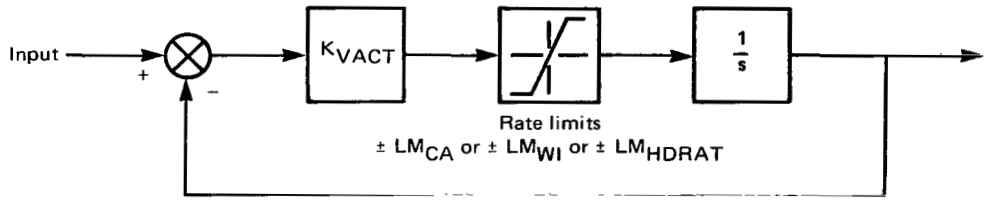

Figure 72.- Cascade and hood actuator model.

TABLE 26.- THRUST-VECTORING ACTUATOR PARAMETERS

Parameter	Symbol	Value
Thrust-vectoring actuator gain	K_{VACT}	5.0/sec
Forward cascade actuator rate limit	LM_{CA}	100 deg/sec
Wing cascade actuator rate limit	LM_{WI}	100 deg/sec
Hood actuator rate limit	LM_{HDRAT}	50 deg/sec

The force and moment computation and resolution equations are given in table 27. The first four equations give the thrust components in the x, y, and z airplane body axes of each of the six fans. The last set of six equations gives the net forces and moments, about the x, y, and z body axes, due to all six fans.

The fan locations used in the moment equations are given in table 28.

The ram drag forces and moments are computed from the fan airflow and the total linear and angular velocities relative to the air mass. Fan airflow is computed as a function of fan speed, and engine airflow is assumed to be a constant percentage of the fan airflow. The fan airflow is computed separately, for each of six fans, to permit the simulation of engine failure. The ram drag force and moment equations are given in table 29, and the engine and fan air inlet locations are given in table 30.

TABLE 27.- FORCE AND MOMENT COMPUTATION AND RESOLUTION

$$F_{XFR} = F_{TFR} \sin(\phi_{CA} - \alpha_{CA}) \sin \zeta_{CA}$$

$$F_{YFR} = -F_{TFR}[\sin \phi_{CA} \cos(\phi_{CA} - \alpha_{CA}) - \cos \phi_{CA} \sin(\phi_{CA} - \alpha_{CA}) \cos \zeta_{CA}]$$

$$F_{ZFR} = -F_{TFR}[\cos \phi_{CA} \cos(\phi_{CA} - \alpha_{CA}) + \sin \phi_{CA} \sin(\phi_{CA} - \alpha_{CA}) \cos \zeta_{CA}]$$

$$F_{XFL} = F_{TFL} \sin(\phi_{CA} + \alpha_{CA}) \sin \zeta_{CA}$$

$$F_{YFL} = F_{TFL}[\sin \phi_{CA} \cos(\phi_{CA} + \alpha_{CA}) - \cos \phi_{CA} \sin(\phi_{CA} + \alpha_{CA}) \cos \zeta_{CA}]$$

$$F_{ZFL} = -F_{TFL}[\cos \phi_{CA} \cos(\phi_{CA} + \alpha_{CA}) + \sin \phi_{CA} \sin(\phi_{CA} + \alpha_{CA}) \cos \zeta_{CA}]$$

$$F_{XWR} = F_{TWR} \sin(\phi_{CA} - \alpha_{WI}) \sin \zeta_{WI}$$

$$F_{YWR} = -F_{TWR}[\sin \phi_{CA} \cos(\phi_{CA} - \alpha_{WI}) - \cos \phi_{CA} \sin(\phi_{CA} - \alpha_{WI}) \cos \zeta_{WI}]$$

$$F_{ZWR} = -F_{TWR}[\cos \phi_{CA} \cos(\phi_{CA} - \alpha_{WI}) + \sin \phi_{CA} \sin(\phi_{CA} - \alpha_{WI}) \cos \zeta_{WI}]$$

$$F_{XWL} = F_{TWL} \sin(\phi_{CA} + \alpha_{WI}) \sin \zeta_{WI}$$

$$F_{YWL} = F_{TWL}[\sin \phi_{CA} \cos(\phi_{CA} + \alpha_{WI}) - \cos \phi_{CA} \sin(\phi_{CA} + \alpha_{WI}) \cos \zeta_{WI}]$$

$$F_{ZWL} = -F_{TWL}[\cos \phi_{CA} \cos(\phi_{CA} + \alpha_{WI}) + \sin \phi_{CA} \sin(\phi_{CA} + \alpha_{WI}) \cos \zeta_{WI}]$$

$$F_{XAR} = F_{TAR} \sin \zeta_{HD}$$

$$F_{YAR} = -F_{TAR} \sin \gamma_{HD} \cos \zeta_{HD}$$

$$F_{ZAR} = -F_{TAR} \cos \gamma_{HD} \cos \zeta_{HD}$$

$$F_{XAL} = F_{TAL} \sin \zeta_{HD}$$

$$F_{YAL} = -F_{TAL} \sin \gamma_{HD} \cos \zeta_{HD}$$

$$F_{ZAL} = -F_{TAL} \cos \gamma_{HD} \cos \zeta_{HD}$$

$$X_F = F_{XFR} + F_{XFL} + F_{XWR} + F_{XWL} + F_{XAR} + F_{XAL}$$

$$Y_F = F_{YFR} + F_{YFL} + F_{YWR} + F_{YWL} + F_{YAR} + F_{YAL}$$

$$Z_F = F_{ZFR} + F_{ZFL} + F_{ZWR} + F_{ZWL} + F_{ZAR} + F_{ZAL}$$

TABLE 27.- Concluded

$$L_F = E_{YFR}(F_{ZER} - F_{ZFL}) + E_{YWR}(F_{ZWR} - F_{ZWL}) + E_{YAR}(F_{ZAR} - F_{ZAL}) - E_{ZFR}(F_{YFR} + F_{YFL}) - E_{ZAR}(F_{YAR} + F_{YAL}) - E_{ZWR}(F_{YWR} - F_{YWL})$$

$$M_F = -E_{XFR}(F_{ZFR} + F_{ZFL}) - E_{XWR}(F_{ZWR} + F_{ZWL}) - E_{XAR}(F_{ZAR} + F_{ZAL}) + E_{ZFR}(F_{XFR} + F_{XFL}) + E_{ZWR}(F_{XWR} + F_{XWL}) + E_{ZAR}(F_{XAR} + F_{XAL})$$

$$N_F = E_{XFR}(F_{YFR} + F_{YFL}) + E_{XAR}(F_{YAR} + F_{YAL}) - E_{YFR}(F_{XFR} - F_{XFL}) - E_{YWR}(F_{XWR} - F_{XWL}) - E_{YAR}(F_{XAR} - F_{XAL}) + E_{XWR}(F_{YWR} + F_{YWL})$$

TABLE 28.- COORDINATES OF THRUST APPLICATION POINTS

Engine/fan	Coordinate	Symbol	Value
Front right (no. 2)	x	E_{XFR}	7.9 m (25.92 ft)
	y	E_{YFR}	1.65 m (5.42 ft)
	z	E_{ZFR}	1.24 m (4.08 ft)
Wing right (no. 4)	x	E_{XWR}	0 m (0 ft)
	y	E_{YWR}	9.20 m (30.17 ft)
	z	E_{ZWR}	.79 m (2.58 ft)
Aft right (no. 6)	x	E_{XAR}	-8.56 m (-28.08 ft)
	y	E_{YAR}	2.46 m (8.08 ft)
	z	E_{ZAR}	-.85 m (-2.79 ft)

TABLE 29.- RAM DRAG FORCE AND MOMENT EQUATIONS

$$\overline{XU} = -(1 + \Lambda)[\dot{M}_{FR} + \dot{M}_{FL} + \dot{M}_{WR} + \dot{M}_{WL} + \dot{M}_{AR} + \dot{M}_{AL})$$

$$\overline{MU} = -[(Z_{FF} + \Lambda Z_{FE})(\dot{M}_{FR} + \dot{M}_{FL}) + (Z_{WF} + \Lambda Z_{WE})(\dot{M}_{WR} + \dot{M}_{WL}) + (Z_{AF} + \Lambda Z_{AE})(\dot{M}_{AR} + \dot{M}_{AL})]$$

$$\overline{MW} = (X_{FF} + \Lambda X_{FE})(\dot{M}_{FR} + \dot{M}_{FL}) + (X_{WF} + \Lambda X_{WE})(\dot{M}_{WR} + \dot{M}_{WL}) + (X_{AF} + \Lambda X_{AE})(\dot{M}_{AR} + \dot{M}_{AL})$$

$$\overline{MQ} = -[X_{FF}^2 + Z_{FF}^2 + \Lambda(X_{FE}^2 + Z_{FE}^2)](\dot{M}_{FR} + \dot{M}_{FL}) - [X_{WF}^2 + Z_{WF}^2 + \Lambda(X_{WE}^2 + Z_{WE}^2)](\dot{M}_{WR} + \dot{M}_{WL}) - [X_{AF}^2 + Z_{AF}^2 + \Lambda(X_{AE}^2 + Z_{AE}^2)](\dot{M}_{AR} + \dot{M}_{AL})$$

$$\overline{ZW} = \overline{XU} \qquad \overline{XQ} = \overline{MU} \qquad \overline{ZQ} = \overline{MW}$$

$$\overline{LP} = -[Y_{FF}^2 + Z_{FF}^2 + \Lambda(Y_{FE}^2 + Z_{FE}^2)](\dot{M}_{FR} + \dot{M}_{FL}) - [Y_{WF}^2 + Z_{WF}^2 + \Lambda(Y_{WE}^2 + Z_{WE}^2)](\dot{M}_{WR} + \dot{M}_{WL}) - [Y_{AF}^2 + Z_{AF}^2 + \Lambda(Y_{AE}^2 + Z_{AE}^2)](\dot{M}_{AR} + \dot{M}_{AL})$$

$$\overline{NR} = -[X_{FF}^2 + Y_{FF}^2 + \Lambda(X_{FE}^2 + Y_{FE}^2)](\dot{M}_{FR} + \dot{M}_{FL}) - [X_{WF}^2 + Y_{WF}^2 + \Lambda(X_{WE}^2 + Y_{WE}^2)] + (\dot{M}_{WR} + \dot{M}_{WL}) - [X_{AF}^2 + Y_{AF}^2 + \Lambda(X_{AE}^2 + Y_{AE}^2)](\dot{M}_{AR} + \dot{M}_{AL})$$

$$\overline{LR} = [X_{FF}Z_{FF} + \Lambda X_{FE}Z_{FE}](\dot{M}_{FR} + \dot{M}_{FL}) + [X_{WF}Z_{WF} + \Lambda X_{WE}Z_{WE}](\dot{M}_{WR} + \dot{M}_{WL}) + [X_{AF}Z_{AF} + \Lambda X_{AE}Z_{AE}](\dot{M}_{AR} + \dot{M}_{AL})$$

$$\overline{NP} = \overline{LR} \qquad \overline{YP} = \overline{LV} = -\overline{XQ} \qquad \overline{YR} = \overline{NY} = -\overline{ZQ} \qquad \overline{YV} = \overline{ZW}$$

$$\dot{W}_{F_k} = 56.11\left(\frac{N_{F_k}}{1000}\right)^{1.0594} \text{ kg/sec} \quad \left\{ 123.7\left(\frac{N_{F_k}}{1000}\right)^{1.0594} \text{ lb/sec} \right\}$$

$$\dot{M}_{FL} = \dot{W}_{F_1}/g \qquad L_{RAM} = \overline{LV}\, v_B + \overline{LP}\, p_T + \overline{LR}\, r_T$$

$$\dot{M}_{FR} = \dot{W}_{F_2}/g \qquad Y_{RAM} = \overline{YV}\, v_B + \overline{YP}\, p_T + \overline{YR}\, r_T$$

$$\dot{M}_{WL} = \dot{W}_{F_3}/g \qquad N_{RAM} = \overline{NV}\, v_B + \overline{NP}\, p_T + \overline{NR}\, r_T$$

$$\dot{M}_{WR} = \dot{W}_{F_4}/g \qquad X_{RAM} = \overline{XU}\, u_B + \overline{XQ}\, q_T$$

$$\dot{M}_{AL} = \dot{W}_{F_5}/g \qquad Z_{RAM} = \overline{ZW}\, w_B + \overline{ZQ}\, q_T$$

$$\dot{M}_{AR} \quad \dot{W}_{F_6}/g \qquad M_{RAM} = \overline{MU}\, u_B + \overline{MW}\, w_B + \overline{MQ}\, q_T$$

Λ = ratio of engine airflow to fan airflow = 0.131

TABLE 30.- ENGINE AND FAN AIR INLET LOCATIONS

Engine / Fan	Coord	Symbol	Value
Front right (no. 2)	x	X_{FE} / X_{FF}	3.38 m (11.08 ft) / 7.90 m (25.92 ft)
	y	Y_{FE} / Y_{FF}	1.98 m (6.50 ft) / 1.30 m (4.25 ft)
	z	Z_{FE} / Z_{FF}	0.025 m (0.083 ft) / -0.878 m (-2.88 ft)
Wing right (no. 4)	x	X_{WE} / X_{WF}	-3.89 m (-12.75 ft) / 0 m (0 ft)
	y	Y_{WE} / Y_{WF}	8.89 m (29.17 ft) / 6.35 m (20.83 ft)
	z	Z_{WE} / Z_{WF}	-1.12 m (-3.67 ft) / -0.457 m (-1.50 ft)
Aft right (no. 6)	x	X_{AE} / X_{AF}	-3.53 m (-11.58 ft) / -6.12 m (-20.08 ft)
	y	Y_{AE} / Y_{AF}	1.73 m (5.67 ft) / 2.46 m (8.08 ft)
	z	Z_{AE} / Z_{AF}	-1.63 m (-5.33 ft) / -0.85 m (-2.79 ft)

APPENDIX D — AIRFRAME AERODYNAMIC FORCES AND MOMENTS

NOMENCLATURE FOR APPENDIX D

b_w	wing span
$\bar{c}_w$	wing mean aerodynamic chord
C_D	drag coefficient, $-\frac{X_{ST}}{\bar{q}S_w}$
C_{Dt}	drag coefficient of horizontal tailplane
C_{DTO}	drag coefficient of airplane less tailplane
C_l	rolling-moment coefficient, $\frac{L_{ST}}{\bar{q}S_w b_w}$
C_{l_p}	coefficient of rolling moment due to roll rate, $\frac{\partial C_l}{\partial (p_{ST} b_w / 2V_a)}$
C_{l_r}	coefficient of rolling moment due to yaw rate, $\frac{\partial C_l}{\partial (r_{ST} b_w / 2V_a)}$
C_{l_β}	coefficient of rolling moment due to sideslip, $\frac{\partial C_l}{\partial \beta}$
$C_{l_{\delta_R}}$	coefficient of rolling moment due to rudder deflection, $\frac{\partial C_l}{\partial \delta_R}$
C_L	lift coefficient, $-\frac{Z_{ST}}{\bar{q}S_w}$
C_{Lt}	lift coefficient of horizontal tailplane
C_{LTO}	lift coefficient of airplane less tailplane
C_{L_q}	coefficient of lift due to pitch rate, $\frac{\partial C_L}{\partial (q_{ST} \bar{c}_w / 2V_a)}$
$C_{L_{\dot{\alpha}}}$	coefficient of lift due to $\dot{\alpha}$, $\frac{\partial C_L}{\partial (\dot{\alpha} \bar{c}_w / 2V_a)}$
C_m	pitching-moment coefficient, $\frac{M_{ST}}{\bar{q}S_w \bar{c}_w}$
C_{m_q}	coefficient of pitching moment due to pitch rate, $\frac{\partial C_m}{\partial (q_{ST} \bar{c}_w / 2V_a)}$
C_{MTO}	pitching-moment coefficient of airplane less horizontal tailplane
$C_{m_{\dot{\alpha}}}$	coefficient of pitching moment due to $\dot{\alpha}$, $\frac{\partial C_m}{\partial (\dot{\alpha} \bar{c}_w / 2V_a)}$

C_{m_α} coefficient of pitching moment due to angle of attack, $\frac{\partial C_m}{\partial \alpha}$

C_n yawing-moment coefficient, $\frac{N_{ST}}{\bar{q} S_w b_w}$

C_{n_p} coefficient of yawing moment due to roll rate, $\frac{\partial C_n}{\partial (p_{ST} b_w / 2V_a)}$

C_{n_r} coefficient of yawing moment due to yaw rate, $\frac{\partial C_n}{\partial (r_{ST} b_w / 2V_a)}$

C_{n_β} coefficient of yawing moment due to sideslip angle, $\frac{\partial C_n}{\partial \beta}$

$C_{n_{\delta_R}}$ coefficient of yawing moment due to rudder deflection, $\frac{\partial C_n}{\partial \delta_R}$

C_y side-force coefficient, $\frac{Y_{ST}}{\bar{q} S_w}$

C_{y_p} coefficient of sideforce due to roll rate, $\frac{\partial C_y}{\partial (p_{ST} b_w / 2V_a)}$

C_{y_r} coefficient of sideforce due to yaw rate, $\frac{\partial C_y}{\partial (r_{ST} b_w / 2V_a)}$

C_{y_β} coefficient of sideforce due to sideslip angle, $\frac{\partial C_y}{\partial \beta}$

$C_{y_{\delta_R}}$ coefficient of sideforce due to rudder deflection, $\frac{\partial C_y}{\partial \delta_R}$

l_t distance from airplane center of gravity to 25 percent of mean aerodynamic chord of horizontal tailplane, projected on the x stability axis

L_{ST}, M_{ST}, N_{ST} aerodynamic moments (excluding ram drag effects) about x, y, and z stability axes

p_{ST}, q_{ST}, r_{ST} total effective airplane rotation rates about x, y, and z stability axes

$\bar{q}$ dynamic pressure, $\frac{1}{2} \rho V_a^2$

S_t horizontal tailplane area

S_w wing area

u_B, v_B, w_B components of the true airspeed along the x, y, and z body axes

V_a airspeed, $\sqrt{u_B^2 + v_B^2 + w_B^2}$

X_{ST}, Y_{ST}, Z_{ST}	aerodynamic force components (excluding ram drag effects) along x, y, and z stability axes
Z_t	distance from the airplane center of gravity to the 25 percent of mean aerodynamic chord of horizontal tailplane, projected on the z stability axis
α or α_w	airplane angle of attack, $\tan^{-1} \frac{w_B}{u_B}$
$\dot{\alpha}$	rate of change of angle of attack
α_t	horizontal tailplane angle of attack, $\alpha - \varepsilon_t + \delta_{HT}$
β	airplane sideslip angle, $\tan^{-1} \frac{v_B}{\sqrt{u_B^2 + w_B^2}}$
$\Delta C_{D_{lg}}$	drag coefficient change due to landing gear
$\Delta C_{M_{lg}}$	pitching-moment coefficient change due to landing gear
ΔC_{ls}	rolling-moment coefficient change due to spoiler deflection
ΔC_{ns}	yawing-moment coefficient change due to spoiler deflection
δ_F	wing flap angle
ε_t	downwash angle at the horizontal tailplane
η_t	horizontal tailplane efficiency coefficient
ρ	atmospheric density

The lift, drag, and moment coefficients and stability derivatives, relative to stability axes, are given in figures 73 to 97. These data are for a constant flap setting of 50°, with all lift-fan and engine doors open and all six fans running. The coefficients and derivatives are given as functions of wing angle of attack α_w, defined to be identical with body-axis angle of attack α. The figures span an angle-of-attack range of ±90°. To obtain continuity of data over the entire angle-of-attack range of ±180°, the curves are linearly extended as shown in table 31. The increments in drag and pitching moment due to the landing gear are given in table 32.

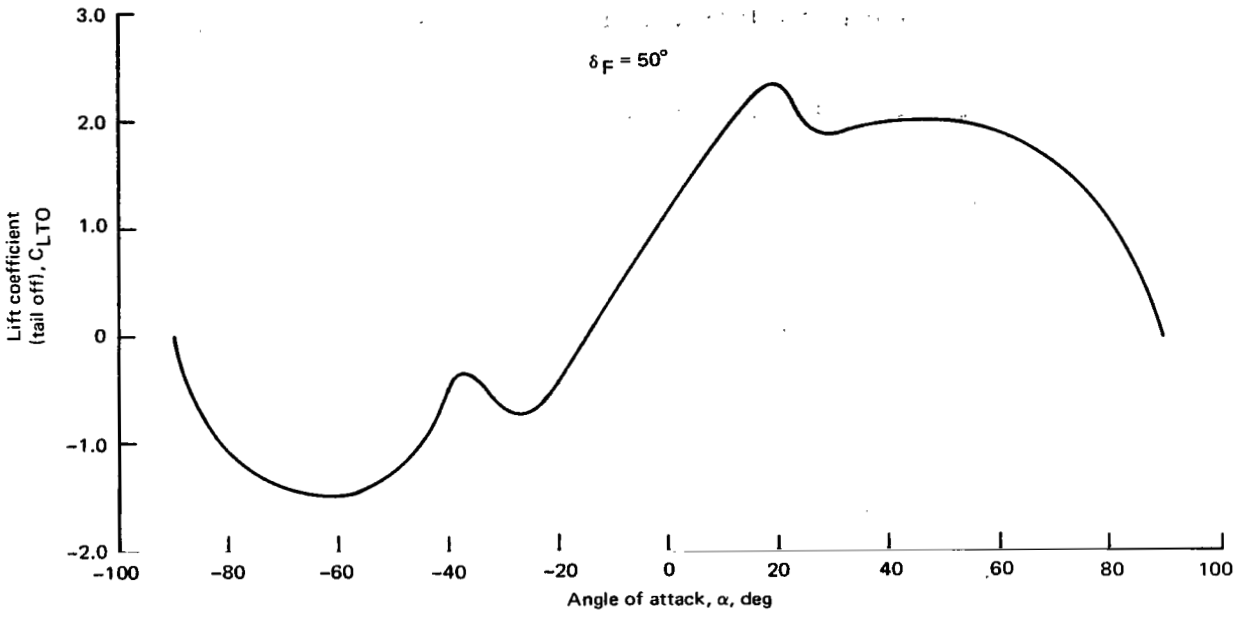

Figure 73.- Estimated tail-off lift coefficient (power on).

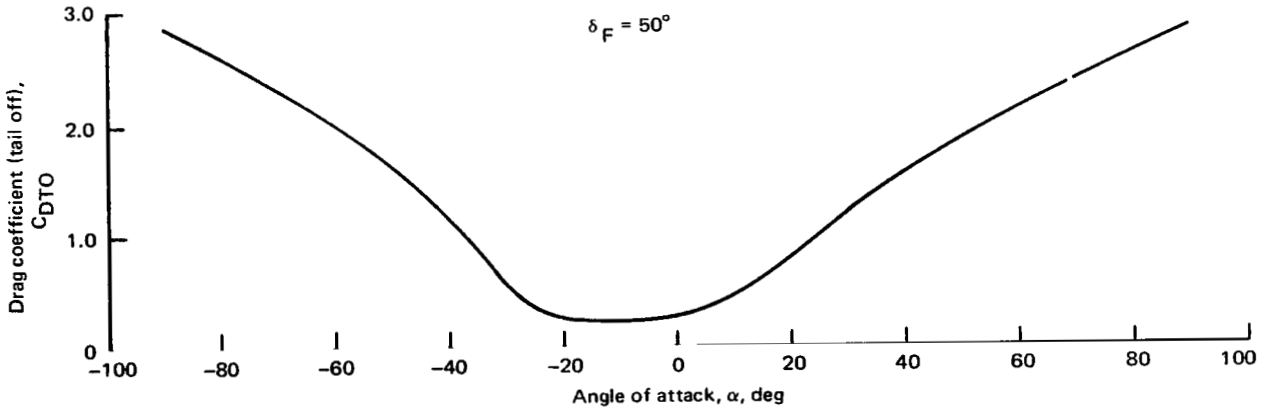

Figure 74.- Estimated tail-off drag coefficient (power on).

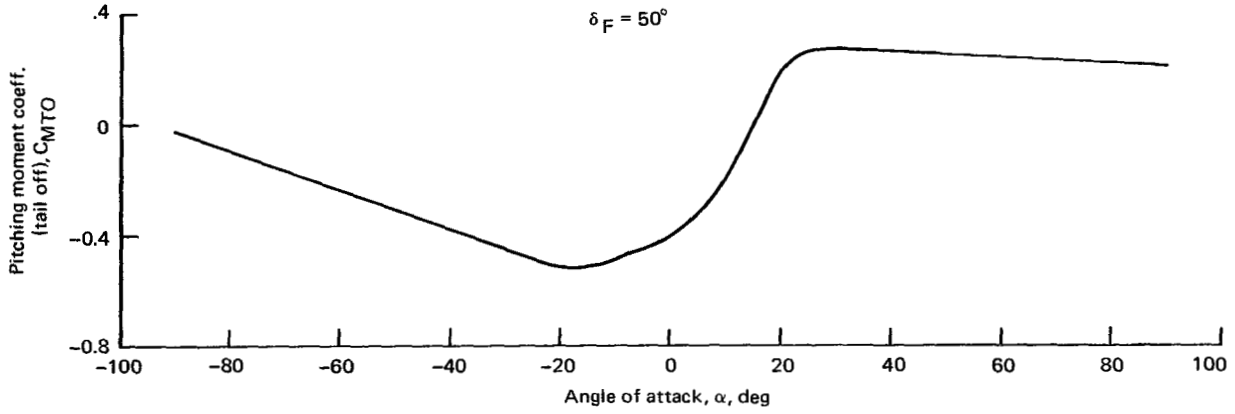

Figure 75.- Estimated tail-off pitching-moment coefficient C_{MTO} (note moment reference center = $\bar{c}/4$).

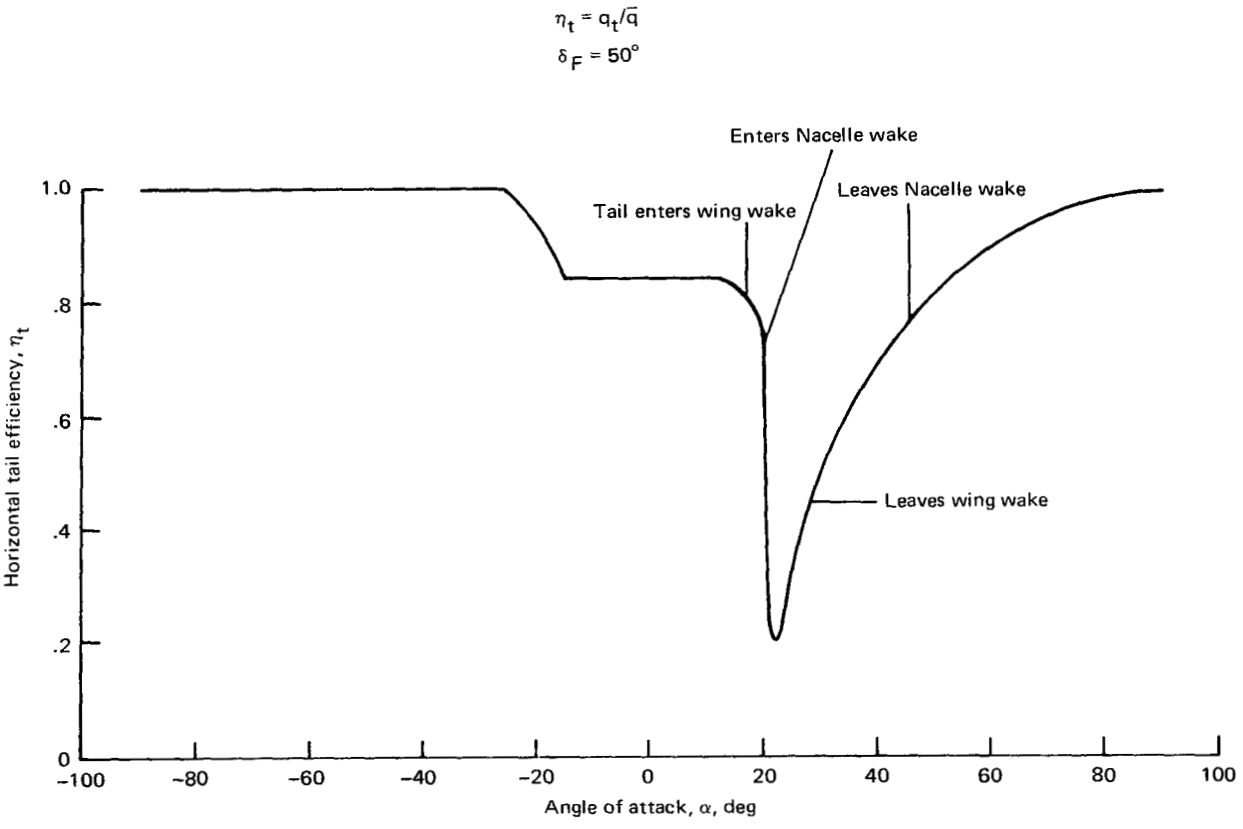

Figure 76.- Horizontal tail efficiency η_t.

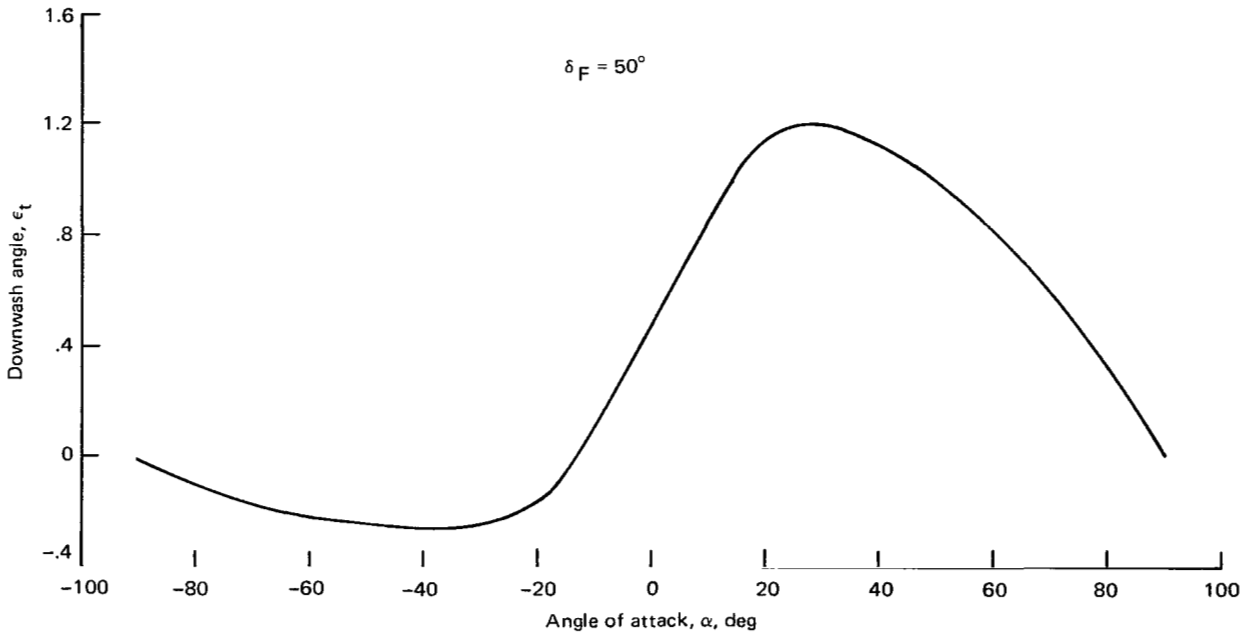

Figure 77.- Estimated average downwash angle at horizontal tail ε_t.

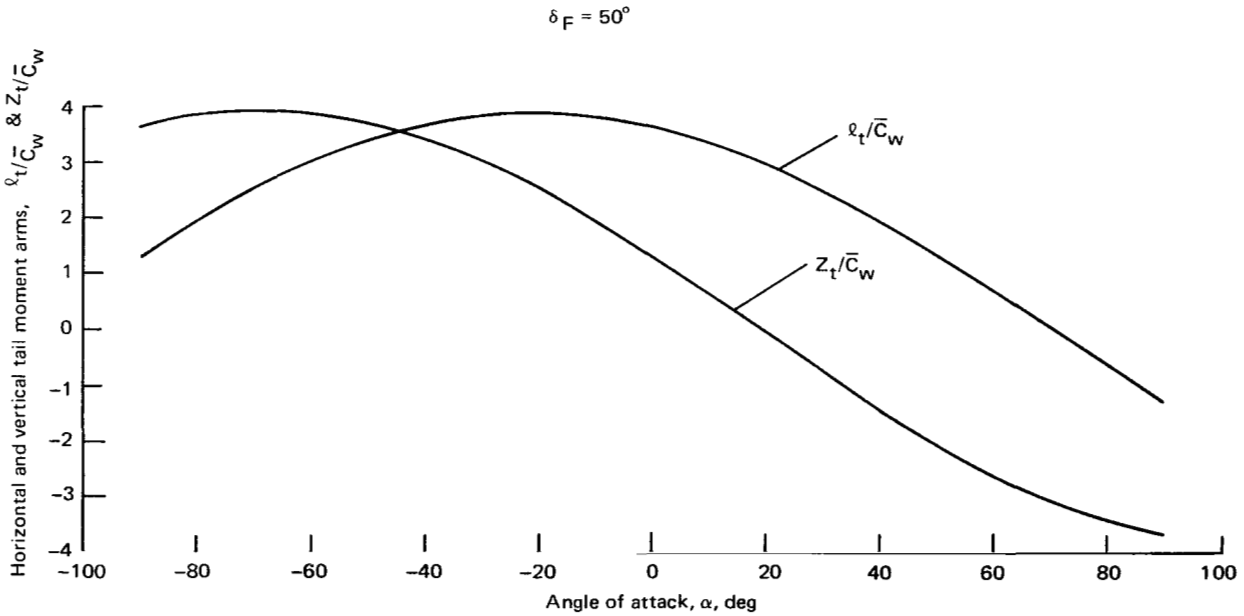

Figure 78.- Horizontal tail moment arms.

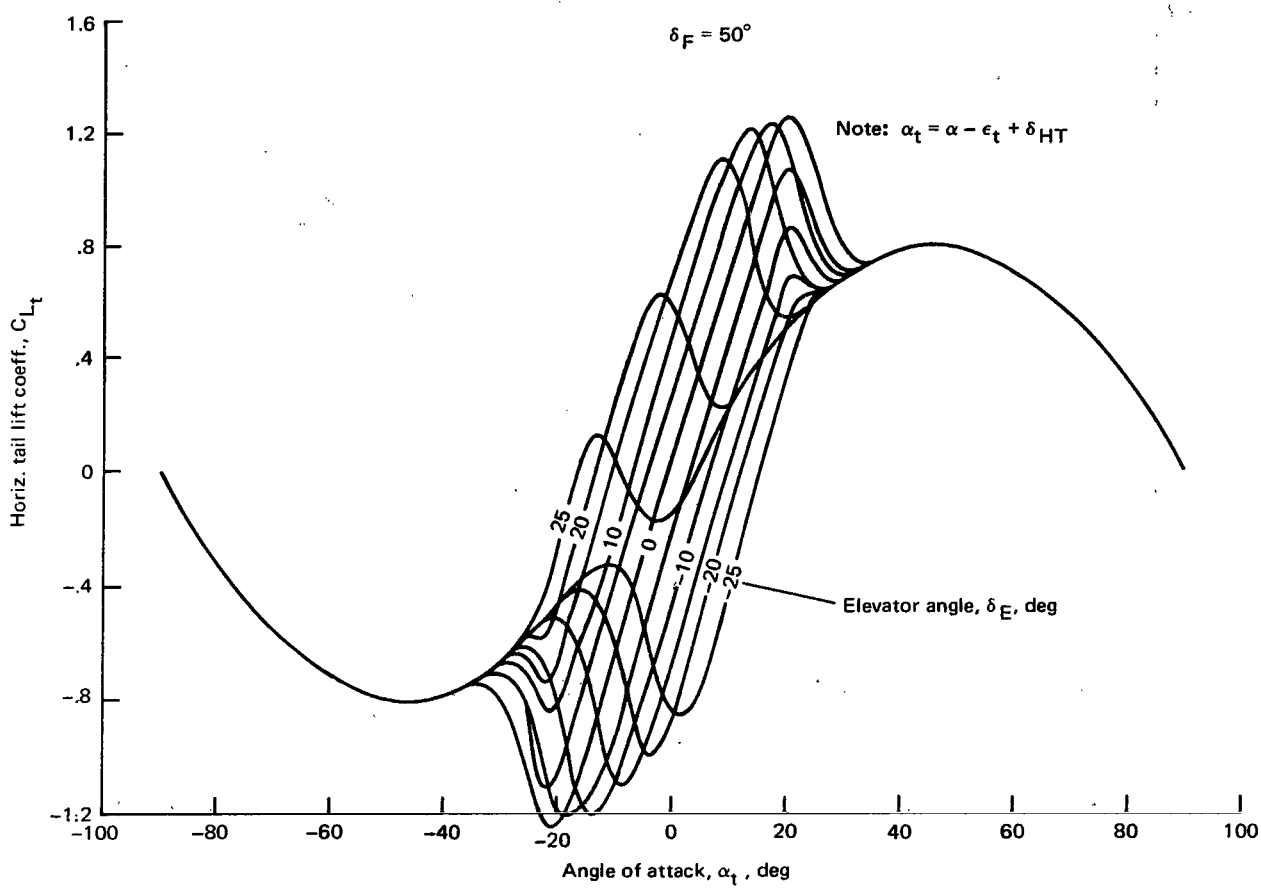

Figure 79.- Estimated horizontal tail lift coefficient (based on horizontal tail area).

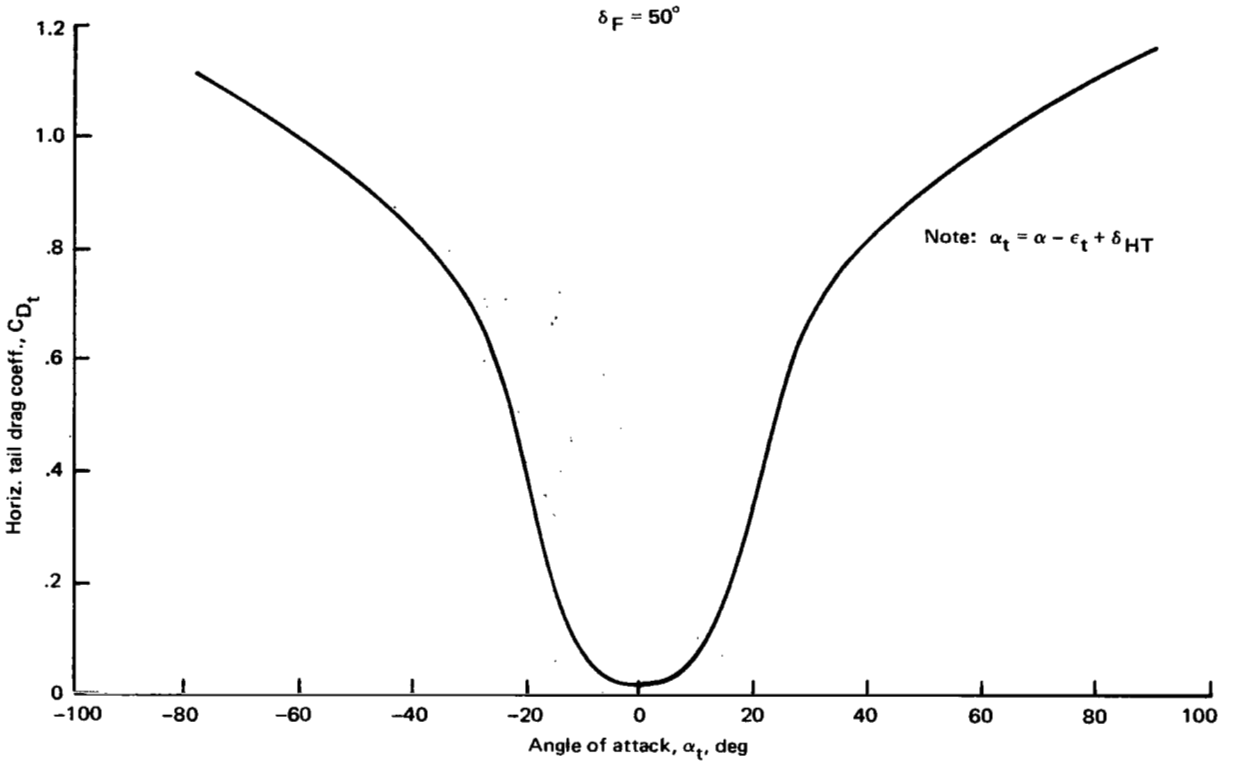

Figure 80.- Estimated horizontal tail drag coefficient (based on horizontal tail area).

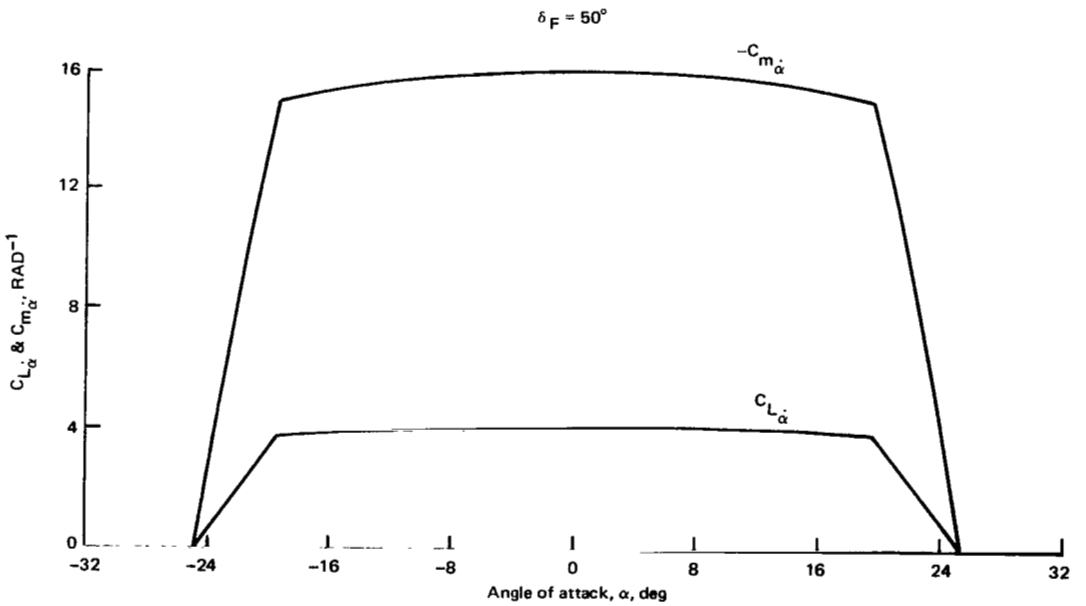

Figure 81.- Estimated lift and pitching-moment coefficients due to $\dot\alpha$.

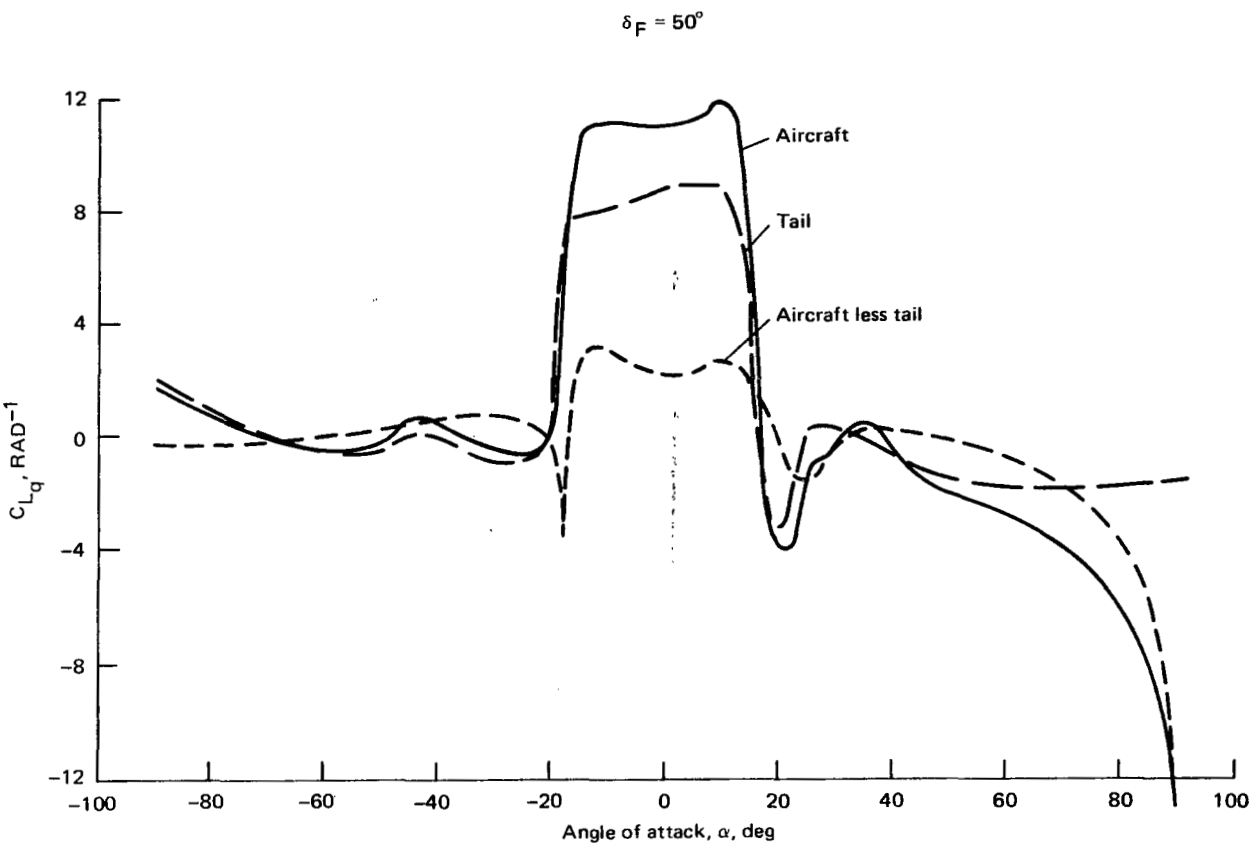

Figure 82.- Estimated lift coefficient due to pitch rate.

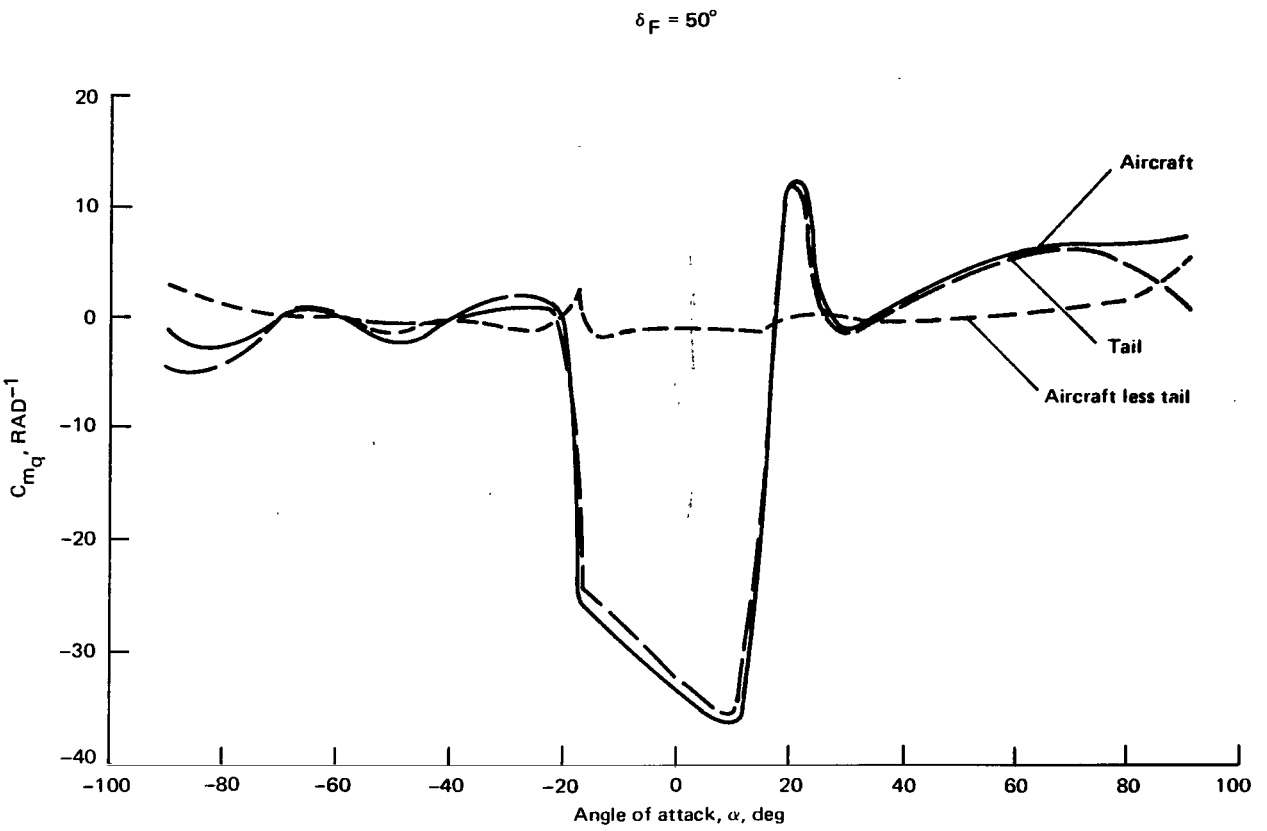

Figure 83.- Estimated pitching-moment coefficient due to pitch rate.

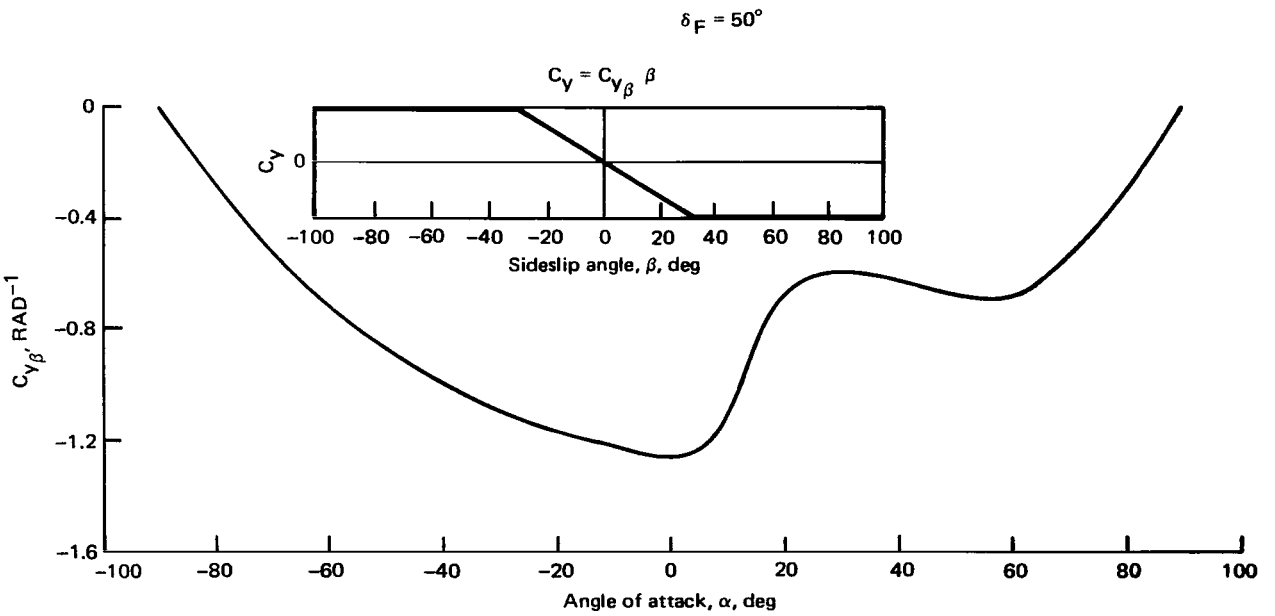

Figure 84.- Estimated sideforce coefficient due to sideslip.

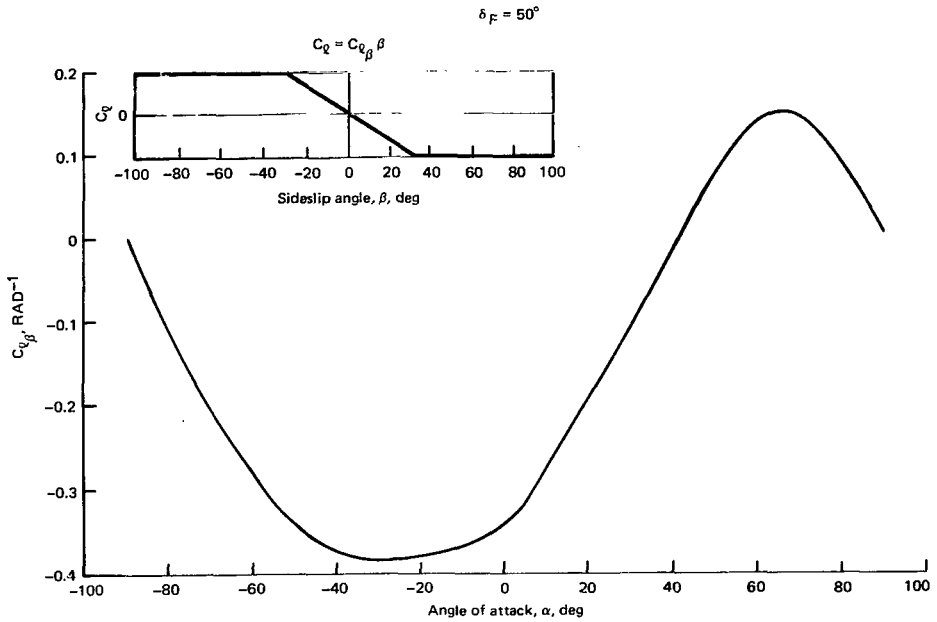

Figure 85.- Estimated rolling-moment coefficient due to sideslip.

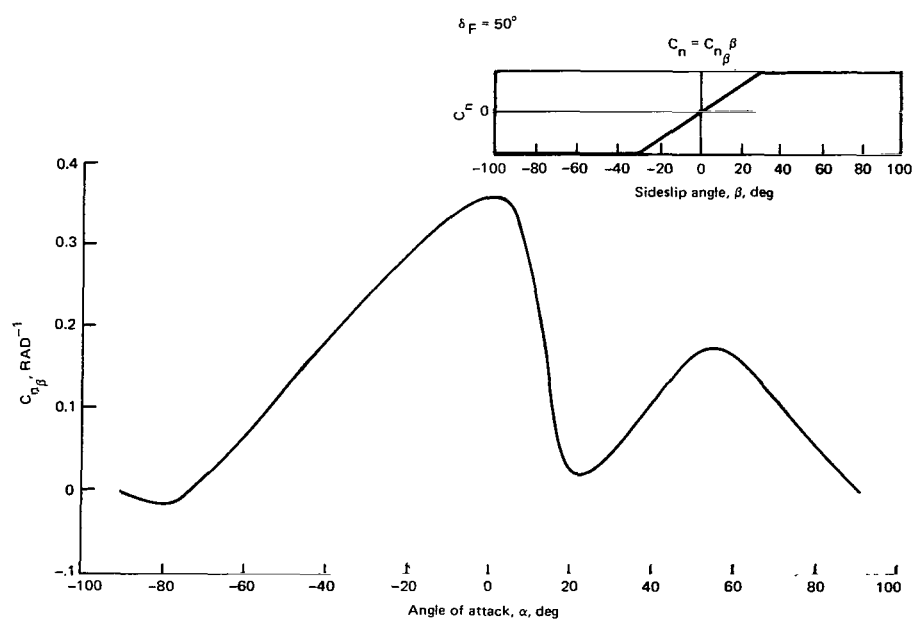

Figure 86.- Estimated yawing-moment coefficient due to sideslip.

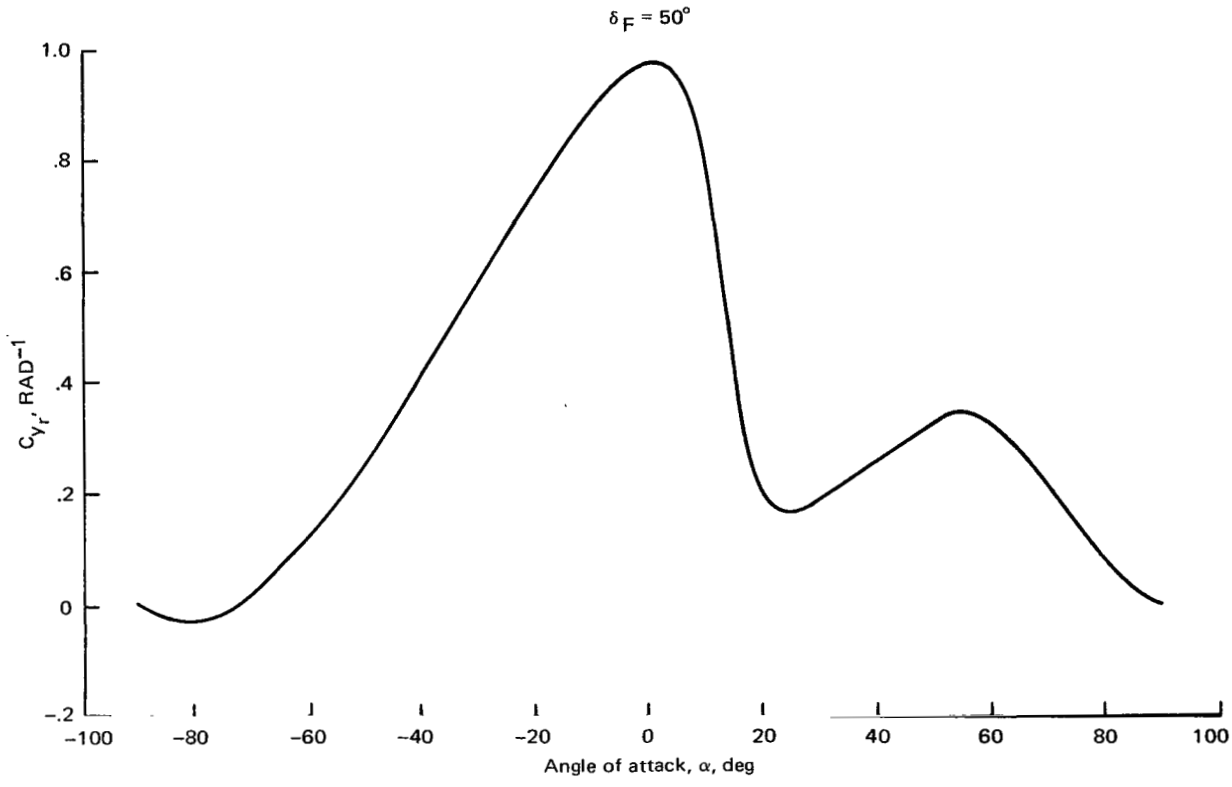

Figure 87.- Estimated sideforce coefficient due to yaw rate.

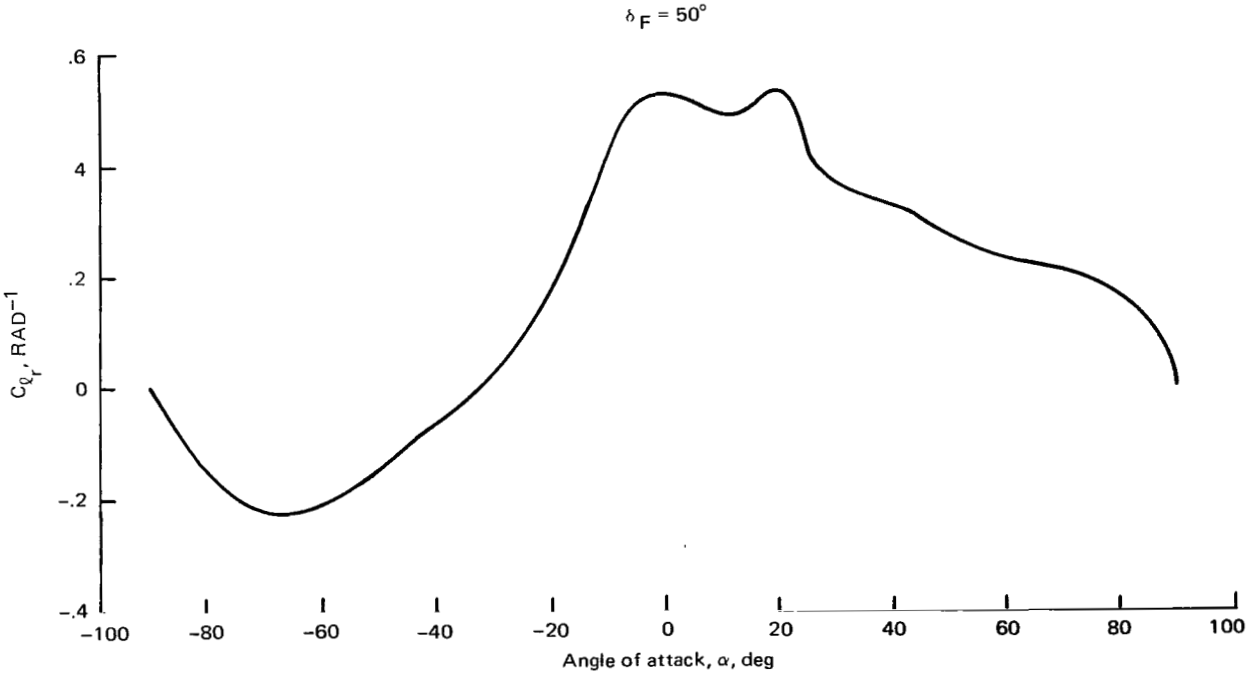

Figure 88.- Estimated rolling-moment coefficient due to yaw rate.

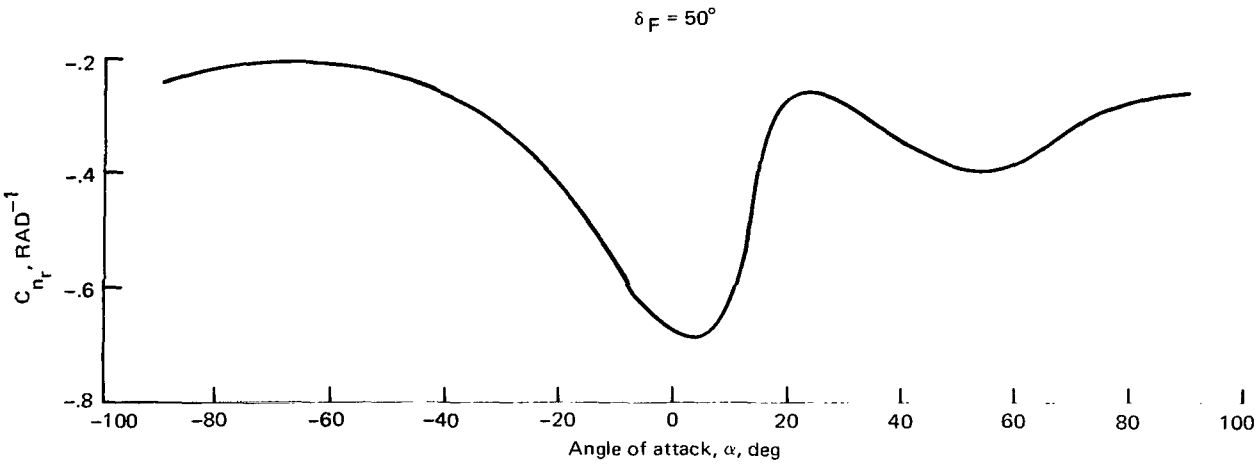

Figure 89.- Estimated yawing-moment coefficient due to yaw rate.

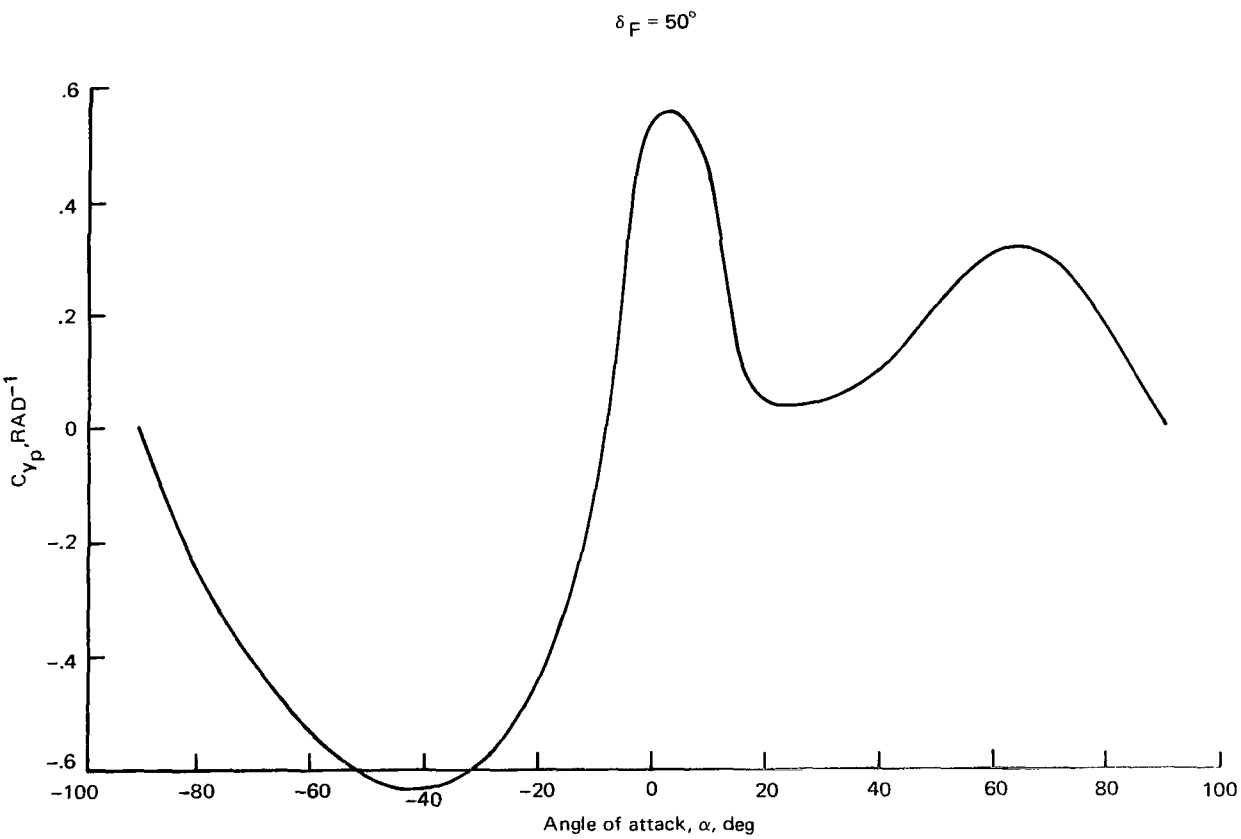

Figure 90.- Estimated sideforce coefficient due to roll rate.

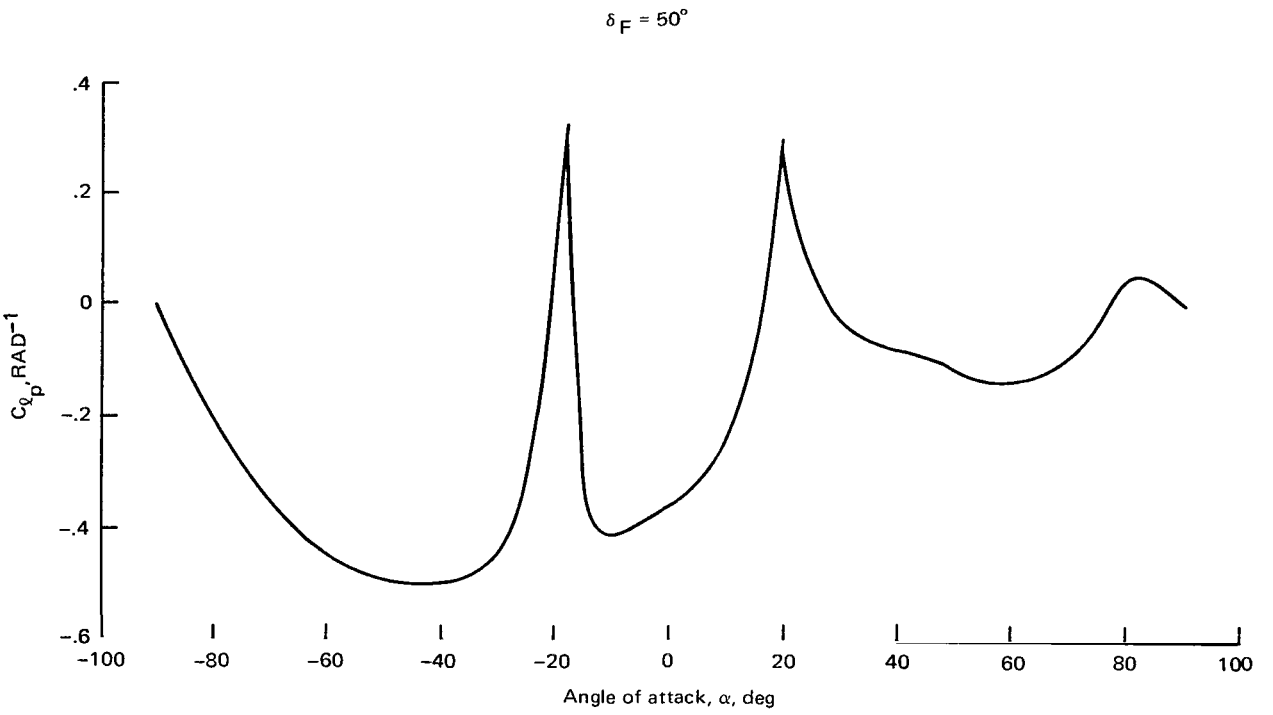

Figure 91.- Estimated rolling-moment coefficient due to roll rate.

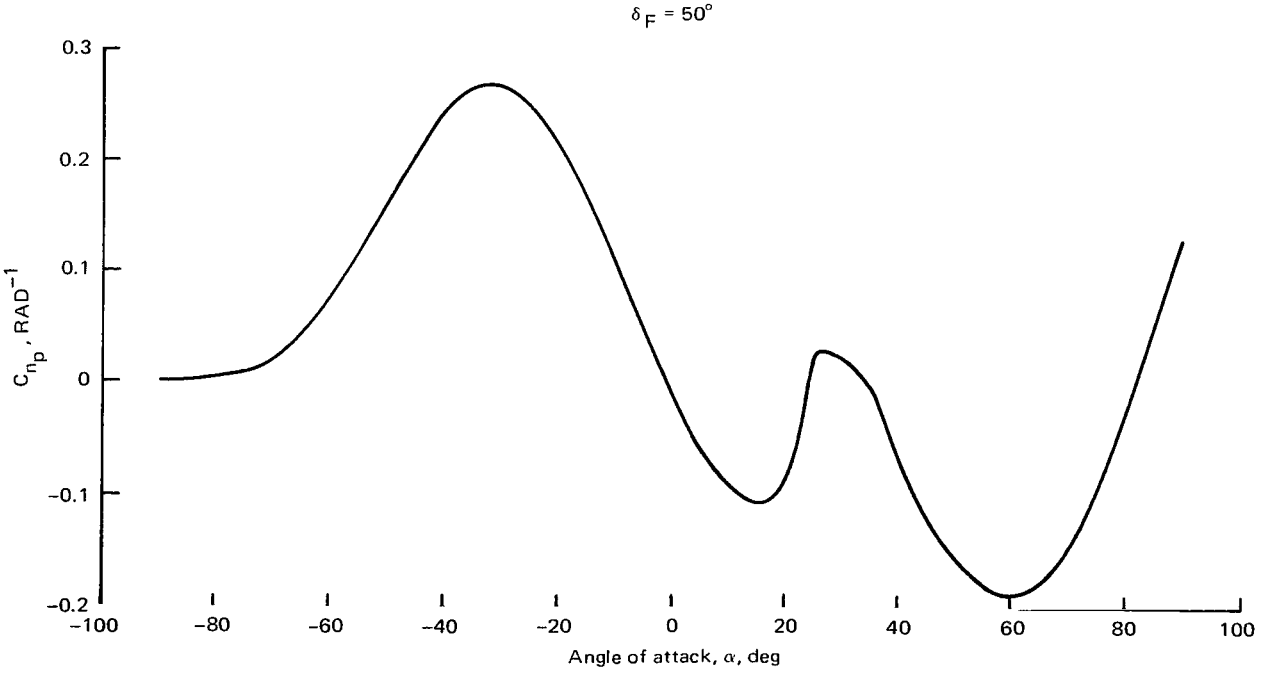

Figure 92.- Estimated yawing-moment coefficient due to roll rate.

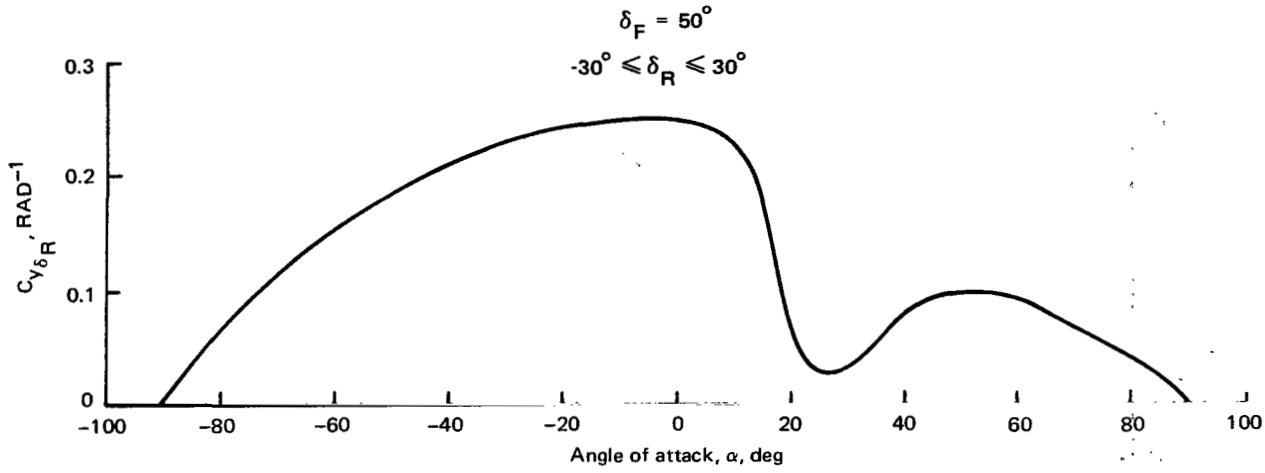

Figure 93.- Estimated sideforce coefficient due to rudder.

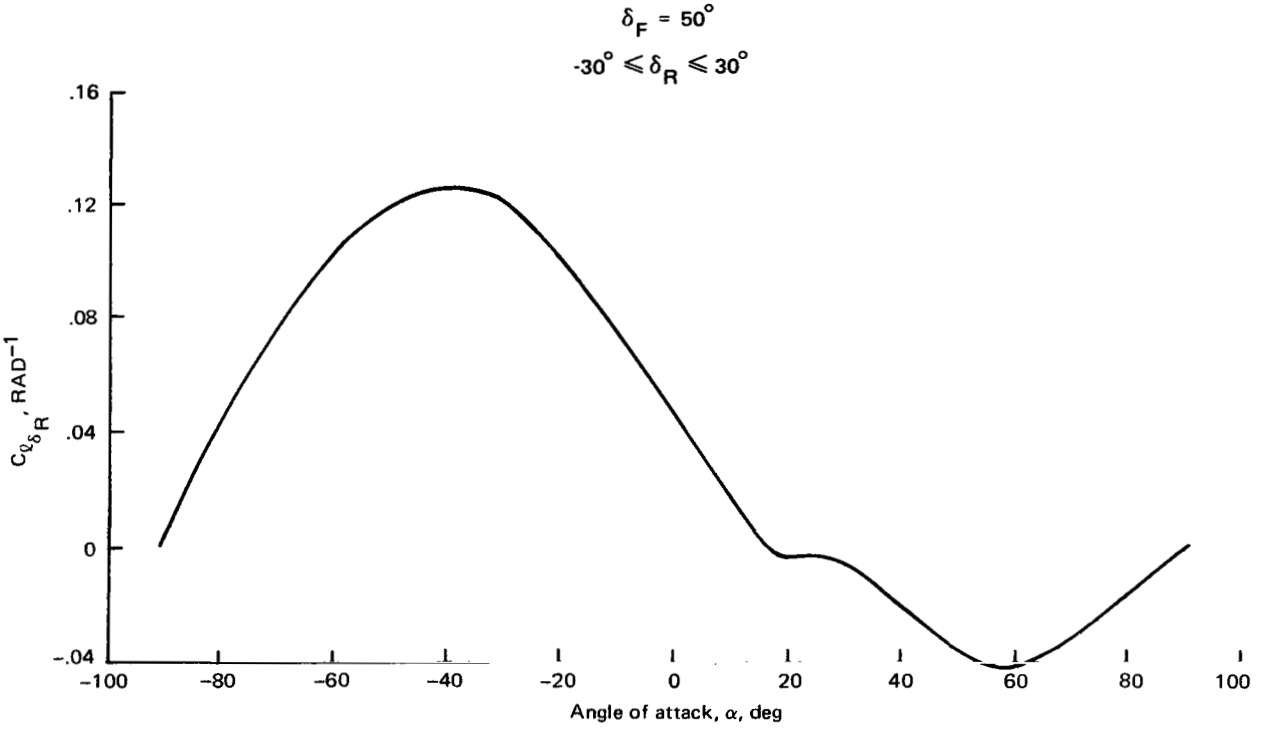

Figure 94.- Estimated rolling-moment coefficient due to rudder.

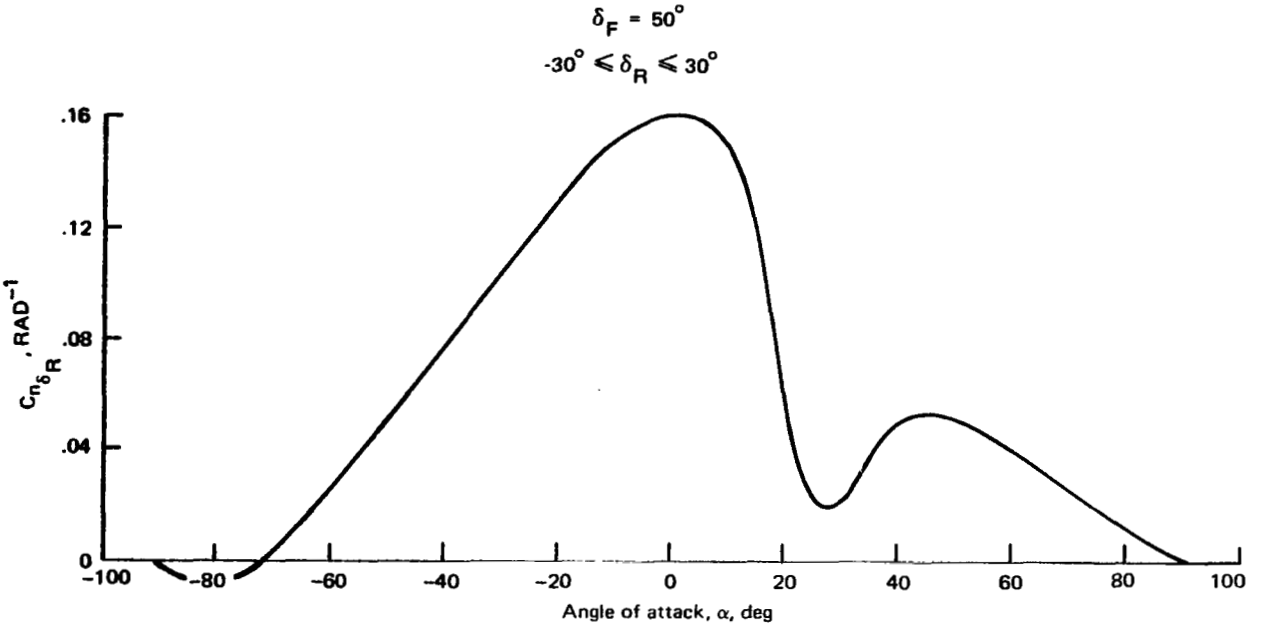

Figure 95.- Estimated yawing-moment coefficient due to rudder.

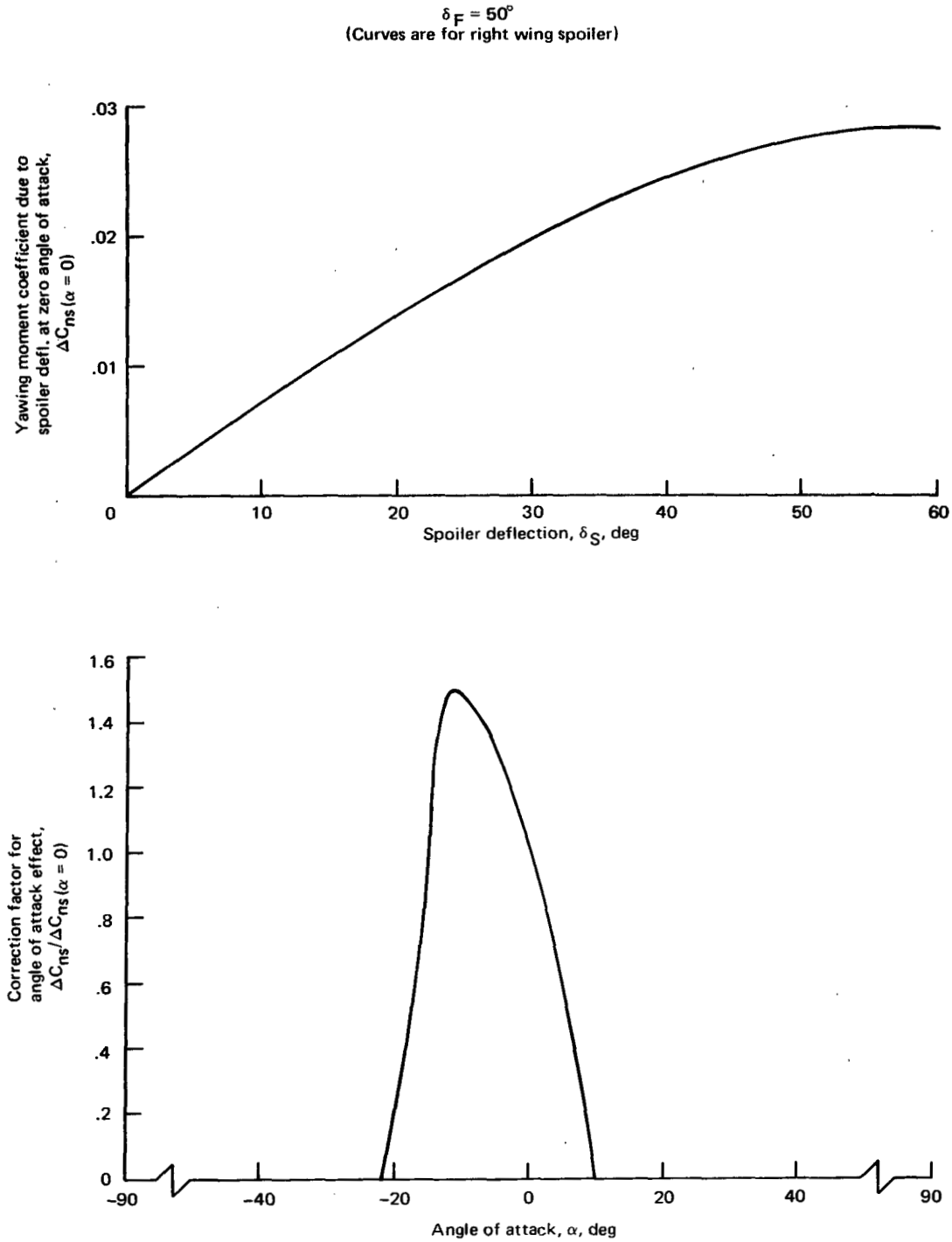

Figure 96.- Estimated yawing-moment coefficient due to spoiler deflection.

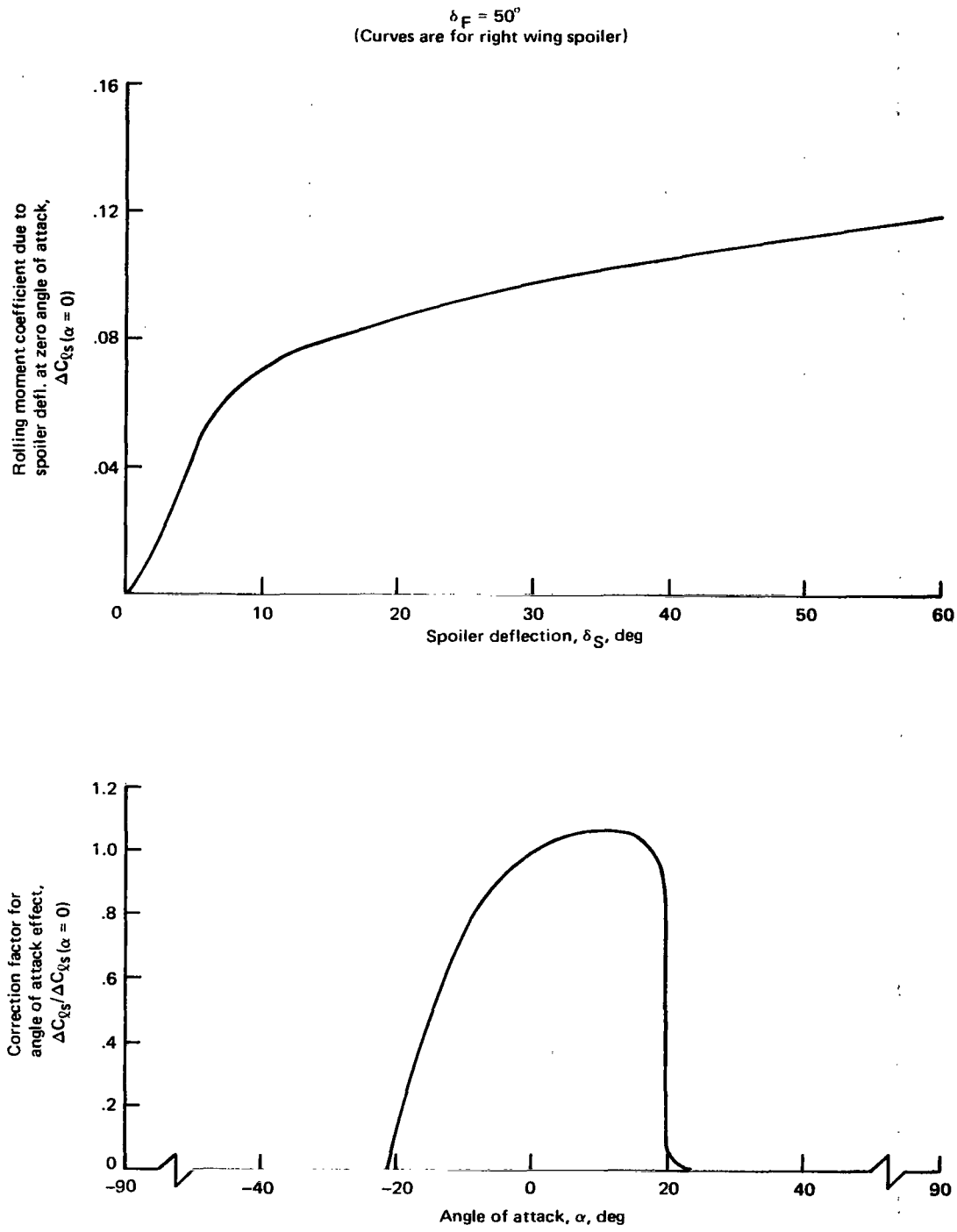

Figure 97.- Estimated rolling-moment coefficient due to spoiler deflection.

TABLE 31.- AERODYNAMIC COEFFICIENTS FOR ANGLES OF ATTACK GREATER THAN 90°

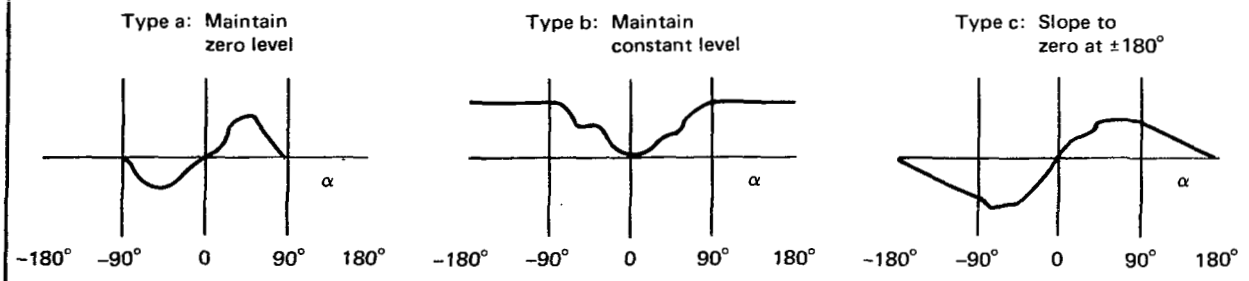

Figure	Type	Figure	Type	Figure	Type
73	a	81	a	89	b
74	b	82	b	90	a
75	c	83	b	91	a
76	b	84	a	92	a
77	a	85	a	93	a
78	c	86	a	94	a
79	a	87	a	95	a
80	b	88	a		

TABLE 32.- AERODYNAMIC EFFECT OF LANDING GEAR (INCLUDING DOORS)

Parameter	Symbol	Value
Drag increment due to gear	$\Delta C_{D_{lg}}$	0.0255
Pitching-moment increment due to gear	$\Delta C_{M_{lg}}$	.055

The equations needed to compute the total aerodynamic forces and moments, in stability axes, are given in table 33, along with the equations needed to transform these forces and moments to body axes. Note that the equations contain angular velocities (p_{ST}, q_{ST}, and r_{ST}) relative to air mass. These velocities are the sums of the inertial velocities, computed from the equations of motion, and the wind and turbulence velocities.

The airplane dimensions used in the force and moment equations are given in table 1.

TABLE 33.- EQUATIONS USED TO CALCULATE AERODYNAMIC FORCES AND MOMENTS

$$X_{ST} = -\frac{\rho V_a^2 S_w}{2}\left(C_{DTO} + \eta_t \frac{S_t}{S_w} C_{Dt} + \Delta C_{D_{lg}}\right)$$

$$Y_{ST} = \frac{\rho V_a^2 S_w}{2}\left[C_{Y_\beta}\beta + \frac{b_w}{2V_a}\left(C_{Y_r} r_{ST} + C_{Y_p} p_{ST}\right) + C_{Y_{\delta_R}}\delta_R\right]$$

$$Z_{ST} = -\frac{\rho V_a^2 S_w}{2}\left[C_{LTO} + \eta_t \frac{S_t}{S_w} C_{Lt} + \frac{\bar{c}_w}{2V_a}\left(C_{L_q} q_{ST} + C_{L_{\dot{\alpha}}}\dot{\alpha}\right)\right]$$

$$L_{ST} = \frac{\rho V_a^2 S_w b_w}{2}\left[C_{l_\beta}\beta + \frac{b_w}{2V_a}\left(C_{l_r} r_{ST} + C_{l_p} p_{ST}\right) + C_{l_{\delta_R}}\delta_R + \Delta C_{l_s}\right]$$

$$M_{ST} = \frac{\rho V_a^2 S_w \bar{c}_w}{2}\left[C_{MTO} - \frac{l_t S_t}{\bar{c}_w S_w}\eta_t C_{L_t} + \frac{Z_t S_t}{\bar{c}_w S_w}\eta_t C_{Dt} + \Delta C_{m_{lg}} + \frac{\bar{c}_w}{2V_a}\left(C_{m_q} q_{ST} + C_{m_{\dot{\alpha}}}\dot{\alpha}\right)\right]$$

$$N_{ST} = \frac{\rho V_a^2 S_w b_w}{2}\left[C_{n_\beta}\beta + \frac{b_w}{2V_a}\left(C_{n_r} r_{ST} + C_{n_p} p_{ST}\right) + C_{n_{\delta_R}}\delta_R + \Delta C_{n_s}\right]$$

APPENDIX E — APPROACH PATH EQUATIONS

NOMENCLATURE FOR APPENDIX E

h_A	reference altitude at point A
$\dot{h}_A$	first time derivative of h_A
h_H	reference altitude of point H
h_R	reference altitude at ground-range R
$\dot{h}_R$, $\ddot{h}_R$	first and second time derivatives of h_R
$\ddot{h}_{max}$	reference maximum vertical acceleration
R_A	ground range of point A
R_B	ground range of point B
R_C	ground range of point C
R	ground range
t	time to hover point H
t_A	time from point A to point H
t_B	time from point B to point H
t_C	time from point C to point H
V_{XR}	reference horizontal velocity
$\dot{V}_{XR}$	reference horizontal acceleration
$\dot{V}_{X_{max}}$	reference maximum horizontal acceleration
V_{XA}	initial horizontal velocity
γ_A	initial flight-path angle
Δt_F	time from point F to point C

The types of approach used in the simulation are described in "Scope of Piloted Simulation" (see figs. 35-38). The horizontal and vertical acceleration profiles indicated in figure 35 are shown in detail in figures 98 and 99, respectively. These profiles were integrated twice, first to find the velocities and then the positions. The resulting equations are given in table 34.

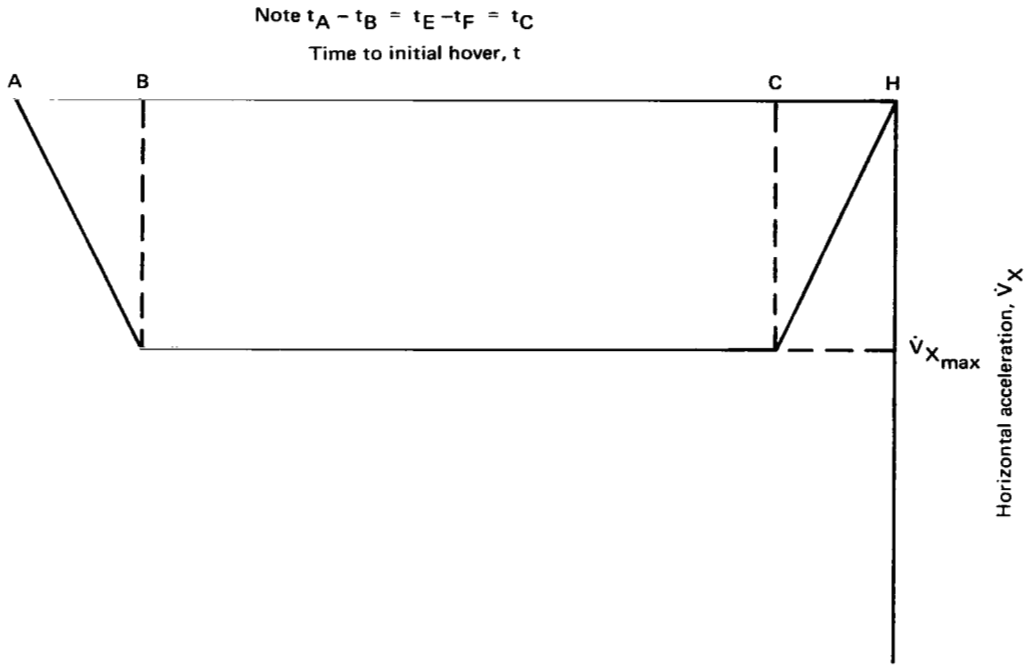

Figure 98.- Horizontal acceleration profile.

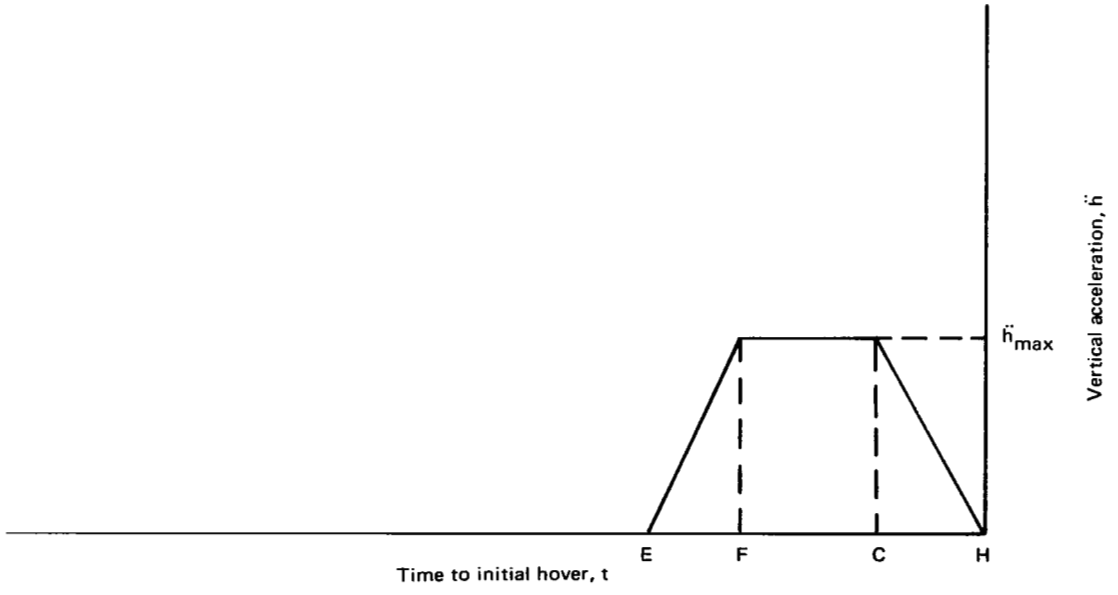

Figure 99.- Vertical acceleration profile.

TABLE 34.- APPROACH PATH EQUATIONS
(a) Parameter equations.

Parameter	Curved approach (input quantities V_{XA}, γ_A, $\dot{h}_A$, $\ddot{h}_{max}$, h_H, t_C)	Straight approach (input quantities V_{XA}, γ_A, $\dot{V}_{X_{max}}$, h_H, t_C)
$\dot{h}_A$ =	$V_{XA} \tan \gamma_A$	
$\ddot{h}_{max}$ =	Input	$\dot{V}_{X_{max}} \tan \gamma_A$
Δt_F =	$-\frac{\dot{h}_A}{\ddot{h}_{max}} - t_C$	$t_B - t_C$
t_A =	$\frac{-[h_A - h_H + \ddot{h}_{max}(t_C^2 + \frac{3}{2} t_C \Delta t_F + \frac{1}{2} \Delta t_F^2)]}{\dot{h}_A}$	$t_B + t_C$
t_B =	$t_A - t_C$	$-\frac{V_{XA}}{\dot{V}_{X_{max}}}$
h_A =	Input	$h_H - \frac{t_A \dot{h}_A}{2}$
$\dot{V}_{X_{max}}$ =	$-\frac{V_{XA}}{t_B}$	Input
R_C =	$-\frac{\dot{V}_{X_{max}} t_C^2}{6}$	
R_B =	$-\frac{\dot{V}_{X_{max}} [t_C^2 + 3t_B(t_B - t_C)]}{6}$	
R_A =	$-\frac{\dot{V}_{X_{max}} t_B(t_B + t_C)}{2}$	

TABLE 34.- Concluded
(b) Final equations.

$R > R_A$	$R_A \geq R > R_B$	$R_B \geq R > R_C$	$R_C \geq R > 0$	$0 > R$
$t = \frac{(t_B + t_C)}{2} - \frac{R}{\dot{V}_{X_{max}} t_B}$	$t = t_B + t_C - 2\sqrt{t_B t_C}\cos\left(\frac{\pi + \phi}{3}\right)$ $\cos\phi = \frac{\dot{V}_{X_{max}}(6t_B t_C^2 - t_C^3) + (R - R_B)6t_C}{2\dot{V}_{X_{max}}(2t_B t_C)^{3/2}}$	$t = \frac{t_C\sqrt{\frac{-8R}{\dot{V}_{X_{max}}} - \frac{t_C^2}{3}}}{2}$	$t = \left(\frac{-6t_C R}{\dot{V}_{X_{max}}}\right)^{1/3}$	$t = -1$
$\dot{V}_{XR} = 0$	$\dot{V}_{XR} = \frac{\dot{V}_{X_{max}}(t_B + t_C - t)}{t_C}$	$\dot{V}_{XR} = \dot{V}_{X_{max}}$	$\dot{V}_{XR} = \frac{\dot{V}_{X_{max}} t}{t_C}$	$\dot{V}_{XR} = 0$
$V_{XR} = -\dot{V}_{X_{max}} t_B$	$V_{XR} = \frac{\dot{V}_{X_{max}}}{2}\left[(t_C - 2t_B) + \frac{(t - t_B)(t - t_B - 2t_C)}{t_C}\right]$	$V_{XR} = \dot{V}_{X_{max}}\left(\frac{t_C}{2} - t\right)$	$V_{XR} = \frac{-\dot{V}_{X_{max}} t^2}{2t_C}$	$V_{XR} = 0$

$t > 2t_C + \Delta t_F$	$2t_C + \Delta t_F \geq t > t_C + \Delta t_F$	$t_C + \Delta t_F \geq t > t_C$	$t_C \geq t > 0$	$t \leq 0$
$\ddot{h}_R = 0$	$\ddot{h}_R = \frac{\ddot{h}_{max}}{t_C}(2t_C + \Delta t_F - t)$	$\ddot{h}_R = \ddot{h}_{max}$	$\ddot{h}_R = \frac{\ddot{h}_{max} t}{t_C}$	$\ddot{h}_R = 0$
$\dot{h}_R = \dot{h}_A = -\ddot{h}_{max}(t_C + \Delta t_F)$	$\dot{h}_R = -\left[\ddot{h}_{max}\left(\Delta t_F + \frac{t_C}{2}\right) + \frac{\ddot{h}_{max}}{2t_C}(t - t_C - \Delta t_F)(-t + 3t_C + \Delta t_F)\right]$	$\dot{h}_R = -\ddot{h}_{max}\left(t - \frac{t_C}{2}\right)$	$\dot{h}_R = \frac{-\ddot{h}_{max} t^2}{2t_C}$	$\dot{h}_R = 0$
$h_R = h_H - \ddot{h}_{max}(t_C^2 + \frac{3}{2} t_C \Delta t_F + \frac{1}{2}\Delta t_F^2) - \dot{h}_A t$	$h_R = h_H + \frac{\ddot{h}_{max}}{6}(t_C^2 + 3t_C\Delta t_F + 3\Delta t_F^2) + \frac{\ddot{h}_{max}}{6t_C}(t - t_C - \Delta t_F)[-t^2 + t(5t_C + 2\Delta t_F) - t_C^2 + t_C\Delta t_F - \Delta t_F^2]$	$h_R = h_H + \frac{\ddot{h}_{max}}{6}[t_C^2 + 3(t - t_C)t]$	$h_R = h_H + \frac{\ddot{h}_{max} t^3}{6t_C}$	$h_R = h_H$

APPENDIX F — SIMULATOR MOTION DRIVE LOGIC

NOMENCLATURE FOR APPENDIX F

$A_{IC_{x,y,z}}$	initial conditions (IC) of simulator x, y, and z
$A_{SD_{x,y,z}}$	simulator x, y, and z commands (including IC)
$\ddot{A}_{SD_{x,y,z}}$	simulator drive accelerations used to calculate load factors along x, y, and z axes
$A_{S_{x,y,z}}$	desired simulator x, y, and z (excluding IC)
$\dot{A}_{S_{x,y,z}}$	desired simulator $\dot{x}$, $\dot{y}$, and $\dot{z}$
$\ddot{A}_{TS_{x,y,z}}$	equivalent translational acceleration along x, y, and z axes
$A_{FU_{x,y,z}}$	simulator position (from cab or computer) along x, y, and z axes
$\ddot{A}_{x,y,z}$	calculated earth-axes accelerations at the pilot station along x, y, and z axes (inputs to high-pass filter)
$\ddot{A}_{CH_{x,y,z}}$	output of high-pass filter (multiplied by gains $K_{x,y,z}$) along x, y, and z axes
$\ddot{A}_{CN_{x,y,z}}$	gravitational accelerations due to cab residual tilt along x, y, and z axes
$A_{ML_{x,y,z}}$	limits of x, y, and z
$\dot{A}_{ML_{x,y,z}}$	limits of $\dot{x}$, $\dot{y}$, and $\dot{z}$
$\ddot{A}_{ML_{x,y,z}}$	limits of $\ddot{x}$, $\ddot{y}$, and $\ddot{z}$
$A_{IC_{\phi,\theta,\psi}}$	initial conditions (IC) of simulator ϕ, θ, and ψ
$A_{SD_{\phi,\theta,\psi}}$	simulator ϕ, θ, and ψ commands (including IC)
$A_{S_{\phi,\theta,\psi}}$	desired simulator ϕ, θ, and ψ (excluding IC)
$\ddot{A}_{\phi,\theta,\psi}$	calculated body-axes accelerations at pilot station for ϕ, θ, and ψ rotations (input to high-pass filter)

$\dot{A}_{N_{\phi,\theta,\psi}}$	output of high-pass filter (multiplied by gains $K_{\phi,\theta,\psi}$) for ϕ, θ, and ψ rotations
$\dot{A}_{CN_{\phi,\theta,\psi}}$	$\dot{\phi}$, $\dot{\theta}$, and $\dot{\psi}$ of simulator cab from high-pass filter
$A_{CL_{\phi,\theta}}$	ϕ and θ due to residual cab tilt
$\dot{A}_{CL_{\phi,\theta}}$	$\dot{\phi}$ and $\dot{\theta}$ due to residual cab tilt
$A_{ML_{\phi,\theta,\psi}}$	limits of ϕ, θ, and ψ
$\dot{A}_{ML_{\phi,\theta,\psi}}$	limits of $\dot{\phi}$, $\dot{\theta}$, and $\dot{\psi}$
g	acceleration due to gravity
$K_{x,y,z}$	washout gains for x, y, and z axes
$K_{LL_{x,y}}$	low-frequency gains, residual tilt for x and y axes
$K_{O_{x,y,z}}$	gains for modifying calculated gravitational acceleration components corresponding to residual tilt for x, y, and z axes
$K_{N_{x,y,z}}$	gains for modifying contribution of gravitational accelerations to required simulator translational accelerations for x, y, and z axes
$K_{\phi,\theta,\psi}$	washout gains for ϕ, θ, and ψ rotations
TM_{ij} $(i,j = 1,2,3)$	transformation between cab-fixed axes and earth-fixed axes
x, y, z	cab position relative to earth-fixed axes; also used to designate translational axes
$\zeta_{H_{xi,yi,zi}}$ $(i = 1,2)$	high-pass washout filter damping factors for x, y, and z axes
$\zeta_{H_{\phi i,\theta i,\psi i}}$ $(i = 1,2)$	high-pass washout filter damping factors for ϕ, θ, and ψ rotations
$\zeta_{D_{x,y,z}}$	long-term filter damping factors for x, y, and z axes
$\eta_{C_{x,y}}$	load factors along x and y axes
$\eta_{CLL_{x,y}}$	load factor contributions produced by residual tilt

$\omega_{H_{xi,yi,zi}}$ $(i = 1,2)$	high-pass washout filter undamped frequencies for x, y, and z axes
$\omega_{H_{\phi i,\theta i,\psi i}}$ $(i = 1,2)$	high-pass washout filter undamped frequencies for ϕ, θ, and ψ rotations
$\omega_{D_{x,y,z}}$	long-term filter undamped frequencies for x, y, and z axes
$\omega_{L_{x,y}}$	factors used in residual tilt calculations
$\omega_{E_{\phi,\theta,\psi}}$	gains multiplying contribution to required $\dot{\phi}$, $\dot{\theta}$, and $\dot{\psi}$ of error between cab position and required residual tilt
ϕ, θ, ψ	Euler angles used to orient cab relative to earth-fixed axes; Euler angle sequence is θ, ψ, and ϕ. Also used to designate roll, pitch, and yaw rotations

The motion drive logic is designed to convert the calculated motion of the simulated aircraft into drive signals that move the simulator cab, within its physical limits, so that the combined effects of cab acceleration and gravity subject the pilot to forces that are the best approximation to those he would experience flying the real aircraft. The "best approximation" is that which gives the best representation of those forces that provide the pilot with motion cues and that therefore can influence his control of the aircraft.

The motion drive logic is shown in figures 100 and 101. The inputs are the calculated accelerations at the pilot station ($\ddot{A}_{x,y,z}$ and $\ddot{A}_{\phi,\theta,\psi}$) and the actual position of the simulator cab ($A_{FU_{x,y,z}}$). The output is the required cab position ($A_{SD_{x,y,z}}$, $A_{SD_{\phi,\theta,\psi}}$). As shown in figures 100 and 101, the calculated aircraft accelerations at the pilot station are passed through fourth-order washout filters, which strongly attenuate the low-frequency components while they allow the high-frequency components to pass virtually unchanged. If the low-frequency components of acceleration were passed unattenuated to the simulator drive system, they would quickly cause the cab to move to its position limits. To recover the motion cues associated with the low-frequency translational accelerations, the cab is rotated (residual tilt) so that gravity provides components of force, acting on the pilot, roughly equivalent to the calculated low-frequency translational inertial forces. This residual tilt technique can be used only for force compensation in the horizontal plane and must be accomplished at cab rotational accelerations sufficiently low to be undetectable to the pilot. The residual tilt is calculated as shown in figure 101, and its degree is controlled through parameters ω_{L_k} and K_{LL_k} ($k = x,y$).

The cab rotational commands, A_{SD_i} ($i = \phi,\theta,\psi$), from the motion drive logic, contain some high-frequency components that, if uncompensated, would produce false translational motion cues, through the effects of gravity. These spurious motion cues are removed by cab translational accelerations so that the corresponding inertial forces cancel the unwanted high-frequency gravitational forces, but not the low-frequency (residual tilt) gravitational forces. This type of compensation is produced in computations such as shown at the top of figure 100, and its degree is controlled by parameters K_{O_j} and K_{N_j} ($j = x,y,z$).

The signals resulting from the calculations described above may still contain some residual low-frequency translational acceleration components. To ensure that these acceleration components do not cause excessive cab translation, the translational velocities and positions derived from accelerations $\ddot{A}_{TS_j}$ ($j = x,y,z$) are passed through second-order washout (high-pass) filters (fig. 100).

Additional translational position limiting is provided to protect against inadvertently driving the simulator hard into its stops. For each translational axis, calculations are performed which continually determine the travel remaining in the direction of motion of the cab. This distance, the drive acceleration limits, computation frame time, and computed cab velocity are

used to determine whether the cab must be given additional deceleration to avoid contact with the stops. Deceleration commands from this logic are continued until both the commanded acceleration and velocity change sign. If this additional translation position-limiting logic becomes active during a simulation test, it will introduce spurious motion cues.

In setting up the simulation, the parameters of the motion drive logic are adjusted until the motion cues feel subjectively correct for the type of aircraft simulated and the type of task to be flown. The motion drive logic parameters used for the simulation described here are given in table 35.

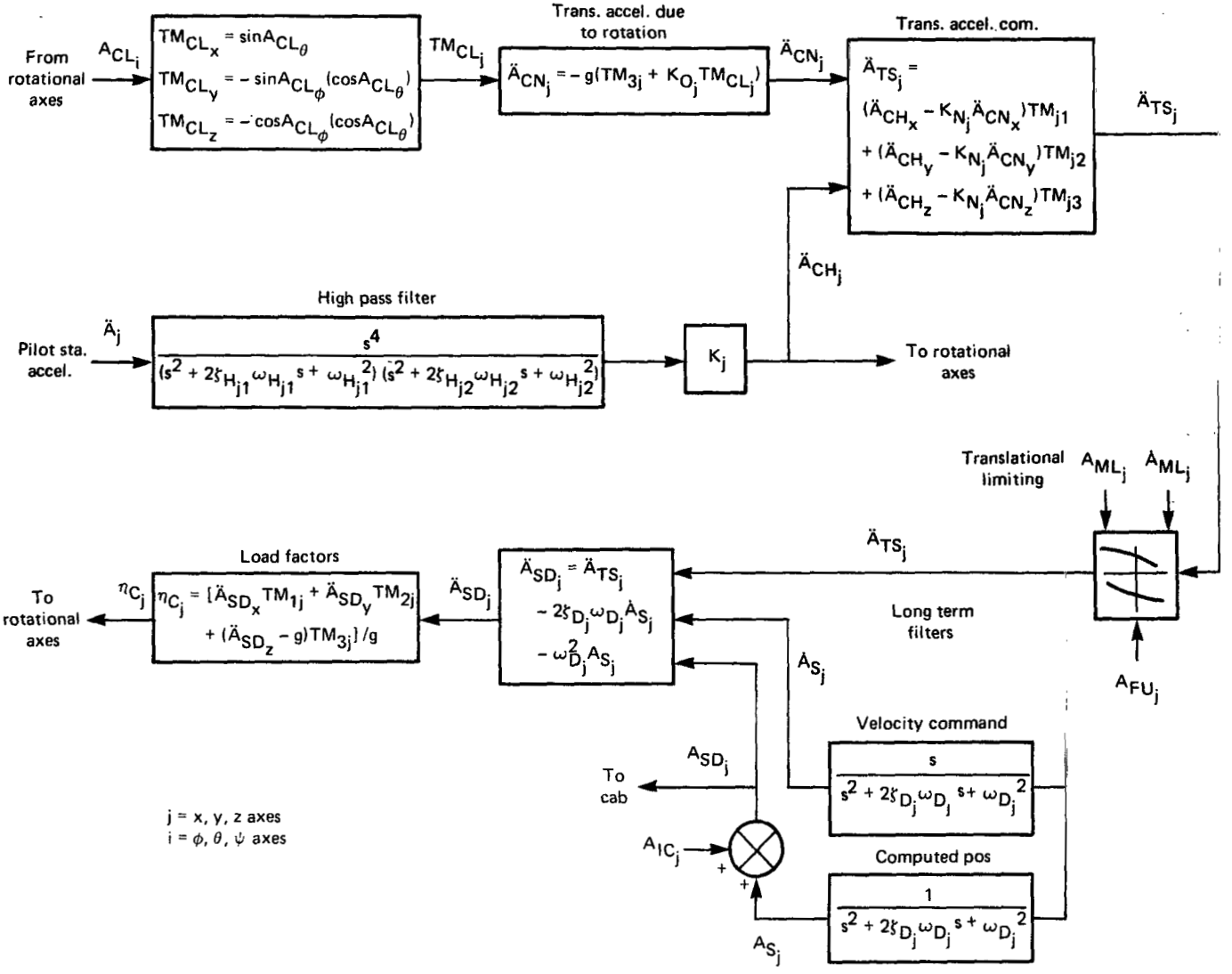

Figure 100.- Translational motion drive logic for S.01 simulator.

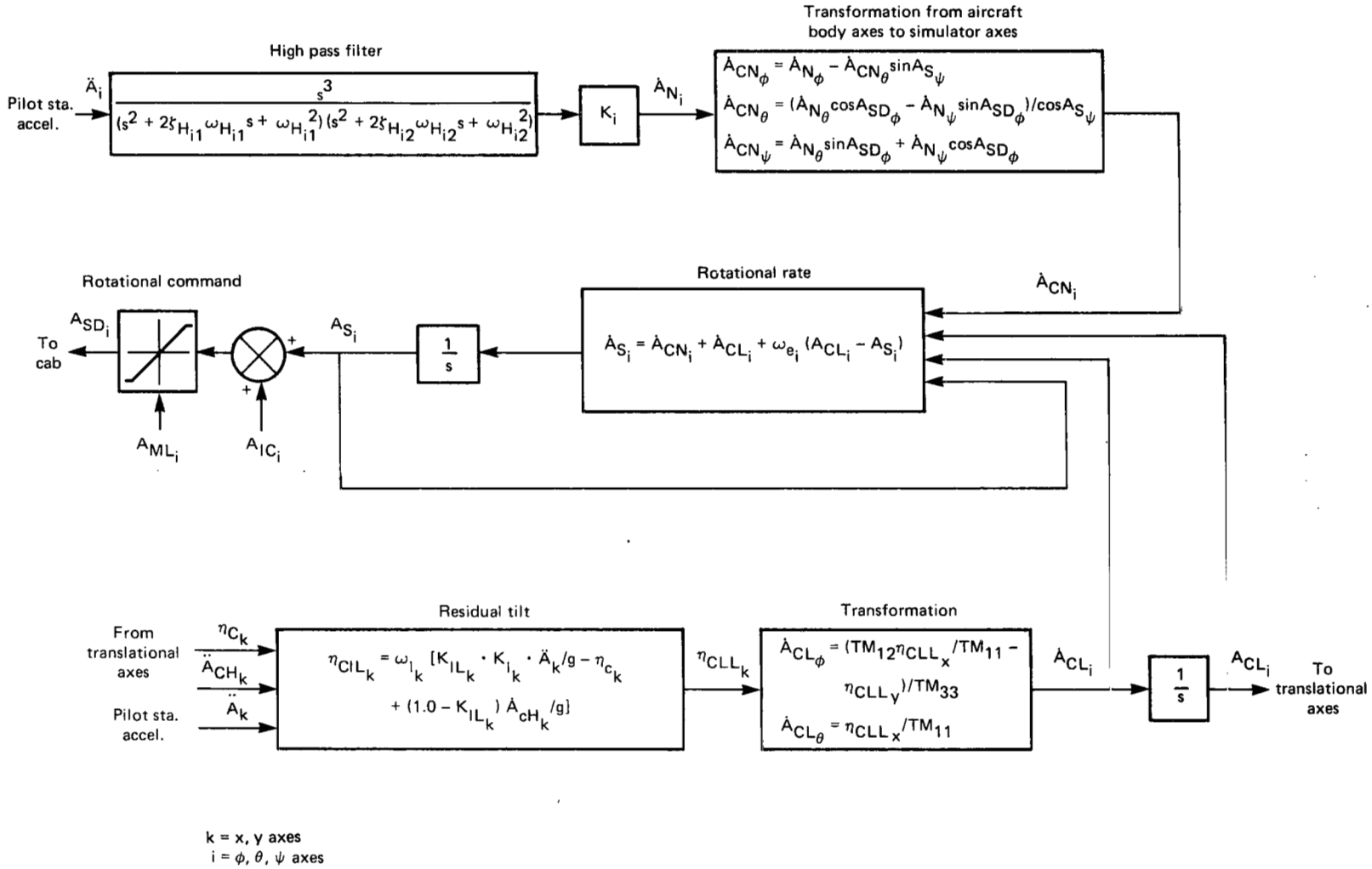

Figure 101.- Rotational motion drive logic for S.01 simulator.

TABLE 35.- COEFFICIENT VALUES FOR S.01 SIMULATOR MOTION DRIVE LOGIC

Symbol	Value	Units
$\omega_{H_{x1}}$, $\omega_{H_{x2}}$	0.4, 0.1	rad/sec
$\omega_{H_{y1}}$, $\omega_{H_{y2}}$	0.4, 0.1	rad/sec
$\omega_{H_{z1}}$, $\omega_{H_{z2}}$	0.4, 0.1	rad/sec
$\omega_{H_{\phi 1}}$, $\omega_{H_{\phi 2}}$	0.4, 0.4	rad/sec
$\omega_{H_{\theta 1}}$, $\omega_{H_{\theta 2}}$	0.4, 0.4	rad/sec
$\omega_{H_{\psi 1}}$, $\omega_{H_{\psi 2}}$	0.4, 0.4	rad/sec
$\zeta_{H_{x1}}$, $\zeta_{H_{x2}}$	1.4, 1.4	
$\zeta_{H_{y1}}$, $\zeta_{H_{y2}}$	1.4, 1.4	
$\zeta_{H_{z1}}$, $\zeta_{H_{z2}}$	1.4, 1.4	
$\zeta_{H_{\phi 1}}$, $\zeta_{H_{\phi 2}}$	1.4, 1.4	
$\zeta_{H_{\theta 1}}$, $\zeta_{H_{\theta 2}}$	1.4, 1.4	
$\zeta_{H_{\psi 1}}$, $\zeta_{H_{\psi 2}}$	1.4, 1.4	
K_x, K_y, K_z	0.5, 0.5, 0.5	
K_ϕ, K_θ, K_ψ	0.5, 0.5, 0.5	
ω_{L_x}, ω_{L_y}	2.0, 2.0	rad/sec
K_{LL_x}, K_{LL_y}	0.4, 1.0	
ω_{D_x}, ω_{D_y}, ω_{D_z}	0.3, 0.3, 0.3	rad/sec
ζ_{D_x}, ζ_{D_y}, ζ_{D_z}	0.707, 0.707, 0.707	
K_{N_x}, K_{N_y}, K_{N_z}	0, 1.0, 1.0	
K_{O_x}, K_{O_y}, K_{O_z}	1.0, 1.0, 1.0	
ω_{E_ϕ}, ω_{E_θ}, ω_{E_ψ}	0.5, 0.5, 0.5	rad/sec
$\ddot{A}_{ML_x}$, $\ddot{A}_{ML_y}$, $\ddot{A}_{ML_z}$	1.71, 2.07, 1.68	m/sec^2
$\dot{A}_{ML_x}$, $\dot{A}_{ML_y}$, $\dot{A}_{ML_z}$	2.59, 2.29, 2.13	m/sec
A_{ML_x}, A_{ML_y}, A_{ML_z}	2.44, 2.44, 2.44	m
$\dot{A}_{ML_\phi}$, $\dot{A}_{ML_\theta}$, $\dot{A}_{ML_\psi}$	1.2, 1.5, 2.8	rad/sec
A_{ML_ϕ}, A_{ML_θ}, A_{ML_ψ}	0.5326, 0.5326, 0.5326	rad

REFERENCES

1. Gerdes, Ronald M. and Hynes, Charles S.: Factors Affecting Handling Qualities of a Lift-Fan Aircraft During Steep Terminal Area Approaches. NASA TM X-62,424, April 1975.

2. Abramson, R.; and Cambell, J. E.: Lift Fan V/STOL Flight Control Systems Development, Vol. I, Flight Controls Analysis. NASA CR-114,584, Nov. 1972.

3. North American Rockwell: Lift Fan V/STOL Flight Control Systems Development, Vol. II, Simulation Experiment. NASA CR-114,585, June 1973.

4. McDonnell Aircraft Co.: Lift Fan V/STOL Transport Control System Investigation, Phase I, Analytical Study. NASA CR-114,528, May 1971.

5. McDonnell Aircraft Co.: Lift Fan V/STOL Transport Control System Investigation, Phase II, Moving Base Simulation. NASA CR-114,529, Nov. 1971.

6. McDonnell Aircraft Co.: Lift Fan V/STOL Transport Flight Control System Development Continuation, Vol. I, Interim Simulation Experiment. NASA CR-114,540, July 1972.

7. McDonnell Aircraft Co.: Lift Fan V/STOL Transport Flight Control System Development Continuation, Vol. II, Analytical Studies and Display Development. NASA CR-114,643, Sept. 1973.

8. McDonnell Aircraft Co.: Lift Fan V/STOL Transport Flight Control System Development Continuation, Vol. III, Total System Simulation Experiment. NASA CR-114,683, Jan. 1974.

9. Eldridge, W. M.; Lambregts, A. A.; and Spitzer, R. E.: Piloted Simulation of the Boeing R 984-33 V/STOL Research Aircraft, Vol. I, Analysis of Flight Control Systems and Flight Characteristics. NASA CR-114,557, Feb. 1973.

10. Eldridge, W. M.; Lambregts, A. A.; and Spitzer, R. E.: Piloted Simulation of the Boeing R 984-33 V/STOL Research Aircraft, Vol. II, Results of Piloted Simulation. NASA CR-114,558, Feb. 1973.

11. Lebacqz, J. V.; and Aiken, E. W.: Results of a Flight Investigation of Control-Display Interactions for VTOL Decelerating Descending Instrument Approaches Using the X-22A Aircraft. NASA TM X-62,464, 1975.

12. Anon.: Flying Qualities of Piloted V/STOL Aircraft, Military Specification. MIL-F-83300, Dec. 13, 1970.

13. Anon.: V/STOL Handling-Qualities Criteria I - Criteria and Discussion. AGARD R-577-70, Dec. 1970.

14. Greif, Richard K.; Fry, Emmett B.; and Gerdes, Ronald M.: Effect of Stabilization on VTOL Aircraft in Hovering Flight. NASA TN D-6900, Aug. 1972.

15. McDonnell Aircraft Co.: A Full Scale Test of a New V/STOL Control System Energy Transfer Control (ETC). NASA CR-114,541, June 1972.

16. McFarland, Richard E.: A Standard Kinematic Model for Flight Simulation at NASA-Ames. NASA CR-2497, Jan., 1975.

17. Sammonds, Robert I.; and Stinnett, Glen W., Jr.: Hazard Criteria for Wake Vortex Encounters. NASA TM X-62,473, Aug. 1975.

18. Corliss, Lloyd D.; and Dugan, Daniel C.: A VTOL Translational Rate Control System Study on a Six-Degrees-of-Freedom Motion Simulator. NASA TM X-62,194, Oct. 1972.

1. Report No.	2. Government Accession No.	3. Recipient's Catalog No.
NASA TP-1040		

4. Title and Subtitle	5. Report Date
STUDY OF THE APPLICATION OF AN IMPLICIT MODEL-FOLLOWING FLIGHT CONTROLLER TO LIFT-FAN VTOL AIRCRAFT	November 1977
	6. Performing Organization Code

7. Author(s)	8. Performing Organization Report No.
Vernon K. Merrick	A-6712

9. Performing Organization Name and Address	10. Work Unit No.
NASA Ames Research Center Moffett Field, Calif. 94035	505-10-32
	11. Contract or Grant No.

12. Sponsoring Agency Name and Address	13. Type of Report and Period Covered
National Aeronautics and Space Administration Washington, D. C. 20546	Technical Paper
	14. Sponsoring Agency Code

15. Supplementary Notes

16. Abstract

An implicit model-following flight controller is proposed. This controller is relatively simple in concept: it provides an input/output relationship that is approximately that of any selected second-order system; it provides good gust alleviation; and it is self-trimming.

The flight controller was applied to all axes of a comprehensive mathematical model of a lift-fan V/STOL transport. Power management controls and displays were designed to match the various modes of control provided by the flight controller. A piloted simulation was performed using the Ames six-degree-of-freedom simulator.

The fixed-operating-point handling qualities throughout the powered lift flight envelope received pilot ratings of 3-1/2 or better. Approaches and vertical landings in IFR zero-zero conditions received pilot ratings varying from 2-1/2 to 4 depending on the type of approach and weather conditions.

17. Key Words (Suggested by Author(s))	18. Distribution Statement
VTOL handling qualities Flight controller design Landing approach Simulation (piloted)	Unlimited STAR Category - 08

19. Security Classif. (of this report)	20. Security Classif. (of this page)	21. No. of Pages	22. Price*
Unlcassified	Unclassified	183	$7.50

* For sale by the National Technical Information Service, Springfield, Virginia 22161

*U.S. GOVERNMENT PRINTING OFFICE: 1977 - 735-078/57